Editorial corner – a personal view
Interphase engineering in polymer composites: Challenging the devil…

A. Pegoretti[1], J. Karger-Kocsis[2]*

[1]University of Trento, Department of Industrial Engineering, Via Sommarive 9, 38123 Trento, Italy
[2]Budapest University of Technology and Economics, Faculty of Mechanical Engineering, Department of Polymer Engineering, and MTA–BME Research Group for Composite Science and Technology, Műegyetem rkp. 3, H-1111 Budapest, Hungary

The aphorism 'God made the bulk; surfaces were invented by the devil' is credited to Wolfgang Pauli, Nobel Prize in Physics in 1945. The interphase is a key issue for polymer composites since it guarantees the necessary stress transfer from the 'weak' matrix to the 'strong' reinforcement. Since the interphase is the key factor of composite performance, its engineering design is being under spot of interest from both academia and industry. New impetus to interphase engineering was provided by the worldwide extensive research on polymer nanocomposites. The mechanical properties of this new generation of materials did not fully meet the expectations, which might have been exaggerated as far as the replacement of traditional reinforcements by nanoadditives is concerned.

However, nanofillers and nanocomposites have recently attracted great interests as potential solutions to some acute problems with composites' interphase. Among these problems the detection of failure/damage, their eventual healing, poor out-of-plane performance including low delamination resistance and inherently missing properties should be mentioned. Failure/damage start at the interface or in the interphase. Therefore, creating a 'smart' interphase the properties (e.g. electrical conductivity, piezoresistivity…) of which change with progressing damage would allow a structural health monitoring (DOI: 10.1016/j.carbon.2012.04.008). The load bearing of traditional fibers can be promi-

nently improved when nanoscaled additives (nanotube, graphene, clay…) are deposited on their surfaces by suitable manners. The related 'hierarchical' fibers enhance the delamination resistance, support a more homogenous stress distribution and improve other out-of-plane properties. The encapsulation strategy of healing agent was successfully adapted for the interphase by creating and depositing submicron-size capsules onto the fiber surface (DOI: 10.1016/j.compscitech.2013.02.007).

Most of the above concepts, well summarized in recent reviews (DOI: 10.1016/j.pmatsci.2015.02.003 and DOI: 10.1016/j.compscitech.2014.07.005), have been conceptually proved at a laboratory level and need to be up-scaled to in industrial praxis. New strategies to overcome deficiencies with polymer composites are still needed. However, the interphase engineering is not yet finished (the devil has his fingers still there…) – why not to play in this exciting research arena?

Prof. Dr. Alessandro Pegoretti
Member of Int. Adv. Board

Prof. Dr. Dr. h.c. József Karger-Kocsis
Editor-in-Chief

*Corresponding author, e-mail: alessandro.pegoretti@unitn.it

A review on electrospun bio-based polymers for water treatment

T. C. Mokhena[1,3]*, V. Jacobs*[1,2*]*, A. S. Luyt*[3,4]

[1]CSIR Materials Science and Manufacturing, Polymer and Composites, Port Elizabeth, South Africa
[2]Department of Chemistry, Faculty of Science, Nelson Mandela Metropolitan University, Port Elizabeth, South Africa
[3]Department of Chemistry, Faculty of Natural and Agricultural Sciences, University of the Free State (Qwaqwa Campus), Phuthaditjhaba, South Africa
[4]Center for Advanced Materials, Qatar University, Doha, Qatar

Abstract. Over the past decades, electrospinning of biopolymers down to nanoscale garnered much interest to address most of the millennia issues related to water treatment. The fabrication of these nanostructured membranes added a new dimension to the current nanotechnologies where a wide range of materials can be processed to their nanosize. Electrospinning is a simple and versatile technique to fabricate unique nanostructured membranes with fascinating properties for a wide spectrum of applications such as filtration and others. These nanostructured membranes, fabricated by electrospinning, were found to be of a paramount importance because of their advanced inherited properties such as large surface-to-volume ratio, as well as tuneable porosity, stability, and high permeability. The extensive research conducted on these materials extended the success of electrospinning not only to bio-based polymer nanofibres, but to their hybrids and their derivatives. The technique also created avenues for advanced and massive production of nanofibres. This paper reviews the recent developments in the electrospinning technique. Electrospinning of biopolymers, their blends and functionalization using metals/metal oxides, and the potential applications of electrospun nanofibrous membranes in water filtration are discussed.

Keywords: nanomaterials, electrospinning, nanofibre materials, biopolymers, biocomposites

1. Introduction

The exponential growth of the population, water scarcity, and man undesirable practices have spurred efforts to develop innovative technologies to produce high quality water at relatively low cost and energy [1, 2]. Urbanization, industrial activities, waste dumping, and alien plants are common practices contributing to the current environmental crisis [3, 4]. For example, the mining industries, although serving as a one of the driving forces of many countries' economy, dump billions of tons of hazardous materials into the environment. The emissions of such pollutants into the air and water are seriously considered as primary factors to the common respiratory, neural and intestinal diseases. A safe and healthy environment is a priority that needs immediate intervention in both developing and well-developed countries [5, 6]. These challenges call upon novel and effective technologies to address the current environmental issues, either by protecting the environment and current water sources or by producing high quality water from available sources (oceans and wastewater) without harmful by-products [5, 6].

Over the past decades, the production of nanofibres gained much interest and attention to develop innovative materials with properties that are suitable to address the challenges related to water treatment. Nanofibres are a new class of nanomaterials with

inherited properties such as the large surface-to-area ratio, high porosity, flexibility, stability, and permeability. Several routes have been utilized to fabricate these nanostructured materials from different materials such as drawing, templates synthesis, phase separation, self-assembly, electrospinning etc. [8–10]. Amongst them, electrospinning technique received a considerable interest due to its simplicity, efficiency and versatility in producing nanofibres [8–10]. In the electrospinning process, an electric field is introduced to the solution (or melt) to produce extremely long fibres with diameters down to a few nanometers. Almost all soluble materials can be electrospun into nanofibres. These include synthetic and natural polymers, polymer alloys and polymers loaded with chromophores, nanoparticles, or active agents, as well as metals and ceramics [8]. This technique gained much interest in the past two decades not only because of its simplicity, but also due to its feasibility to produce consistent long nanofibres with desirable properties which cannot be fabricated through other techniques. The resulting nanostructured materials with an extremely large surface to volume ratio, and engineered porosity, malleability, stability and functionality, have been applied in a wide variety of fields [8, 10].

Research has escalated in electrospinning of biopolymers, their hybrids and derivatives, for various applications because of their unique properties such as renewability, biodegradability and their abundant availability [7, 11]. Generally, biopolymers are defined as polymeric biomolecules generated by living organisms. They are categorized according to the monomeric units that build up the complex polymeric structure, namely polynucleids (ribonucleic acid (RNA) and deoxyribonucleic acid (DNA)), polypeptides (proteins), and polysaccharides (cellulose, and chitosan). The electrospinnability of most biopolymers is still a challenge because of numerous factors [11–15]. These include their rigid structure, high conductivity, high surface tension, and their gelation at fairly low concentrations. Several routes have been proposed to improve their electrospinnability such as the use of copolymers [16] and the modification of the processing device [13, 15].

A number of biopolymers, such as DNA [17], silk [18], chitosan [19], collagen [20], fibrinogen [21], gelatin [22], hyaluronic [13, 15], cellulose [23], and alginate [24] were successfully electrospun into nanofibres for their application in various fields such as filtration, biomedical and tissue engineering. Only few of them were, however, applied in air and water treatment [25–27]. Their readily water solubility and biodegradation are common factors that disrupt the success of electrospun bio-based nanofibrous membranes, especially in water filtration. The addition of nanoparticles [28, 29], functionalization and the use of co-polymers [30] to enhance stability and biocidal activity have been the major object of research in electrospun nanofibrous membranes (ENM).

Even though there is some success in electrospinning a broad spectrum of materials since its invention a century ago, the throughput of nanofibres is still a limiting factor in the industrial production for commercial practice. However, there were several modifications on the classical laboratory electrospinning setup and new technological innovations to increase the production rate of the electrospun nanofibres. These technologies include bubble electrospinning [31], multi-jet [32] and bowl electrospinning [33].

In this review we discuss the fabrication of electrospun biobased nanofibres, their hybrids and derivatives using electrospinning technique. The factors that influence the properties of the electrospun nanofibres, and their functionalization using various methods, to enhance their performance in water and wastewater treatment, are discussed. We also look at other innovative technologies to modify classic electrospinning and to improve the properties and production of electrospun nanofibres.

2. Electrospinning process
2.1. Historical background on electrospinning
Electrospinning was initially not considered a viable technique because of difficulties with drying and collection of the nanofibres during its execution. However, it gained scientific and commercial publicity in the past two decades. Raleigh was the first to discover electrospinning in 1897, and a thorough study on electrospraying was done by Zeleny in 1914 [34, 35]. Cooley [36] was one of the scientists that patented the electrospinning technique about 100 years ago. However, the electrospinning technique gained enormous interest later in the early 1990s, thanks to the Reneker group. The group studied the mechanisms involved during electrospinning which spurred much interest in the nanotechnology arena because of the size of the resulting nanofibres. In Germany (in the early 1930s to 1940s), Formhals published a series

of patents based on the process and apparatus to execute this simple and versatile technique [37–39]. Later in the 1960s, Taylor studied the initiation of the jet from the drop on the apex of the needle when an electric field was applied. The conical shape formed because of the electric forces surmounting the solution surface tension was later named after him, '*Taylor cone*' [10, 40]. By that time the technique was called '*electrostatic spinning*'. The considerable interest in the electrospinning technique in the 1990s resulted in the new name '*electrospinning*' [40, 41]. The name '*electrospinning*' was then accepted and is now widely used in the literature as a description of this viable technique to produce ultrathin fibres from a polymer solution or melt through application of electrical forces. The success of this technique is evidenced by the number of publications each year by universities, research institutes, and about 20 commercial enterprises, who are involved in the application of electrospun nanofibres (Donalson company Inc., Espin technologies Inc., and Elmarco etc.) [31].

2.2. Fundamentals of electrospinning

Almost all soluble materials can be electrospun into nanofibres, with diameters ranging from several micrometres down to tens of nanometres. Over 200 polymers were successfully electrospun into long ultrathin fibres for a wide variety of applications, mostly from polymer solutions [40, 42]. A classical setup of the electrospinning technique is shown in Figure 1. It consists of a spinneret with a metallic needle, a syringe pump, a high voltage power supply, and a grounded collector [8, 40, 43]. Horizontal and vertical setups are commonly adapted configurations, but in some cases upward electrospinning was also utilized [44].
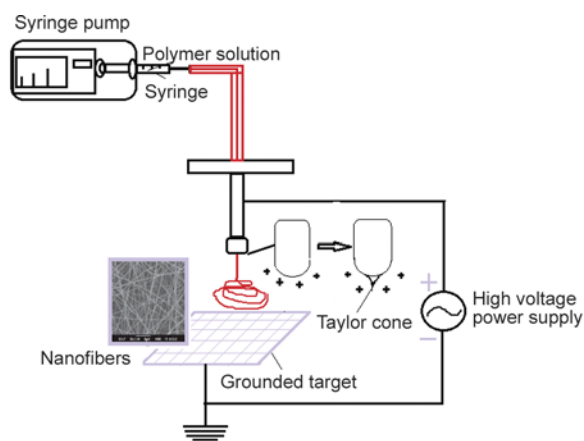

Figure 1. Schematic representation of electrospinning apparatus
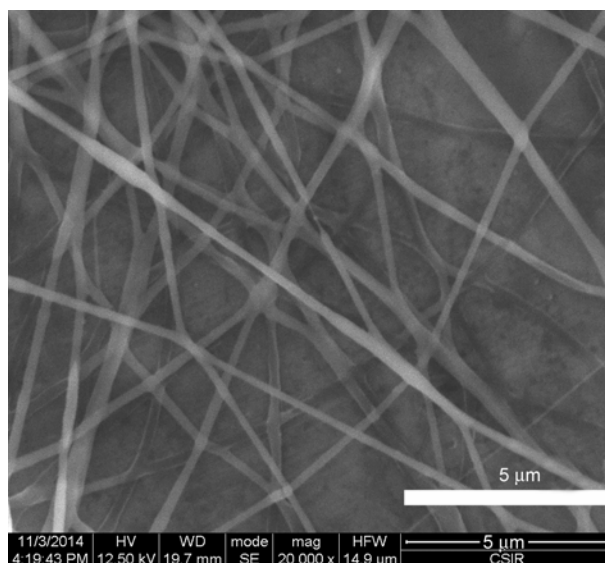

Figure 2. SEM micrograph of alginate nanofibres

Basically, the sol-gel, blend, composite, or polymer solution/melt is loaded in the syringe is driven to the needle tip by a syringe pump, forming a hemispherical droplet at the tip. A voltage (5–40 kV) is applied to the solution on the needle which causes the drop to stretch into a conical shape (known as Taylor cone) [45]. Depending on the viscosity of the solution (which must be sufficient enough to withstand stretching and whipping to avoid any varicose breakup, which forms nanoparticles) an electrified jet is formed and moves towards to an oppositely charged collector. During this trip the solvent evaporates and the jet solidifies to form nonwoven webs on the collector. The jet is only stable from the tip of the needle, whereafter instability starts. Interestingly, this technique offers the processor a platform to control the resulting morphology and structure of the nanofibres through changing of solution properties and physical parameters. Many well-organized papers describe in detail the effect of these parameters [8, 34, 43, 45]. Furthermore, the solvent and co-solvent play a significant effect in determining the resulting morphology and structure. The resulting nanofibres have high porosity, large surface to volume ratio, and good mechanical properties, which open doors for a wide variety (Figure 2) [8, 46].

3. Factors affecting the electrospinning process

Although electrospinning is a simple and straightforward technique, there are several parameters that are important (solution properties, processing parameters, and ambient conditions), that must be consid-

ered since they significantly affect the quality of the resulting nanofibrous membranes. The solution properties include conductivity, concentration, surface tension, and molecular weight; the processing parameters include voltage, tip-to-collector distance, collector shape, diameter of the needle and feeding rate; the ambient conditions such as humidity and temperature of the surroundings are also important.

3.1. Solution parameters

Despite the fact that all these parameters have a significant effect on the resulting product, the solution properties serve as a more decisive parameter. The solution concentration and/or viscosity have to be sufficient enough to prevent the varicose breakup of jet to allow a continuous stream in the spinning solution. Both are directly dependent on the polymer molecular weight which defines the entanglement of the chains to withstand the Coulombic stretching force to prevent the jet breakage into droplets by surface tension [47–50]. The optimal concentration and/or viscosity are required because too high concentration/viscosity may result in larger diameter and clogging of the capillary [47–50]. Nevertheless, the gelation (highly viscous) at fairly low concentrations (below entanglement concentration) disrupts the electrospinnability of the biopolymers, resulting in collection of droplets. Moreover, most of these polymers are inherently polyelectrolytic (e.g. alginate and chitosan) which increases the solution conductivity. This also contributes to the difficulties in electrospinning of natural polymers from their aqueous solutions [47, 51]. Several modifications have been done

to improve their spinnability. The use of copolymers such as poly(vinyl alcohol) (PVA) and polyethylene oxide (PEO) was found to be suitable to reduce the conductivity of the natural polymeric spinning solutions [47, 52–54].

On the other hand, some solvents may be added either to increase [55, 56] or decrease the electric properties of the spinning solution [12, 19]. The most used solvents in electrospinning are shown in Table 1.

Solvents with good volatility, moderate vapour pressure, moderate boiling point, good conductivity and good cohesion with the polymer is important in the electrospinning process [12, 56–61]. The solubility of the polymer, however, does not guarantee the solution spinnability [12]. For example, partial solubility in a solvent can result in smooth bead-free nanofibres. Some reports suggested that a single solvent system could result in beaded nanofibres, whereas the addition of partially soluble solvent could improve the nanofibre morphology [57, 59, 61].

3.2. Setup parameters

Essentially, the electrospinning process begin directly at the point at which electrostatic forces overcomes the solution surface tension and viscoelastic forces. Typically, a critical voltage is required to eject the charged jet from the drop at the nozzle (Taylor cone) [15, 62]. For instance as the concentration, or similarly, the viscosity increases, higher electrical forces are required to overcome both the surface tension and the viscoelastic forces for fibre stretching. The size of the droplet at tip of the nozzle depends on

Table 1. Properties of solvents and liquids used in electrospinning

Solvent	Density [g·cm^{-3}]	Viscosity [cP]	Boiling point [°C]	Dipole moment [D]	Dielectric constant	Surface tension [mN·m^2]
Acetic acid	1.05	1.12	118.0	1.68	6.15	26.9
Acetone	1.39	0.32	78.0	2.88	27.0	21.4
Chloroform	1.50	0.53	61.6	1.15	4.80	26.5
Dichloromethane	1.33	0.41	40.0	1.60	8.93	28.1
Dimethylacetamide	0.94	1.96	165.0	3.72	37.8	36.7
Dimethylformamide	0.99	0.80	153.0	36.70	38.3	37.1
Dimethyl sulfoxide	1.10	2.00	189.0	3.90	46.7	43.0
Ethylene glycol	1.11	16.13	197.0	2.20	37.7	47.0
Formamide	1.13	3.30	211.0	3.37	110.	59.1
Formic acid	1.22	1.57	101.0	1.41	57.9	37.6
Glycerol	1.26	950	290.0	2.62	42.5	64.0
Hexafluoro isopropanol	1.60	1.02	58.2	1.85	16.7	16.1
Methanol	0.79	0.54	65.0	1.70	33.0	22.7
Tetrahydrofuran	0.89	0.46	66.0	1.75	7.52	26.4
Triflouroethanol	1.38	1.24	74.0	2.52	8.55	43.3
Water	1.00	1.00	100.0	–	21.0	25.2

the feeding rate as well as the needle shape and diameter [13, 62–64]. Therefore, these factors influence the forces acting on the drop which contribute to the jet initiation and stretching. The optimal distance is required to give the electrified jet sufficient time for nanofibre dryness [65–67]. At longer tip-to-collector distance (TCD), the fibre will have sufficient time to solidify before reaching the collector, but if the distance is too long, either beaded fibres or no fibres are collected [65]. Similarly, when the distance is too short, it reduces the flight distance and solvent evaporation, and increases electric field, which results in beads.

One of the essential aspects in electrospinning is the type of collector used. These collectors act as a conductive substrate to collect the charged fibres. Aluminium foil [61] is usually used to collect the nanofibres. However, due to the difficulty to transfer the nanofibres from this collector [13, 15], other collectors such as liquid baths [68], metal plates [69], grids [70], parallel or gridded bars [71, 72], rotating disks [73], and rotating drums [74] were investigated as possible collectors. Different collectors used in electrospun nanofibres were recently reviewed in [46]. The collectors specifically used in electrospun biopolymers as well as the optimal conditions are summarized in Table 2. The collectors are often used to engineer and design the structure and morphology of the fibres. For example, Matthews *et al.* [75] observed that collagen nanofibres, collected at lower speeds, were random filaments, whereas collection at higher speeds resulted in deposition of the nanofibres along the rotation axis.

3.3. Ambient conditions
Ambient conditions, temperature and humidity, can also affect the morphology and diameter of the nanofibres [77]. It was deduced that the increase in temperature reduces the viscosity of the solution and enhances the solvent evaporation, which results in thinner nanofibres [89]. Depending on the system under investigation, two antagonistic effects are observed: (1) reduction in fibre diameters, and (2) increase in diameter which may result in fusion of the nanofibres [90]. Tripatanasuwan *et al.* [91] reported that an increase in relative humidity resulted in smaller diameters of the nanofibres. They stated that at the lower relative humidity the rate of solvent evaporation increased, with the opposite effect at higher humidity. Furthermore, the humidity can generate pores of different size and depth depending on the molecular weight of the polymer [92].

4. Recent advances in electrospinning techniques
During the past years research on various advancements and modifications on standard needle electrospinning (SNE) with the aim to scale up the nanofibres production, to enhance the stability of the electrospinning technique, and to engineer patterns and desired morphologies of the resulting nanofibres for various applications, has escalated. The production rate has been one of the inhibiting factors for the commercial implementation and industrial viability of the electrospinning processing technique. In SNE the mass production rate is approximately 0.01–0.1 g·h^{-1}, where the nanofibre source is a single jet arising from a single needle apex through which the polymer solutions is ejected. Various innovative ways to produce electrospun nanofibres with enhanced functionalities were developed. These advances, namely multi-needle and needleless electrospinning, gas-jet electroblowing spinning, and co-axial electrospinning (Table 3) are described in the following sections. However, most of these technological advances are mostly applied in synthetic polymers as deliberated in Table 3.

4.1. Multi-needle electrospinning
An increase in the number of nozzles is the most convenient way to increase the production rate of the nanofibres [100, 101]. However, there are some drawbacks associated with multi-needle electrospinning, such as complicated design and large operating space, and repulsion between the nanofibres that causes the uneven deposition of the nanofibres [102]. Furthermore, the clogging of needles discourages the industrial viability of multijet spinning. In industry the needles would require regular cleaning, which would result in complex processes and too much labour. Therefore, several modifications were suggested to overcome the nanofibre repulsions without compromising the production rate. For example, Kim and Park [103] electrospun alginate/PEO nanofibres using multi-nozzle electrospinning with an extra auxiliary electrode to alleviate the repulsion between the jets. PEO (2 wt%)/alginate (2 wt%) doped with lecithin (0.7 wt%) as surfactant produced smooth nanofibres using SNE. The same composition was used for a comparison between nanofibres

Table 2. The optimal conditions of electrospun biopolymer nanofibres

Type of collector	Polymer system	Solvent system	Conditions	Morphology	Diameters	Reference
	Cellulose ($DP = 210$)	NMMO/water	9 wt%, 15–20 kV, 15 cm, 0.05 mL·min⁻¹	Film	–	[76]
	Alginate (37 kDA)/PEO (600 kDA)	Distilled water	Alginate-PEO-Pluronic (10.0:0.8:1.5 wt%), 12 cm, 0.5 mL·h⁻¹, 30% relative humidity (*RH*)	Three dimensional (3D)	237±33 nm	[77]
	Carbomethyl cellulose (CMC)/PEO (1:1 ratio)	1:1 water:ethanol	8%, 20 cm, 35 kV	Uniform	200–250 nm	[11]
	Hydroxypropyl methyl cellulose (HPMC) (with 29.2% methoxy and 8.8% hydroxypropyxy)	1:1 water:ethanol	2.14%, 20 cm, 35 kV	Uniform	128 nm	[11]
	Cellulose ($DP = 1140$)	LiCl/DMAc	3 wt%, 15–20 kV, 15 cm, 0.05 mL·min⁻¹	Film	–	[76]
	Chitosan (106 kDA)	90% Acetic acid	7%, 3 kV·cm⁻¹, 20 μlL·min⁻¹	Uniform	180 nm	[67]
		90% Acetic acid	5 wt% (hydrolyzed in 50% NaOH at 95°C for 48 hours), 16 cm, 17 kV, 8·10⁻² mg·h⁻¹, $ID = 0.7$ mm	Uniform	50–250 nm	[78]
	Chitosan	80% Acetic acid	7 wt%	Uniform	250±76 nm	[78]
		70% Acetic acid	7.5 wt%	Uniform	284±94 nm	[78]
Aluminium foil	Chitosan ($DD = 85\%$)/agarose	TFA/DCM (7/3 v/v)	7% (50% of agarose), 15 kV, 12 cm, 0.5 ml·h⁻¹	Cylindrical	0.14±0.09 μm	[79]
	Chitosan (8–20 kDA)/PLA (5 kDA)	TFA	17.4 wt% (1:20 chitosan:PLA)	Uniform	–	[80]
	Carboxymethyl chitosan (89 kDa, 0.36 DS)/PVA (124–186 kDa, 87–89% hydrolysed)	Water	8% mixture of 60/40 (CMCS/PVA) with 0.5 Triton X100, 10–15 kV, 17–20 cm	Uniform	135 nm	[81]
	Hexanoyl chitosan	Chloroform	14 wt%, viscosity = 956 mPa·s, 1 kV·cm⁻¹	Ribbon-like	3.93 μm	[82]
	Quaternized chitosan(QCh)/PVP	Distilled water	20 wt%(QCh)/PVP (4:1), 2.2 kV·cm⁻¹, viscosity = 25550 cP,	cylindrical	1.53±0.48 μm	[83]
	PEG-N,O-chitosan ($DS = 1.50$)	75/25 v/v (THF/DMF)	15% with 0.5 wt% Triton X100, 10–15 kV, 17–20 cm	Uniform	162 nm	[84]
	Gelatin	Distilled water	At 37°C, 14 cm, 13 kV	Beaded cylindrical	295 nm	[85]
	Gelatin	Formic acid	8 wt%, 7.5 cm, 1 kV·cm⁻¹	smooth	79±14 nm	[66]
	Thiolated HA (158 kDA)/PEO (900 kDA)	Dulbecco's modified eagle's medium	HA-DTPH (2.5%, w/v)/ PEO (2.5%, w/v), 20 μL·min⁻¹, 10 cm, 18 kV	3D	90±15 nm	[86]
Rotating mandrel	N-carboxyethyl chitosan/PEO/AgNO₃	Formic acid	37 kV, 14 cm, 800 rpm, 1.1 mL·h⁻¹	Self-bundled/yarn	460±87 nm and 200±40 nm	[87]
	Collagen (calf skin type 1)	HFIP	0.083 g·mL⁻¹, 25 kV, 125 mm, 5.0 mL·h⁻¹	3D	100–40 nm	[75]
	Ethyl cellulose	TFA	10 wt%, 20 kV, 5 cm, 0.01 mL·min⁻¹	Uniform	100 nm	[88]
	Cellulose acetate (CA)(40 kDA)	DMAc/acetone(1/2)	10%, 15 cm, 20 kV	Uniform	420 nm	[29]
Liquid bath	Cellulose	1-butyl-3-methylimi-dazolium chloride	10% cellulose, 15 cm ethanol bath, 15–20 kV, 0.03–0.05 mL·min⁻¹	Highly-branched	8.65±7.70 μm	[14]
	Alginate (3500 cps)	Glycol/water (2/1)	2 w/v%, 28 kV, 12 cm, copper mesh in 10 wt% of CaCl₂ in ethanol, 105 μL·min⁻¹	Uniform	200 nm	[12]
Rotating collector immersed in liquid bath	Cellulose ($DP = 210$)	NMMO/water	9 wt%,15–20 kV, 15 cm, 0.01 mL·min⁻¹, 1.2 rpm, water bath	Uniform	300 nm and	[76]
	Cellulose ($DP = 1140$)	NMMO/water	2.5 wt%, 15–20 kV, 15 cm, 0.01 mL·min⁻¹, 1.2 rpm, water bath	Uniform	250–750 nm	[76]

Table 3. The novel advances on standard laboratory electrospinning

Technique	Polymer concentration [wt%]	Average diameter [nm] and voltage[kV]	Throughput [g·h^{-1}]	Reference
Bowl	6 (PEO) and 12 (PCL)	268±25 at 16 and 344±97 at 30	7.0	[31]
Bubble	10 (PVA)	111–48.6 at 10–30	–	[33]
Conical wire coil	9 (PVA)	275±113 at 50	2.8	[93, 94]
Gas jet	8 (PVA)	220 at 25	1.1	[95]
Multi-jet	15 (PVA)	230000	0.66–0.72	[96]
Nanospider	15 (PU)	193 at 81.2	96.6[a]	[97]
Porous tubular	20 (nylon-6)	170.6±5.0 at 20	5.0	[98]
Splashing	9 (PEO)	368±45.37 at 60	3.0	[99]

[a]Units g·h^{-1}·m^{-1}

produced with and without auxiliary electrodes in multi-nozzle spinning. The auxiliary supported multi-nozzle showed a higher production rate and smoother nanofibres with diameters of 174±62 nm compared to unsupported spun nanofibres that had diameters of 246±62 nm. A wide variety of multijet electro-spinning heads, namely series, elliptic, concentric, line, rectangular and matrix can be utilized to produce nanofibres [96]. The biodegradable blend of cellulose acetate and PVA was prepared by varying the ratio of the jets from 1:3 to 3:1. The average diameters of the fibres increased (220 to 290 nm) with a decrease in the number ratio of PVA/CA from 3:1 to 1:3. The tensile strength and the modulus increased from 7.0 to 9.4 MPa and 18.1 to 34.0 MPa with an increasing the number ratio of the jets of PVA/CA from 1:3 to 3:1 [26].

4.2. Needleless electrospinning
4.2.1. Confined needleless electrospinning
One of the promising processes to scale-up the nano-fibre production is needleless electrospinning. This technique avoids the issues of clogging and cleaning of the needles and the complexity of the multi-axial spinning setup. The needleless process is divided into two categories depending on the feeding system: confined feeding and unconfined feeding. The difference between the confined and unconfined needleless electrospinning is the fact that in confined electrospinning the electrospun fluid is enclosed in a reservoir such as an insulating tube [98, 104, 105] or any other material in which the polymer is protruded, whereas in unconfined systems there is no reservoir for the spinning solution and the droplets are projected naturally from the surface of the solution.

The replacement of the needles in multi-jet spinning is the most convenient way to resolve the complexity and difficulties without compromising the mass throughput [92, 99]. In this route the polymer fills a porous hollow tube [93, 104]. The drilled holes on the surface of the tube can be made in different configurations. The positive electrode is immersed into the solution and by using a small pressure the polymer solution is driven through the holes. The production rate is 3–250 times that of the standard electrospinning (SNE), while the nanofibre diameters may range from 300 nm to several hundreds of microns. Dosunmu *et al*. [98] used a porous polyethylene tube with pore sizes 10–100 μm as reservoir for a 20 wt% nylon 6 spinning solution. The polymer solution was pushed with air pressure to form multiple jets on the porous surface. The jets protruding from the tube surface were collected on a surrounding vertically placed grounded co-axial wire mesh. The resulting nanofibres have equivalent mean diameters to those produced by SNE, with a much broader distribution. Moreover, different polymers can be electrospun via this method and the porous tube can be made from different materials such as ceramic.

Rotary-jet spinning (RJS) is composed of a rotating motor, a reservoir and a stationary or rotating collector [106]. The polymer solution is loaded into a punched reservoir, either continuously or once in one measurement or production. The perforated reservoir has two side wall orifices which rotate vertically to the surrounding collector. Because of the centrifugal forces on the solution, the polymer jets are forced out of the reservoir through the punched side wall, and subsequent jet extension and dryness yield three dimensions of nanofibres. The advantages include the use of low voltages, the production of three dimensional (3D) morphologies, controlled porosity, independence of solution conductivity, and larger mass production than SNE. Various polymer solutions (poly(lactic acid) (PLA) in chloroform, polyethylene oxide (PEO) in water,

poly(acrylic acid) (PAA) in water, gelatin in acetic acid were successfully electrospun to three dimensional nanofibres by Badrossamay *et al.* [106]. They indicated that with the control over the spinning solution concentration and rotating speed the morphology of the nanofibres can be tuned.

4.2.2. Unconfined needleless electrospinning

Unconfined needleless electrospinning is the electrospinning the solutions naturally from a liquid surface. Yarin and Zussman [107] prepared nanofibres by a needleless method using the ferromagnetic liquid sub-layer below the polymer solution. It was established that the nanofibres can also be produced without a ferromagnetic sub-layer, but at a much higher voltage. The disadvantage of this method is that the number of jets and their location cannot be controlled since the jets protrude naturally from the liquid surface. Nevertheless, they produced nanofibres with diameters ranging from 200 to 800 nm.

Another technique involves the use of charged cylindrical rotators dipped in the spinning solution [108, 109]. This is the only technique that was applied industrially since research on the enhancement of the production rate started, and is known as nanospider™ [97]. The technique involves a polymer solution in a container and a cylindrical charged metal rotating at a certain speed. The charged rotating metal is partially immersed in the solution. When the solution is electrified by the voltage supplied to the cylindrical rotators, the multiple polymer jets are launched from the circumference of the cylindrical rotators to the grounded collector. Nanofibres with average diameters between 50 and 200 nm are produced at a rate of 2.53 g·h^{-1}, compared to conventional electrospinning with a rate of 0.01–0.1 g·h^{-1}. Various shapes of rotating nozzles, such as disk and spiral coils, can be used to generate narrow distribution nanofibres with a higher mass production than SNE. A rotating spiral coil made of metal wire was used by Wang *et al.* [94] to eject the jets from the surface of each spiral wire. Depending on the concentration and applied voltage, ultrafine nanofibres were produced. Nanofibres with narrower distribution were generated with the mass production increasing with voltage from 2.94 to 9.42 g·h^{-1} for 45 and 60 kV, respectively. The disadvantage of these nozzle processes is the uneven electric field distribution on the spiral wire. Niu *et al.* [110] com-

pared a rotating disk and cylinder to envisage the effect of the shape on the resulting nanofibre production. They indicated that the disk nozzle requires a lower voltage to initiate the fibre production than the cylinder nozzle, with finer nanofibre than those from the cylinder at similar conditions. The mass production was equivalent for both the rotating disk and cylinder, but higher than that of SNE.

Another approach is the polymer solution dripping from the reservoir onto a rotating cylinder, known as splashing electrospinning. In this case the reservoir is held horizontal to a charged cylinder rotating at a certain speed. With a controlled speed, gap distance, and solution parameters the nanofibre structure can be tuned with enhanced production (24–45 times) compared to SNE [99] (Table 3). The influence of processing and solution properties on the resulting nanofibres via splashing was studied by Tang *et al.* [111]. Increased concentration was found to increase the mean diameter of the fibre, whereas an increase in the voltage decreased it. A decrease in mean diameter was reported with an increase in both rotating speed and gap distance. They found that using statistical analysis (analysis of variance (ANOVA)), the optimal conditions for fine nanofibres with narrower distribution (PEO in water) were as follows: concentration (6.94 wt%), voltage (12.38 kV), gap distance (3.5 cm), and rotational speed (0.76 rpm). Also, nanofibres with mean diameters ranging from 100 to 400 nm, were obtained.

In the bowl-edge unconfined process, the primary interaction between the electric field and the polymer solution caused fluid perturbations within the bath reservoir filled with polymer solution [31, 41]. These fluid perturbations were responsible for Raleigh-Taylor instabilities formed by gravity forces in the polymer solution. The polymer solutions, due to the instabilities, produced jets protruding from the edge of the bowl which are similar to the jets ejected from the SNE. The bowl has a thin-lipped edged structure where the droplets are ejected to the concentric collector. At the beginning, a high voltage is supplied and then the voltage to initiate the jet formation is reduced to a lower operational value. Stable nanofibres are formed on the collector with high quality nanofibres similar to the optimal nanofibres from SNE, with 40 times faster production.

Bubble electrospinning is primarily based on the bubbles on the surfaces of polymer solutions [28]. These bubbles serve as the droplets in which the

Taylor cone is formed. The gas tube and metal electrode are inserted in the solution to produce the bubbles. When the gas is blown into the solution, the bubbles are formed (in a spherical shape) on the surface of the solution, and when the voltage is applied the bubble shape changes into a conical shape. When the voltage is above a critical value, multiple jets are ejected from the bursting bubble to the collector, while new bubbles are formed and broken again – the process repeats itself until the solution is depleted.

Another process necessitates the drops of a polymer solution dripped onto a standard spin coater followed by rotation of the chuck [112]. The fibres are produced by the instability of the spin-coated liquid that results from the competition of the centrifugal force and the Laplace force induced by the surface curvature. By adjusting the solution parameters (concentration, spinning speed, surface tension) and solvent evaporation rate, different polymers can be processed to their nanofibres. Dabirian *et al.* [113] modified the centrifugal spinning method by enclosing a nozzle to avoid the influence of the surrounding air on the dryness of the protruding polymer solution. They also applied a voltage which was not applied in the centrifugal spinning proposed by Weitz *et al.* [112]. They obtained uniform aligned nanofibres with an average diameter of 440±11.3 nm. The mechanical properties of the resulting nanofibres were significantly improved compared to those of the electrospun nanofibres from SNE.

Yet another proposed electrospinning process necessitates the use of one or more plates held at a certain angle with respect to the horizontal and vertical oriented collector [114]. The reservoir on top of the plates drops the polymer solution onto the metal plate (which serves as a spinneret), and because of the angle and gravitational force the solution slowly flows until reaching the edge of the plate. At this point, the solution forms a drop that changes its shape to Taylor cone as a result of the electric field at the edge of the plate. More plates were used, given a '*waterfall geometry*'. However, the plates resulted in an irregular spinning due to the electric field difference and the polymer solution on each of the plates. The *waterfall geometry* process displayed lower production rate than the SNE and single edge-plate geometry. The advantage of the single plate method lies in its simplicity and ease of operation with a large number of jets ejected from the plate edge.

The disadvantage is the inhomogeneous electric field distribution in the solution, which contributes to the nanofibre structures.

Another needleless setup involves concurrently provoking numerous jets from a sufficiently large liquid surface [115]. The electrospinning is carried out on the free liquid surface with a stainless steel cleft with a certain width. Numerous jets are generated on the surface of the conductive liquid when sufficient voltage is applied. Mathematical equations were proposed and found to be well applicable to SNE and to most of the theories based on this processing technique. The hypothesis from different parameters and dimensionless analysis created a comprehensive description which affords the opportunity for the development of the liquid surface technique.

Nanofibres were also synthesized from conical wire coils as a spinneret [94]. The technique involves a copper wire-coil nozzle with a conical shape with a certain distance between the wires connected to the voltage supply. This technique falls in between the confined and unconfined, because the dripping solution is inside the cone held upside-down, while the reservoir is not enclosed since the droplets are ejected from the solution flowing through the space (gaps) between the wires. The flowing solution is exposed to a high voltage (40–70 kV) to produce the jets which travel towards the collector where the nanofibres are collected.

4.3. Gas-jet electrospinning

One of the recent advances includes new designs of the needle to fabricate the desired morphology and patterns for various applications. It necessitates a gas jet device connected to the needle and is known as the gas-jet electrospinning technique [13, 15, 116–118]. In this technique the needle of the spinning solution is encircled by the tube of the gas jet. Lin *et al.* [116] studied the effect of ID and gas flow rate while keeping the other parameters fixed. They found that a smaller ID led to smaller average diameters, while the average diameter decreased monotonically as the gas flow rate increased. It was suggested that the blown gas imposes an additional drawing action on the polymer jet. Other groups used hot stream air-blowing to control the solution properties, solvent dryness and to impose additional stretching to the jet [13, 15]. The blown air is heated by passing through heating elements offering con-

trol over the rate and temperature of the blown air. The tip-to-collector distance is much shorter than conventional electrospinning with very high voltages (~40 kV). The method offers an opportunity to increase the processing window boundaries. Ultra-high molecular weight polymers, and polymers that are difficult or impossible to electrospin from their aqueous solutions, can easily be electrospun through a gas jet process [13, 15, 86]. However, the throughput is still equivalent to that of SNE, while the diameters of the nanofibres range between 500 and 1000 nm. The disadvantage of this process is the difficulty of solvent recovery. An increase in the throughput will also require an increase in the number of the needles as well as large gas volumes [118].

Another gas jet process necessitates the exploitation of the protruding jet by applying compressed air to further stretch the jet [119, 120]. This process is known as gas jet nanofibre (GJF). The GJF consists of a syringe pump, modified nozzle, jet compressed gas (often air), and a collector. Several parameters, such as air jet pressure, feeding rate, and tip to collector distance, can be adjusted to engineer the nanofibres morphology. The mass production ranges between 0.9 and 8.6 g·h^{-1} depending on the polymer properties, solution parameters and processing parameters. However, bi-component and co-shell morphologies can easily be fabricated. Benavides *et al*. [120] produced nanofibres with average diameters of 280, 186 and 425 nm from 6% v/v PEO, 6% v/v poly(vinyl pyrrolidone) (PVP) and poly(vinyl acetate) (PVAc) using a 276 kPa compressed air jet with a feeding rate of 0.8 mL·min^{-1}. They demonstrated that the nanofibre diameter can be reduced by increasing the air pressure. They also indicated that core-shell by co-axial syringe and side-by-side morphologies from immiscible polymers can easily be prepared.

4.4. Nozzle configurations for multi-component nanofibres
4.4.1. Co-electrospinning
The modifications of the standard electrospinning devices created a new avenue to combine one or more components with ease of functionalization. One of the simplest ways to fabricate one or more polymeric components is through the use of two or more needles containing different solutions (double electrospinning). This can be done by spinning both

solutions, fed from different reservoirs, in a programmed way such that both solutions reach the collector at the same time [121]. Another way is the depositing of the nanofibres in a sequential way, where one polymer solution is first deposited followed by the other [122]. In these methods the syringes filled with different polymers are placed opposite each other with the collector between them, and perpendicular to the principal axis of the collector. The ejected jets are collected using the same collector (mandrel). Nanofibrous membranes containing chitosan and alginate were produced *via* the dual-jet system by Hu and Yu [123]. The PEO/chitosan and PEO/alginate were fed from two different nozzles and the jetting difference was 15 seconds [123]. X-ray photon-electron spectroscopy (XPS) confirmed the compositions of the two biopolymers, and fluorescent microscopy micrographs showed that these polymers were evenly dispersed onto each other. A hybrid of chitin and silk fibroin (SF) were also electrospun simultaneously from their solutions fed from two syringes on opposite sides facing a rotating target [124]. Chitin/SF (75/25, 50/50, 25/75) hybrids were prepared from chitin (5 wt% in 1.1.1.3.3.3-hexaflouro-2-propanol (HFIP)) and SF (7 wt% in HFIP) and fed to two syringe in opposite directions. The resulting bimodal type of distribution consisted of thinner chitin nanofibres and thicker SF nanofibres with each component dominant depending on their concentration in the composition.

Similarly, the two polymer solutions in the syringes can be placed on opposite sides of the collector. The voltage applied to the syringes result in ejection of the jets which come into contact (merge into single nanofibres) moving towards the collector (Figure 3) [125]. Duan *et al*. [126] simultaneously electrospun poly(lactide-co-glycolide) (PLGA) and chitosan/poly(vinyl alcohol) (PVA) from different syringes and mixed them on the collector (drum). The solutions from the two syringes connected to a high voltage (15 kV) were fed by a double-way syringe pump at a feeding rate of 0.2 mL·h^{-1} to a grounded drum (TCP = 10 cm). The composite nanofibres with a diameter of 275±175 nm consisted of both smooth nanofibres with large diameters and beaded nanofibres. Ji *et al*. [86] crosslinked hyaluronic acid (HA) hydrogel nanofibres by a primary syringe (2.5% w/v/ 2.5% w/v HA/PEO) connected to a T-shaped three-way steel adapter, and the secondary syringe
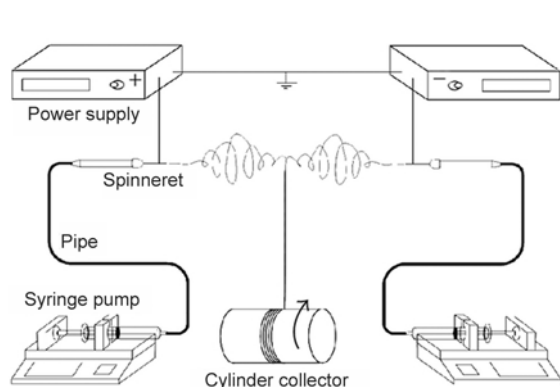
Figure 3. Schematic representation of other side-by-side electrospinning (Reprinted with permission from Xu *et al.* [125] Copyright © 2012 Fu Xu *et al.*)

(9.0% w/v PEGDA) connected by Teflon tubing. A voltage of 18 kV was applied with a TCP of 10 cm. The primary syringe feeding rate was 20 µL·min⁻¹ and secondary syringe feeding rate was maintained at 5 µL·min⁻¹ to yield a final 3.3′-dithiobis(propanoic dihydrazide)-modified HA (HA-DTPH) concentration of 2.0% (w/v) in the mixture. Ultrafine nanofibres with diameters of 90±15 nm were obtained. The fibrous structure was maintained after dissolution of PEO in water, but the average diameter moved to 110±28 nm.

The most convenient way to electrospin two polymers is through blending the two or more polymers in a suitable solvent [127]. In this case, the selection of the polymers and the solvent is important due to
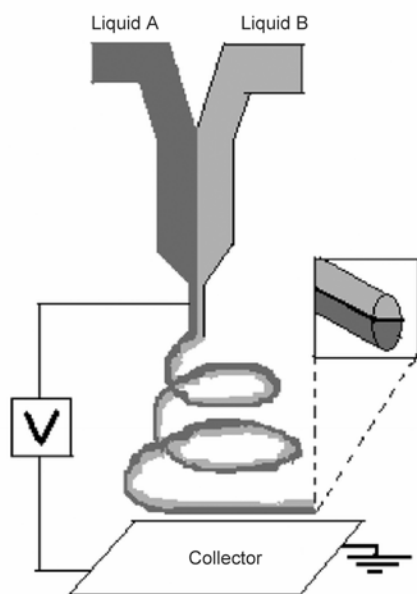
Figure 4. Schematic diagram of side-by-side dual spinneret (Reprinted with the permission from Liu *et al.* [128]. Copyright (2007) American Chemical Society)

the fact that the interactions between the polymers must not cause phase separation during electrospinning. Nonetheless, the proposition to use a single nozzle with two polymer solutions lying in a side-by-side fashion and coming into contact at the tip of the needle and flowing towards the counter electrode overcame the complications of blending the polymers [127]. This technique is known as side-by-side dual spinneret (Figure 4) [128]. These authors synthesized bicomponent nanofibres made up of two small fibres bound together and respectively containing titanium dioxide (TiO₂) and tin dioxide (SnO₂). This was confirmed by SEM-EDS results showing that TiO₂ and SnO₂ were on different surfaces of the fibre.

4.4.2. Co-axial electrospinning

Other designs include co-axial electrospinning where hollow or core-shell fibres can be produced with easy functionalization (Figure 5). Various materials such as polymers, oligomers, nanoparticles, metal salts, proteins, oils, and enzymes immobilized into the core can be produced to achieve integrated multifunctional materials [1, 129–132]. Coaxial electrospinning offers an avenue to prepare nanofibres from the materials which are difficult or impossible to be electrospun into nanofibres using conventional electrospinning processes [129, 132]. It can be used in various applications where the stability and control release of small molecules are of significance [133–136]. With appropriate choice of solvent and components a variety of functionalised hollow structures can be fabricated from blend to composite materials [134]. A core-shell of collagen-r-poly(ε-caprolactone) was prepared by this technique [136]. The inner and outer solutions were – poly(ε-caprolactone) (PCL)/triflouroethanol (TFE) (100 mg·mL⁻¹) and collagen/TFE (72 mg·mL⁻¹), respectively. TEM revealed a core-shell structure with a dark PCL component inside with a diameter 385±82 nm, and a lighter collagen shell with a thickness of 64±26 nm. The variation of the concentration of the solutions for the inner and outer layers influences the overall diameters of the nanofibres, the thickness of the shell and the diameter of the core. Gulfam *et al.* [137] produced porous co-shell structured nanofibres by utilizing a collecting water bath. They varied the concentration of PCL (outer shell) to evaluate its effect on the overall diameter of the resulting nanofibres. The overall diameters of the gelatin-
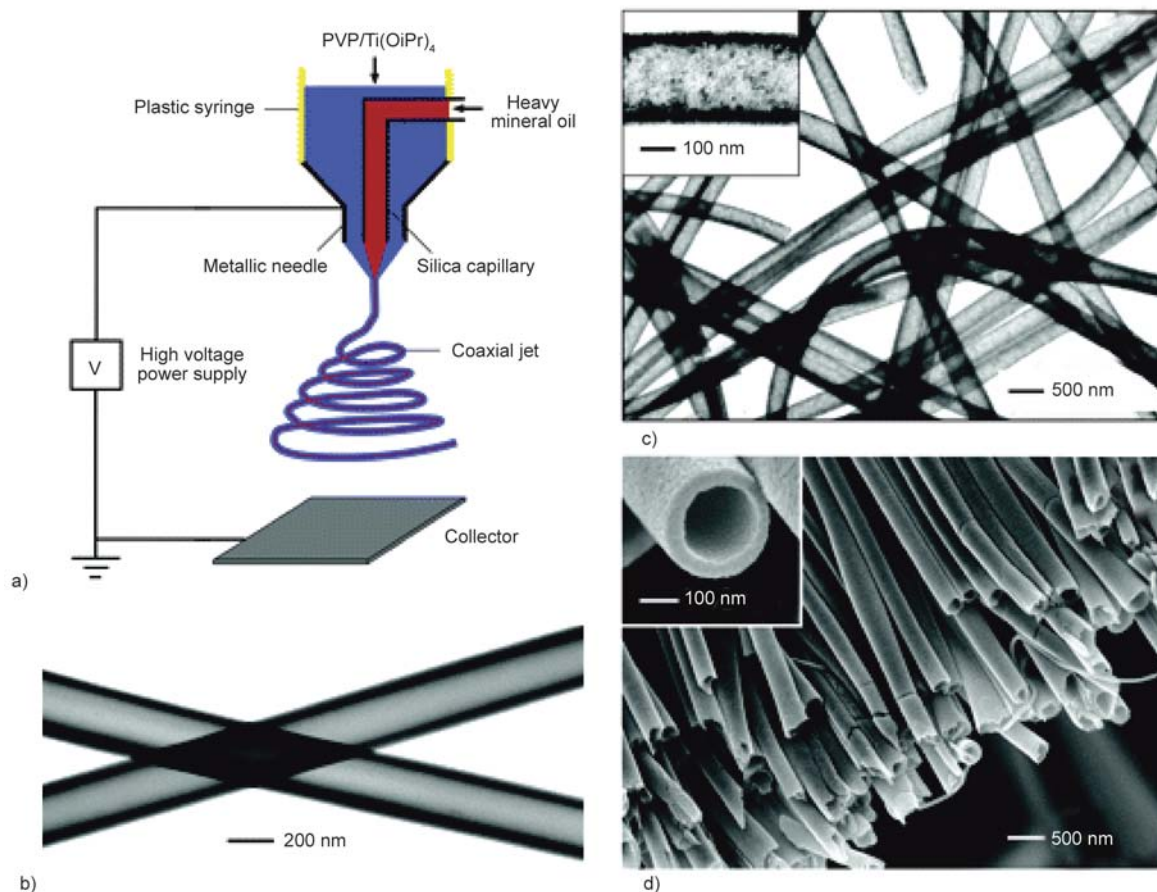
Figure 5. Schematic representations for co-axial electrospinning (a). It consists of a spinneret with two coaxial capillaries in which the polymer solution, mineral oil and functional group are ejected simultaneously to fabricate functionalized hollow fibres. TEM image of two as-spun hollow fibres (b). TEM image of TiO_2 (anatase) hollow fibres (c). SEM image of a uniaxially aligned array of anatase hollow fibres (d). (Reprinted with the permission from Li and Xia [134]. Copyright (2004) American Chemical Society).

PCL core-shell nanofibres gradually increased with an increase in PCL concentration from 105±31 nm at 4% PCL to 210±49 nm at 12% PCL.

4.4.3. Tri-axial electrospinning
Additional to the conventional co-axial electrospinning, various researchers developed a novel tri-axial electrospinning technique [130, 138, 139]. The method uses a nozzle with three concentric needles and three solutions are delivered by different pumps to meet at the tip of the nozzle. Liu *et al*. [140] produced multi-layered biodegradable nanofibres made of gelatin as core and sheath and PCL as middle layer by triaxial electrospinning (Figure 6). The gelatin shell (17 wt%) and core (10 wt%) solutions in 80/20 w/w TFE/deionized water and middle layer PCL (11 wt%) solution in TFE were fed from the triaxial concentric nozzle at 1.0, 0.15, and 0.4 mL·h⁻¹, respectively. The confocal fluorescence microscopy (with the aid of dyes) and FIB-SEM images con-

firmed the presence of the gelatin/PCL/gelatin layers. The thickness of the sheath was 130 nm, that of the intermediate layer 240 nm, and that of the core layer 230 nm. Even miscible and immiscible polymer solutions, that were impossible to electrospin with traditional co-axial electrospinning, can be fabricated by introduction of the solvent between the two solutions and a reasonable flow rate [130, 140]. The incorporated multilayers can perform different functions and incorporate functional groups to target specific applications of the nanofibres.

5. Electrospinning of biopolymers
A wide array of biopolymers have been electrospun into ultrafine fibres with some difficulty due to the rigid structure and lack of solubility in common solvents. The functional groups, biocompatibility, biodegradability and non-toxicity of biopolymers are unique properties that afford their applications in various fields. The major disadvantage of some bio-
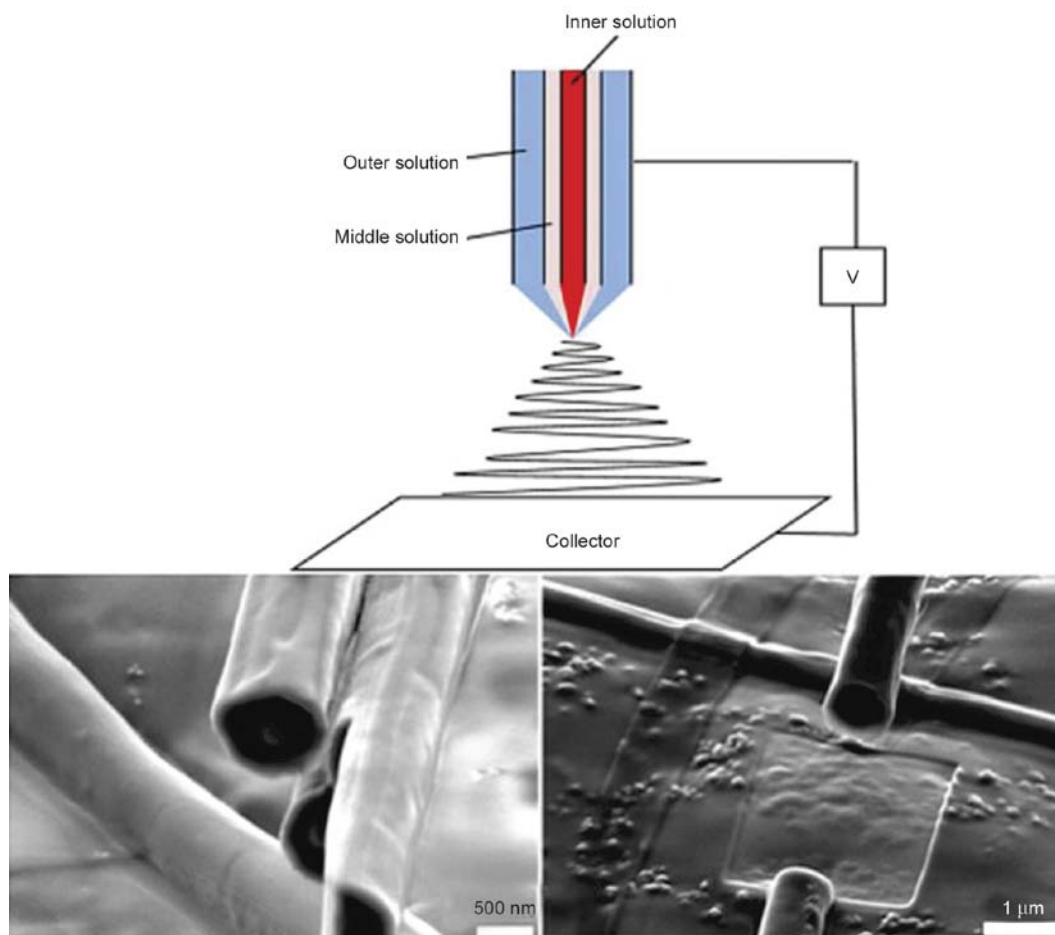
Figure 6. Schematic presentation of triaxial and FIB-FESEM images of triaxial electrospun nanofibres (Reprinted with permission from Liu *et al*. [140]. Copyright (2013) American Chemical Society.)

Table 4. The potential applications of electrospun biopolymer membranes in water treatment

Biopolymer	Desirable properties	Current application	Potential future applications
Cellulose and derivatives	Easy functionalization, hydroxyl groups, and functional groups from derivatives	Drug delivery, food, tissue scaffolds, personal care, detergent, paper making, textile, mining flotation, Pharmaceuticals, personal care, cigarette filters	Bioadsorbent, metal and impurities separation, ultralfitration, microfiltration and bioadsorbent, trace metal detection
Cellulose nanowhiskers	High specific area, easy functionalization, high crystallinity, high modulus	Polymer reinforcement	Selective layer in ultrafiltration and nanofiltration membranes, microfiltration, reinforcement
Chitin and derivatives	Easy functionalization, availability of amino groups and other functional groups from derivatives	Drug delivery, environmental engineering, tissue scaffolds, food wraps, flocculants in water, biocidal membranes, tissue scaffolds	Anti-biofouling membranes, membrane coating, flocculation agent
Chitin nanowhiskers	High specific area, easy functionalization, high crystallinity, high modulus	Polymer reinforcement	Barrier layer in TNFC, reinforcement
Alginate	Carboxyl groups and hydroxyl groups	Food texturing, tissue scaffolds	Metal chelation, anti-biofouling membrane, heavy metal detectors
Collagen	Unique triple-helical structure	Food, tissue scaffolds, cosmetics	Metal chelation
Gelatin	Thermoreversible viscosity, independent of pH	Cosmetics, food industry, pharmaceutical, coatings	Membrane coating, controlled release and encapsulation of disinfection agents
Hyaluronic and derivatives	Easy functionalization	Dermal fillers, tissue scaffolds	Metal chelation
Aloe vera	Different functional groups	Antibacterial creams, lotions, ointment, tissue scaffolds	Immobilizer of bacteria, enzymes and other biological molecules

polymers in water treatment is their solubility and biodegradation in an aqueous medium, giving the edge to synthetic polymers to be the most applied in water filtration and treatment. As already mentioned earlier, different metal oxides were incorporated into the polymers to enhance their biocidal efficacy and the mechanical strength of the electrospun membranes. Most of these biopolymers bear unique functional groups that can be explored in wastewater treatment to adsorb various heavy metals via different mechanisms such as chelation, electrostatic attraction and ion-exchange. They have abundant availability, biocompatibility, large surface-to-area ratio, high porosity, and malleable mechanical properties and structure, with some unique and interesting potential applications (Table 4).

5.1. Cellulose

Cellulose is the most abundant natural polymer on earth derived from a wide variety of cellulose-containing sources such as plants, animals and bacteria [26, 141]. It is composed of a linear chain of β(1-4) linked D-glucose units as shown in Figure 7. Cellulose has interesting properties such as biocompatibility, biodegradability, and recyclability. Electrospinning of pure cellulose, from its aqueous solutions, like most biopolymers poses many challenges, where some modifications of the electrospinning setup/ devices are needed [11, 14]. For example, Frenot *et al*. [11] found that the collected fibre stood straight up on the collector when plastic and aluminium covered plates are used as collectors. However, the use of a rotating drum/copper or liquid bath collector in a suitable humidity resulted in smooth bead-free fibres [76, 142, 143]. Cellulose cannot melt and is insoluble in water and most of the common organic solvents because of the dense hydrogen network which limits its applications and processability. Only a few solvents such as paraformaldehyde (PF)/N.N-dimethylformamide (DMF), lithium chloride (LiCl)/N.N-dimethylacetamide (DMAc), N-methylmorpholine-N-oxide (NMMO), urea/sodium
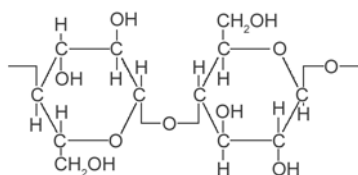
Figure 7. Structure of cellulose

hydroxide (NaOH) and ionic liquids can dissolve cellulose [23, 76].

The possibility to functionalize cellulose *via* the hydroxyl side groups on the backbone offers the opportunity to electrospin it in a derivative-form followed by its regeneration *via* deacetylation or hydrolysis treatments.

The cellulose derivatives through –OH (hydroxyl group) functionalization include cellulose acetate, hydroxyl propyl cellulose, hydroxyl propyl methyl cellulose, and methyl cellulose [11]. These derivatives are soluble in most of the common organic solvents and they can be converted to pure cellulose via hydrolysis and deacetylation. Stephen *et al*. [142] functionalized cellulose nanofibrous membrane with oxolane-2,5-dione to enhance their heavy metal adsorption efficiency. They first electrospun cellulose acetate, followed by deacetylation of the resulting nanofibres membrane using sodium hydroxide (0.3M NaOH) to generate pure cellulose. The nanofibrous membrane displayed a large surface area of 13.7 $m^2 \cdot g^{-1}$ compared to raw cellulose fibres membrane with a surface area of only 3.2 $m^2 \cdot g^{-1}$. The adsorption capacity for lead (Pb) and cadmium (Cd) were respectively 1.0 and 2.9 $mmol \cdot g^{-1}$. The regeneration of the mats was done through nitric acid (HNO_3) treatment, and the regenerated mats performed quite well.

5.1.1. Cellulose nanowhiskers

Cellulose nanowhiskers can be extracted from their abundant source (cellulose) by mechanical and chemical means [141, 144]. The high aspect ratio, high crystallinity, easy functionalization, and large surface areas make the nanowhiskers the next generation of wastewater treatment nanomaterials. Several researchers incorporated various whiskers in different polymers such as poly(2-hydroxy ethyl methacrylate) [145], PVA [146], and PEO [147] to improve the mechanical properties of the resulting electrospun nanofibres. These researchers found that the higher modulus and stiffer nanowhiskers improved the mechanical properties of the electrospun nanofibres despite the observed agglomeration of the whiskers [147].

Oxidized jute cellulose whiskers with diameters ranging between 3 and 10 nm were coated onto polyacrylonitrile (PAN) nanofibres membrane (mean diameter ~173 nm) either once (single layer) or

twice (double layer) by using a glass rod [148]. This method afforded pore sizes ranging between 5 and 65 nm. The membrane was tested under both ultra-filtration (UF) and nanofiltration (NF) conditions, in which the rejection of both nanosilica (in the case of UF) and oil and water (in the case of NF) was above 99%. The mechanical properties of the result-ing electrospun nanofibrous membrane (ENM) were improved by the presence of the whiskers, with the tensile strength increasing from 4 to 10 MPa (for one coating of the whiskers onto the ENM) and 14 MPa (for double coating).

Cellulose nanowhiskers and nanofibres have also been thoroughly studied by the Chu and Hsiao group in water treatment and filtration applications [149–152]. The cellulose nanowhiskers were either employed as barrier layer of thin-film nanofibrous composite membranes (TFNC) (Figure 8), or they were infused into the electrospun membrane, depend-ing on the intended filtration application (microfil-tration (MF) or UF).

The cellulose nanowhiskers were prepared through a [2.2.6.6-tetramethylpiperidinooxy (TEMPO)/ sodium bromide (NaBr)/sodium hypochlorite (NaClO)] oxidation method. The length of the cellu-lose nanowhiskers ranged between 200 and 400 nm and the diameters between 5 and 10 nm. In the case of MF, the infusion of the whiskers resulted in a reduction of the mean pore size with a narrower dis-tribution than the electrospun PAN nanofibrous membrane. In comparison with the commercial membrane GS0.22 made of nitrocellulose and acetyl cellulose ester, the water flux cellulose nanowhisker-based membrane was better because of the differ-ence in porosity (>80% versus 52%) [144]. The mechanical properties were improved with Young's modulus and tensile strength values of 375±15 and 14.3±0.4 MPa, respectively, compared to the unmod-ified membrane (226±20 and 8.5±0.3 MPa) which was still higher than the commercial membrane with a tensile strength of 5.6±0.3 MPa. The adsorption of crystal violet (CV) dye was better in the case of the cellulose nanowhiskers-based membrane than in GS0.22 (Figure 9a). The adsorption was two times higher at 10 mg·L^{-1} of CV dye with a high rate of adsorption because of the hydrophilicity and large surface area. The adsorption data fitted the Langmuir isotherm showing monolayer adsorption (Figure 9b). The adsorption capacity was 16 times higher for the cellulose nanowhiskers-based mem-brane. The cellulose nanowhiskers as a thin barrier layer in TNFC displayed superior performance com-pared to the commercial known membranes [144]. The hydrophilicity, large surface area to volume ratio and the surface charges of the cellulose nano-whiskers played a significant role in improving the rejection and flux of the membrane.
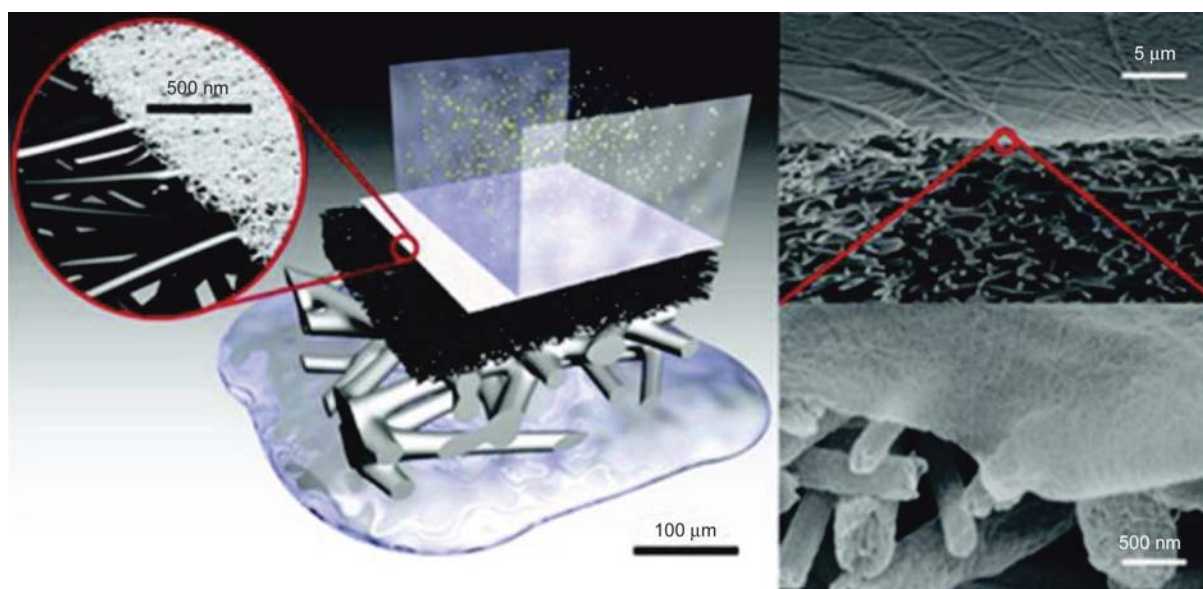
Figure 8. (Left) A schematic representation of a thin-film nanofibre composite membrane (TNFC) with three layers: selec-tive/barrier layer, mid-layer of electrospun nanofibres, and nonwoven supporting mat (poly(ethylene terephtha-late) (PET)). (Right) Cross-sectional SEM views of the barrier layer and electrospun nanofibres in a typical TNFC membrane. (Reprinted with permission from Ma *et al*. [150]. Copyright (2012) American Chemical Society).
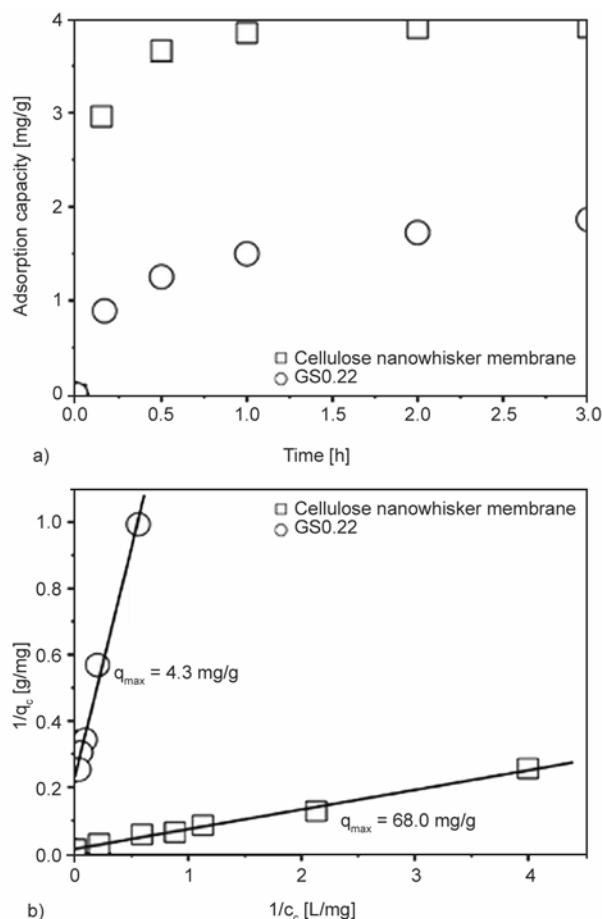
Figure 9. (a) Adsorption capacity of cellulose nanowhiskers-based nanofibrous MF membrane and GS0.22 against time; (b) respective Langmuir adsorption isotherms for the two membranes (Reprinted with permission from Ma *et al*. [144]. Copyright (2012) American Society.)

5.1.2. Cellulose derivatives

Cellulose acetate

Among the cellulose derivatives, cellulose acetate (CA) is the most studied derivative due to its potential to regenerate pure cellulose via deacetylation [23, 152]. Cellulose acetate is synthesized by acetylation of the hydroxyl groups on cellulose with an average of 2–4 degree of substitution per glucose units (Figure 10). The CA enjoyed its success in membrane filtration for more than seven decades
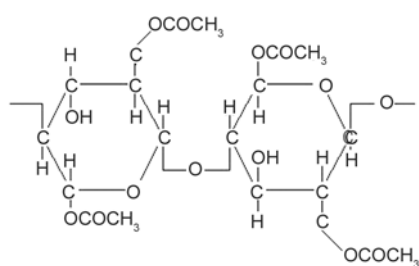
Figure 10. Structure of cellulose acetate

now [149, 153, 154]. It has been widely used as a selective layer in nanofiltration and ultrafiltration. With its unique functional groups that can be modified, it is rated as one of the good metal adsorbents [149, 150]. The functionalization of CA with –COOH, –SO$_3$H and NH$_2$ offers an opportunity for the application of CA in heavy metal complexation [155–158]. Some nanofillers can be added to a cellulose acetate membrane to enhance the metal adsorption capacity [149, 155, 156].

Zhou *et al*. [159] prepared cellulose acetate nanofibrous membranes from various solvents (dichloromethane, formic acid, acetic acid, and triflouroacetic acid). Only trifluoroacetic acid afforded the production of smooth nanofibres with diameters ranging between 100 and 300 nm. This membrane displayed a porosity and surface area of respectively 87% and 2.02·10^7 m^{-1} with high water permeability and hydrolytic stability. Aluigi *et al*. [61] studied the influence of various solvents and their mixtures on the electrospinning of CA. Using a single solvent like chloroform, N,N-dimethylformamide (DMF), dichloromethane (DCM), methanol (MeOH), formic acid, or pyridine, it was not possible to fabricate smooth nanofibres. Only discrete beads were formed, and acetone produced short beaded nanofibres. CA (5% w/v) in a mixture of chloroform-MeOH and DCM-MeOH produced beaded and smooth fibres, especially at 4:1 (v/v). The average diameters were 0.79–1.09 μm and 0.67–1.06 μm respectively for the binary mixtures of chloroform-MeOH and DCM-MeOH. Smooth fibres were formed at solvent mixture concentrations of a 16% (w/v) solution of CA in 1:1, 2:1 and 3:1 acetone-N,N-dimethylacetamide (DMAc), 14–20 % (w/v) solution of CA in 2:1 acetone-DMAc, and 8–12 % (w/v) solutions of CA in 4:1 (v/v) DCM-MeOH. The diameters ranged between 0.14–0.37 μm and 0.48–1.58 μm for fibres prepared from acetone-DMAc and DCM-MeOH, respectively.

Chen *et al*. [160] functionalized cellulose acetate nanofibrous membrane with chlorhexidine for their biocidal efficacy. To facilitate electrospinnability in N,N-dimethylformamide (DMF), high molecular weight PEO was added. The electrospun nanofibrous membrane was crosslinked using titanium triethanolamine in isopropanol. The biocidal efficiency against *E. coli* and *S. epidermisidis* increased with concentration of chlorohexidine. The membrane displayed biocidal efficiency above 99%. Moreover,

different drugs can be incorporated in cellulose acetate as carrier [69, 161, 162]. Suwatong *et al*. [162] incorporated curcumin in cellulose acetate nanofibres to investigate its releasing character. The cellulose acetate nanofibres retained their structure and morphology after the addition curcumin. A 95% release without toxicity was established. This property can be explored in incorporating different functions/biocides for controlled release in water treatment. For example, Ma and Ramakrishna [163], covalently bond protein A/G onto the oxidized CA membrane to bind IgG molecules and a capturing capacity of 18 µg/mg was reported. Similarly, Chen *et al*. [164] functionalized hydrolysed CA with cobalt tetraaminophthalocyanine (CoPc) for the adsorption of reactive red X-3B dye and more than 95% of the dye was eliminated within 3 hours.

Other cellulose derivatives
Four different carboxymethyl cellulose sodium salts (CMC) were electrospun by Frenot *et al*. [11]. CMCs with different molecular weight and degree of substitution were electrospun in the presence of PEO as copolymer, dissolved in a water and ethanol mixture at a ratio of 1:1. The nanofibres displayed similar homogeneous structures with mean diameters of 200–250 nm, regardless of the molecular weight and degree of substitution. In the same study, two hydroxypropyl methyl cellulose (HMPC) samples with equal M_w, and with varying contents of methoxy and hydroxypropoxy groups, were compared. Mean diameters of 127 and 128 nm were obtained for the two HMPCs, regardless of the functional group contents, but at different spinnable concentrations. Lim *et al*. [88] studied the effect of different parameters (concentration, voltage, flow rate and tip-to-collector distance) on the electrospinning of ethyl cellulose (EC). At a low concentration (6 wt%) a mixture of smooth and beaded-fibre structures was observed, which disappeared as the concentration was increased to 8 wt% of the EC and above. The mean diameter of the nanofibres gradually increased with flow rate, whereas an increase in voltage reduced the mean diameter of the nanofibres.

5.2. Chitin
Chitin is the second most abundant natural polymer on earth after cellulose. It appears as ordered crystalline structure of microfibrils in the exoskeleton of arthropods, and the cell walls of fungi and yeast
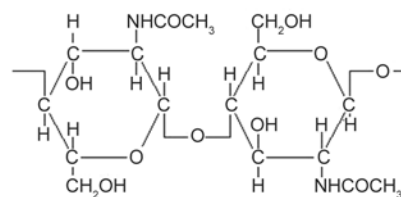
Figure 11. Structure of chitin

[165]. Chitin, the mucopolysaccharides that is made up of ß-(1-4)-N-acetyl-D-glucosamine units linked by 1-4 glycosidic bonds, acts as mechanical strength and supporting structure in crustaceans, insects, etc. (Figure 11) [51, 166, 167]. Chitin with desirable properties such as good biocompatibility, biodegradability and ubiquitous availability has been used in various fields such as cosmetic, biomedical and in food additives [165].
Very few studies dealt with electrospinning chitin from its aqueous solution, because of its poor solubility [168, 169]. In these studies the solubility of chitin was enhanced by Co^{60} gamma ray irradiation. Chitin nanofibres with diameters ranging between 50 nm and several microns were electrospun in 1.1.1.3.3.3-hexaflouro-2-propanol (HFIP), with the diameters depending on the electrospinning technique parameters such as concentration [167–169]. Min *et al*. [168] irradiated chitin (200 kGy) and obtain an average molecular weight of 91 000 to enhance its dissolution in HFIP. They produced chitin nanofibres with a broad fiber diameter distribution (40 to 640 nm) and most were less than 100 nm.

5.2.1. Chitin nanowhiskers
The nanocomposites of PVA and chitin whiskers were reported for the first time by Junkasem *et al*. [170]. Nanowhiskers with the lengths in the range 231–969 nm and widths of 12 to 65 nm were produced. Nanocomposite nanofibres (prepared from water) with diameters ranging between 175 and 214 nm, depending on the concentration of the chitin whiskers, were obtained. The thermomechanical properties of PVA were enhanced by the presence of the chitin whiskers [171]. Naseri *et al*. [172] reinforced a blend of chitosan and PEO with chitin nanowhiskers. The modulus and tensile strength were significantly increased from 0.4 to 4.3 GPa and and from 4.6 to 34.9 MPa, respectively. An antibacterial TNFC membrane was developed by including chitin nanowhiskers as barrier layer onto electrospun PAN nanofibres (as a mid-layer on top of a PET nonwoven support) [144]. The flux permeation was

217.0 L·m^{-2}·h^{-1} (which was 8–10 times higher than that of commercial PAN10) for two days at 30 psi with a rejection above 99.7%.

5.2.2. Chitin with synthetic/biopolymers

A nanofibre blend of poly(glycolic acid) (PGA) and chitin was prepared by Park *et al.* [173]. The nanofibres had a broad diameter distribution in the range of 50–350 nm, with most of the nanofibres having an average diameter of 150 nm. Chitin/silk blend nanofibres were prepared by several researchers using HFIP as a solvent [124, 173]. The nanofibres had diameters ranging between 340 to 920 nm depending on the content of silk in the composite material. Irradiation and little deacetylation (8% DD) of chitin was also adopted to reduce its molecular weight and improve its solubility.

5.2.3. Chitin derivatives

Dibutyryl chitin

One of the readily soluble chitin derivatives in most common organic solvents (acetone, ethanol) is dibutyryl chitin. It is synthesized from butyric anhydride and perchloric acid. Błasińsk *et al.* [174] electrospun an ester derivative of chitosan, dibutyrylchitin (DBC), from ethanol. 9 wt/v of DBC at 25 kV was the optimal conditions to establish bead-free nanofibres with a transverse dimension of 0.3 μm. DBC and a cellulose acetate hybrid were electrospun in a 1:1 ratio of acetone and acetic acid [175]. The mixture of CA/DBC at a concentration of 5% from 100/0 to 0/100 ratio compositions produced bead-free nanofibres with 30–350 nm diameters. Pant *et al.* [176] synthesized chitin butyrate from a mixture of butyric acid, trifluoro acetic anhydride and phosphoric acid, followed by the addition of ethyl alcohol and filtration. The resulting solution was washed repeatedly with diethyl ether and water, followed by drying for 3 days in a hood and then in a 60°C oven for 6 hours. The resulting butyric chitosan was electrospun with nylon-6 in formic acid/acetic acid to give spider-web-like nanofibres with an average diameter of 15 nm at a low butyric chitosan content (90/10 nylon-6/butyric chitosan).

Carboxymethyl chitin

To circumvent the solubility issues of chitin and chitosan, some of their derivatives have been electrospun into nanofibres either from their aqueous solutions or by blending with other polymers. This

not only to improved their spinnability, but also alleviated the use of a toxic solvent utilized in electrospinning both chitin and chitosan. Carbomethyl chitin (CMC) is one of the chitin derivatives that are readily soluble in water. However, the electrospinning of CMC from its aqueous solution results in spherical drops [177]. Nevertheless, ultrafine nanofibres from a CMC/PVA blend at a 20:80 ratio (CMC (7%):PVA (8%)) was reported. Sohofi *et al.* [178] were the first to fabricate CMC electrospun nanofibres from its aqueous solutions using binary solvents. The 6 wt% CMC (with degree of substitution of 0.65) was electrospun in a 30/70 dichloromethane/trifluoroacetic acid mixture to ultrafine nanofibres with an average diameter of 260±42 nm. Although the carbomethylated chitosan showed a potential in metal adsorption [179], nanofiltration [180], and microfiltration [181] processes, not much has been done on electrospun CMC in wastewater treatment.

Chitosan

Chitosan results from the deacetylation of chitin under alkaline conditions, or from enzymatic hydrolysis in the presence of chitin deacetylase. It is an aminopolysaccharide with unique properties and functionalities for a wide spectrum of applications from biomedical to industrial areas. Chitosan is a copolymer made up of 2-acetamido-2-deoxy-β-D-glucopyranose and 2-amino-2-deoxy-β-glycopyranose linked together through (1-4)-β-glycosidic bonds (Figure 12). Similar to alginates, different forms of chitin and chitosan such as gels, membranes, beads, microparticles, nanoparticles and nanofibres have been produced for various applications [51, 166]. Chitosan is well-known for its unique antimicrobial activity and metal adsorption [182, 183]. These result from the protonation of NH_2^- groups on its backbone. It is capable of chelating ions from aqueous media and inhibiting the growth of a broad spectrum of fungi, yeasts and bacteria. The cations along the chitosan repeating units can be varied through deacetylation. A higher the degree of deacetylation results in a larger number of cations on the backbone of the chi-
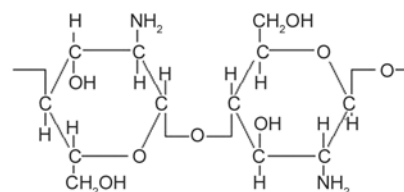

Figure 12. Structure of chitosan

tosan. Chitosan is soluble in most acids, which protonate it into a polyelectrolyte.

Different solvents such as dilute hydrochloric acid, acetic acid, formic acid and triflouroacetic acid (TFA) were tested to envisage the electrospinnability of chitosan [184]. Only with TFA as solvent chitosan nanofibres were successfully established [184]. It was indicated that the TFA either forms amino groups on chitosan, which results in the destruction of the rigid interaction between the chitosan molecules, or that the high volatility of TFA caused rapid solidification of the electrified jet. More homogeneous nanofibres were obtained by addition of dichloromethane, due to its high volatility. Geng *et al*. [67] successfully electrospun chitosan from concentrated acetic acid. 30% of acetic acid in water resulted in a combination of droplets and thinner nanofibres with an average diameter of 40 nm, whereas at 90% acid concentration the diameter of the nanofibres increased to 130 nm without beads.

Chitosan with synthetic polymers
Over the past decades, electrospun chitosan hybrids have been fabricated using various synthetic polymers such as polyvinyl alcohol (PVA) [126, 185], poly(lactide-co-glycolide) (PLGA) [126], polyethylene oxide (PEO) [186], polyvinyl pyrrolidone (PVP) [83], poly(lactic acid) (PLA) [80], and poly (ethylene terephthalate) (PET) [187]. Interestingly, the synthetic polymer did not only improve the electrospinnability of chitosan, but significantly enhanced the biocompatibility, antibacterial, mechanical strength and other properties of the hybrid nanofibres. These broadened the applicability of the chitosan-based nanofibres in a broad spectrum of applications. PEO is a biocompatible synthetic polymer favourable for biomedical and tissue engineering. Su *et al*. [186] prepared chitosan/PEO blends doped with monovalent (Na^+), divalent (Ca^{2+}) and trivalent (Fe^{3+}) metal chlorides to enhance the homogeneity of the resulting nanofibres. They found that these metal chlorides promoted the fibrous morphology of the chitosan/PEO blends, opening doors for the use of these nanofibres in various applications such wound dressing, bone regeneration, etc.

Chitosan with other biopolymers
The electrospun nanofibres of chitosan and other natural polymer blends were studied by several researchers [188, 189]. Torres-Giner *et al*. [188] pre-

pared a bioblend of chitosan and zein for biocidal applications. Low zein content (1 wt%) in the bioblend resulted in ribbon-like nanofibres with an average diameter of 320.9±92.3 nm. An increase in the percentage of chitosan in the blend yielded beaded-fibres with smaller average diameters between 161.7±39.6 and 128.5±26.2 nm. The electrospun bioblend inhibited bacterial growth. Bioblend electrospun nanofibrous membrane of chitosan and a type I collagen were fabricated with the aid of PEO, followed by crosslinking with glutaraldehyde [190]. The ultrafine fibres had average diameters of 134±42 nm before crosslinking and 98±76 nm after crosslinking. The difficulty of electrospinning CS/collagen, due to its high conductivity/charge density, was improved by the addition of PEO. Young modulus was improved from 0.29±0.04 to 0.65±0.02 MPa by crosslinking. Maeda *et al*. [191] electrospun chitosan with the aid of PEO, followed by coating with hyaluronic acid. The composite was made by dissolving PEO in water and coating with hyaluronic acid, and it was stable in water with an improved swelling ratio due to the increased hydrophilicity as a result of the presence of hyaluronic acid. PVA/CS was electrospun onto a PVDF micro-filter, followed by crosslinking with glutaraldehyde [192]. The membrane was immersed in glutaraldehyde (5 mM) and an HCl (0.01 N) solution for six hours, and the membrane shrinked by ~5%. Dead-end filtration was utilized to evaluate the metal adsorption capacity of the membrane. A 5% adsorption capacity was reported.

Chitosan derivatives
Quaternized chitosan (QCh) nanofibrous membrane for antibacterial activity were electrospun by Ignatova *et al*. [83, 193, 194] using poly(vinyl pyrrolidone), polyvinyl alcohol, and poly(lactic acid). The addition of these synthetic polymers significantly improved the electrospinnability of quaternized chitosan. The composite nonwoven mats showed good antibacterial activity against Gram negative and Gram positive bacteria. Kangwansupamonkon *et al*. [195] prepared chitosan/PEO mats followed by functionalization to form N-(2-hydroxyl) propyl-3-trimethyl ammonium chitosan chloride (HTACC) and N-benzyl-N,N-dimethyl chitosan iodide (QBzCS) membranes. They prepared the nanofibres from a blend of chitosan and PEO (6.7:0.3% w/v) in a mixture of trifluoroacetic acid/dichloromethane (70/30 v/v) followed by functionalization. They obtained

ultrafine nanofibres with average diameters of 272±56 nm. The membranes displayed good antibacterial efficiency against both *S. aureus* and *E. coli*. Ultrathin nanofibres of N-[(2-hydroxy-3-trimethlammonium) propyl] chitosan chloride (HTTC) through blending with PVA was reported by Alipour *et al.* [196]. The HTTC was synthesized from a reaction between chitosan and glycidyl-trimethylammonium chloride. The water soluble derivative, HTTC, was electrospun through blending with PVA to give nanofibres with 200-600 nm diameters. Good antibacterial efficiency was reported for these membranes.

Chitosan can be modified by various acyl chlorides (dodecyl, hexanoyl, decanoyl, and lauronyl) in the presence of mixed pyridine and chloroform as solvents [197]. These modifications are usually adapted to improve the solubility of the chitosan. Hexanoylchitosan from chitosan modification by hexanoyl chloride in chloroform was electrospun by Neamark *et al.* [82]. The ribbon-like fibres with average diameter of 3.93±1.82 μm at a concentration of 14% w/v were obtained. This was due to the rapid evaporation of the chloroform from the electrified jet. Peesan *et al.* [198] fabricated a blend of hexanoyl chitosan/polylactide using chloroform, dichloromethane and tetrahydrofuran as solvents. The smooth bead-free nanofibres were obtained at 50 wt% of chitosan in the blends using chloroform as spinning solvent. Patanaik *et al.* [27] electrospun lactic acid modified chitosan using TFA as solvent and MC as co-solvent. The nanofibres were stabilized using thermal treatment to convert the lactate to lactamide. The resulting nanofibres showed good nanofibrous integrity, even after exposure to a BSA medium for 72 hours.

Different molecular weights (40–405 kDa) and degrees of substitution (DS) (0.25–1.19) carbomethyl chitosan (CMCS) were synthesized via chitosan alkalization, followed by carbomethylation with monochloroacetic acid [81]. Despite the difference in DS and M_w, and with the incorporation of Triton X-100 (to reduce both solution surface tension and conductivity) into the aqueous CMCS solution, the spinning solution still led to drops (6–20% concentration). The blending of the CMCS with hydrosoluble synthetic polymers (PVA, polyacrylic acid (PAA), polyacrylamide (PAAm) and PEO) enhanced the spinnability of CMCS into smooth nanofibres, but it depended on the polymer used. PEO (100 kDa) with

30% CMCS gave merged non-cylindrical nanofibres mostly with 300 nm diameter, while PAAm at 1/10 w/w of 5000 kDa/10 kDa (18 wt%) resulted into a similar structure as the PEO/CMCS blend. A 10 wt% binary aqueous mixture with equal mass PAA (450 kDa), produced straight cylindrical nanofibres with elongated beads (100 nm diameter). A mixture of PAAm and PAA resulted in higher CMCS content (50%), but with a large number of beads. In the case of a PVA binary solution with a concentration of 8.5 wt% (CMCS 405 kDa), nanofibres with average diameters ranging between 210 and 170 nm were obtained on increasing the CMCS content from 20 to 50%. The PVA/CMCS system is therefore feasible to produce bead-free nanofibres. The stability of the PVA/CMCS in water was further enhanced by heat treatment at 140°C for 30 minutes.

Another interesting approach to overcome the problem of solubility of chitosan is PEGylation. Du and Hsieh [84] synthesized PEG-N-chitosan and PEG-*N,O*-chitosan *via* reductive amination and acylation of the chitosan. A small DS value of 0.2 for the solubility of the derivatives in water was reported. For PEG-*N,O*-chitosan a DS of 1.5 was sufficient for its solubility in CHCl$_3$, DMF, DMSO and THF. Regardless of the degree of substitution of PEG (DS) and the derivative of chitosan, only droplets were collected due to a lack of chain entanglements. All the aqueous solutions of PEG-N-chitosan (from reductive amination) resulted in spraying (drops), regardless of the DS of PEG. Smooth nanofibres with diameters ranging between 40 and 306 nm (average 162) were obtained by increasing the concentration of the PEG-*N,O*-chitosan with the aid of a surfactant (0.5% Triton X-100™) and co-solvent (75/25 v/v THF/DMF).

5.3. Alginate
Alginate is a well-known polyelectrolyte binary copolymer derived from seaweeds/algae [199–202]. It contributes to the flexibility and strength of the seaweeds against adverse water forces. It is usually found in the cell wall matrix and intercellular material (mucilage). Alginate is a linear polysaccharide made up of D-mannuronic (M) and L-guluronic (G) units linked together by 1–4 glycosidic bond (Figure 13). These units appear in varying sequences and ratios, M/G, along the polymer chain depending on the source or specie, the growth conditions, season and depth at which is extracted. The varia-
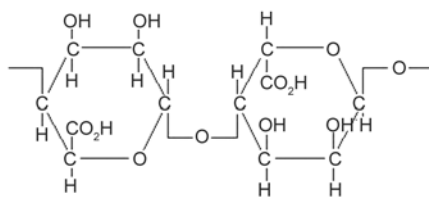
Figure 13. Structure of alginate

tion of M and G along the alginate chain determines its physical properties and reactivity. The molecular conformation and functional groups (especially carbonate ions) have been found to play a significant role in the heavy metal affinity of the alginates [202]. Alginate can gel at room temperature in the presence of polyvalent or divalent metal ions. This phenomenon has been exploited to prepare different morphologies and structures for certain applications. Beads [203], films [204, 205], hydrogels [206], as well as porous membranes and nanofibers [200] were fabricated for different applications such as wound dressings and metal adsorption. There has been significant interest in the use of alginate in biomedical applications because of its antimicrobial efficiency and structural resemblance to glycosamineglycan (GAG) (one of the significant components of natural extracellular matrices (EMCs) found in mammalian tissues). Furthermore, the good cellular compatibility, non-toxicity, biodegradability, and availability of alginate opened doors for its exploitation in various applications such as metals recovery [202, 203].

Until now the electrospinnability (in this case electrospinnability is used to describe bead-free smooth nanofibres) of sodium alginate is still impossible. In most studies carrier polymers are generally used to improve this. Alginate is readily soluble in water. However, it is still controversial on why it is not possible to electrospin alginate on its own. It has been postulated that a high conductivity, lack of entanglements, and gelation of the alginate solution at low concentration (below the concentration for the formation of entanglements) are responsible for this. The rigidity of the chains, worm-like molecular structure and high surface tension also contribute to this. Nevertheless, Nie *et al*. [12] managed to prepare pure alginate nanofibres using glycol as a solvent. They found that the glycol altered the chain conformation of the alginate and improved chain entanglements (viscosity and elasticity). Glycol decreased the surface tension and conductivity which contributed to the electrospinnability of pure alginate. Bonino *et al*.

[207] tried to electrospin pure alginate using water as a solvent, which resulted in large droplets on the collector, that were reduced by a surfactant. The production of alginate nanofibres from its aqueous solution was also reported by Fang *et al*. [24]. Calcium ions improved the intermolecular interaction which enhanced its electrospinnability from water. 1 wt% Ca^{2+} was sufficient to ensure continuous electrospinning and long nanofibres. The hydrolysis degradation of alginate in water *via* glycosidic hydrolysis after 15 days (reducing alginate solution viscosity) was exploited to electrospin alginate solution (4wt%) with the aid of a Triton X-100 surfactant and dimethyl formamide (DMF) as a cosolvent [208].

5.3.1. Alginate with synthetic polymers
One of the convenient ways to enhance the electrospinnability of biopolymers consists of choosing a compatible copolymer to co-spin with. Polyethylene (PEO) is a biocompatible and biodegradable synthetic polymer. It is non-ionic and hydrosoluble. Alginate is also hydrosoluble and therefore offers the opportunity to co-spin the two without difficulties [54]. The two interact with each other through hydrogen bonding which reduces the viscosity of the alginate solution. Cylindrical nanofibres from alginate/PEO with a mean diameter of ~75 nm were prepared by Jeong *et al*. [52]. Recently, Saquing *et al*. [54] reported that higher molecular weight PEO is required to increase the concentration of alginate in the PEO/alginate blend. They indicated that the PEO-PEO interaction is responsible for the electrospinnability of alginate. Co-axial electrospinning of alginate (core) and PEO (shell) was recently reported. PEO was easily extracted by dissolving the nanofibres in water containing calcium chloride to crosslink the alginate [129]. They successfully incorporated 85 wt% of alginate in the blend with the aid of the surfactant. Another hydrosoluble synthetic polymer, with good mechanical properties, thermal stability, chemical stability and biocompatibility, is poly (vinyl alcohol) (PVA). A number of researchers utilized this polymer as copolymer for alginate electrospinning [208–210]. Similar to PEO, the flexible PVA interacts with the alginate *via* hydrogen bonding, thus improving the electrospinnability of the rigid alginate [208]. Different morphologies of PVA/alginate were reported by Lee *et al*. [210]. At low alginate concentrations, ultrafine nanofibres were produced, and when the concentration was increased,

electrospinning led to bigger beads with smaller average distances between the beads.

The solubility of alginate has been one difficulty facing its applicability in various fields. In order to improve the stability of the electrospun alginate, various crosslinking agents were investigated [211]. The electrospun nanofibrous membrane retained their fibrous structure after incubation for 7 days in aqueous medium (BSF). The morphology of the electrospun alginate/PEO blend as vitamin carrier was directly dependent on the viscosity of the alginate [212]. Higher viscosity alginate favoured beaded nanofibres with smaller average diameters, compared to low viscosity alginate-based nanofibres that were bead-free with larger diameters. The most significant part of using PEO as copolymer, beside the fact of enhancing the electrospinnability, is the opportunity to extract PEO from the nanofibres by incubation in water [53]. In this case the alginate is crosslinked through ionic bonds followed by leaching the PEO. A natural surfactant such as lecithin has been used to impart uniformity to the nanofibres [213]. The surfactant readily renders the opportunity to increase the alginate content in the blend without losing the uniformity of the nanofibres.

5.3.2. Alginate with other biopolymers
A blend of gelatin/sodium alginate produced smooth nanofibres in heated water (45°C) [22]. A blend of chitosan and alginate was also electrospun with the aid of PEO as copolymer [214]. Because chitosan is a cationic copolymer and alginate is an anionic copolymer, they form a polyionic complex that does not need further crosslinking. Due to the gelation of these polymers, side-by-side electrospinning was used where the alginate and chitosan meet at the tip of the spinneret. The swelling of the nanofibres was reduced by the incorporation of chitosan which is not soluble in water. Core-sheath morphology of alginate and chitosan was achieved by spinning the alginate into a chitosan coagulation bath [133]. The average diameter of the nanofibres ranged between 600 and 900 nm coated with chitosan. This enhanced the stability of the alginate in saline solution.

5.4. Collagen
One of the most abundant proteins is collagen. Collagen is a kind of protein that gives strength, elasticity and structural support. The two most electrospun collagen types are collagen type I and type III [75,

215]. Collagen is soluble in a water/ethanol mixture, HIFP [216], TFE [217] and acetic acid [218]. Most research based on collagen was aimed to develop collagen nanofibrous membrane from non-toxic solvents, since collagen is usually used in biomedical applications [219]. These authors established that collagen nanofibrous membrane electrospun from fluoroalcohols lost their natural inherited properties. Matthews *et al*. [75] fabricated aligned collagen nanofibres using 1,1,1,3,3,3 hexafluoro-2-propanol as solvent with a rotating drum collector. The nanofibres were randomly oriented at a mandrel rotating speed of less than 500 rpm, and an increase to 4500 rpm aligned the fibres along the rotation axis. Optimization of the collagen nanofibres was studied by Li *et al*. [218] . Through manipulation of the processing and solution parameters it was possible to produce smooth nanofibres with diameters below 100 nm, but at the expense of the fibre structure. A decrease in concentration from 5% gradually reduced the fibre diameter from ~500 to ~200 nm, and a further decrease in concentration led to fibres with diameters below 100 nm, but with significant formation of beads. It was concluded that the minimal concentration of collagen in 1,1,1,3,3,3 hexafluoro-2-propanol to produce smooth and uniform nanofibres is 5%.

5.4.1. Collagen with synthetic polymers
Another feasible approach to avoid the use of toxic solvents is to co-spin collagen with a spinnable polymer. Chakrapani *et al*. [220] produced collagen nanofibrous membrane from a blend of PCL and collagen in acetic acid. The nanofabric network was made up of fibres with diameters ranging between 100 and 200 nm having a porosity of about 60%. Dong *et al*. [20] prepared collagen nanofibres from phosphate-buffered saline (PBS) and ethanol in the presence of the salt (NaCl). They found out that 16 wt% of collagen was readily soluble when the salt was 5 wt% or more. Nanofibres with diameter ranging between 210 and 540 nm, depending on the salt concentration, were produced. A co-axial morphology of collagen (outer shell) and PCL (inner core) as structural support was produced using both TFE and 1.1.1.3.3.3-hexaflouro-2-propanol (HFP). The coaxial structure was fabricated by using a co-axial nozzle or by coating the electrospun membrane by immersion into a collagen solution [217]. The coaxially electrospun nanofibres displayed a similar morphology as pure PCL nanofibres, with an aver-

age diameter of 385±82 nm, and a coating thickness of 64±26 nm. Another copolymer often used to enhance the spinnability of collagen without toxic solvents is poly(L-lactide-co-ε-caprolactone) [221]. Zhong *et al.* [222] prepared collagen-glycosaminoglycan scaffolds through electrospinning in a mixture of TFE and water, followed by glutaraldehyde vapour crosslinking. The biostability of the smooth nanofibres with a mean diameter of 260 nm was improved. Although much work has been done on collagen in clinical applications, not much has been done on the application of the collagen in water treatment [219, 223]. However, Davis and Maffia [224] successfully prepared collagen from type 1 bovine for water treatment and sludge dewatering. The collagen showed good potential as a coagulant of colloidal solids.

5.5. Gelatin

Gelatin, similar to other naturally occurring polymers, is biocompatible, biodegradable and non-toxic [12]. It is derived from animal tissue such as skin, muscle and bone. Gelatin is subdivided into Type A and Type B, depending on the extraction and chemical treatment. Gelatin type A is obtained from the acidic pre-treatment of collagen, whereas Type B is from alkali pre-treatment. The glutamine and asparagine are converted into glutamic and aspartic acid during alkali pre-treatment, yielding a high carboxylic acid content in gelatin Type B. Gelatin has been processed into various forms for a wide spectrum of applications such as food products, cosmetics and pharmaceuticals [225]. Although gelatin is readily soluble in water and polar solvents, the electrospinnability of gelatin is still a challenge. However, some reports indicated the possibility of electrospinning gelatin using solvents such as using 2.2.2-trifluoroethanol TFE [226], formic acid [66], and 1.1.1.3.3.3-hexaflouro-2-propanol (HIFP) [85]. Electrospinning gelatin in water can be done by applying heat above 37°C [220].

The use of copolymers is another conducive route, not only to electrospin gelatin, but also to improve the mechanical and chemical stability [85, 136]. Huang *et al.* [227] indicated that gelatin can be electrospun into smooth nanofibres with a diameter of 140 nm using 2,2,2-trifluoroethanol (TFE) as a solvent. With a concentration of 7.5 wt% of gelatin, the modulus was 117 MPa and the ultimate strength 4.9 MPa. Similar to collagen the gelation of gelatin and its sol-
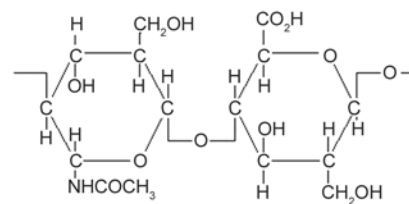
Figure 14. Structure of hyaluronic acid

ubility in water is the reason why it cannot be used in water treatment applications. The limitations of the application of gelatin are its weak mechanical strength and its ready solubility in water. The cross-linking of electrospun gelatin nanofibrous membrane is the most convenient way to improve the stability and mechanical strength [227].

5.6. Hyaluronic acid

Hyaluronic acid (HA), a natural polysaccharide, is often found in connective tissues in the body, such as the vitreous humour, the umbilical cord, and the joint fluid. It is a polyanionic acid made-up of N-acetyl-D-glucosamine and D-glucuronic repeating units as shown in Figure 14.

Thanks to the advancements in electrospinning, pure hyaluronic has been successfully electrospun into nanofibrous membrane from its solution [13, 15]. The electro-blowing of hyaluronic acid affords the preparation of its nanofibres with diameters ranging from 49 to 83 nm depending on the preparation and solution properties used. HA mats with an average fibre diameter of 39±12 nm were produced from NH_4OH:DMF at ratio 2:1 [228]. Many researchers studied the application of the hyaluronic acid in biomedical applications. The hyalorunic was immobilized on the surface of silica microspheres to fabricate a magnetic adsorbent. This shows the possibility to develop new adsorbents for wastewater treatment [229].

5.6.1. Hyaluronic acid with other biopolymers

Hyaluronic acid/chitosan electrospun bioblend nanofibres were prepared by Ma *et al.* [230] in a mixture of formic acid and water. Smooth fibres with smaller average diameters (83 nm) were obtained at higher contents of hyaluronic acid (hyaluronic/chitosan at 9/1), while at low contents beaded-fibres (7/3) and drops (6/4) formed.

5.6.2. Hyaluronic acid derivatives

A thiolated HA derivative, 3,3′-dithiobis(propanoic dihydrazide)-modified HA (HA-DTPH), was syn-

thesized and electrospun into nanofibrous membrane by Ji *et al.* [86]. The dithiobis(propanoic dihydrazine) was synthesized and coupled to the carboxylic groups of HA via carbodiimide chemistry. The thiolated bond formed were reduced using dithiothreitol to produce thiolated HA-DTPH. HA-DTPH (2% w/v)/PEO (2% w/v) resulting in uniform nanofibres with diameters ranging from 70 to 110 nm. The resulting fibres were crosslinked with PGEDA (9 w/v), followed by the dissolution of PEO in deionized water for 48 hours. After the extraction of PEO the fibre diameter distribution became much wider (with 85% of the fibre diameters ranging between 50 and 300 nm). The crosslinking of the nanofibres reduced the swelling ratio of the mats. Another group investigated a similar system, but they used dual-syringe reactive electrospinning with thiolated HA/PEO into contact with PEGDA before electrospinning to induce crosslinking [86].

5.7. Aloe vera
Aloe vera is one of the oldest herbal products used for medicinal purposes. It contains more than 200 nutrients which include amino acids, saliycilic acid, absorbic acid, enzymes and lots of minerals and vitamins [231, 232]. It is largely made up of water with long chain polysaccharides of acetylated glucomannan and carbohydrates. So far there is no work based on the electrospinning of aloe vera alone, but blends of synthetic and biopolymers were used to facilitate its electrospinnability. We included aloe vera as biopolymer because of its biocidal efficacy (towards different pathogenic organisms), and the possibility to functionalize electrospun mats in water filtration and treatment to reduce the biofouling of the electrospun membrane. Nonetheless, aloe vera enjoyed its success over a wide array of medical applications [233].

5.7.1. Aloe Vera with synthetic/biopolymers
A hybrid of hydroxypropyl methylcellulose (HPMC), poly(vinyl alcohol) PVA, poly(vinyl pyrrolidone), iodine PVP and poly(ethylene glycol) (PEG) were doped with aloe vera to investigate the effect of aloe vera on the properties of the resulting nanofibrous membrane. Like any biopolymer, aloe vera influenced the solution properties such as viscosity and conductivity. The addition of aloe vera increased both the viscosity and conductivity of the spinning solution, and decreased the mean diameter of the ensuing nanofibres from 660 to 596 nm at 1% of aloe

vera. SEM showed an interfuse with each other when the content of aloe vera increased in the composition. In another study the addition of aloe vera (at 6%) resulted in finer and more homogeneous nanofibres with mean diameters of 150 to 350 nm [232]. A similar study on the hybrid of biodegradable PCL and aloe vera to prepare transdermal biomaterial showed homogeneity and small average diameters of the nanofibres in the presence of aloe vera (519±28 versus 215±63 nm at 10% aloe vera), and greatly improved mechanical properties and hydrophilicity [234].

6. Electrospun biopolymers with nanomaterials
In the past few years there has been an ever increasing interest in incorporating different nanoparticles in biopolymers for a broad range of applications [26, 235]. Nanoparticles have a promising potential in wastewater/water treatment as biocidal agents, sensors, and adsorbents. If these nanoparticles are used alone for water/wastewater treatment there are some limitations such as their recovery and reuse, cost and their long-term effect on health and/or the environment. The biocidal activities of these nanoparticles are depicted in Table 5. A possible solution is to immobilize and control their release to overcome these complications/limitations [236, 237]. Electrospinning these nanomaterials (with known content) with biopolymers offers the possibility to retain their nanosize and their release into streams without any harmful by-products, thus reducing the overall cost.

6.1. Silver nanoparticles
Silver is well-known for centuries for its attractive antimicrobial, antiviral and fungicidal activity [236, 238]. The metal enjoyed its success in a broad spectrum of consumer products, such as plastics, soaps, pastes, food and textiles. The antimicrobial and antifungal activity of silver nanoparticles (AgNP) makes it the most studied metal nanoparticle for different applications [234–236]. There are several ways by which ionic silver can be reduced into silver nanoparticles [26, 238]. There is still a lot of controversy on the mechanism behind the antibacterial, fungicidal, and antiviral activity displayed by silver nanoparticles. Three mechanisms were postulated, namely i) attachment of the silver nanoparticles on the surface of the cell membrane and disturbing its permeability and respiration, ii) penetrating the cell and

Table 5. Summary of common antibacterial nanomaterials and applications

Nanomaterial	Proposed antimicrobial mechanism	Potential water treatment applications
Silver (AgNP)	Release of Ag^+ ions, disruption of cell membrane and electron transport, DNA damage	Surface coatings, membranes, membrane reinforcement
Carbon nanotube (CNT)	Disruption of intracellular metabolic pathways, oxidative stress, physical membrane damage	Biofouling resistance membranes, carbon hollow fibres, membrane reinforcement
Hydroxyapatite (Hap)	Easy functionalization with different biocidal metal oxide	Membrane reinforcement
Zinc (ZnO)	Intracellular accumulation of nanoparticles, disruption of cell membrane, H_2O_2 production, release of Zn^+ ions	Surface coating, membranes, membrane reinforcement

reacting with some compounds containing sulphur and phosphorus such as DNA and proteins, and iii) releasing silver ions which contributes to its activity towards pathogens [236]. These mechanisms depend on the distribution, shape and size of the silver nanoparticles.

Formic acid was used as solvent to prepare chitosan/PVA nanofibres with optimal conditions of 0.5 mL·h^{-1} flow rate, 18 kV voltage and a TCD of 7.5 cm. Chitosan/PVA was doped with silver oxides and titanium oxides to significantly improve the antibacterial activity of the ensuing nanofibres [26]. The prepared nanofibres with mean diameters ranging between 270 and 360 nm were cultured to find their antibacterial activity against both Gram negative and Gram positive bacteria. The antibacterial activity of AgNO$_3$ loaded composite nanofibres increased with an increase in AgNO3 content with 99% bacteria eradicated for *S. aures* and 98% for *Escherichia coli* at only 0.04 wt% of AgNO$_3$. TiO$_2$ loaded composite nanofibres showed a maximum of 90% bacteria for *S. aures* and 85% bacteria for *Escherichia coli* eradicated at concentrations above 0.03 wt% of TiO$_2$.

The diameter of the nanofibres also influenced the antibacterial activity, with smaller diameters showing better efficiency because of the large surface to volume ratio giving more contact with the bacteria. A similar blend of chitosan and PVA was doped with AgNPs [239]. A 12 wt% PVA solution containing AgNO$_3$ blended with a 6 wt% chitosan solution (15 wt% in acetic acid) was electrospun, followed by either refluxing for 48 hours or annealing at 130°C for 16 hours (to reduce Ag ions of the nanofibres). The intensities of surface plasmon resonance (SPR) of AgNPs increased in the presence of chitosan compared to that of PVA and AgNO$_3$ only, indicating that chitosan can act as a stabilizer as well as a reducing agent for the formation of AgNPs. The spherical AgNPs on the surface of the electrospun nanofibrous membranes were fairly uniform and smaller in size when refluxed, while larger particles were asso-

ciated with diffusion and agglomeration of residual Ag ions and AgNPs formed in the solid during heating were formed when annealed. This resulted in a lower killing efficiency of the annealed samples due to the surface area of the AgNPs coming into contact with the bacteria.

An *et al*. [240] prepared chitosan (CS)/polyethylene oxide (PEO) containing AgNPs nanofibres by means of *in situ* chemical reduction of Ag ions. The average diameter of the nanofibres decreased with an increase in AgNPs because of the increased charge density in the spinning solution, imparting stretching of the electrified jet under the electrical field. The cubic crystal AgNPs were fairly well dispersed in the CS/PEO ultrafine nanofibres with average diameter of less than 5 nm. The tensile modulus and tensile strength of the CS/PEO/AgNP nanofibres were better than that of the CS/PEO nanofibres. The CS/PEO/AgNP nanofibrous membrane exhibited higher antibacterial activity than the CS/PEO nanofibres towards *E. coli*. Silver nanoparticles were also incorporated into PVA/CS blends for their antibacterial activity [241]. The electrospinnability of the PVA/CS was enhanced by the AgNPs, and the size of the AgNPs varied between 2.4 to 10.7 nm depending on the CS concentration in the blends. A biopolymer blend of CS/gelatin containing AgNPs was successfully electrospun by Zhuang *et al*. [242]. The study indicates that the microcrystalline chitosan was used as reducing agent and stabilizer to synthesize the AgNPs at room temperature. Using a noniogenic polymer (PEO), a natural polymer (N-carboxyethyl-chitosan), and silver nanoparticles, Penchev *et al*. [87] observed a complete killing of the bacteria (*Staphylococcus aureus*) within an hour of contact at higher concentrations of silver nanoparticles, whereas at low concentrations the nanoparticles only inhibits bacterial growth. They used a one pot system to fabricate the nanofibre in which all the components were added into the spinning solution. Formic acid was again used as reducing agent and solvent, and the

sizes of the NPs were 4±0.5 and 6±1.5 nm respectively for 5 and 10 wt% of the AgNO₃. Yang *et al.* [31] fabricated antimicrobial membrane using cellulose acetate and AgNO₃ by slow and fast photoreduction. The mats were tested against *Staphylococcus aureus*, *Escherilia coli*, *Klebsiella pneumonia*, and *Pseudomonas aeruginosa* by an attachment method. The mean diameter of the ultrafine nanofibres ranged between 680 and 610 nm for 0.05 and 0.5 wt% of AgNO₃, respectively. Most of the nanoparticles had a mean diameter between 3 and 16 nm, whereas 15.4 nm resulted after rapid photoreduction. The killing efficiency for all the bacteria was 99.9% at a very low concentration of 0.05 wt%. Lee *et al.* [243] produced electrospun chitosan nanofibres with chemically reduced AgNPs via electrospinning. The resulting spherical nanoparticles with sizes ranging between 10 and 11 nm (average diameter of 10±2 nm) were evenly distributed in the chitosan nanofibres. The growth inhibition of *Pseudomonas aeruginosa* (gram negative) and *Staphylococcus aureus* (gram positive) increased with an increase in AgNPs in the composite materials.

6.2. Hydroxyapatite (HAp) nanoparticles
Celebi *et al.* [244] produced electrospun chitosan/PVA nanofibrous membrane containing silver ion-incorporated hydroxyapatite (HAp) nanoparticles. A mean diameter of ~70 nm of silver ions-incorporated HAp particles were obtained with good antibacterial efficiency against *Escherichia coli*. Hydroxyapatite (HAp)/chitosan was synthesized by co-precipitation synthesis followed by electrospinning of 10 wt% UHMPEO in aqueous solution with the solvent composed of acetic acid (HAc) and dimethyl sulphoxide (DMSO). The X-ray diffraction (XRD) and selected area electron diffraction (SAED) spectra confirmed that the crystalline structure of HAp was retained in the nanofibres [217]. The electrospun nanocomposite nanofibrous membrane were finer and more homogeneous with diameters of 214±25 nm with spindle-like HAp parallel to the nanofibres direction. A similar dispersion of HAp and structure were reported using gelatin as matrix [245]. The mechanical properties were also improved in the presence of HAp.

6.3. Carbon nanotubes
Carbon nanotubes have excellent antimicrobial activity and mechanical strength. Similar to Ag nanopar-

ticles, the mechanism of the carbon nanotubes against pathogenic organisms is still controversial [236]. The proposed mechanisms include physical membrane perturbation and oxidative stress. Their antimicrobial activity is also influenced by their distribution, diameter, length, and electronic structure. Most of the carbon nanotubes exhibit good cytotoxicity towards pathogenic organisms, with single-walled carbon nanotubes reported to be the most efficient. Well-aligned single walled carbon nanotube (SWNT) along the fibre axis of the *bombyx mori* silk nanofibre were produced by Ayutsede *et al.* [246]. A very low concentration of SWNT (1 wt%) was enough to increase the crystallinity and mechanical properties. Multiwalled carbon nanotubes (MWNTs) were also incorporated in electrospun cellulose acetate (CA) nanofibres to investigate the effect of these nanoparticles on biopolymers [247]. The mean diameter of the nanofibres reduced from 267 nm for pure CA to 193 nm with MWNTs at only 0.55 wt%. The MWNTs impart significant water wetting, surface area (from 4.3 to 7.7 m·g⁻¹), Young's modulus (doubled from 553 to 1144 MPa), tensile strength (from 21.9 to 40.7 MPa) and elongation at break (from 8.0 to 10.5%). A core-sheath structure of PVA/CS-MWNT with outer and inner sheath-core nanofibres of 200 and 100 nm respectively was reported by Feng *et al.* [248]. The composite nanofibres showed fast transfer kinetics and good electrochemical properties. In one of their recent studies on electrospun silk fibroin (*B. mori*)/multiwalled carbon nanotubes they reported that MWNTs induced crystallization of silk and significantly improved the mechanical properties [249].

6.4. Zinc nanoparticles
Zinc nanoparticles (ZnO) antibacterial activity is still not clear, but several mechanisms were proposed. It was suggested that the lethal effect of ZnO results from disruption of the cell membrane activity and induction of intercellular reactive oxygen species, such as H₂O₂, a strong oxidizing agent harmful to bacterial cells [236]. Zinc oxide was produced by mixing the precursor (zinc acetate) in 0.1 M sodium hydroxide in methanol [250]. The prepared ZnO was introduced in an alginate/PVA blend dissolved in distilled water. With a large contact area the composite exhibited high toxicity to both gram-negative and gram-positive bacteria. Taha *et al.* [156] functionalized a cellulose acetate/silica composite with NH₂ to enhance its affinity towards Cr(IV) ions. They used

tetraethoxysilane (TEOS) as silica source, cellulose acetate as precursor and 3-ureidoptopyltriethoxysilane as a compatibilizer. They produced NH_2 functionalized nanofibres with a mean diameter of 100–500 nm and a porosity and surface area of 73% and 126.5 $m^2 \cdot g^{-1}$. Using static and dynamic experiments the membrane showed adsorption of 98%. ZnO nanoparticles were impregnated into the electrospun cellulose acetate nanofibre membrane by Anitha *et al.* [251]. The membrane displayed a superhydrophobic nature (water contact angle of 124º) and antibacterial property against well-known bacteria.

7. Applications of electrospun biopolymers in water treatment

Electrospun nanofibres afford the opportunity to be applied in various fields such as biosensors, and filtration because of their unique properties such as large surface area and engineered porosity, and physico-mechanical properties. The manipulation of the solution properties and technique advancement rendered the opportunity to produce the desired morphology and structure of the resulting nanofibres for specific applications.

7.1. Bioremediation

Heavy metals in wastewater is still a big problem, and a challenge to researchers to come up with reliable solutions without leaving by-products. Cellulose acetate has been functionalized to increase its adsorption efficiency which depends mostly on the functional groups found on the main chain. Poly(methacrylic acid) (PMAA) with additional carboxyl groups was used to functionalize cellulose acetate to increase the number of metal binding sites [252]. The efficiency was enhanced by the presence of PMAA on the cellulose acetate fibres, but the adsorption was more effective for the removal of mercury (Hg(II)) with an adsorption capacity of 4.8 $mg \cdot g^{-1}$. The efficiency may, however, depend on the metal ion type and the pH. The de-adsorption of the metals is possible with an appropriate solvent such as ethylenedinitrilotetraacetic acid (EDTA). Cellulose acetate/silica composites were tested for Cr(VI) adsorption [156]. In this case the CA/SiO_2 was functionalized with NH2 to enhance the adsorption of the resulting fibre membranes. The membranes displayed a good adsorption, and desorption after washing five times with an aqueous solution of sodium hydroxide (NaOH). The adsorption data of Cr(VI) fitted well with the Langmuir isotherm with an adsorption capacity of 19.5 $mg \cdot g^{-1}$.

Although various mechanisms were proposed to describe the metal ions adsorption of chitosan, the electrostatic attraction on the protonated amine groups is the accepted mechanism [253]. The heavy metal adsorption efficiency of an electrospun chitosan membrane was studied by several researchers [10, 254]. It was found to depend on several aspects such as the degree of deacetylation [254], pH, fibre structure and morphology [181, 254]. Desai *et al.* [254] studied the adsorption efficiency of PEO/chitosan nanofibres electrospun towards chromium using simulated flow conditions at a pH of 7.3. The chromium solution (prepared from 5 $mg \cdot L^{-1}$ K_2CrO_4) was passed ten consecutive times through the chitosan nanofibrous filter. The binding efficiency of the membrane decreased with an increase in nanofibre diameter (81–131 nm). However, the heavy metal adsorption efficiency increased with an increase in the degree of deacetylation. Using static conditions, the same group found that the metal adsorption depends on the molecular weight of chitosan, the degree of deacetylation, the percentage of chitosan in the blend, and the surface area to mass ratio. The molecular weight is related to the length of the chains and therefore to the number of cations on the backbone of the chitosan acting as active binding sites.

Cho *et al.* [10] neutralized the nanofibres with K_2CO_3 to obtain an $-NH_2$ group on the backbone of the chitosan membrane. This improved the stability of the electrospun membrane in water, with negligible weight reduction after 24 hours. The adsorption of the metals (Cu(II), 419.2 $mg \cdot g^{-1}$ and Pb(II), 202.8 $mg \cdot g^{-1}$) increased significantly for the first 15 min to 4 hours and levelled off after 8 hours, due to the unavailability of binding sites (amine, primary and secondary hydroxyl groups), large surface area, and inter- and intrafibrous pores in the fibrous membrane. The Langmuir isotherm data showed that the equilibrium adsorption capacities for Cu(II) and Pb(II) were respectively 485.4 $mg \cdot g^{-1}$ (2.85 mmol g^{-1}) and 263.2 $mg \cdot g^{-1}$ (0.79 $mmol \cdot g^{-1}$). The difference between the values for the two metals was attributed to the differences in their atomic radii. It was suggested that the chitosan' adsorption followed a monolayer mechanism.

A nanofibrous membrane of pure silk fibroin (SF), and a blend of wool keratose and silk fibroin

(WK/SF), were compared with pure silver wool and filter paper for their Cu(II) adsorption capacity [255]. The nanofibrous membranes displayed a significant Cu(II) adsorption capacity compared to silver wool and filter paper because of the large specific area which is ~50 times larger than those of filter paper and silver wool. The blend membrane showed a higher capacity than the SF membrane. The difference in Cu(II) adsorption capacity was related to the different chemical compositions (especially amino acids compositions). Both membranes displayed good desorption percentages. Desorption and re-adsorption was repeated six times, but the membrane kept 90% of its adsorption capacity. The Langmuir isotherm fits the experimental results better than the Freudlinch model. The Cu(II) adsorption followed a monolayer adsorption model.

Yang *et al*. [256] functionalized oxidized cellulose nanofibres embedded in an electrospun polyacrylonitrile (PAN) nanofibrous membrane with thiol groups to evaluate the metal adsorption capacity. Besides the increased stiffness due to the functionalization, the functionalized composite membrane displayed an adsorption of 76.5±2.0 $Cr_2O_7^{2-}$ metal ions per gram of cellulose nanofibre at pH = 4.0, while the adsorption of Pb(II) was 133±2.5 mg·g^{-1} at pH = 5 in static conditions. The membrane also reached 80.0 mg·g^{-1} of Pb(II) within 15 minutes, and 125 mg·g^{-1} within 20 minutes. Under dynamic conditions the membrane showed 60 mg Cr(VI) g^{-1} (pH = 4) and 115 mg Pb(II) g^{-1} were adsorbed. Wang *et al*. [257] grafted cellulose nanowhiskers with amine groups using polyvinylamine (PVAm). The membrane displayed a maximum dynamic adsorption of 100 mg Cr(VI) (at pH = 4) and 260 mg Pb(II) (at a pH of 6) per gram of cellulose nanofibre.

7.2. Filtration membrane

Even though electrospun nanofibrous membranes were successful in air filtration, much work was still needed for water filtration. The breakthrough came when the electrospun nanofibres were spun onto more rigid nonwoven polyesters to improve handling issues and their mechanical properties [29]. The thin composite membrane (TNFC) significantly enhanced the rejection and flux permeation of the membranes, because of the nanofibres with high porosity and controllable pore size for specific filtration processes. TNFC membranes have been one of the growing subjects in water filtration, because of

the performance displayed by these materials since the introduction of electrospun nanofibres as one of the sub-layers.

Several researchers found that the coating of these TNFC with cellulose nanowhiskers imparts significant hydrophilicity and mechanical properties to the membrane [144, 149–152]. The thin top-layer coating enhanced the rejection and flux. Wang *et al*. [258] found that the interfacial polymerization of polyamide around the ultrafine cellulose nanofibres layer in TFNC showed a good rejection of MgCl and MgSO$_4$, depending on the adapted interfacial polymerization (i.e. IP, the organic phase on top of the aqueous phase, or IP-R, the aqueous phase on top of the organic phase). The IP based membrane showed a rejection of 67.6% at 1% of piperazine (PIP), while the IP-R showed a rejection of 91.6% of MgSO$_4$. However, both membranes displayed similar rejection percentages for both MgSO$_4$ and MgCl at higher PIP concentrations. The same group electrospun PAN onto PET and infused cellulose nanowhiskers (diameter 5 nm) for the microfiltration process [257]. The cellulose nanowhiskers were functionalized with different amines such as polyethyleneimine (PEI), ethylenediamine (EA), and polyvinylamine (PVAm) by using N-(3-Dimethylaminopropyl)-N′-ethylcarbodiimide hydrochloride (EDC) and N-Hydroxysuccinimide (NHS) as catalysts. The resulting cellulose-based membrane had a mean pore size of 0.38 μm with a maximum pore size of 0.78 μm, and the water permeation was about 1300 L·m^{-2}·h^{-1}·psi^{-1}. All the membranes showed complete removal of the bacteria by size exclusion. The coating of chitosan on electrospun PAN enhanced the filtration efficiency and rejection for both ultrafiltration and nanofiltration processes [259]. The membrane displayed a rejection of 99% due to the inherited hydrophilicity of chitosan.

7.3. Biocidal membrane

Biofouling is a major problem for most membranes, because it results in the accumulation and biological growth of pathogenic organisms, and the deterioration of the membrane performance. A variety of metal oxides have been added to the electrospun biopolymer nanofibres to impart biocidal activity to the resulting nanofibres. Most of the diseases in developing countries are caused by pathogenic organisms. There has been an escalation of research in incorporating silver nanoparticles in the electro-

spun membrane to impart biocidal activity [156, 239, 240, 243, 244]. Even though there is still much controversy over the biocidal activity of the silver nanoparticles, electrospun nanofibres displayed enhanced antibacterial efficiency when the membranes contained silver. ZnO particles were introduced in an alginate/PVA blend dissolved in distilled water, followed by electrospinning [250]. With the high contact area the electrospun composite displayed toxicity to both negative and positive bacteria. ZnO nanoparticles were also incorporated in a cellulose acetate membrane to enhance the antibacterial efficiency against *Staphylococcus aureus*, *E. coli*, and *Citrobacter freundii*. [251]. The impregnated ZnO nanoparticles significantly inhibited the growth of the bacteria and the inhibition zone diameters were 27, 22, and 14 mm for *Staphylococcus aureus*, *Escherichia coli*, and *Citrobacter freundii*. The functionalization of the electrospun membrane also enhanced the biocidal efficiency [83, 193, 195]. A quaternized chitosan membrane displayed inhibition of bacterial growth on the mat. Blending biopolymers with good antibacterial efficiency was also significantly reduced the biocidal activity of the resulting membrane [83].

7.4. Chemosensors

Chemosensors are detectors to selectively identify and recognize ions and molecules. A number of studies have been done on implanting the chemosensing agent onto solid matrices to improve the sensitivity, robustness, and lifetime [260]. A variety of polymers and nanomaterials were used as supporting materials in solid-state sensors. The sensitivity detection and exposure of the chemosensors was found to be directly dependent on the structure of the supporting material [261].

The sensing agent embedded onto electrospun nanofibres (with large surface areas) improves the detection sensitivity and response time, and reduces the concentration detection value (lowest detection value (LOD)) compared to commonly used films. The presence and concentration of the heavy metals can therefore be traced and removed at fairly low concentrations. Several biobased nanofibres such as ethyl acetate, cellulose acetate and cellulose have been functionalized with different fluorescent compounds to detect Cu [260–262]; Cr [260], Fe [263] and Hg ions [261, 264]. Due to the large surface areas of the electrospun nanofibres, the sensitivity, selectivity,

response time, and stability were enhanced. Kacmaz *et al.* [263] produced electrospun EC doped with dye to detect Fe^{3+} ions. The membrane sensed Fe^{3+} ions over a concentration range of 10^{-12}–10^{-6} M (with an LOD of 0.07 pM), with a sensitivity response time of less than 30 s and sensor regeneration within 60 s.

Zdyrko [265] developed a self-deployable colorimetric sensor by taking advantage of the superabsorbency of alginate, and functionalizing it with a heavy metal sensitive compound/dye. A blend of alginate and PEO electrospun onto rigid nonwoven (PET) absorbed metal ions from contaminated water.

8. Limitations of electrospun biopolymers in water treatment

Besides the hurdles based on the production scaleup of biopolymers, properties from the same source differ and the growth conditions influence the resulting properties. The harsh chemical treatment used to extract some biopolymers put an additional burden onto the water and the environment. It is important to do a lot of research on genetically engineering organisms and novel designed productions to scale up the production of biopolymers with high purity/quality and having identical properties. Electrospun nanofibrous membranes have limited mechanical strength to withstand the pressures involved in water filtration, thus they are only applicable in membrane technologies were low pressures are involved (MF, UF and NF). Even though the work done on electrospun biopolymers shows potential to use ecofriendlier solvents, their application in water/wastewater treatment is still in its infancy. Most of these polymers are naturally prone to biodegradation and some are readily soluble in water, hence their lifetime is too short and they will need to be regularly replaced over time. This results in increasing the price of the membrane. The enhancement of the stability *via* either chemical or physical treatment without altering the unique valuable properties of the biobased membranes is important for their application in water/wastewater treatment. The dispersion of the nanomaterials in electrospun nanofibres (without agglomeration to retain their nanosize), and their exposure and release into the stream requires a lot of understanding. Most methods used to prepare the electrospun composite materials revolve around coating the mat (immersing the mat in a metal oxide

solution) or adding the nanomaterial into the spinning solution. Nanomaterials from these methods have different release rates and exposure to the water stream. In the near future, investigation of the controlled release and exposure of the nanomaterials is required to understand and control their disinfection efficiency.

9. Conclusions

In the past decades, electrospinning has been highly recognized as a new class of nanotechnology providing access to a range of nanomaterials with unique properties. Significant progress has been made on the fundamental understanding of the mechanism, and the modelling of the envisaged processes governing the fibre formation. This was proven by advanced developments to engineer desired nanostructured materials through electric field manipulation, solution properties and new designs. Control over their deposition, dimensions and assemblies created new avenues to generate desired configurations for specific applications. There is currently a big paradigm shift towards the industrialization and commercialization of the electrospun nanofibres. The new technical advances (fibre collections strategies, needle shapes, and high throughput production) proved to

be successful in the synthesis of these fascinating nanostructured materials. A fair amount of work has been done on electrospinning biopolymers for a broad array of applications, especially in the biomedical field. Much of this work was based on electrospinning of biopolymers with and without copolymers and using non-toxic solvents. Water filtration and wastewater treatment received little attention, despite the unique properties of biopolymers that are important in addressing environmental concerns. The biodegradation and mechanical strength of the electrospun mats are critical limitations in water filtration and wastewater treatment. In future the mutual relation to protect and improve the strength of the electrospun biopolymers by blending, chemical and physical treatment, and the addition of metal oxides and their controlled release into water streams will revolutionize wastewater treatment and water filtration. Through further research it will be possible to bridge the gap to enable the application of biopolymers in water filtration and treatment.

Acknowledgements

Abbreviations

3D	three dimensional		HA	hyaluronic acid
AgNP	silver nanoparticles		HA-DTPH	3.3′-dithiobis(propanoic dihydrazide)-modified hyaluronic acid
C	concentration			
CA	cellulose acetate		HAp	hydroxyapatite
CMC	carbomethyl chitin		HFIP/HFP	1.1.1.3.3.3-hexaflouro-2-propanol
CMCs	carboxymethyl cellulose sodium salt		HPMC	hydroxypropyl methyl cellulose
CoPc	cobalt tetraaminophthalocyanine		HTACC	N-(2-hydroxlpropyl-3-trimethyl ammonium chitosan chloride)
CV	crystal violet			
D	diameter		LOD	lowest detection value
DCM	dichloromethane		MeOH	methanol
DD	deacetylation degree		MF	microfiltration
DMAc	N,N-dimethylacetamide		Mw	molecular weight
DMF	N,N-dimethylformamide		MWNT	multiwalled carbon nanotube
DNA	deoxyribonucleic acid		NHS	N-Hydroxysuccinimide
DOSE	dual-opposite-spinneret electrospinning		NMMO	N-methylmorpholine-N-oxide
DS	Degree of substitution		NP	nanoparticles
EA	ethylenediamine		P(CLLA)	poly(L-lactide-co-caprolactome)
EC	ethyl cellulose		P(LLA-CL)	poly (L-lactide-co-caprolactone)
EDC	N-(3-Dimethylaminopropyl)-N′-ethylcarbodiimide hydrochloride		PAA	polyacrylic acid
			PAAm	poly(acrylamide)
EDS	energy-dispersive X-ray spectroscopy		PAN	poly(acrylonitrile)
EDTA	ethylenediaminetetraacetic acid		PBS	phosphate buffered saline
ENM	electrospun nanofibrous membrane		PCL	polycaprolactone
GAG	glycosaminoglycan		PCLDLLA	poly(ε-caprolectome-co-D-L-lactide)
GJF	gas jet nanofibre		PEG	poly(ethylene glycol)

PEGDA	poly(ethylene glycol) diacrylate
PEI	polyethyleneimine
PEO	poly(ethylene oxide)
PES	poly(ether sulphone)
PET	poly(ethylene terephthalate)
PF	paraformaldehyde
PGA	poly(glycolic acid)
PIP	piperazine
PLA	poly(lactic acid)
PMAA	poly(methacrylic acid)
PS	polystyrene
PU	poly urethane
PVA	poly(vinyl alcohol)
PVAc	poly(vinyl acetate)
PVAm	polyvinylamine
PVDF	poly(vinylidene flouride)
PVP	poly(vinyl pyrrolidone)
QBzCSN	N-benzyl-N,N-dimethyl chitosan iodide
QCh	quaternized chitosan
RJS	rotary-jet spinning
RNA	ribonucleic acid
SEM	scanning electron microscopy
SF	silk fibroin
SNE	standard electrospinning
SO3H	sulphonate groups
SWNT	single walled carbon nanotube
TCD	tip-to-collector distance
TEM	transmission electron microscopy
TEMPO	2,2,6,6-tetramethylpiperidiooxy
TFA	trifluoroacetic acid
TFE	triflouroethanol
Tg	glass transition temperature
Tm	melting temperature
TMP	trans-membrane pressure
TNFC	thin film composite membrane
TPU	thermoplastic polyurethane
UF	ultrafiltration
WK	wool keratose
XPS	X-ray photoelectron spectroscopy

References

[1] Pendergast M. M., Hoek E. M.: A review of water treatment membrane nanotechnologies. Energy and Enviromental Science, **4**, 1946–1971 (2011).
DOI: 10.1039/C0EE00541J

[2] Progress on sanitation and drinking water, 2013 update, WHO and UNICEF report (2013).

[3] Ahmad S., Martens P. N., Pateiro F. J., Fuchsschwanz M.: Mine waste dumping and corresponding enviromental impacts at Chihn Bac waste dump in Vietnam. in 'Securing the Future and 8th ICARD. Skellefttes, Sweden' p.6 (2009).

[4] Binns J., Illgner P., Nel E.: Water shortage, deforestation and development: South Africa's working for water programme. Land Degradation and Development, **12**, 341–355 (2001).
DOI: 10.1002/ldr.455

[5] Balamurugan R., Sundarrajan S., Ramakrishna S.: Recent trends in nanofibrous membranes and their suitability for air and water filtrations. Membranes, **1**, 232–248 (2011).
DOI: 10.3390/membranes1030232

[6] Ramakrishna S., Fujihara K., Teo W-E., Yong T., Ma Z., Ramaseshan R.: Electrospun nanofibers: Solving global issues. Materials Today, **9**, 40–50 (2006).
DOI: 10.1016/S1369-7021(06)71389-X

[7] Haider S., Park S-Y.: Preparation of the electrospun chitosan nanofibers and their applications to the adsorption of Cu(II) and Pb(II) ions from an aqueous solution. Journal of Membrane Science, **328**, 90–96 (2009).
DOI: 10.1016/j.memsci.2008.11.046

[8] Greiner A., Wendorff J. H.: Electrospinning: A fascinating method for the preparation of ultrathin fibers. Angewandte Chemie International Edition, **46**, 5670–5703 (2007).
DOI: 10.1002/anie.200604646

[9] Andrady A. L.: Science and technology of polymer nanofibers. Wiley, Hoboken (2008).

[10] Cho H., Min S-Y., Lee T-W.: Electrospun organic nanofiber electronics and photonics. Macromolecular Materials and Engineering, **298**, 475–486 (2013).
DOI: 10.1002/mame.201200364

[11] Frenot A., Henriksson M. W., Walkenström P.: Electrospinning of cellulose-based nanofibers. Journal of Applied Polymer Science, **103**, 1473–1482 (2007).
DOI: 10.1002/app.24912

[12] Nie H., He A., Zheng J., Xu S., Li J., Han C. C.: Effects of chain conformation and entanglement on the electrospinning of pure alginate. Biomacromolecules, **9**, 1362–1365 (2008).
DOI: 10.1021/bm701349j

[13] Um I. C., Fang D., Hsiao B. S., Okamoto A., Chu B.: Electro-spinning and electro-blowing of hyaluronic acid. Biomacromolecules, **5**, 1428–1436 (2004).
DOI: 10.1021/bm034539b

[14] Viswanathan G., Murugesan S., Pushparaj V., Nalamasu O., Ajayan P. M., Linhardt R. J.: Preparation of biopolymer fibers by electrospinning from room temperature ionic liquids. Biomacromolecules, **7**, 415–418 (2006).
DOI: 10.1021/bm050837s

[15] Wang X., Um I. C., Fang D., Okamoto A., Hsiao B. S., Chu B.: Formation of water-resistant hyaluronic acid nanofibers by blowing-assisted electro-spinning and non-toxic post treatments. Polymer, **46**, 4853–4867 (2005).
DOI: 10.1016/j.polymer.2005.03.058

[16] Safi S., Morshed M., Hosseini Ravandi S., Ghiaci M.: Study of electrospinning of sodium alginate, blended solutions of sodium alginate/poly(vinyl alcohol) and sodium alginate/poly(ethylene oxide). Journal of Applied Polymer Science, **104**, 3245–3255 (2007).
DOI: 10.1002/app.25696

[17] Fang X., Reneker D. H.: DNA fibers by electrospinning. Journal of Macromolecular Science Part B: Physics, **36**, 169–173 (1997).
DOI: 10.1080/00222349708220422

[18] Buchko C. J., Chen L. C., Shen Y., Martin D. C.: Processing and microstructural characterization of porous biocompatible protein polymer thin films. Polymer, **40**, 7397–7407 (1999).
DOI: 10.1016/S0032-3861(98)00866-0

[19] Jacobs V., Patanaik A., Anandjiwala R. D., Maaza M.: Optimization of electrospinning parameters for chitosan nanofibres. Current Nanoscience, **7**, 396–401 (2011).
DOI: 10.2174/157341311795542570

[20] Dong B., Arnoult O., Smith M. E., Wnek G. E.: Electrospinning of collagen nanofiber scaffolds from benign solvents. Macromolecular Rapid Communications, **30**, 539–542 (2009).
DOI: 10.1002/marc.200800634

[21] Wnek G. E., Carr M. E., Simpson D. G., Bowlin G. L.: Electrospinning of nanofiber fibrinogen structures. Nano Letters, **3**, 213–216 (2003).
DOI: 10.1021/nl025866c

[22] Moon S., Farris R. J.: Electrospinning of heated gelatin-sodium alginate-water solutions. Polymer Engineering and Science, **49**, 1616–1620 (2009).
DOI: 10.1002/pen.21355

[23] Frey M. W.: Electrospinning cellulose and cellulose derivatives. Polymer Reviews, **48**, 378–391 (2008).
DOI: 10.1080/15583720802022281

[24] Fang D., Liu Y., Jiang S., Nie J., Ma G.: Effect of intermolecular interaction on electrospinning of sodium alginate. Carbohydrate Polymers, **85**, 276–279 (2011).
DOI: 10.1016/j.carbpol.2011.01.054

[25] Barhate R. S., Ramakrishna S.: Nanofibrous filtering media: Filtration problems and solutions from tiny materials. Journal of Membrane Science, **296**, 1–8 (2007).
DOI: 10.1016/j.memsci.2007.03.038

[26] Gopal R., Kaur S., Ma Z., Chan C., Ramakrishna S., Matsuura T.: Electrospun nanofibrous filtration membrane. Journal of Membrane Science, **281**, 581–586 (2006).
DOI: 10.1016/j.memsci.2006.04.026

[27] Patanaik A., Jacobs V., Anandjiwala R. D.: Performance evaluation of electrospun nanofibrous membrane. Journal of Membrane Science, **352**, 136–142 (2010).
DOI: 10.1016/j.memsci.2010.02.009

[28] Son W. K., Youk J. H., Lee T. S., Park W. H.: Preparation of antimicrobial ultrafine cellulose acetate fibers with silver nanoparticles. Macromolecular Rapid Communications, **25**, 1632–1637 (2004).
DOI: 10.1002/marc.200400323

[29] Son B., Yeom B-Y., Song S-H., Lee C-S., Hwang T. S.: Antibacterial electrospun chitosan/poly(vinyl alcohol) nanofibers containing silver nitrate and titanium dioxide. Journal of Applied Polymer Science, **111**, 2892–2899 (2009).
DOI: 10.1002/app.29233

[30] Cooper A., Oldinski R., Ma H., Bryers J. D., Zhang M.: Chitosan-based nanofibrous membranes for antibacterial filter applications. Carbohydrate Polymers, **92**, 254–259 (2013).
DOI: 10.1016/j.carbpol.2012.08.114

[31] Yang R., He J., Xu L., Yu J.: Bubble-electrospinning for fabricating nanofibers. Polymer, **50**, 5846–5850 (2009).
DOI: 10.1016/j.polymer.2009.10.021

[32] Ding B., Kimura E., Sato T., Fujita S., Shiratori S.: Fabrication of blend biodegradable nanofibrous nonwoven mats *via* multi-jet electrospinning. Polymer, **45**, 1895–1902 (2004).
DOI: 10.1016/j.polymer.2004.01.026

[33] Thoppey N., Bochinski J., Clarke L. I., Gorga R. E.: Edge electrospinning for high throughput production of quality nanofibers. Nanotechnology, **22**, 345301/1–345301/11 (2011).
DOI: 10.1088/0957-4484/22/34/345301

[34] Bhardwaj N., Kundu S. C.: Electrospinning: A fascinating fiber fabrication technique. Biotechnology Advances, **28**, 325–347 (2010).
DOI: 10.1016/j.biotechadv.2010.01.004

[35] Zeleny J.: The electrical discharge from liquid points, and a hydrostatic method of measuring the electric intensity at their surfaces. Physical Review, **3**, 69–91 (1914).
DOI: 10.1103/PhysRev.3.69

[36] Cooley J. F.: Apparatus for electrically dispersing fluids. U.S. Patent 692631 A, USA (1902).

[37] Formhals A.: Process and apparatus for preparing artificial threads. U.S. Patent 1975504, USA (1934).

[38] Formhals A.: Method and apparatus for the production of fibers. U.S. Patent 2116942, USA (1938).

[39] Formhals A.: Artificial thread and method of producing same. U.S. Patent 2187306, USA (1940).

[40] Ramakrishna S., Fujihara K., Teo W-E., Lim T-C., Ma Z.: An introduction to electrospinning and nanofibers. World Scientific, Singapore (2005).

[41] Thoppey N. M., Gorga R. E., Bochinski J. R., Clarke L. I.: Effect of solution parameters on spontaneous jet formation and throughput in edge electrospinning from a fluid-filled bowl. Macromolecules, **45**, 6527–6537 (2012).
DOI: 10.1021/ma301207t

[42] Masilela N., Kleyi P., Tshentu Z., Priniotakis G., Westbroek P., Nyokong T.: Photodynamic inactivation of Staphylococcus aureus using low symmetrically substituted phthalocyanines supported on a polystyrene polymer fiber. Dyes and Pigments, **96**, 500–508 (2013).
DOI: 10.1016/j.dyepig.2012.10.001

[43] Huang Z-M., Zhang Y-Z., Kotaki M., Ramakrishna S.: A review on polymer nanofibers by electrospinning and their applications in nanocomposites. Composites Science and Technology, **63**, 2223–2253 (2003).
DOI: 10.1016/S0266-3538(03)00178-7

[44] Abdel-Hady F., Alzahrany A., Hamed M.: Experimental validation of upward electrospinning process. ISRN Nanotechnology, **2011**, 851317/1–851317/14 (2011).
DOI: 10.5402/2011/851317

[45] Subbiah T., Bhat G., Tock R., Parameswaran S., Ramkumar S.: Electrospinning of nanofibers. Journal of Applied Polymer Science, **96**, 557–569 (2005).
DOI: 10.1002/app.21481

[46] Teo W-E., Inai R., Ramakrishna S.: Technological advances in electrospinning of nanofibers. Science and Technology of Advanced Materials, **12**, 013002/1–031002/19 (2011).
DOI: 10.1088/1468-6996/12/1/013002

[47] Haghi A., Akbari M.: Trends in electrospinning of natural nanofibers. Physica Status Solidi (a), **204**, 1830–1834 (2007).
DOI: 10.1002/pssa.200675301

[48] Deitzel J. M., Kleinmeyer J., Harris D., Beck T. N.: The effect of processing variables on the morphology of electrospun nanofibers and textiles. Polymer, **42**, 261–272 (2001).
DOI: 10.1016/S0032-3861(00)00250-0

[49] Eda G., Shivkumar S.: Bead-to-fiber transition in electrospun polystyrene. Journal of Applied Polymer Science, **106**, 475–587 (2007).
DOI: 10.1002/app.25907

[50] Pawlowski K. J., Belvin H. L., Raney D. L., Su J., Harrison J. S., Siochi E. J.: Electrospinning of a micro-air vehicle wing skin. Polymer, **44**, 1309–1314 (2003).
DOI: 10.1016/S0032-3861(02)00859-5

[51] Schiffman J. D., Schauer C. L.: A review: Electrospinning of biopolymer nanofibers and their applications. Polymer Reviews, **48**, 317–352 (2008).
DOI: 10.1080/15583720802022182

[52] Bhattarai N., Li Z., Edmondson D., Zhang M.: Alginate-based nanofibrous scaffolds: Structural, mechanical, and biological properties. Advanced Materials, **18**, 1463–1467 (2006).
DOI: 10.1002/adma.200502537

[53] Jeong S. I., Krebs M. D., Bonino C. A., Khan S. A., Alsberg E.: Electrospun alginate nanofibers with controlled cell adhesion for tissue engineering. Macromolecular Bioscience, **10**, 934–943 (2010).
DOI: 10.1002/mabi.201000046

[54] Saquing C. D., Tang C., Monian B., Bonino C. A., Manasco J. L., Alsberg E., Khan S. A.: Alginate–polyethylene oxide blend nanofibers and the role of the carrier polymer in electrospinning. Industrial and Engineering Chemistry Research, **52**, 8692–8704 (2013).
DOI: 10.1021/ie302385b

[55] Jacobs V., Anandjiwala R. D., Maaza M.: The influence of electrospinning parameters on the structural morphology and diameter of electrospun nanofibers. Journal of Applied Polymer Science, **115**, 3130–3136 (2010).
DOI: 10.1002/app.31396

[56] Lee K. H., Kim H. Y., Khil M. S., Ra Y. M., Lee D. R.: Characterization of nano-structured poly(ε-caprolactone) nonwoven mats *via* electrospinning. Polymer, **44**, 1287–1294 (2003).
DOI: 10.1016/S0032-3861(02)00820-0

[57] Choktaweesap N., Arayanarakul K., Aht-ong D., Meechaisue C., Supaphol P.: Electrospun gelatin fibers: Effect of solvent system on morphology and fiber diameters. Polymer Journal, **39**, 622–631 (2007).
DOI: 10.1295/polymj.PJ2006190

[58] Fryczkowski R., Gorczowska M., Fryczkowska B., Janicki J.: The effect of solvent on the properties of nanofibres obtained by electrospinning from a mixture of poly(3-hydroxybutyrate) and polyaniline. Synthetic Metals, **166**, 14–21 (2013).
DOI: 10.1016/j.synthmet.2013.01.011

[59] Uyar T., Besenbacher F.: Electrospinning of uniform polystyrene fibers: The effect of solvent conductivity. Polymer, **49**, 5336–5343 (2008).
DOI: 10.1016/j.polymer.2008.09.025

[60] Sun Z., Deitzel J. M., Knopf J., Chen X., Gillespie J. W.: The effect of solvent dielectric properties on the collection of oriented electrospun fibers. Journal of Applied Polymer Science, **125**, 2585–2594 (2012).
DOI: 10.1002/app.35454

[61] Tungprapa S., Puangparn T., Weerasombut M., Jangchud I., Fakum P., Semongkhol S., Meechaisue C., Supaphol P.: Electrospun cellulose acetate fibers: Effect of solvent system on morphology and fiber diameter. Cellulose, **14**, 563–575 (2007).
DOI: 10.1007/s10570-007-9113-4

[62] Yuan X., Zhang Y., Dong C., Sheng J.: Morphology of ultrafine polysulfone fibers prepared by electrospinning. Polymer International, **53**, 1704–1710 (2004).
DOI: 10.1002/pi.1538

[63] Aluigi A., Varesano A., Montarsolo A., Vineis C., Ferrero F., Mazzuchetti G., Tonin C.: Electrospinning of keratin/poly(ethylene oxide)blend nanofibers. Journal of Applied Polymer Science, **104**, 863–870 (2007).
DOI: 10.1002/app.25623

[64] Katti D. S., Robinson K. W., Ko F. K., Laurencin C. T.: Bioresorbable nanofiber-based systems for wound healing and drug delivery: Optimization of fabrication parameters. Journal of Biomedical Materials Research Part B: Applied Biomaterials, **70**, 286–296 (2004).
DOI: 10.1002/jbm.b.30041

[65] Arayanarakul K., Choktaweesap N., Aht-ong D., Meechaisue C., Supaphol P.: Effects of poly(ethylene glycol), inorganic salt, sodium dodecyl sulfate, and solvent system on electrospinning of poly(ethylene oxide). Macromolecular Materials and Engineering, **291**, 581–591 (2006).
DOI: 10.1002/mame.200500419

[66] Ki C. S., Baek D. H., Gang K. D., Lee K. H., Um I. C., Park Y. H.: Characterization of gelatin nanofiber prepared from gelatin–formic acid solution. Polymer, **46**, 5094–5102 (2005).
DOI: 10.1016/j.polymer.2005.04.040

[67] Geng X., Kwon O-H., Jang J.: Electrospinning of chitosan dissolved in concentrated acetic acid solution. Biomaterials, **26**, 5427–5432 (2005).
DOI: 10.1016/j.biomaterials.2005.01.066

[68] Ki C. S., Kim J. W., Hyun J. H., Lee K. H., Hattori M., Rah D. K., Park Y. H.: Electrospun three-dimensional silk fibroin nanofibrous scaffold. Journal of Applied Polymer Science, **106**, 3922–3998 (2007).
DOI: 10.1002/app.26914

[69] Tungprapa S., Jangchud I., Supaphol P.: Release characteristics of four model drugs from drug-loaded electrospun cellulose acetate fiber mats. Polymer, **48**, 5030–5041 (2007).
DOI: 10.1016/j.polymer.2007.06.061

[70] Heikkilä P., Harlin A.: Electrospinning of polyacrylonitrile (PAN) solution: Effect of conductive additive and filler on the process. Express Polymer Letter, **3**, 437–445 (2009).
DOI: 10.3144/expresspolymlett.2009.53

[71] Li D., Wang Y., Xia Y.: Electrospinning of polymeric and ceramic nanofibers as uniaxially aligned arrays. Nano Letters, **3**, 1167–1171 (2003).
DOI: 10.1021/nl0344256

[72] Li D., Wang Y., Xia Y.: Electrospinning nanofibers as uniaxially aligned arrays and layer-by-layer stacked films. Advanced Materials, **16**, 361–366 (2004).
DOI: 10.1002/adma.200306226

[73] Theron A., Zussman E., Yarin A. L.: Electrostatic field-assisted alignment of electrospun nanofibres. Nanotechnology, **12**, 384–390 (2001).
DOI: 10.1088/0957-4484/12/3/329

[74] Errico C., Detta N., Puppi D., Piras A. M., Chiellini F., Chiellini E.: Polymeric nanostructured items electrospun on a cylindrical template: A simple procedure for their removal. Polymer International, **60**, 1162–1166 (2011).
DOI: 10.1002/pi.3060

[75] Matthews J. A., Wnek G. E., Simpson D. G., Bowlin G. L.: Electrospinning of collagen nanofibers. Biomacromolecules, **3**, 232–238 (2002).
DOI: 10.1021/bm015533u

[76] Kim C-W., Kim D-S., Kang S-Y., Marquez M., Joo Y. L.: Structural studies of electrospun cellulose nanofibers. Polymer, **47**, 5097–6107 (2006).
DOI: 10.1016/j.polymer.2006.05.033

[77] Bonino C. A., Efimenko K., Jeong S. I., Krebs M. D., Alsberg E., Khan S. A.: Three-dimensional electrospun alginate nanofiber mats *via* tailored charge repulsions. Small, **8**, 1928–1936 (2012).
DOI: 10.1002/smll.201101791

[78] Homayoni H., Ravandi S. A. H., Valizadeh M.: Electrospinning of chitosan nanofibers: Processing optimization. Carbohydrate Polymers, **77**, 656–661 (2009).
DOI: 10.1016/j.carbpol.2009.02.008

[79] Teng S-H., Wang P., Kim H-E.: Blend fibers of chitosan–agarose by electrospinning. Materials Letters, **63**, 2510–2512 (2009).
DOI: 10.1016/j.matlet.2009.08.051

[80] Xu J., Zhang J., Gao W., Liang H., Wang H., Li J.: Preparation of chitosan/PLA blend micro/nanofibers by electrospinning. Materials Letters, **63**, 658–660 (2009).
DOI: 10.1016/j.matlet.2008.12.014

[81] Du J., Hsieh Y-L.: Nanofibrous membranes from aqueous electrospinning of carboxymethyl chitosan. Nanotechnology, **19**, 125707/1–125707/9 (2008).
DOI: 10.1088/0957-4484/19/12/125707

[82] Neamnark A., Rujiravanit R., Supaphol P.: Electrospinning of hexanoyl chitosan. Carbohydrate Polymers, **66**, 298–305 (2006).
DOI: 10.1016/j.carbpol.2006.03.015

[83] Ignatova M., Manolova N., Rashkov I.: Novel antibacterial fibers of quaternized chitosan and poly(vinyl pyrrolidone) prepared by electrospinning. European Polymer Journal, **43**, 1112–1122 (2007).
DOI: 10.1016/j.eurpolymj.2007.01.012

[84] Du J., Hsieh Y-L.: PEGylation of chitosan for improved solubility and fiber formation *via* electrospinning. Cellulose, **14**, 543–552 (2007).
DOI: 10.1007/s10570-007-9122-3

[85] Li M., Guo Y., Wei Y., MacDiarmid A. G., Lelkes P. I.: Electrospinning polyaniline-contained gelatin nanofibers for tissue engineering applications. Biomaterials, **27**, 2705–2715 (2006).
DOI: 10.1016/j.biomaterials.2005.11.037

[86] Ji Y., Ghosh K., Li B., Sokolov J. C., Clark R. A., Rafailovich M. H.: Dual-syringe reactive electrospinning of cross-linked hyaluronic acid hydrogel nanofibers for tissue engineering applications. Macromolecular Bioscience, **6**, 811–817 (2006).
DOI: 10.1002/mabi.200600132

[87] Penchev H., Paneva D., Manolova N., Rashkov I.: Hybrid nanofibrous yarns based on *N*-carboxyethylchitosan and silver nanoparticles with antibacterial activity prepared by self-bundling electrospinning. Carbohydrate Research, **345**, 2374–2380 (2010).
DOI: 10.1016/j.carres.2010.08.014

[88] Lim Y-M., Gwon H-J., Jeun J. P., Nho Y-C.: Preparation of cellulose-based nanofibers using electrospinning. in 'Nanofibers' (ed.: Kumar A.), InTech, Rijeka 179–188 (2010).
DOI: 10.5772/8153

[89] Wang C., Chien H-S., Hsu C-H., Wang Y-C., Wang C-T., Lu H-A.: Electrospinning of polyacrylonitrile solutions at elevated temperatures. Macromolecules, **40**, 7973–7983 (2007).
DOI: 10.1021/ma070508n

[90] De Vrieze S., Van Camp T., Nelvig A., Hagström B., Westbroek P., De Clerck K.: The effect of temperature and humidity on electrospinning. Journal of Materials Science, **44**, 1357–1362 (2009).
DOI: 10.1007/s10853-008-3010-6

[91] Tripatanasuwan S., Zhong Z., Reneker D. H.: Effect of evaporation and solidification of the charged jet in electrospinning of poly(ethylene oxide) aqueous solution. Polymer, **48**, 5742–5746 (2007).
DOI: 10.1016/j.polymer.2007.07.045

[92] Casper C. L., Stephens J. S., Tassi N. G., Chase D. B., Rabolt J. F.: Controlling surface morphology of electrospun polystyrene fibers: Effect of humidity and molecular weight in the electrospinning process. Macromolecules, **37**, 573–578 (2004).
DOI: 10.1021/ma0351975

[93] Wang X., Niu H., Lin T., Wang X.: Needleless electrospinning of nanofibers with a conical wire coil. Polymer Engineering and Science, **49**, 1582–1586 (2009).
DOI: 10.1002/pen.21377

[94] Wang X., Niu H., Wang X., Lin T.: Needleless electrospinning of uniform nanofibers using spiral coil spinnerets. Journal of Nanomaterials, **2012**, 785920/1–785920/9 (2012).
DOI: 10.1155/2012/785920

[95] Liu W., Yao Y., Lin Y., Wang B., Luo Y., Li N., Zhang Q., Wu Y., Niu A.: Electrospinning assisted by gas jet for preparing ultrafine poly(vinyl alcohol) fibres. Iran Polymer Journal, **18**, 89–96 (2009).

[96] Tomaszewski W., Szadkowski M.: Investigation of electrospinning with the use of a multi-jet electrospinning head. Fibres and Textiles in Eastern Europe, **13**, 22–26 (2005).

[97] Cengiz F., Jirsak O.: The effect of salt on the roller electrospinning of polyurethane nanofibers. Fibers and Polymers, **10**, 177–184 (2009).
DOI: 10.1007/s12221-009-0177-7

[98] Dosunmu O. O., Chase G. G., Kataphinan W., Reneker D. H.: Electrospinning of polymer nanofibres from multiple jets on a porous tubular surface. Nanotechnology, **17**, 1123–1127 (2006).
DOI: 10.1088/0957-4484/17/4/046

[99] Nurwaha D., Han W., Wang X.: Investigation of a new needleless electrospinning method for the production of nanofibers. Journal of Engineered Fibers and Fabrics, **8**, 42–49 (2013).

[100] Theron S., Yarin A., Zussman E., Kroll E.: Multiple jets in electrospinning: Experiment and modeling. Polymer, **46**, 2889–2899 (2005).
DOI: 10.1016/j.polymer.2005.01.054

[101] Yamashita Y., Ko F., Miyake H., Higashiyama A.: Establishment of nanofiber preparation technique by electrospinning. Sen'i Gakkaishi, **64**, 24–28 (2008).
DOI: 10.2115/fiber.64.24

[102] Varesano A., Carletto R. A., Mazzuchetti G.: Experimental investigations on the multi-jet electrospinning process. Journal of Materials Processing Technology, **209**, 5178–5185 (2009).
DOI: 10.1016/j.jmatprotec.2009.03.003

[103] Kim G., Park K-E.: Alginate-nanofibers fabricated by an electrohydrodynamic process. Polymer Engineering and Science, **49**, 2242–2248 (2009).
DOI: 10.1002/pen.21472

[104] Varabhas J. S., Chase G. G., Reneker D. H.: Electrospun nanofibers from a porous hollow tube. Polymer, **49**, 4226–4229 (2008).
DOI: 10.1016/j.polymer.2008.07.043

[105] Kumar A., Wei M., Barry C., Chen J., Mead J.: Controlling fiber repulsion in multijet electrospinning for higher throughput. Macromolecular Materials and Engineering, **295**, 701–708 (2010).
DOI: 10.1002/mame.200900425

[106] Badrossamay M. R., McIlwee H. A., Goss J. A., Parker K. K.: Nanofiber assembly by rotary jet-spinning. Nano Letters, **10**, 2257–2261 (2010).
DOI: 10.1021/nl101355x

[107] Yarin A., Zussman E.: Upward needleless electrospinning of multiple nanofibers. Polymer, **45**, 2977–2980 (2004).
DOI: 10.1016/j.polymer.2004.02.066

[108] Huang X., Wu D., Zhu Y., Sun D.: Needleless electrospinning of multiple nanofibers. in 'Poceedings of the 7th IEEE International Conference on Nanotechnology. Hong Kong, China' 823–826 (2007).
DOI: 10.1109/NANO.2007.4601311

[109] Kostakova E., Meszaros L., Gregr J.: Composite nanofibers produced by modified needleless electrospinning. Materials Letters, **63**, 2419–2422 (2009).
DOI: 10.1016/j.matlet.2009.08.014

[110] Niu H., Lin T., Wang X.: Needleless electrospinning. I. A comparison of cylinder and disk nozzles. Journal of Applied Polymer Science, **114**, 3524–3230 (2009).
DOI: 10.1002/app.30891

[111] Tang S., Zeng Y., Wang X.: Splashing needleless electrospinning of nanofibers. Polymer Engineering and Science, **50**, 2252–2257 (2010).
DOI: 10.1002/pen.21767

[112] Weitz R., Harnau L., Rauschenbach S., Burghard M., Kern K.: Polymer nanofibers *via* nozzle-free centrifugal spinning. Nano Letters, **8**, 1187–1191 (2008).
DOI: 10.1021/nl080124q

[113] Dabirian F., Hosseini Ravandi S. A., Pishevar A. R., Abuzade R. A.: A comparative study of jet formation and nanofiber alignment in electrospinning and electrocentrifugal spinning systems. Journal of Electrostatics, **69**, 540–546 (2011).
DOI: 10.1016/j.elstat.2011.07.006

[114] Thoppey N. M., Bochinski J. R., Clarke L. I., Gorga R. E.: Unconfined fluid electrospun into high quality nanofibers from a plate edge. Polymer, **51**, 4928–4936 (2010).
DOI: 10.1016/j.polymer.2010.07.046

[115] Lukas D., Sarkar A., Pokorny P.: Self-organization of jets in electrospinning from free liquid surface: A generalized approach. Journal of Applied Physics, **103**, 084309/1–084309/7 (2008).
DOI: 10.1063/1.2907967

[116] Lin Y., Yao Y., Yang X., Wei N., Li X., Gong P., Li R., Wu D.: Preparation of poly(ether sulfone) nanofibers by gas-jet/electrospinning. Journal of Applied Polymer Science, **107**, 909–917 (2008).
DOI: 10.1002/app.26445

[117] Wang B., Yao Y., Peng J., Lin Y., Liu W., Luo Y., Xiang R., Li R., Wu D.: Preparation of poly(ester imide) ultrafine fibers by gas-jet/electrospinning. Journal of Applied Polymer Science, **114**, 883–891 (2009).
DOI: 10.1002/app.30505

[118] Zhmayev E., Cho D., Joo Y. L.: Nanofibers from gas-assisted polymer melt electrospinning. Polymer, **51**, 4140–4144 (2010).
DOI: 10.1016/j.polymer.2010.06.058

[119] Benavides R. E., Jana S. C., Reneker D. H.: Role of liquid jet stretching and bending instability in nanofiber formation by gas jet method. Macromolecules, **46**, 6081–6090 (2013).
DOI: 10.1021/ma400900s

[120] Benavides R. E., Jana S. C., Reneker D. H.: Nanofibers from scalable gas jet process. ACS Macro Letters, **1**, 1032–1036 (2012).
DOI: 10.1021/mz300297g

[121] Bonani W., Maniglio D., Motta A., Tan W., Migliaresi C.: Biohybrid nanofiber constructs with anisotropic biomechanical properties. Journal of Biomedical Materials Research Part B: Applied Biomaterials, **96**, 276–286 (2011).
DOI: 10.1002/jbm.b.31763

[122] Bonani W., Motta A., Migliaresi C., Tan W.: Biomolecule gradient in micropatterned nanofibrous scaffold for spatiotemporal release. Langmuir, **28**, 13675–13687 (2012).
DOI: 10.1021/la302386u

[123] Hu W-W., Yu H-N.: Coelectrospinning of chitosan/alginate fibers by dual-jet system for modulating material surfaces. Carbohydrate Polymers, **95**, 716–727 (2013).
DOI: 10.1016/j.carbpol.2013.02.083

[124] Yoo C. R., Yeo I-S., Park K. E., Park J. H., Lee S. J., Park W. H., Min B-M.: Effect of chitin/silk fibroin nanofibrous bicomponent structures on interaction with human epidermal keratinocytes. International Journal of Biological Macromolecules, **42**, 324–334 (2008).
DOI: 10.1016/j.ijbiomac.2007.12.004

[125] Xu F., Li L., Cui X.: Fabrication of aligned side-by-side TiO$_2$/SnO$_2$ nanofibers *via* dual-opposite-spinneret electrospinning. Journal of Nanomaterials, **2012**, 575926/1–575926/5 (2012).
DOI: 10.1155/2012/575926

[126] Duan B., Yuan X., Zhu Y., Zhang Y., Li X., Zhang Y., Yao K.: A nanofibrous composite membrane of PLGA–chitosan/PVA prepared by electrospinning. European Polymer Journal, **42**, 2013–2022 (2006).
DOI: 10.1016/j.eurpolymj.2006.04.021

[127] Bazilevsky A. V., Yarin A. L., Megaridis C. M.: *Co*-electrospinning of core–shell fibers using a single-nozzle technique. Langmuir, **23**, 2311–2314 (2007).
DOI: 10.1021/la063194q

[128] Liu Z., Sun D. D., Guo P., Leckie J. O.: An efficient bicomponent TiO$_2$/SnO$_2$ nanofiber photocatalyst fabricated by electrospinning with a side-by-side dual spinneret method. Nano Letters, **7**, 1081–1085 (2007).
DOI: 10.1021/nl061898e

[129] Díaz J. E., Fernández-Nieves A., Barrero A., Márquez M., Loscertales I. G.: Fabrication of structured micro and nanofibers by coaxial electrospinning. Journal of Physics: Conference Series, **127**, 1–8 (2008).
DOI: 10.1088/1742-6596/127/1/012008

[130] Jiang S., Duan G., Zussman E., Greiner A., Agarwal S.: Highly flexible and tough concentric triaxial polystyrene fibers. ACS Applied Materials and Interfaces, **6**, 5918–5923 (2014).
DOI: 10.1021/am500837s

[131] Pakravan M., Heuzey M-C., Ajji A.: Core–shell structured PEO-chitosan nanofibers by coaxial electrospinning. Biomacromolecules, **13**, 412–421 (2012).
DOI: 10.1021/bm201444v

[132] Tong H-W., Zhang X., Wang M.: A new nanofiber fabrication technique based on coaxial electrospinning. Materials Letters, **66**, 257–260 (2012).
DOI: 10.1016/j.matlet.2011.08.095

[133] Chang J-J., Lee Y-H., Wu M-H., Yang M-C., Chien C-T.: Preparation of electrospun alginate fibers with chitosan sheath. Carbohydrate Polymers, **87**, 2357–2361 (2012).
DOI: 10.1016/j.carbpol.2011.10.054

[134] Li D., Xia Y.: Direct fabrication of composite and ceramic hollow nanofibers by electrospinning. Nano Letters, **4**, 933–938 (2004).
DOI: 10.1021/nl049590f

[135] Sakuldao S., Yoovidhya T., Wongsasulak S.: Coaxial electrospinning and sustained release properties of gelatin-cellulose acetate core-shell ultrafine fibres. ScienceAsia, **37**, 335–343 (2011).
DOI: 10.2306/scienceasia1513-1874.2011.37.335

[136] Zhang Y., Huang Z-M., Xu X., Lim C. T., Ramakrishna S.: Preparation of core–shell structured PCL-r-gelatin Bi-component nanofibers by coaxial electrospinning. Chemistry of Materials, **16**, 3406–3409 (2004).
DOI: 10.1021/cm049580f

[137] Gulfam M., Lee J. M., Kim J-E., Lim D. W., Lee E. K., Chung B. G.: Highly porous core–shell polymeric fiber network. Langmuir, **27**, 10993–10999 (2011).
DOI: 10.1021/la201253z

[138] Chen H., Wang N., Di J., Zhao Y., Song Y., Jiang L.: Nanowire-in-microtube structured core/shell fibers *via* multifluidic coaxial electrospinning. Langmuir, **26**, 11291–11296 (2010).
DOI: 10.1021/la100611f

[139] Kim W., Kim S. S.: Synthesis of biodegradable triple-layered capsules using a triaxial electrospray method. Polymer, **52**, 3325–3336 (2011).
DOI: 10.1016/j.polymer.2011.05.033

[140] Liu W., Ni C., Chase D. B., Rabolt J. F.: Preparation of multilayer biodegradable nanofibers by triaxial electrospinning. ACS Macro Letters, **2**, 466–468 (2013).
DOI: 10.1021/mz4000688

[141] Mokhena T. C., Luyt A. S.: Investigation of polyethylene/sisal whiskers nanocomposites prepared under different conditions. Polymer Composites, **35**, 2221–2233 (2014).
DOI: 10.1002/pc.22887

[142] Stephen M., Catherine N., Brenda M., Andrew K., Leslie P., Corrine G.: Oxolane-2,5-dione modified electrospun cellulose nanofibers for heavy metals adsorption. Journal of Hazardous Materials, **192**, 922–927 (2011).
DOI: 10.1016/j.jhazmat.2011.06.001

[143] Xu S., Zhang J., He A., Li J., Zhang H., Han C. C.: Electrospinning of native cellulose from nonvolatile solvent system. Polymer, **49**, 2911–2917 (2008).
DOI: 10.1016/j.polymer.2008.04.046

[144] Ma H., Burger C., Hsiao B. S., Chu B.: Nanofibrous microfiltration membrane based on cellulose nanowhiskers. Biomacromolecules, **13**, 180–186 (2011).
DOI: 10.1021/bm201421g

[145] Rao S. S., Jeyapal S. G., Rajiv S.: Biodegradable electrospun nanocomposite fibers based on poly(2-hydroxy ethyl methacrylate) and bamboo cellulose. Composites Part B: Engineering, **60**, 43–48 (2014).
DOI: 10.1016/j.compositesb.2013.12.068

[146] Peresin M. S., Habibi Y., Vesterinen A-H., Rojas O. J., Pawlak J. J., Seppälä J. V.: Effect of moisture on electrospun nanofiber composites of poly(vinyl alcohol) and cellulose nanocrystals. Biomacromolecules, **11**, 2471–2477 (2010).
DOI: 10.1021/bm1006689

[147] Park W-I., Kang M., Kim H-S., Jin H-J.: Electrospinning of poly(ethylene oxide) with bacterial cellulose whiskers. Macromolecular Symposia, **249–250**, 289–294 (2007).
DOI: 10.1002/masy.200750347

[148] Cao X., Huang M., Ding B., Yu J., Sun G.: Robust polyacrylonitrile nanofibrous membrane reinforced with jute cellulose nanowhiskers for water purification. Desalination, **316**, 120–126 (2013).
DOI: 10.1016/j.desal.2013.01.031

[149] Chu B., Hsiao B. S., Ma H.: High flux high efficiency nanofiber membranes and methods of production thereof. U.S. Patent 20110198282 A1, USA (2009).

[150] Ma H., Burger C., Hsiao B. S., Chu B.: Highly permeable polymer membranes containing directed channels for water purification. ACS Macro Letters, **1**, 723–726 (2012).
DOI: 10.1021/mz300163h

[151] Ma H., Burger C., Hsiao B. S., Chu B.: Ultrafine polysaccharide nanofibrous membranes for water purification. Biomacromolecules, **12**, 970–-976 (2011).
DOI: 10.1021/bm1013316

[152] Sato A., Wang R., Ma H., Hsiao B. S., Chu B.: Novel nanofibrous scaffolds for water filtration with bacteria and virus removal capability. Journal of Electron Microscopy, **60**, 201–209 (2011).
DOI: 10.1093/jmicro/dfr019

[153] Ma Z., Kotaki M., Ramakrishna S.: Electrospun cellulose nanofiber as affinity membrane. Journal of Membrane Science, **265**, 115–123 (2005).
DOI: 10.1016/j.memsci.2005.04.044

[154] Wenten I. G.: Recent development in membrane science and its industrial applications. Membrane Science Technology, **24**, 1009–1024 (2002).

[155] Ji F., Li C., Tang B., Xu J., Lu G., Liu P.: Preparation of cellulose acetate/zeolite composite fiber and its adsorption behavior for heavy metal ions in aqueous solution. Chemical Engineering Journal, **209**, 325–333 (2012).
DOI: 10.1016/j.cej.2012.08.014

[156] Taha A. A., Wu Y-N., Wang H., Li F.: Preparation and application of functionalized cellulose acetate/silica composite nanofibrous membrane *via* electrospinning for Cr(VI) ion removal from aqueous solution. Journal of Environmental Management, **112**, 10–16 (2012).
DOI: 10.1016/j.jenvman.2012.05.031

[157] Bódalo A., Gómez J-L., Gómez E., León G., Tejera M.: Ammonium removal from aqueous solutions by reverse osmosis using cellulose acetate membranes. Desalination, **184**, 149–155 (2005).
DOI: 10.1016/j.desal.2005.03.062

[158] Konwarh R., Karak N., Misra M.: Electrospun cellulose acetate nanofibers: The present status and gamut of biotechnological applications. Biotechnology Advances, **31**, 421–437 (2013).
DOI: 10.1016/j.biotechadv.2013.01.002

[159] Zhou W., He J., Cui S., Gao W.: Studies of electrospun cellulose acetate nanofibrous membranes. The Open Materials Science Journal, **5**, 51–55 (2011).
DOI: 10.2174/1874088X01105010051

[160] Chen L., Bromberg L., Hatton T. A., Rutledge G. C.: Electrospun cellulose acetate fibers containing chlorhexidine as a bactericide. Polymer, **49**, 1266–1275 (2008).
DOI: 10.1016/j.polymer.2008.01.003

[161] Taepaiboon P., Rungsardthong U., Supaphol P.: Vitamin-loaded electrospun cellulose acetate nanofiber mats as transdermal and dermal therapeutic agents of vitamin A acid and vitamin E. European Journal of Pharmaceutics and Biopharmaceutics, **67**, 387–397 (2007).
DOI: 10.1016/j.ejpb.2007.03.018

[162] Suwantong O., Opanasopit P., Ruktanonchai U., Supaphol P.: Electrospun cellulose acetate fiber mats containing curcumin and release characteristic of the herbal substance. Polymer, **48**, 7546–7557 (2007).
DOI: 10.1016/j.polymer.2007.11.019

[163] Ma Z., Ramakrishna S.: Electrospun regenerated cellulose nanofiber affinity membrane functionalized with protein A/G for IgG purification. Journal of Membrane Science, **319**, 23–28 (2008).
DOI: 10.1016/j.memsci.2008.03.045

[164] Chen S-L., Huang X-J., Xu Z-K.: Functionalization of cellulose nanofiber mats with phthalocyanine for decoloration of reactive dye wastewater. Cellulose, **18**, 1295–1303 (2011).
DOI: 10.1007/s10570-011-9572-5

[165] Muzzarelli R. A.: Chitins and chitosans as immunoadjuvants and non-allergenic drug carriers. Marine Drugs, **8**, 292–312 (2010).
DOI: 10.3390/md8020292

[166] Jayakumar R., Menon D., Manzoor K., Nair S., Tamura H.: Biomedical applications of chitin and chitosan based nanomaterials – A short review. Carbohydrate Polymers, **82**, 227–232 (2010).
DOI: 10.1016/j.carbpol.2010.04.074

[167] Sun K., Li Z.: Preparations, properties and applications of chitosan based nanofibers fabricated by electrospinning. Express Polymer Letters, **5**, 342–361 (2011).
DOI: 10.3144/expresspolymlett.2011.34

[168] Min B-M., Lee S. W., Lim J. N., You Y., Lee T. S., Kang P. H., Park W. H.: Chitin and chitosan nanofibers: Electrospinning of chitin and deacetylation of chitin nanofibers. Polymer, **45**, 7137–7142 (2004).
DOI: 10.1016/j.polymer.2004.08.048

[169] Noh H. K., Lee S. W., Kim J-M., Oh J-E., Kim K-H., Chung C-P., Choi S-C., Park W. H., Min B-M.: Electrospinning of chitin nanofibers: Degradation behavior and cellular response to normal human keratinocytes and fibroblasts. Biomaterials, **27**, 3934–3944 (2006).
DOI: 10.1016/j.biomaterials.2006.03.016

[170] Junkasem J., Rujiravanit R., Supaphol P.: Fabrication of α-chitin whisker-reinforced poly(vinyl alcohol) nanocomposite nanofibres by electrospinning. Nanotechnology, **17**, 4519–4528 (2006).
DOI: 10.1088/0957-4484/17/17/039

[171] Junkasem J., Rujiravanit R., Grady B. P., Supaphol P.: X-ray diffraction and dynamic mechanical analyses of α-chitin whisker-reinforced poly(vinyl alcohol) nanocomposite nanofibers. Polymer International, **59**, 85–91 (2010).
DOI: 10.1002/pi.2693

[172] Naseri N., Algan C., Jacobs V., John M., Oksman K., Mathew A. P.: Electrospun chitosan-based nanocomposite mats reinforced with chitin nanocrystals for wound dressing. Carbohydrate Polymers, **109**, 7–15 (2014).
DOI: 10.1016/j.carbpol.2014.03.031

[173] Park K. E., Kang H. K., Lee S. J., Min B-M., Park W. H.: Biomimetic nanofibrous scaffolds: Preparation and characterization of PGA/chitin blend nanofibers. Biomacromolecules, **7**, 635–643 (2006).
DOI: 10.1021/bm0509265

[174] Błasińska A., Krucińska I., Chrzanowski M.: Dibutyrylchitin nonwoven biomaterials manufactured using electrospinning method. Fibres and Textiles in Eastern Europe, **12**, 51–55 (2004).

[175] Du J., Hsieh Y-L.: Cellulose/chitosan hybrid nanofibers from electrospinning of their ester derivatives. Cellulose, **16**, 247–260 (2009).
DOI: 10.1007/s10570-008-9266-9

[176] Pant H. R., Kim H. J., Bhatt L. R., Joshi M. K., Kim E. K., Kim J. I., Abdal-hay A., Hui K., Kim C. S.: Chitin butyrate coated electrospun nylon-6 fibers for biomedical applications. Applied Surface Science, **285**, 538–544 (2013).
DOI: 10.1016/j.apsusc.2013.08.089

[177] Shalumon K., Binulal N., Selvamurugan N., Nair S., Menon D., Furuike T., Tamura H., Jayakumar R.: Electrospinning of carboxymethyl chitin/poly(vinyl alcohol) nanofibrous scaffolds for tissue engineering applications. Carbohydrate Polymers, **77**, 863–869 (2009).
DOI: 10.1016/j.carbpol.2009.03.009

[178] Sohofi N., Tavanai H., Morshed M., Abdolmaleki A.: Electrospinning of 100% carboxymethyl chitosan nanofibers. Journal of Engineered Fibers and Fabrics, **1**, 87–92 (2014).

[179] Qin Y., Hu H., Luo A., Wang Y., Huang X., Song P.: Effect of carboxymethylation on the absorption and chelating properties of chitosan fibers. Journal of Applied Polymer Science, **99**, 3110–3115 (2006).
DOI: 10.1002/app.22917

[180] Miao J., Li L., Chen G., Gao C., Dong S.: Preparation of *N*, *O*-carboxymethyl chitosan composite nanofiltration membrane and its rejection performance for the fermentation effluent from a wine factory. Chinese Journal of Chemical Engineering, **16**, 209–213 (2008).
DOI: 10.1016/S1004-9541(08)60064-6

[181] Zhao Z-P., Wang Z., Wang S-C.: Formation, charged characteristic and BSA adsorption behavior of carboxymethyl chitosan/PES composite MF membrane. Journal of Membrane Science, **217**, 151–158 (2003).
DOI: 10.1016/S0376-7388(03)00105-4

[182] Muzzarelli R. A. A.: Potential of chitin/chitosan-bearing materials for uranium recovery: An interdisciplinary review. Carbohydrate Polymers, **84**, 54–63 (2011).
DOI: 10.1016/j.carbpol.2010.12.025

[183] Wan Ngah W. S., Teong L. C., Hanafiah M. A. K. M.: Adsorption of dyes and heavy metal ions by chitosan composites: A review. Carbohydrate Polymers, **83**, 1446–1456 (2011).
DOI: 10.1016/j.carbpol.2010.11.004

[184] Ohkawa K., Cha D., Kim H., Nishida A., Yamamoto H.: Electrospinning of chitosan. Macromolecular Rapid Communications, **25**, 1600–1605 (2004).
DOI: 10.1002/marc.200400253

[185] Jia Y-T., Gong J., Gu X-H., Kim H-Y., Dong J., Shen X-Y.: Fabrication and characterization of poly (vinyl alcohol)/chitosan blend nanofibers produced by electrospinning method. Carbohydrate Polymers, **67**, 403–409 (2007).
DOI: 10.1016/j.carbpol.2006.06.010

[186] Su P., Wang C., Yang X., Chen X., Gao C., Feng X-X., Chen J-Y., Ye J., Gou Z.: Electrospinning of chitosan nanofibers: The favorable effect of metal ions. Carbohydrate Polymers, **84**, 239–246 (2011).
DOI: 10.1016/j.carbpol.2010.11.031

[187] Jung K-H., Huh M-W., Meng W., Yuan J., Hyun S. H., Bae J-S., Hudson S. M., Kang I-K.: Preparation and antibacterial activity of PET/chitosan nanofibrous mats using an electrospinning technique. Journal of Applied Polymer Science, **105**, 2816–2823 (2007).
DOI: 10.1002/app.25594

[188] Torres-Giner S., Ocio M. J., Lagaron J. M.: Novel antimicrobial ultrathin structures of zein/chitosan blends obtained by electrospinning. Carbohydrate Polymers, **77**, 261–266 (2009).
DOI: 10.1016/j.carbpol.2008.12.035

[189] Chen Z., Mo X., Qing F.: Electrospinning of collagen–chitosan complex. Materials Letters, **61**, 3490–3494 (2007).
DOI: 10.1016/j.matlet.2006.11.104

[190] Chen J-P., Chang G-Y., Chen J-K.: Electrospun collagen/chitosan nanofibrous membrane as wound dressing. Colloids and Surfaces A: Physicochemical and Engineering Aspects, **313–314**, 183–188 (2008).
DOI: 10.1016/j.colsurfa.2007.04.129

[191] Maeda N., Miao J., Simmons T. J., Dordick J. S., Linhardt R.: Composite polysaccharide fibers prepared by electrospinning and coating. Carbohydrate Polymers, **102**, 950–955 (2014).
DOI: 10.1016/j.carbpol.2013.10.038

[192] Santos C., Silva C. J., Büttel Zs., Guimarães R., Pereira S. B., Tamagnini P., Zille A.: Preparation and characterization of polysaccharides/PVA blend nanofibrous membranes by electrospinning method. Carbohydrate Polymers, **99**, 584–592 (2014).
DOI: 10.1016/j.carbpol.2013.09.008

[193] Ignatova M., Starbova K., Markova N., Manolova N., Rashkov I.: Electrospun nano-fibre mats with antibacterial properties from quaternised chitosan and poly (vinyl alcohol). Carbohydrate Research, **341**, 2098–2107 (2006).
DOI: 10.1016/j.carres.2006.05.006

[194] Ignatova M., Manolova N., Markova N., Rashkov I.: Electrospun non-woven nanofibrous hybrid mats based on chitosan and PLA for wound-dressing applications. Macromolecular Bioscience, **9**, 102–111 (2009).
DOI: 10.1002/mabi.200800189

[195] Kangwansupamonkon W., Tiewtrakoonwat W., Supaphol P., Kiatkamjornwong S.: Surface modification of electrospun chitosan nanofibrous mats for antibacterial activity. Journal of Applied Polymer Science, **131**, 1–9 (2014).
DOI: 10.1002/app.40981

[196] Alipour S. M., Nouri M., Mokhtari J., Bahrami S. H.: Electrospinning of poly(vinyl alcohol)–water-soluble quaternized chitosan derivative blend. Carbohydrate Research, **344**, 2496–2501 (2009).
DOI: 10.1016/j.carres.2009.10.004

[197] Zong Z., Kimura Y., Takahashi M., Yamane H.: Characterization of chemical and solid state structures of acylated chitosans. Polymer, **41**, 899–906 (2000).
DOI: 10.1016/S0032-3861(99)00270-0

[198] Peesan M., Rujiravanit R., Supaphol P.: Electrospinning of hexanoyl chitosan/polylactide blends. Journal of Biomaterials Science, Polymer Edition, **17**, 547–565 (2006).
DOI: 10.1163/156856206776986251

[199] Alsberg E., Anderson K. W., Albeiruti A., Franceschi R. T., Mooney D. J.: Cell-interactive alginate hydrogels for bone tissue engineering. Journal of Dental Research, **80**, 2025–2029 (2001).
DOI: 10.1177/00220345010800111501

[200] Dar A., Shachar M., Leor J., Cohen S.: Optimization of cardiac cell seeding and distribution in 3D porous alginate scaffolds. Biotechnology and Bioengineering, **80**, 305–312 (2002).
DOI: 10.1002/bit.10372

[201] Hashimoto T., Suzuki Y., Tanihara M., Kakimaru Y., Suzuki K.: Development of alginate wound dressings linked with hybrid peptides derived from laminin and elastin. Biomaterials, **25**, 1407–1414 (2004).
DOI: 10.1016/j.biomaterials.2003.07.004

[202] Davis T. A., Volesky B., Mucci A.: A review of the biochemistry of heavy metal biosorption by brown algae. Water Research, **37**, 4311–4330 (2003).
DOI: 10.1016/S0043-1354(03)00293-8

[203] Papageorgiou S. K., Katsaros F. K., Kouvelos E. P., Kanellopoulos N. K.: Prediction of binary adsorption isotherms of Cu^{2+}, Cd^{2+} and Pb^{2+} on calcium alginate beads from single adsorption data. Journal of Hazardous Materials, **162**, 1347–1354 (2009).
DOI: 10.1016/j.jhazmat.2008.06.022

[204] Xiao C., Lu Y., Liu H., Zhang L.: Preparation and physical properties of blend films from sodium alginate and polyacrylamide solutions. Journal of Macromolecular Science Part A: Pure and Applied Chemistry, **37**, 1663–1675 (2000).
DOI: 10.1081/MA-100102332

[205] Caykara T., Demirci S., Eroğlu M. S., Güven O.: Poly (ethylene oxide) and its blends with sodium alginate. Polymer, **46**, 10750–10757 (2005).
DOI: 10.1016/j.polymer.2005.09.041

[206] Omidian H., Rocca J. G., Park K.: Elastic, superporous hydrogel hybrids of polyacrylamide and sodium alginate. Macromolecular Bioscience, **6**, 703–710 (2006).
DOI: 10.1002/mabi.200600062

[207] Bonino C. A., Krebs M. D., Saquing C. D., Jeong S. I., Shearer K. L., Alsberg E., Khan S. A.: Electrospinning alginate-based nanofibers: From blends to crosslinked low molecular weight alginate-only systems. Carbohydrate Polymers, **85**, 111–119 (2011).
DOI: 10.1016/j.carbpol.2011.02.002

[208] Islam M. S., Ashaduzzaman M., Masum S. M., Yeum J. H.: Mechanical and electrical properties: Electrospun alginate/carbon nanotube composite nanofiber. Dhaka University Journal of Science, **60**, 125–128 (2012).
DOI: 10.3329/dujs.v60i1.10350

[209] Tarun K., Gobi N.: Calcium alginate/PVA blended nano fibre matrix for wound dressing. Indian Journal of Fibre and Textile Research, **37**, 127–132 (2012).

[210] Lee Y. J., Shin D. S., Kwon O. W., Park W. H., Choi H. G., Lee Y. R., Han S. S., Noh S. K., Lyoo W. S.: Preparation of atactic poly(vinyl alcohol)/sodium alginate blend nanowebs by electrospinning. Journal of Applied Polymer Science, **106**, 1337–1342 (2007).
DOI: 10.1002/app.26568

[211] Bhattarai N., Zhang M.: Controlled synthesis and structural stability of alginate-based nanofibers. Nanotechnology, **18**, 455601/1–455601/10 (2007).
DOI: 10.1088/0957-4484/18/45/455601

[212] Alborzi S., Lim L. T., Kakuda Y.: Electrospinning of sodium alginate-pectin ultrafine fibers. Journal of Food Science, **75**, C100–C107 (2010).
DOI: 10.1111/j.1750-3841.2009.01437.x

[213] Park S. A., Park K. E., Kim W.: Preparation of sodium alginate/poly(ethylene oxide) blend nanofibers with lecithin. Macromolecular Research, **18**, 891–896 (2010).
DOI: 10.1007/s13233-010-0909-y

[214] Jeong S. I., Krebs M. D., Bonino C. A., Samorezov J. E., Khan S. A., Alsberg E.: Electrospun chitosan–alginate nanofibers with *in situ* polyelectrolyte complexation for use as tissue engineering scaffolds. Tissue Engineering Part A, **17**, 59–70 (2010).
DOI: 10.1089/ten.tea.2010.0086

[215] Buttafoco L., Kolkman N. G., Engbers-Buijtenhuijs P., Poot A. A., Dijkstra P. J., Vermes I., Feijen J.: Electrospinning of collagen and elastin for tissue engineering applications. Biomaterials, **27**, 724–734 (2006).
DOI: 10.1016/j.biomaterials.2005.06.024

[216] Telemeco T., Ayres C., Bowlin L. G., Wnek G. E., Boland E. D., Cohen N., Baumgarten C. M., Mathews J., Simpson D. G.: Regulation of cellular infiltration into tissue engineering scaffolds composed of submicron diameter fibrils produced by electrospinning. Acta Biomaterialia, **1**, 377–385 (2005).
DOI: 10.1016/j.actbio.2005.04.006

[217] Zhang Y. Z., Venugopal J., Huang Z-M., Lim C. T., Ramakrishna S.: Characterization of the surface biocompatibility of the electrospun PCL-collagen nanofibers using fibroblasts. Biomacromolecules, **6**, 2583–2589 (2005).
DOI: 10.1021/bm050314k

[218] Li M., Mondrinos M. J., Gandhi M. R., Ko F. K., Weiss A. S., Lelkes P. I.: Electrospun protein fibers as matrices for tissue engineering. Biomaterials, **26**, 5999–6008 (2005).
DOI: 10.1016/j.biomaterials.2005.03.030

[219] Zeugolis D. I., Khew S. T., Yew E. S., Ekaputra A. K., Tong Y. W., Yung L-Y. L., Hutmacher D.W., Sheppard C., Raghunath M.: Electro-spinning of pure collagen nano-fibres – Just an expensive way to make gelatin? Biomaterials, **29**, 2293–2305 (2008).
DOI: 10.1016/j.biomaterials.2008.02.009

[220] Chakrapani V. Y., Gnanamani A., Giridev V. R., Madhusoothanan M., Sekaran G.: Electrospinning of type I collagen and PCL nanofibers using acetic acid. Journal of Applied Polymer Science, **125**, 3221–3227 (2012).
DOI: 10.1002/app.36504

[221] Kwon I. K., Matsuda T.: *Co*-electrospun nanofiber fabrics of poly(l-lactide-*co*-ε-caprolactone) with type I collagen or heparin. Biomacromolecules, **6**, 2096–2105 (2005).
DOI: 10.1021/bm050086u

[222] Zhong S., Teo W. E., Zhu X., Beuerman R., Ramakrishna S., Yung L. Y. L.: Formation of collagen–glycosaminoglycan blended nanofibrous scaffolds and their biological properties. Biomacromolecules, **6**, 2998–3004 (2005).
DOI: 10.1021/bm050318p

[223] Haugh M. G., Jaasma M. J., O'Brien F. J.: The effect of dehydrothermal treatment on the mechanical and structural properties of collagen-GAG scaffolds. Journal of Biomedical Materials Research Part A, **89**, 363–369 (2009).
DOI: 10.1002/jbm.a.31955

[224] Davis J. F., Maffia G. J.: Collagen dispersions for liquid-solid separations in water treatment and sludge dewatering. Separations Technology, **5**, 147–152 (1995).
DOI: 10.1016/0956-9618(94)00120-H

[225] Zhang Y., Ouyang H., Lim C. T., Ramakrishna S., Huang Z-M.: Electrospinning of gelatin fibers and gelatin/PCL composite fibrous scaffolds. Journal of Biomedical Materials Research Part B: Applied Biomaterials, **72**, 156–165 (2005).
DOI: 10.1002/jbm.b.30128

[226] Elliott D. E., Davis F. J., Mitchell G. R., Olley R. H.: Structure development in electrospun fibres of gelatin. Journal of Physics: Conference Series, **183**, 012021/1–012021/4 (2009).
DOI: 10.1088/1742-6596/183/1/012021

[227] Huang Z-M., Zhang Y., Ramakrishna S., Lim C. T.: Electrospinning and mechanical characterization of gelatin nanofibers. Polymer, **45**, 5361–5368 (2004).
DOI: 10.1016/j.polymer.2004.04.005

[228] Brenner E. K., Schiffman J. D., Thompson E. A., Toth L. J., Schauer C. L.: Electrospinning of hyaluronic acid nanofibers from aqueous ammonium solutions. Carbohydrate Polymers, **87**, 926–929 (2012).
DOI: 10.1016/j.carbpol.2011.07.033

[229] Lan S., Wu X., Li L., Li M., Guo F., Gan S.: Synthesis and characterization of hyaluronic acid-supported magnetic microspheres for copper ions removal. Colloids and Surfaces A: Physicochemical and Engineering Aspects, **425**, 42–50 (2013).
DOI: 10.1016/j.colsurfa.2013.02.059

[230] Ma G., Liu Y., Fang D., Chen J., Peng C., Fei X., Nie J.: Hyaluronic acid/chitosan polyelectrolyte complexes nanofibers prepared by electrospinning. Materials Letters, **74**, 78–80 (2012).
DOI: 10.1016/j.matlet.2012.01.012

[231] Uslu İ., Aytimur A.: Production and characterization of poly(vinyl alcohol)/poly(vinylpyrrolidone) iodine/poly(ethylene glycol) electrospun fibers with (hydroxypropyl)methyl cellulose and aloe vera as promising material for wound dressing. Journal of Applied Polymer Science, **124**, 3520–3524 (2012).
DOI: 10.1002/app.35525

[232] Uslu I., Keskin S., Gül A., Karabulut T. C., Aksu M. L.: Preparation and properties of electrospun poly (vinyl alcohol) blended hybrid polymer with aloe vera and HPMC as wound dressing. Hacettepe Journal of Biology and Chemistry, **38**, 19–25 (2010).

[233] Surjushe A., Vasani R., Saple D. G.: Aloe vera: A short review. Indian Journal of Dermatology, **53**, 163–166 (2008).
DOI: 10.4103/0019-5154.44785

[234] Suganya S., Venugopal J., Mary S. A., Ramakrishna S., Lakshmi B., Dev V. G.: Aloe vera incorporated biomimetic nanofibrous scaffold: A regenerative approach for skin tissue engineering. Iranian Polymer Journal, **23**, 237–248 (2014).
DOI: 10.1007/s13726-013-0219-2

[235] Abdelgawad A. M., Hudson S. M., Rojas O. J.: Antimicrobial wound dressing nanofiber mats from multicomponent (chitosan/silver-NPs/polyvinyl alcohol) systems. Carbohydrate Polymers, **100**, 166–178 (2014).
DOI: 10.1016/j.carbpol.2012.12.043

[236] Li Q., Mahendra S., Lyon D. Y., Brunet L., Liga M. V., Li D., Alvarez P. J.: Antimicrobial nanomaterials for water disinfection and microbial control: Potential applications and implications. Water Research, **42**, 4591–4602 (2008).
DOI: 10.1016/j.watres.2008.08.015

[237] Qu X., Alvarez P. J. J., Li Q.: Applications of nanotechnology in water and wastewater treatment. Water Research, **47**, 3931–3946 (2013).
DOI: 10.1016/j.watres.2012.09.058

[238] Tran Q. H., Nguyen V. Q., Le A-T.: Silver nanoparticles: Synthesis, properties, toxicology, applications and perspectives. Advances in Natural Sciences: Nanoscience and Nanotechnology, **4**, 033001/1–033001/20 (2013).
DOI: 10.1088/2043-6262/4/3/033001

[239] Nguyen T. T. T., Tae B., Park J. S.: Synthesis and characterization of nanofiber webs of chitosan/poly(vinyl alcohol) blends incorporated with silver nanoparticles. Journal of Materials Science, **46**, 6528–6537 (2011).
DOI: 10.1007/s10853-011-5599-0

[240] An J., Zhang H., Zhang J., Zhao Y., Yuan X.: Preparation and antibacterial activity of electrospun chitosan/poly(ethylene oxide) membranes containing silver nanoparticles. Colloid and Polymer Science, **287**, 1425–1434 (2009).
DOI: 10.1007/s00396-009-2108-y

[241] Hang A. T., Tae B., Park J. S.: Non-woven mats of poly(vinyl alcohol)/chitosan blends containing silver nanoparticles: Fabrication and characterization. Carbohydrate Polymers, **82**, 472–479 (2010).
DOI: 10.1016/j.carbpol.2010.05.016

[242] Zhuang X., Cheng B., Kang W., Xu X.: Electrospun chitosan/gelatin nanofibers containing silver nanoparticles. Carbohydrate Polymers, **82**, 524–527 (2010).
DOI: 10.1016/j.carbpol.2010.04.085

[243] Lee S. J., Heo D. N., Moon J-H., Ko W-K., Lee J. B., Bae M. S., Park S. W., Kim J. E., Lee D. H., Kim E-C., Lee C. H., Kwon I. K.: Electrospun chitosan nanofibers with controlled levels of silver nanoparticles. Preparation, characterization and antibacterial activity. Carbohydrate Polymers, **111**, 530–537 (2014).
DOI: 10.1016/j.carbpol.2014.04.026

[244] Celebi H., Gurbuz M., Koparal S., Dogan A.: Development of antibacterial electrospun chitosan/poly(vinyl alcohol) nanofibers containing silver ion-incorporated HAP nanoparticles. Composite Interfaces, **20**, 799–812 (2013).
DOI: 10.1080/15685543.2013.819700

[245] Kim H-W., Song J-H., Kim H-E.: Nanofiber generation of gelatin–hydroxyapatite biomimetics for guided tissue regeneration. Advanced Functional Materials, **15**, 1988–1994 (2005).
DOI: 10.1002/adfm.200500116

[246] Ayutsede J., Gandhi M., Sukigara S., Ye H., Hsu C-M., Gogotsi Y., Ko F.: Carbon nanotube reinforced *Bombyx mori* silk nanofibers by the electrospinning process. Biomacromolecules, **7**, 208–214 (2006).
DOI: 10.1021/bm0505888

[247] Lu P., Hsieh Y-L.: Multiwalled carbon nanotube (MWCNT) reinforced cellulose fibers by electrospinning. ACS Applied Materials and Interfaces, **2**, 2413–2420 (2010).
DOI: 10.1021/am1004128

[248] Feng W., Wu Z., Li Y., Feng Y., Yuan X.: The fabrication and electrochemical properties of electrospun nanofibers of a multiwalled carbon nanotube grafted by chitosan. Nanotechnology, **19**, 105707/1–105707/6 (2008).
DOI: 10.1088/0957-4484/19/10/105707

[249] Pan H., Zhang Y., Hang Y., Shao H., Hu X., Xu Y., Feng C.: Significantly reinforced composite fibers electrospun from silk fibroin/carbon nanotube aqueous solutions. Biomacromolecules, **13**, 2859–2867 (2012).
DOI: 10.1021/bm300877d

[250] Shalumon K. T., Anulekha K. H., Nair S. V., Nair S. V., Chennazhi K. P., Jayakumar R.: Sodium alginate/poly(vinyl alcohol)/nano ZnO composite nanofibers for antibacterial wound dressings. International Journal of Biological Macromolecules, **49**, 247–254 (2011).
DOI: 10.1016/j.ijbiomac.2011.04.005

[251] Anitha S., Brabu B., Thiruvadigal D. J., Gopalakrishnan C., Natarajan T. S.: Optical, bactericidal and water repellent properties of electrospun nano-composite membranes of cellulose acetate and ZnO. Carbohydrate Polymers, **87**, 1065–1072 (2012).
DOI: 10.1016/j.carbpol.2011.08.030

[252] Tian Y., Wu M., Liu R., Li Y., Wang D., Tan J., Wu R., Huang Y.: Electrospun membrane of cellulose acetate for heavy metal ion adsorption in water treatment. Carbohydrate Polymers, **83**, 743–748 (2011).
DOI: 10.1016/j.carbpol.2010.08.054

[253] Guibal E.: Interactions of metal ions with chitosan-based sorbents: A review. Separation and Purification Technology, **38**, 43–74 (2004).
DOI: 10.1016/j.seppur.2003.10.004

[254] Desai K., Kit K., Li J., Davidson P. M., Zivanovic S., Meyer H.: Nanofibrous chitosan non-wovens for filtration applications. Polymer, **50**, 3661–3669 (2009).
DOI: 10.1016/j.polymer.2009.05.058

[255] Ki C. S., Gang E. H., Um I. C., Park Y. H.: Nanofibrous membrane of wool keratose/silk fibroin blend for heavy metal ion adsorption. Journal of Membrane Science, **302**, 20–26 (2007).
DOI: 10.1016/j.memsci.2007.06.003

[256] Yang R., Aubrecht K. B., Ma H., Wang R., Grubbs R. B., Hsiao B. S., Chu B.: Thiol-modified cellulose nanofibrous composite membranes for chromium (VI) and lead (II) adsorption. Polymer, **55**, 1167–1176 (2014).
DOI: 10.1016/j.polymer.2014.01.043

[257] Wang R., Guan S., Sato A., Wang X., Wang Z., Yang R., Hsiao B. S., Chu B.: Nanofibrous microfiltration membranes capable of removing bacteria, viruses and heavy metal ions. Journal of Membrane Science, **446**, 376–382 (2013).
DOI: 10.1016/j.memsci.2013.06.020

[258] Wang X., Yeh T-M., Wang Z., Yang R., Wang R., Ma H., Hsiao B. S., Chu B.: Nanofiltration membranes prepared by interfacial polymerization on thin-film nanofibrous composite scaffold. Polymer, **55**, 1358–1366 (2014).
DOI: 10.1016/j.polymer.2013.12.007

[259] Yoon K., Kim K., Wang X., Fang D., Hsiao B. S., Chu B.: High flux ultrafiltration membranes based on electrospun nanofibrous PAN scaffolds and chitosan coating. Polymer, **47**, 2434–2441 (2006).
DOI: 10.1016/j.polymer.2006.01.042

[260] Wang M., Meng G., Huang Q., Qian Y.: Electrospun 1,4-DHAQ-doped cellulose nanofiber films for reusable fluorescence detection of trace Cu^{2+} and further for Cr^{3+}. Environmental Science and Technology, **46**, 367–373 (2011).
DOI: 10.1021/es202137c

[261] Kacmaz S., Ertekin K., Suslu A., Ergun Y., Celik E., Cocen U.: Sub-nanomolar sensing of ionic mercury with polymeric electrospun nanofibers. Materials Chemistry and Physics, **133**, 547–552 (2012).
DOI: 10.1016/j.matchemphys.2012.01.081

[262] Ongun M. Z., Ertekin K., Gocmenturk M., Ergun Y., Suslu A.: Copper ion sensing with fluorescent electrospun nanofibers. Spectrochimica Acta Part A: Molecular and Biomolecular Spectroscopy, **90**, 177–185 (2012).
DOI: 10.1016/j.saa.2012.01.042

[263] Kacmaz S., Ertekin K., Gocmenturk M., Suslu A., Ergun Y., Celik E.: Selective sensing of Fe^{3+} at picomolar level with ethyl cellulose based electrospun nanofibers. Reactive and Functional Polymers, **73**, 674–682 (2013).
DOI: 10.1016/j.reactfunctpolym.2013.02.003

[264] Ongun M. Z., Ertekin K., Hizliates C. G., Oter O., Ergun Y., Celik E.: Determination of Hg(II) at subnanomolar levels: A comparative study with nanofibrous materials and continuous thin films. Sensors and Actuators B: Chemical, **181**, 244–250 (2013).
DOI: 10.1016/j.snb.2013.01.055

[265] Zdyrko B.: Nanofibrous materials as sensors for heavy metals. NTC Project: M10-CL03 report (2011).

The effect of intramolecular donor–acceptor moieties with donor–π-bridge–acceptor structure on the solar photovoltaic performance

T. L. Wang[1*]*, S. C. Huang*[1]*, C. H. Yang*[1]*, Y. Y. Chuang*[2]*, C. H. Chen*[3]

[1]Department of Chemical and Materials Engineering, National University of Kaohsiung, 811 Kaohsiung, Taiwan,
 Republic of China
[2]Department of Applied Chemistry, National University of Kaohsiung, 811 Kaohsiung, Taiwan, Republic of China
[3]Department of Electronic Engineering, Cheng Shiu University, 833 Kaohsiung, Taiwan, Republic of China

Abstract. A series of intramolecular donor–acceptor polymers containing different contents of (*E*)-1-(2-ethylhexyl)-6,9-dioctyl-2-(2-(thiophen-3-yl)vinyl)-1*H*-phenanthro[9,10-*d*]imidazole (thiophene-DOPI) moiety and 4,4-diethylhexyl-cyclopenta[2,1-b:3,4-*b′*]dithiophene (CPDT) unit was synthesized via Grignard metathesis (GRIM) polymerization. The synthesized random copolymers and homopolymer of thiophene-DOPI contain the donor–π-bridge–acceptor conjugated structure to tune the absorption spectra and energy levels of the resultant polymers. UV-vis spectra of the three polymer films exhibit panchromatic absorptions ranging from 300 to 1100 nm and low band gaps from 1.38 to 1.51 eV. It is found that more thiophene-DOPI moieties result in the decrease of band gap and lower the highest occupied molecular orbital (HOMO) and lowest unoccupied molecular orbital (LUMO) values of polymers. Photovoltaic performance results indicate that if the content of the intramolecular donor–acceptor moiety is high enough, the copolymer structure may be better than homopolymer due to more light-harvesting afforded by both monomer units.

Keywords: polymer synthesis, intramolecular donor–acceptor, Grignard metathesis polymerization, polymer solar cells

1. Introduction

In order to harvest the sunlight over the range of maximum photon flux (500–800 nm) to achieve the high performance of polymer solar cells (PSCs), the most promising approach is to lower the band gaps of conjugated polymer donor materials. One of the effective ways to lower the band gap of conjugated polymers is to make $-(A)_m-(B)_n-$ random type copolymers by adjusting the ratio of the two monomer unit [1–3]. On the other hand, it is found that the introduction of electron-acceptor units onto the side chain of conjugated polymers could extend the absorption breadth of sunlight and lower the energy gap to some extent [4, 5]. In other words, conjugated polymers that contain side-chain-tethered acceptor moieties can not only exhibit multiple absorptions but also enhance charge transfer ability. This type of conjugated polymers falls into the intramolecular donor–acceptor systems. This system typically consists of conjugated polymers as electron donating groups, another conjugated groups or long alkyl chains as the bridges, and electron acceptors which can increase the interior charge transfer rate of molecules and broaden the absorption spectrum [5, 6]. For this type of conjugated polymers, the electron donating groups are present in the main chain, while the electron accepting units are pendent as side chains. After photoexcitation, the generated excitons are stabilized and fur-

ther separated because of the extended conjugation length, and the electrons are subsequently transferred from the donors to the acceptors very rapidly [6, 7]. Furthermore, the charge separation and transfer process within the planar intramolecular donor-acceptor structure is more effective than the one in the twisted intramolecular donor-acceptor structure, therefore, the charge transfer rate will be higher if the acceptor units are tethered on the polymeric main chains in a coplanar manner [5, 6, 8].

Recently, a series of intramolecular donor–acceptor conjugated copolymers of –(A)$_m$-(B)$_n$– random type have been synthesized by Wei's group and used as the donor materials in the active layers of PSCs [4, 5, 9]. For this kind of conjugated polymers, thiophene derivatives were used as the electron donating groups and presented in the main chain, and phenanthrenyl-imidazole (PI) moieties with the characteristic of coplanar were employed as the side-chain-tethered electron accepting units. More recently, a new imidazole unit as the acceptor moiety has been synthesized by Neophytou *et al.* [10] and this kind of copolymer exhibits fast exciton dissociation at the polymer–fullerene heterointerfaces. Lee *et al.* [11] also reported a kind of intramolecular donor–acceptor copolymer with electron-rich carbazole presenting in the backbone as the donor unit and electron-deficient 14H-benzo[4,5]isoquino[2,1-a]perimidin-14-one moiety as pendant side chains. In a recent report, we have presented a new kind of intramolecular donor–acceptor copolymers containing side-chain-tethered perylenebis(dicarboximide) (PDI) moieties [12]. For the above-mentioned intramolecular donor–acceptor polymers, by the attachment of electron accepting moieties as side chains, the electrons can be transferred sequentially from the donor main chains to the pendant side chains, and then to n-type PCBM after photoexcitation, hence the charge separation and transfer process occurs more efficiently.

For choosing suitable monomer units to achieve the high performance of PSCs, it has been stated that using the fused thiophene family as the donor resulting in a low band gap accompanied by good electrochemical stability [13–16]. Molecules containing fused-ring systems can make the polymer backbone more rigid and coplanar, therefore enhancing effective π-conjugation, lowering band gap and extending absorption. The carbon-bridged 4,4-diethyl-hexyl-cyclopenta[2,1-*b*:3,4-*b*′]dithiophene (CPDT) has attracted considerable research interests due to

the forced coplanarity of the two thienyl subunits resulting in the low energy gaps of the D-A copolymers based on this donor unit [17–23]. Recently, poly[2,6-(4,4-bis(2-ethylhexyl)-4*H*-cyclopenta[2,1-*b*; 3,4-*b*′]dithiophene)-*alt*-4,7-(2,1,3-benzothiadiazole)] (PCPDTBT) comprising of CPDT and benzothiadiazole (BT) unit was demonstrated to be one of the most promising low band gap polymers for the use in PSCs [21]. Even if the PCPDTBT is promising for PSCs, the highest power conversion efficiency (PCE) in this family of polymers has been presented very recently by Yau *et al.* [24]. By using the CPDT as the donor unit, an extremely low band gap ($E_g = 1.20$ eV) donor-acceptor copolymer with a panchromatic absorption ranging from 280 to 1285 nm was synthesized by our group [22].

Furthermore, to optimize the material properties, conjugated polymers with an electron-rich main chain and a donor–π-bridge–acceptor (D–π–A) conjugated side chain has been proposed [25]. The designed polymers take advantage of the well-established knowledge of nonlinear optical chromophores to optimize the absorption spectra and energy levels of the resultant polymers [26, 27]. Based on this design concept, the PSC devices using these donor materials exhibited a high V_{oc} (0.99 V) and their absorption spectra can be easily tuned by controlling the acceptor strength of their side chains or by using a more efficient π-bridge.

As stated above, to build a low band gap and wide optical absorption conjugated polymer to raise the PCE of the devices, the intramolecular donor–acceptor structure with side-chain-tethered acceptor moieties might be an efficient approach. In addition, insertion of a π-bridge between the donor main chain and pendant side chains to tune the molecular energy levels and absorption spectra of the resultant polymers might also be a promising way. Consequently, we synthesized a series of intramolecular donor–acceptor polymers consisting of different molar ratios of 4,4-diethylhexyl-cyclopenta[2,1-*b*:3,4-*b*′]dithiophene (CPDT) unit and (*E*)-1-(2-ethylhexyl)-6,9-dioctyl-2-(2-(thiophen-3-yl)vinyl)-1*H*-phenanthro [9,10-*d*]imidazole (thiophene-DOPI) moiety. In the thiophene-DOPI unit (DOPI tethered to thiophene unit), an ethylenic double bond as the π-bridge was inserted into the side-chain-tethered phenanthrenyl-imidazole (PI) moiety and thiophene backbone, where the thiophene, π-bridge and PI moiety formed the intramolecular charge transfer system. The effect

of molar ratio of thiophene-DOPI unit on the opto-electronic properties and the photovoltaic performance of the fabricated PSCs were investigated.

2. Experimental
2.1. Materials
Palladium acetate (Sigma-Aldrich, USA), 1,4-benzoquinone (Sigma-Aldrich, USA), acrolein (Sigma-Aldrich, USA), acetonitrile (J. T. Baker, USA), neocuproine (Sigma-Aldrich, USA), 3-thienylboronic acid (Alfa Aesar, USA), diethyl ether (Echo Chemical, Taiwan), 9,10-phenanthraquinone (Acros, Belgium), bromine (Sigma-Aldrich, USA), nitrobenzene (Acros, Belgium), dibenzoyl peroxide (Sigma-Aldrich, USA), acetic acid (Acros, Belgium), ammonium acetate (Showa Chemical Co., Japan), 2-ethyl-1-hexylamine (Alfa Aesar, USA), ammonium hydroxide (Acros, Belgium), 2-ethylhexyl magnesium bromide (1.0 M in diethyl ether, Acros, Belgium)), [1,3-bis(diphenylphosphino)propane] nickel (II) chloride (Acros, Belgium), n-bromosuccinimide (Acros, Belgium), ethyl acetate (Echo Chemical, Taiwan), sodium bicarbonate (Showa Chemical Co., Japan), magnesium sulfate anhydrous (Showa Chemical Co., Japan), o-dichlorbenzene (DCB, Echo Chemical, Taiwan), poly(3,4-ethylenedioxythiophene)-poly(styrenesulfonate) (PEDOT:PSS, Sigma-Aldrich, USA) and [6,6]-phenyl-C$_{71}$-butyric acid methyl ester (PC$_{71}$BM, FEM Tech., Germany) were used as received. All other reagents were used as received.

2.2. Monomer synthesis
The monomer M1, 4,4-diethylhexyl-cyclopenta[2,1-*b*:3,4-*b'*]dithiophene (CPDT), was prepared according to a reported literature method [19]. The monomer M2, (*E*)-2-(2-(2,5-dibromothiophen-3-yl)vinyl)-1-(2-ethylhexyl)-6,9-dioctyl-1*H*-henanthro[9,10-*d*]imidazole, was synthesized according to the following steps and the synthetic route is shown in Figure 1. For convenience, the monomer M2 is also designated as thiophene-DOPI.

2.2.1. Synthesis of
(E)-3-(thiophen-3-yl)acrylaldehyde (1)
A glass reactor charged with a mixture of acrolein (0.144 g, 2.57 mmol), 1,4-benzoquinone (0.275 g, 2.52 mmol) and 3-thienylboronic acid (0.660 g, 5.06 mmol) in 10 mL of acetonitrile was purged with argon bubbling for 10 min. To prepare the solution of

catalyst, neocuproine (0.015 g, 0.07 mmol) and palladium acetate (0.013 g, 0.06 mmol) were dissolved in 5 mL of acetonitrile with stirring and argon bubbling for 30 min. To the above reactor was then added the catalyst solution. The reaction mixture was stirred at room temperature for 24 h. The solution was evaporated to dryness by rotary evaporation. The residue was chromatographically purified on silica gel eluting with n-pentane/diethyl ether (2:1, v:v) to afford **1** as a brown oil. Yield: 0.549 g, 65%. ^{1}H NMR (500 MHz, CDCl$_3$): δ (ppm) 6.75 (t, 1H), 6.88 (t, 1H), 7.08 (d, 1H), 7.22 (d, 1H), 7.32 (s, 1H). ^{13}C NMR (125 MHz, CDCl$_3$): δ (ppm) 126.1, 126.7, 128.3, 130.2, 134.9, 152.6, 193.5. Anal. Calcd for C$_7$H$_6$OS: C, 60.84; H, 4.38. Found: C, 60.81; H, 4.42.

2.2.2. Synthesis of
3,6-dibromophenanthrene-9,10-dione (3)
9,10-Phenanthrenequinone (7.03 g, 33.4 mmol) (compound **2**) was dissolved in 50 mL of nitrobenzene with stirring and argon bubbling for 10 min and then 0.35 g of benzoyl peroxide was added. The solution was heated by a tungsten lamp with stirring and argon bubbling for 30 min. Liquid bromine (5 mL, 97.6 mmol) was added dropwise into the reactor through a dropping funnel under the illumination of a tungsten lamp with stirring for 8 h. After turning off the tungsten lamp, the reaction had been continuously run for 18 h at room temperature. The reaction mixture was then poured into 50 mL of diethyl ether. The precipitate was then triturated in diethyl ether for 30 min followed by filtration. The residue was washed twice with diethyl ether and then dried in a vacuum to afford **3** as a golden yellow solid. Yield: 6.41 g, 52%. ^{1}H NMR (500 MHz, CDCl$_3$): δ (ppm) 7.0 (s, 1H), 7.74 (d, 2H), 7.51 (s, 2H). ^{13}C NMR (125 MHz, CDCl$_3$): δ (ppm) 180.2, 136.3, 134.0, 132.5, 131.5, 130.2, 129.4. Anal. Calcd for C$_{14}$H$_6$Br$_2$O$_2$: C, 45.94; H, 1.65. Found: C, 45.98; H, 1.62.

2.2.3. Synthesis of (E)-6,9-dibromo-1-(2-
ethylhexyl)-2-(2-(thiophen-3-yl)vinyl)-1H-
phenanthro[9,10-d]imidazole (4)
In a 100 ml glass reactor was suspended compound **3** (0.549 g, 1.50 mmol) with stirring in acetic acid (30 mL) and ammonium acetate (0.238 g, 3.00 mmol) for 10 min then 2-ethyl-1-hexylamine (0.528 g, 4.00 mmol) was added dropwise over a period of 20 min. Compound **1** (0.207 g, 1.50 mmol) was dis-
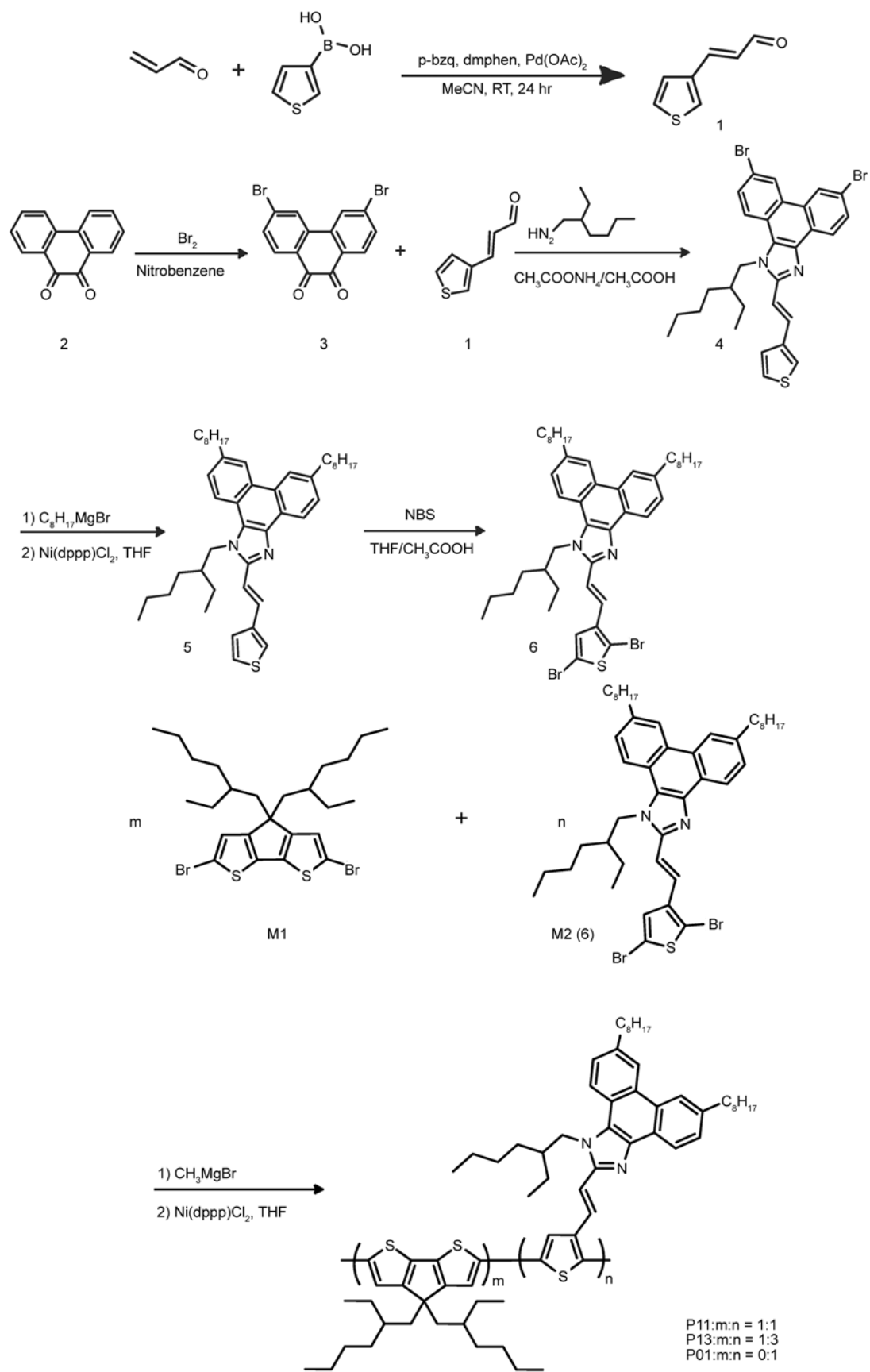
Figure 1. Synthetic route for the preparation of P11, P13 and P01 conjugated polymers

solved in 10 mL of acetic acid and then added dropwise into the reaction. The stirring mixture was heated at reflux for 3 h. After cooling down to room temperature, the reaction mixture was filtered and the solid was washed with an aqueous solution of acetic acid (1:1, v:v) until the washings were almost colorless. The washings were discarded and the solid was further washed with distilled water (~200 mL) until the washings were colorless. The residue was recrystallized from isopropyl alcohol. The product was dried under vacuum giving **4** as a red solid. Yield: 0.501 g, 56%. ^{1}H NMR (500 MHz, CDCl$_3$): δ (ppm) 8.80 (s, 1H), 8.01 (d, 1H), 7.35 (s, 2H), 7.55 (d, 2H), 8.65 (d, 2H), 4.65 (d, 2H), 2.01 (t, 1H), 0.9~1.5 (m, 15H). ^{13}C NMR (125 MHz, CDCl$_3$): δ (ppm) 11.6, 14.1, 23.0, 26.0, 29.3, 32.0, 37.2, 52.0, 118.7, 120.9, 125.7, 126.1, 126.5, 126.6, 126.7, 128.3, 130.2, 130.5, 133.4, 133.6, 141.5. Anal. Calcd for C$_{29}$H$_{28}$Br$_2$N$_2$S: C, 58.40; H, 4.73; N, 26.79. Found: C, 58.32; H, 4.85; N, 26.73.

2.2.4. Synthesis of (E)-1-(2-ethylhexyl)-6,9-dioctyl-2-(2-(thiophen-3-yl)vinyl)-1H-phenanthro[9,10-d]imidazole (5)

In a glass reactor, (*E*)-6,9-dibromo-1-(2-ethylhexyl)-2-(2-(thiophen-3-yl)vinyl)-1H-phenanthro[9,10-*d*]imidazole (0.700 g, 1.18 mmol) was dissolved in 10 mL dry THF with stirring and argon bubbling for 10 min. (2-Ethylhexyl)magnesium bromide (2.37 mL, 2.37 mmol) was then added dropwise into the reactor in an ice bath under argon atmosphere. After returning to room temperature, this mixture was heated at 60°C for 2 h and then Ni(dppp)Cl$_2$ (0.005 g, 0.010 mmol) was added. The stirring mixture was continuously heated for 24 h. After cooling down to room temperature, the reaction mixture was filtered and the solid was washed with distilled water (~200 mL) until the washings were colorless. The product was dried under vacuum to give **5** as a dark red solid. Yield: 0.492 g, 63%. ^{1}H NMR (500 MHz, CDCl$_3$): δ (ppm) 8.35 (s, 1H), 7.90 (d, 1H), 7.75 (d, 1H), 9.20 (s, 2H), 7.95 (d, 2H), 8.55 (d, 2H), 3.81 (m, 6H), 0.9~3.5 (m, 45H). ^{13}C NMR (125 MHz, CDCl$_3$): δ (ppm) 11.6, 14.1, 22.7, 23.0, 26.0, 28.9, 29.3, 31.2, 31.8, 32.0, 36.0, 37.2, 52.0, 118.7, 120.5, 124.7, 126.1, 126.3, 126.6, 126.7, 128.1, 128.3, 130.2, 131.2, 133.4, 137.2, 141.5. Anal. Calcd for C$_{37}$H$_{45}$N$_2$S: C, 80.82; H, 8.25; N, 5.10. Found: C, 80.36; H, 8.14; N, 5.21.

2.2.5. Synthesis of (E)-2-(2-(2,5-dibromothiophen-3-yl)vinyl)-1-(2-ethylhexyl)-6,9-dioctyl-1H-phenanthro[9,10-d]imidazole (6)

N-bromosuccinimide (NBS) (0.284 g, 1.60 mmol) was added into a solution of (*E*)-1-(2-ethylhexyl)-6,9-dioctyl-2-(2-(thiophen-3-yl)vinyl)-1*H*-phenanthro[9,10-*d*]imidazole (0.530 g, 0.800 mmol) in 20 mL of THF and 20 mL of acetic acid. The mixture was stirred at room temperature under an argon atmosphere for 1 h. Water (50 mL) was added to the mixture and it was extracted with ethyl acetate three times. Organic fractions were combined and washed with 5% (w/w) NaHCO$_3$ and then distilled water three times. After drying over anhydrous MgSO$_4$, the organic phase was purified by column chromatography on silica gel with chloroform to afford a dark brown solid. Yield: 0.288 g, 44%. ^{1}H NMR (500 MHz, CDCl$_3$): δ (ppm) 9.25 (s, 2H), 8.5 (d, 2H), 7.80 (d, 2H), 7.65 (s, 1H), 3.81 (m, 6H), 0.9~3.8 (m, 45H). ^{13}C NMR (125 MHz, CDCl$_3$): δ (ppm) 11.6, 14.1, 22.7, 23.0, 26.0, 29.2, 29.3, 29.6, 31.2, 31.8, 32.0, 36.0, 37.2, 52.0, 110.5, 115.0, 118.7, 120.5, 124.7, 126.3, 126.6, 128.1, 131.2, 133.4, 137.2, 140.0, 141.5. Anal. Calcd for C$_{37}$H$_{45}$Br$_2$N$_2$S: C, 62.62; H, 6.39; N, 3.95. Found: C, 63.15; H, 6.18; N, 3.72.

2.2.6. Synthesis of the copolymers (P11 and P13) and homopolymer (P01)

All polymers were synthesized through Grignard metathesis (GRIM) polymerizations in THF except the molar ratio of M1 to M2 was different. The copolymer P11 was synthesized using a 1:1 molar ratio of M1 to M2, while the molar ratio of M1:M2 for the copolymer P13 and homopolymer P01 was 1:3 and 0:1, respectively. The detail synthetic procedures for the copolymer P11 are described below.

In a three-necked 100 mL round-bottom flask, (*E*)-2-(2-(2,5-dibromothiophen-3-yl)vinyl)-1-(2-ethylhexyl)-6,9-dioctyl-1*H*-phenanthro[9,10-*d*]imidazole (1.20 g, 1.49 mmol) and 2,6-dibromo-4,4-di-(2-ethylhexyl)-4H-cyclopenta[2,1-*b*:3,4-*b′*]dithiophene (0.834 g, 1.49 mmol) were dissolved in 40 mL of freshly distilled THF and then flushed by argon for 10 min and CH$_3$MgBr (0.672 mL, 2.98 mmol) was added dropwise to the solution. After reflux for 1 h, Ni(dppp)Cl$_2$ (0.016 g, 0.03 mmol) was added, and the solution was purged by argon for another 20 min.

Another portion of Ni(dppp)Cl$_2$ (0.016 g, 0.03 mmol) was added after refluxed for 45 min. The reaction mixture was then refluxed for 48 h under the protection of argon. The solution was cooled and poured into 200 mL of methanol, where the crude polymer was precipitated and collected as a dark brown solid, which was then subjected to Soxhlet extraction with methanol, hexane, and THF. The polymer was recovered from the THF fraction by rotary evaporation to afford a brownish-yellow solid. The synthetic route is shown in Figure 1. Yield: 0.672 g, 28%. ^{1}H NMR (500 MHz, CDCl$_3$): δ (ppm) 7.7 (d, 2H), 7.5 (s, 2H), 7.2 (d, 2H), 5.02 (d, 2H), 3.81 (m, 6H), 2.50 (d, 4H), 0.9~0 (m, 90H). ^{13}C NMR (125 MHz, CDCl$_3$): δ (ppm) 11.6, 11.9, 14.1, 15.1, 15.5, 22.7, 23.0, 26.0, 26.5, 29.2, 29.3, 29.6, 31.2, 31.8, 32.0, 33.5, 33.6, 36.0, 37.2, 49.0, 50.5, 52.0, 118.7, 120.5, 121.9, 124.7, 126.3, 126.6, 128.1, 128.2, 131.2, 133.4, 133.9, 134.4, 135.2, 135.9, 136.1, 137.1, 137.2, 138.0, 139.1, 141.5. Anal. Calcd for (C$_{62}$H$_{81}$N$_2$S$_3$)$_n$: C, 78.34; H, 8.59; N, 2.95. Found: C, 77.86; H, 8.83; N, 3.14.

2.3. Device fabrication

The device structure of PSCs for current density-voltage (*J-V*) measurements is ITO/PEDOT:PSS/Polymer:PC$_{71}$BM/Al. P11, P13, and P01 were used as the p-type donor polymers and PC$_{71}$BM acted as the n-type acceptor in the active layer. Before device fabrication, the ITO-coated glass substrates were first cleaned by ultrasonic treatment in acetone, detergent, de-ionized water, methanol and isopropyl alcohol sequentially. The ITO surface was spin-coated with ca. 80 nm layer of poly(3,4-ethylene dioxythiophene): poly(styrene) (PEDOT:PSS) in the nitrogen-filled glove-box. The substrate was dried for 10 min at 150°C and then continued to spin coat the active layer. The polymer:PC$_{71}$BM blend solutions were prepared with a weight ratio of 1:1 in 1,2-dichlorobenzene (DCB) as the active layer. The solution blends were spin-cast onto the PEDOT:PSS layer at 800 rpm for 30 s. The obtained thicknesses for the blend films were ca. 110 nm. The devices were completed by evaporation of metal electrodes Al with area of 6 mm^2 defined by masks.

2.4. Instrumentation

Thermogravimetric analyses (TGA) were performed using a TA Instruments SDT-2960 analyzer operated at a heating rate of 10°C/min in the air. Differential canning calorimetry (DSC) thermograms were obtained with a TA Instruments modulated DSC 2920 analyzer operated at a heating rate of 10°C/min under a dry nitrogen purge. Ultraviolet-visible (UV-vis) spectroscopic analysis was conducted on a Perkin–Elmer Lambda 35 UV-vis spectrophotometer. Photoluminescence (PL) spectrum was recorded on a Hitachi F-7000 fluorescence spectrophotometer. The *J-V* curves were measured under illumination from a solar simulator, using a Keithley 2400 source meter. The intensity of solar simulator was set with a primary reference cell and a spectral correction factor to give the performance under the AM 1.5 (100 mW/cm^2) global reference spectrum (IEC 60904-9). EQE was detected with a QE-3000 (Titan Electro-Optics Co., Ltd.) lock-in amplifier under monochromatic illumination. Calibration of the incident light was performed with a monocrystalline silicon diode. Molecular weights of the copolymers were determined by gel permeation chromatography (GPC) using Young Lin Acme 9000 liquid chromatograph equipped with a 410 RI detector and a μ-Styragel columns with THF as the carrier solvent. Cyclic voltammetric (CV) measurements were performed in 0.1 M tetrabutylammonium perchlorate solution using a PGSTAT30 electrochemical analyzer (AUTOLAB Electrochemical Instrument, The Netherlands).

3. Results and discussion
3.1. Material design and structural characterization

Since the charge separation and transfer process within a planar intramolecular donor-acceptor structure is more effective than that of a twisted intramolecular donor-acceptor structure, therefore, the charge transfer rate will be higher if the acceptor units are tethered on the polymeric main chains in a coplanar manner. As reported by Wei's group, the electron transfer probability of the polymer with the planar intramolecular donor-acceptor structure is at least twice higher than the pure poly(3-hexylthiophene) when blended with PC$_{61}$BM [5, 9]. This type of random copolymer synthesized by Wei's group contains a thiophene monomer and a side-chain-tethered phenanthrenyl-imidazole moiety as the other monomer unit, as shown in Figure 2a. Although the intramolecular donor–acceptor conjugated copolymers reported by Wei and coworkers exhibit lower band gaps (1.77–1.89 eV) than regioregular poly(3-
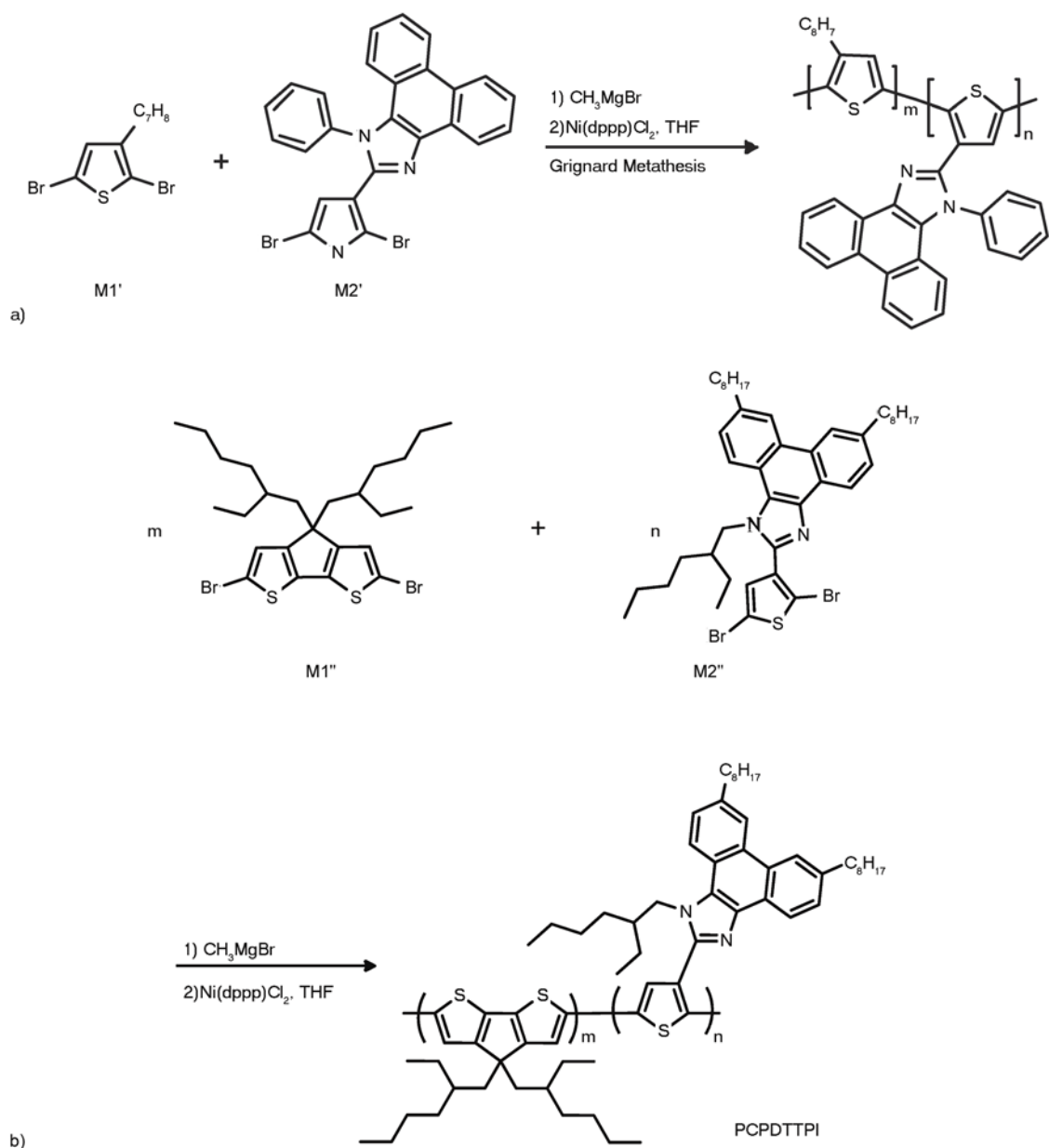
Figure 2. (a) The synthesized copolymers reported by Chang *et al.* [4] (b) Synthetic route of PCPDTTPI copolymers

hexylthiophene) (rr-P3HT), the optical band gaps are still considered too large and ranges of light-harvesting are not broad enough [4, 5, 9]. To compare with the results of Wei's group, in an unpublished report, we designed and synthesized an intramolecular donor–acceptor type of conjugated copolymer with an ethylhexyl and two octyl chains attached to the PI moiety. The molecular structure is shown in Figure 2b and the copolymer is designated as PCPDTTPI. For the copolymer PCPDTTPI synthesized from 1:1 molar ratio of M1″ to M2″, although the UV-vis spectrum of the polymer film exhibited a panchromatic absorption ranging from 280 to 1170 nm and a low band gap of 1.42 eV as seen in Figure 3, the
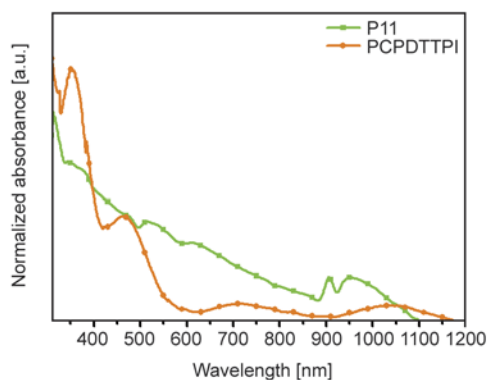
Figure 3. Normalized UV-vis absorption spectra of P11 and PCPDTTPI

weak absorption in the range between 600 to 1170 nm resulted in a low PCE of 0.52%.

Therefore, further improvement based on this structure was carried out to obtain a copolymer with an enhanced absorption of UV-vis spectrum in the long wavelength region to afford a higher PCE. In the present study, we designed a new random copolymer containing the donor–π-bridge–acceptor moiety as a monomer unit (M2 in Figure 1). As compared to the molecular structure reported by Wei's group (Figure 2a) [4], because the structure of PI moiety was too rigid to be soluble in common organic solvents, we attached an ethylhexyl and two octyl chains to the PI moiety. In addition, to reduce the steric hindrance of the copolymer for increasing the effective packing and to tune the molecular energy levels and absorption spectra of the resultant polymers for charge transfer and light-harvesting, an ethylenic double bond as the π-bridge was inserted into the PI moiety and thiophene backbone. For the other monomer unit, CPDT was chosen due to the forced coplanarity of the two thienyl subunits resulting in the more extended conjugation and stronger intermolecular interaction. In this regard, we synthesized a series of intramolecular donor–acceptor polymers containing the conjugated thiophene-DOPI moieties and CPDT units via GRIM polymerization (Figure 1). Employing the GRIM method can shorten polymerization times and lower reaction temperatures, facilitating the preparation of aryl and heteroaryl conjugating polymers. Using this approach also paves the way toward the production of block or random copolymers. Because our synthesized copolymers are also the intramolecular donor–acceptor type, which is similar to the copolymers synthesized by Wei's group (Figure 2a), we adopt the same synthetic approach and the same Grignard reagent like them. Their synthetic approach is referred to McCullough's publication [28], so we also used CH_3MgBr as the Grignard reagent in our synthesis. However, it was found that yields of this series

of copolymer were relatively low. Hence, it is suggested that for the synthesis of this series of copolymers, other Grignard regents such as isopropylmagnesium chloride (*i*-PrMgCl) or isopropylmagnesium bromide (*i*-PrMgBr) together with lithium chloride (LiCl) may be used to afford the copolymers in good yields [29, 30].

Since the copolymer synthesized by Wei's group comprising of equal molar ratio of M1′ and M2′ (Figure 2a) exhibited an optical bandgap of 1.82 eV and a HOMO value of –5.21 eV [4], the copolymer consisting of equal molar ratio of CPDT unit and thiophene-DOPI unit was synthesized for comparison and designated as P11. As shown in Table 1 (the data will be discussed in the following section), it can be seen that the incorporation of CPDT unit and insertion of an ethylenic double bond could significantly reduce the band gap (1.40 eV) and lower the energy level of HOMO (–5.27 eV) of the conjugated polymer. On the other hand, compared to the UV-vis spectrum of the copolymer PCPDTTPI synthesized from equal molar ratio of M1″ and M2″ (Figure 2b), the copolymer P11 exhibited much enhanced absorption in the region between 550 to 1050 nm. From the TGA thermogram of P11, the onset decomposition temperature of this copolymer is around 275°C in the air. The thermal stability of this kind of copolymer is adequate for its application in PSCs and other optoelectronic devices. In addition, due to the insertion of an ethylenic double bond into the PI moiety and thiophene backbone, the copolymer P11 is more flexible, exhibiting a lower T_g of 53.5°C compared with the similar type of copolymer synthesized by Chang *et al*. [5]. These findings encouraged us to vary the content of thiophene-DOPI moiety to proceed further study. Therefore, we further synthesized a copolymer with a mole ratio of 1:3 for CPDT to thiophene-DOPI. The copolymer was designated as P13. Besides, the homopolymer of thiophene-DOPI, P01, was also prepared for comparison. The data of synthesized polymers are summarized in Table 1. In

Table 1. Molecular weights and optoelectronic properties of the synthesized polymers

Polymer	M_n [kg·mol^{-1}]	M_w [kg·mol^{-1}]	PDI	E_g^a [eV]	HOMO^b [eV]	LUMO^c [eV]
P11	11.8	16.0	1.36	1.40	–5.27	–3.87
P13	10.5	13.4	1.28	1.38	–5.39	–4.01
P01	12.3	16.9	1.37	1.51	–5.42	–3.91
P3HT (commercial)	13.2	17.0	1.29	1.90	–5.20	–3.30

[a]Obtained by Tauc relation.
[b]Obtained by cyclic voltammetry.
[c]Obtained from LUMO = HOMO + E_g.

particular, for this kind of intramolecular donor-acceptor polymer, the electron donating groups (CPDT and thiophene units) are present in the main chain as the polymer backbone, while the electron accepting units (DOPI moieties) are pendent as side chains. By the attachment of a coplanar type of DOPI moieties as side chains, the electrons can be transferred sequentially from the donor main chains to the acceptor side chains, and then to n-type PCBM after photoexcitation, hence the charge separation and transfer process are more readily and enhanced in this intramolecular donor-acceptor system. Therefore, it was expected that a low band gap polymer with wide sunlight absorption band and high power conversion efficiency could be achieved for this type of copolymer using the thiophene-DOPI moieties as the intramolecular donor-acceptor units.

3.2. Optical properties and band gaps

The normalized UV-vis absorption spectra for the films of the three synthesized polymers and P3HT are presented in Figure 4. As seen from Figure 4, the UV–vis absorption spectrum of the P11 film exhibits a wide absorption band ranging from 300 to 1100 nm with four absorption peaks positioned at about 312, 516, 906 and 952 nm. The strong absorption at 312 nm is attributed to π–π* transition within the polymer backbone, whereas the other weak absorption peaks are ascribed to the intramolecular charge transfer (ICT) between CPDT and thiophene units in the polymer backbone and thiophene donor and DOPI acceptor units of the thiophene-DOPI moieties. In other words, the weak and broadened absorption bands may imply that an effective and enhanced ICT between thiophene backbone and DOPI moieties has occurred. Consequently, with the incorporation of DOPI moieties as acceptor side chains and thiophene unit as the donor backbone, the synthesized copolymer exhibits the enhanced characteristic of intramolecular donor–acceptor polymers. Moreover, since the UV-vis absorption regions of the copolymers stated in Wei's report only extend to ca. 700 nm, the incorporation of CPDT unit and insertion of an ethylenic double bond as the π-bridge between thiophene and PI moiety may extend the absorption breadth of sunlight and lower the energy gap. In addition, as compared to the spectrum of PCPDTTPI and evident from Figure 3, the intensified absorption for P11 in the region from 550 to 1050 nm may indicate that an enhanced ICT has occurred. This tes-
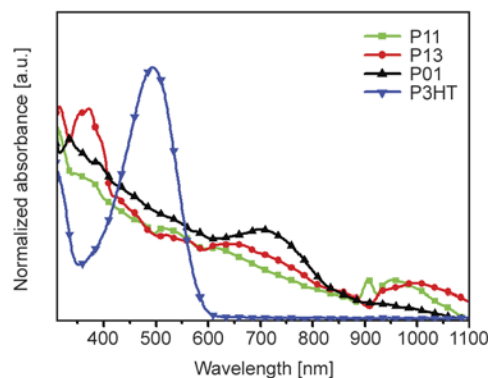

Figure 4. Normalized UV-vis absorption spectra of P11, P13, and P01

tifies to the fact that the insertion of a π-bridge between the donor and acceptor unit may optimize the absorption spectrum and harvest more light.

In a similar manner, the spectrum of P13 film also exhibits a panchromatic absorption ranging from 300 to 1100 nm with two strong π–π* transitions (centered at 314 and 373 nm) arising from both CPDT and thiophene units of the polymer backbone. As compared to the spectrum of P11 film, it is noticeable that the absorption bands in the region of 600–900 and 900–1100 nm are significantly enhanced. It may be ascribed to the increased mole ratio of thiophene-DOPI unit raising the ICT between the thiophene donor and DOPI acceptor. For the homopolymer of thiophene-DOPI, the absorption peak at 334 nm is assigned to the π–π* transition of thiophene backbone, while the broad absorption band ranging from 600 to 850 nm and centered at 700 nm is attributed to the ICT between thiophene and DOPI. It is worth noting that the absorption band in the region of 600–850 nm is stronger as compared to that of P11 and P13 film, indicating that the thiophene-DOPI structure has a remarkable effect of ICT between thiophene backbone and DOPI side chains. On the other hand, for the copolymer P11 and P13, the broad absorption around 900 to 1100 nm may arise from the ICT of the polymer backbone between CPDT and thiophene-DOPI units since no obvious absorption for P01 was observed in this region.

The optical band gaps obtained from the Tauc relation [31] $\alpha h v = B(h v - E_{\text{opt}})^n$ for P11, P13 and P01 are 1.40, 1.38, and 1.51 eV (Figure 5), respectively, and are shown in Table 1. The HOMO and LUMO energy levels of the three polymers can be determined from the oxidation potentials of cyclic voltammetry (CV) measurements and the curve-fitting opti-
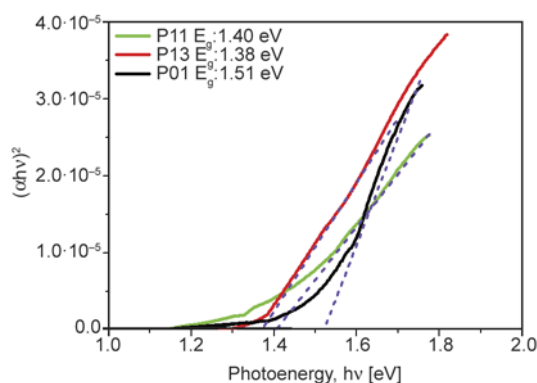
Figure 5. Plot of $(\alpha h\nu)^2$ vs. $h\nu$ via Tauc relation for P11, P13, and P01 film

Figure 6. UV-vis absorption spectra of P11, P13, and P01 blended with $PC_{71}BM$ in a weight ratio of 1:1

cal band gaps (E_g^{opt} by Tauc relation). The related data are listed in Table 1. As compared to the data reported by Chang *et al*. [4], it is noteworthy that the incorporation of CPDT unit and insertion of an ethylenic double bond can not only lower the HOMO of the copolymer but also reduce the band gap. Both of them are important characteristics for high-performance solar cells. In addition, comparing the data of P13 with those of P11, it may suggest that more thiophene-DOPI moieties may result in the decrease of band gap and lower the HOMO and LUMO values. However, if no CPDT units present in the polymer backbone, as in the case of P01, only the HOMO value is reduced whereas the band gap is raised. Therefore, for reducing the band gap and extending the sunlight absorption of the conjugated polymer, the copolymer structure may be more favorable than that of the homopolymer structure.

Since $PC_{71}BM$ possesses a strong absorption of UV-vis spectrum around 450–600 nm to compensate the weak absorptions of the three synthesized polymers in this region, we expected that the polymer/$PC_{71}BM$ blend films would be beneficial to raise the power conversion efficiency of the fabricated solar cells. Figure 6 displays the UV-vis absorption spectra of the three polymers blended with $PC_{71}BM$ in a weight ratio of 1:1. As evident from Figure 4 and Figure 6, the absorption range of UV-vis spectrum for the three blend films increases in the order of P01/$PC_{71}BM$ ≈ P11/$PC_{71}BM$ < P13/$PC_{71}BM$, resembling the absorption profiles of the three polymers. It is apparent that the ICT interaction between donor (thiophene) and acceptor (DOPI) moieties in this kind of intramolecular donor-acceptor polymers is a practical approach to lower the band gap and broaden the absorption bands of conjugated polymers. In addition, in comparison of copolymer P13 with P11, it is
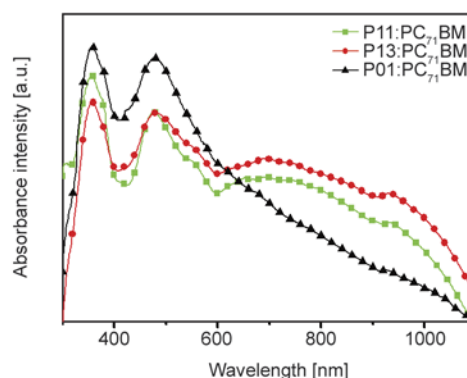
obvious that the increase of molar ratio of thiophene-PDI enhances the absorption intensity in both the π–π* transition and ICT (600–1100 nm) regions, and results in the red-shifted absorption bands as well. Conversely, for the homopolymer P01, the weak absorption in the ICT region (600–1100 nm) results in the lower PCE as compared to that of P13, which we will see in the following section.

3.3. Photoluminescence spectra

The photoluminescence (PL) emission spectra of the three polymers in comparison with that of P3HT are shown in Figure 7. All of the spectra were obtained from the blend film of polymer/$PC_{71}BM$ in a weight ratio of 1:1 without annealing and any additives. The PL of the P11 blend film is dramatically quenched relative to that of P3HT blend film with two peaks centered at 379 and 468 nm. The former peak may result from the PL of CPDT units while the latter peak is associated with the PL of thiophene-DOPI moieties. Upon increasing the content of thiophene-DOPI unit in the copolymer, as in the case of P13, the degree of quenching in both regions is further
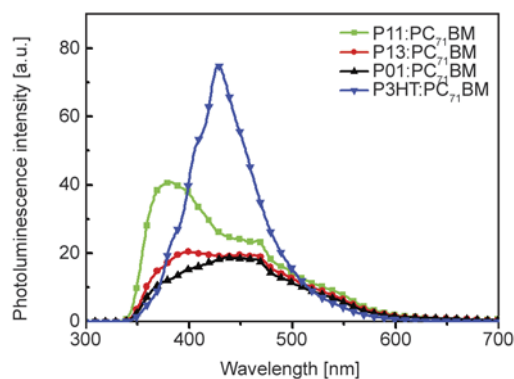

Figure 7. Photoluminescence emission spectra of the polymer/$PC_{71}BM$ blend films in a weight ratio of 1:1 with excitation at 320 nm

enhanced, especially in the region around 379 nm because of the reduction of the CPDT content, as seen in Figure 7. It is evident that an efficient intramolecular charge transfer between CPDT and thiophene unit in the polymer backbone and thiophene backbone and the electron-withdrawing DOPI side chains has occurred. For the homopolymer P01, the peak arising mainly from CPDT units is further reduced, whereas the PL around 468 nm shows not much change. Therefore, it seems that a 3:1 mole ratio of thiophene-DOPI to CPDT may be enough for the efficient intramolecular charge transfer to occur.

3.4. Photovoltaic properties

The photovoltaic performances of the devices for the blend films cast at room temperature (RT) with a 1:1 weight ratio of polymer:$PC_{71}BM$ as the active layer were measured under illumination from solar simulator at 100 mW/cm^2 light intensity. The current density-voltage (J-V) curves of the cells are shown in Figure 8. The corresponding V_{oc}, short-circuit current (J_{sc}), fill factor (FF), and power conversion efficiency (PCE) are also listed in Table 2. As seen in Figure 8 and Table 2, comparing both copolymers (P11 and P13), the value of J_{sc} increases with the increase of the molar ratio of thiophene-DOPI moiety. In addition, it is worth noting that the V_{oc} value is also related with the content of the thiophene-DOPI unit and the more the thiophene-DOPI content, the higher the V_{oc}. Since the values of J_{sc} and V_{oc} increase with the increase of the thiophene-PDI moiety simultaneously, the PCE of the solar cell increases with the increase of thiophene-DOPI moiety in the copolymers. However, the homopolymer P01 displays a lower J_{sc} and results in a lower PCE as compared to those of P13. This
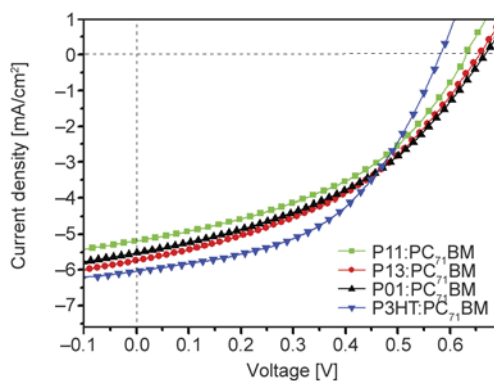
Table 2. Photovoltaic characteristics of the polymer solar cells

Polymer	V_{oc} [V]	J_{sc} [mA/cm^2]	FF [%]	PCE [%]
P11	0.63	5.18	34.5	1.13
P13	0.66	6.15	34.7	1.41
P01	0.67	5.87	34.0	1.34
P3HT (commercial)	0.58	6.25	46.4	1.68

may imply that if the content of the intramolecular donor–acceptor moiety is high enough, the copolymer structure may be a better choice than homopolymer due to more light-harvesting afforded by both monomer units (CPDT and thiophene-DOPI).

3.5. External quantum efficiency

External quantum efficiency (EQE) measurements with monochromatic wave from 300 to 1100 nm were also performed on the solar cell devices with a 1:1 weight ratio of polymer:$PC_{71}BM$ (Figure 9). As seen in the figure, both of the EQE spectra of the copolymer P11 and P13 blend films exhibit a dominant region ranging from 300–600 and 300–640 nm, respectively, along with a remarkable peak positioned at 480 nm. Both spectra also show a broad band in the region of 600–1100 and 640–1100 nm, respectively. The broad band in the red to near-infrared region fulfills the expectations for panchromatic photovoltaic applications. Comparing both spectra, it is apparent that the EQE value increases with the increase of thiophene-DOPI content and shows a red-shifted trend for the P13 blend film. The higher EQE values and enhanced J_{sc} for P13 blend film are attributed to the rapid electron transfer of the dissociated excitons in polythiophene backbone to the conjugated DOPI side chains. It may indicate that more thiophene-DOPI
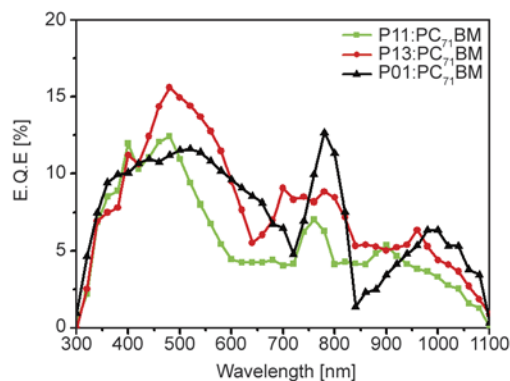

Figure 8. J-V characteristics of devices under AM 1.5 simulated solar illumination at an intensity of 100 mW/cm^2 for the polymer/$PC_{71}BM$ blend films cast at room temperature in a weight ratio of 1:1

Figure 9. External quantum efficiency curves of polymer/$PC_{71}BM$ blends in a weight ratio of 1:1

units may facilitate the charge separation and the intramolecular charge transfer between the thiophene backbone and DOPI moieties. As for the P01 film, the EQE spectrum displays three dominant regions ranging from 300–720, 720–840, and 840–1100 nm with three peaks positioned at 518, 780, and 990 nm, respectively. The EQE values in the first dominant region are apparently smaller than those of P11 and P13 blend films. Conversely, due to the remarkable effect of ICT between thiophene backbone and DOPI side chains in the region of 600–850 nm from the UV-vis spectrum of P01 (Figure 4) as mentioned above, the EQE values are higher in this region as compared to both copolymers. This may suggest that more thiophene-DOPI moiety may facilitate the charge separation and charge transfer process.

4. Conclusions

We have designed and synthesized a series of intramolecular donor–acceptor polymers with different contents of thiophene-DOPI unit that has the D–π–A structure. The spectra of the polymer films exhibited panchromatic absorptions and low band gaps (1.38 to 1.51 eV), which were attributed to the incorporation of thiophene-DOPI moieties. A more efficient charge transfer occurred between thiophene (donor) backbone and DOPI (acceptor) side chains, which could be ascribed to the intramolecular donor–acceptor structure. When increasing the content of the thiophene-DOPI unit, the V_{oc} could be raised and the PCEs of the photovoltaic devices showed significant improvements. In comparison with the device of P11, since the values of J_{sc} and V_{oc} increased with the increase of the thiophene-DOPI moiety in the polymers, the PCEs of the solar cells for P13 and P01 were much enhanced.

Acknowledgements

References

[1] Zhou Q., Hou Q., Zheng L., Deng X., Yu G., Cao Y.: Fluorene-based low band-gap copolymers for high performance photovoltaic devices. Applied Physics Letters, **84**, 1653–1655 (2004).
DOI: 10.1063/1.1667614

[2] Chen C-P., Chan S-H., Chao T-C., Ting C., Ko B-T.: Low-bandgap poly(thiophene-phenylene-thiophene) derivatives with broaden absorption spectra for use in high-performance bulk-heterojunction polymer solar cells. Journal of the American Chemical Society, **130**, 12828–12833 (2008).
DOI: 10.1021/ja801877k

[3] Peng Q., Park K., Lin T., Durstock M., Dai L.: Donor-π-acceptor conjugated copolymers for photovoltaic applications: Tuning the open-circuit voltage by adjusting the donor/acceptor ratio. The Journal of Physical Chemistry B, **112**, 2801–2808 (2008).
DOI: 10.1021/jp7105428

[4] Chang Y-T., Hsu S-L., Su M-H., Wei K-H.: Soluble phenanthrenyl-imidazole-presenting regioregular poly(3-octylthiophene) copolymers having tunable bandgaps for solar cell applications. Advanced Functional Materials, **17**, 3326–3331 (2007).
DOI: 10.1002/adfm.200700423

[5] Chang Y-T., Hsu S-L., Chen G-Y., Su M-H., Singh T. A., Diau E. W-G., Wei K-H.: Intramolecular donor–acceptor regioregular poly(3-hexylthiophene)s presenting octylphenanthrenyl-imidazole moieties exhibit enhanced charge transfer for heterojunction solar cell applications. Advanced Functional Materials, **18**, 2356–2365 (2008).
DOI: 10.1002/adfm.200701150

[6] Yoshihara T., Druzhinin S. I., Zachariasse K. A.: Fast intramolecular charge transfer with a planar rigidized electron donor/acceptor molecule. Journal of the American Chemical Society, **126**, 8535–8539 (2004).
DOI: 10.1021/ja049809s

[7] de la Escosura A., Martínez-Díaz M. V., Guldi D. M., Torres T.: Stabilization of charge-separated states in phthalocyanine–fullerene ensembles through supramolecular donor–acceptor interactions. Journal of the American Chemical Society, **128**, 4112–4118 (2006).
DOI: 10.1021/ja058123c

[8] Yuan M-C., Su M-H., Chiu M-Y., Wei K-H.: Synthesis and characterization of donor–bridge–acceptor alternating copolymers containing perylene diimide units and their application to photovoltaic cells. Journal of Polymer Science Part A: Polymer Chemistry, **48**, 1298–1309 (2010).
DOI: 10.1002/pola.23889

[9] Chang Y-T., Hsu S-L., Su M-H., Wei K-H.: Intramolecular donor–acceptor regioregular poly(hexylphenanthrenyl-imidazole thiophene) exhibits enhanced hole mobility for heterojunction solar cell applications. Advanced Materials, **21**, 2093–2097 (2009).
DOI: 10.1002/adma.200802379

[10] Neophytou M., Ioannidou H. A., Ioannou T. A., Chochos C. L., Economopoulos S. P., Koutentis P. A., Itskos G., Choulis S. A.: 2-(2,3,4,5,6-Pentafluorophenyl)-1*H*-benzo[*d*]imidazole, a fluorine-rich building block for the preparation of conjugated polymer donors for organic solar cell applications. Polymer Chemistry, **3**, 2236–2243 (2012)
DOI: 10.1039/c2py20198d

[11] Lee J. F., Hsu S. L. C., Lee P. I., Chuang H. Y., Yang M. L., Chen J. S., Chou W. Y.: Low bandgap carbazole copolymers containing an electron-withdrawing side chain for solar cell applications. Solar Energy Materials and Solar Cells, **95**, 2759–2804 (2011).
DOI: 10.1016/j.solmat.2011.05.029

[12] Wang T-L., Chuang Y-Y., Shieh Y-T., Yang C-H., Chen C-H., Ho T-H.: Intramolecular donor–acceptor copolymers containing side-chain-tethered perylenebis(dicarboximide) moieties for panchromatic solar cells. Journal of Polymer Science Part A: Polymer Chemistry, **52**, 1978–1988 (2014).
DOI: 10.1002/pola.27205

[13] Lee B., Yavuz M. S., Sotzing G. A.: Poly(thieno[3,4-b] thiophene)s from three symmetrical thieno[3,4-*b*]thiophene dimers. Macromolecules, 39, 3118–3124 (2006).
DOI: 10.1021/ma0526746

[14] Lee K., Sotzing G. A.: Poly(thieno[3,4-*b*]thiophene). A new stable low band gap conducting polymer. Macromolecules, **34**, 5746–5747 (2001).
DOI: 10.1021/ma0106245

[15] Biniek L., Fall S., Chochos C. L., Leclerc N., Lévêque P., Heiser T.: Optimization of the side-chain density to improve the charge transport and photovoltaic performances of a low band gap copolymer. Organic Electronics, **13**, 114–120 (2012).
DOI: 10.1016/j.orgel.2011.10.011

[16] Biniek L., Chochos C. L., Leclerc N., Boyron O., Fall S., Lévêque P., Heiser T.: 3,6-Dialkylthieno[3,2-*b*]thiophene moiety as a soluble and electron donating unit preserving the coplanarity of photovoltaic low band gap copolymers. Journal of Polymer Science Part A: Polymer Chemistry, **50**, 1861–1868 (2012).
DOI: 10.1002/pola.25961

[17] Chen C-H., Hsieh C-H., Dubosc M., Cheng Y-J., Hsu C-S.: Synthesis and characterization of bridged bithiophene-based conjugated polymers for photovoltaic applications: Acceptor strength and ternary blends. Macromolecules, **43**, 697–708 (2010).
DOI: 10.1021/ma902206u

[18] Bijleveld J. C., Shahid B., Gilot J., Wienk M. M., Janssen R. A. J.: Copolymers of cyclopentadithiophene and electron-deficient aromatic units designed for photovoltaic applications. Advanced Functional Materials, **19**, 3262–3270 (2009).
DOI: 10.1002/adfm.200900412

[19] Coppo P., Turner M. L.: Cyclopentadithiophene based electroactive materials. Journal of Materials Chemistry, **15**, 1123–1133 (2005).
DOI: 10.1039/B412143K

[20] Zhu Z., Waller D., Gaudiana R., Morana M., Mühlbacher D., Scharber M., Brabec C.: Panchromatic conjugated polymers containing alternating donor/acceptor units for photovoltaic applications. Macromolecules, **40**, 1981–1986 (2007).
DOI: 10.1021/ma062376o

[21] Mühlbacher D., Scharber M., Morana M., Zhu Z., Waller D., Gaudiana R., Brabec C.: High photovoltaic performance of a low-bandgap polymer. Advanced Materials, **18**, 2884–2889 (2006).
DOI: 10.1002/adma.200600160

[22] Wang T-L., Yang C-H., Shieh Y-T., Chen Y-C., Ho T-H., Chen C-H.: An extremely low bandgap donor–acceptor copolymer for panchromatic solar cells. Solar Energy Materials and Solar Cells, **107**, 298–306 (2012).
DOI: 10.1016/j.solmat.2012.06.050

[23] Chochos C. L., Choulis S. A.: How the structural deviations on the backbone of conjugated polymers influence their optoelectronic properties and photovoltaic performance. Progress in Polymer Science, **36**, 1326–1414 (2011).
DOI: 10.1016/j.progpolymsci.2011.04.003

[24] Yau C. P., Fei Z., Ashraf R. S., Shahid M., Watkins S. E., Pattanasattayavong P., Anthopoulos T. D., Gregoriou V. G., Chochos C. L., Heeney M.: Influence of the electron deficient *co*-monomer on the optoelectronic properties and photovoltaic performance of dithienogermole-based *co*-polymers. Advanced Functional Materials, **24**, 678–687 (2014).
DOI: 10.1002/adfm.201302270

[25] Huang F., Chen K. S., Yip H. L., Hau S. K., Acton O., Zhang Y., Luo J. D., Jen A. K. Y.: Development of new conjugated polymers with donor–π-bridge–acceptor side chains for high performance solar cells. Journal of the American Chemical Society, **131**, 13886–13887 (2009).
DOI: 10.1021/ja9066139

[26] Marder S. R., Cheng L-T., Tiemann B. G., Friedli A. C., Blanchard-Desce M., Perry J. W., Skindhøj J.: Large first hyperpolarizabilities in push-pull polyenes by tuning of the bond length alternation and aromaticity. Science, **263**, 511–514 (1994).
DOI: 10.1126/science.263.5146.511

[27] Liu S., Haller M. A., Ma H., Dalton L. R., Jang S. H., Jen A. K-Y.: Focused microwave-assisted synthesis of 2,5-dihydrofuran derivatives as electron acceptors for highly efficient nonlinear optical chromophores. Advanced Materials, **15**, 603–607 (2003).
DOI: 10.1002/adma.200304813

[28] Sheina E. E., Khersonsky S. M., Jones E. G., McCullough R. D.: Highly conductive, regioregular alkoxy-functionalized polythiophenes: A new class of stable, low band gap materials. Chemistry of Materials, **17**, 3317–3319 (2005).
DOI: 10.1021/cm050083o

[29] Knochel P., Dohle W., Gommermann N., Kneisel F. F., Kopp F., Korn T., Sapountzis I., Vu V. A.: Highly functionalized organomagnesium reagents prepared through halogen–metal exchange. Angewandte Chemie International Edition, **42**, 4302–4320 (2003).
DOI: 10.1002/anie.200300579

[30] Stefan M. C., Javier A. E., Osaka I., McCullough R. D.: Grignard metathesis method (GRIM): Toward a universal method for the synthesis of conjugated polymers. Macromolecules, **42**, 30–32 (2009).
DOI: 10.1021/ma8020823

[31] Tauc J.: Amorphous and liquid semiconductors. Plenum Press, New York (1974).

Crystalline plasticity in isotactic polypropylene below and above the glass transition temperature

G. Polt[1], F. Spieckermann[1], H. Wilhelm[1,2], Ch. Fischer[2], E. Schafler[1], S. Bernstorff[3], M. Zehetbauer[1]*

[1]Research Group Physics of Nanostructured Materials, Faculty of Physics, University of Vienna, Boltzmanngasse 5, Vienna, Austria
[2]Laboratory of Polymer Engineering LKT-TGM, Wexstrasse 19–23, 1200 Vienna, Austria
[3]Sincrotrone Trieste, Strada Statale 14 km 163.5 in AREA Science Park, 34149 Basovizza, Trieste, Italy

Abstract. In-situ X-ray diffraction was applied to isotactic polypropylene with a high volume fraction of α-phase (α-iPP) while it has been compressed at temperatures below and above its glass transition temperature T_g. The diffraction patterns were evaluated by the Multi-reflection X-ray Profile Analysis (MXPA) method, revealing microstructural parameters such as the density of dislocations and the size of coherently scattering domains (CSD-size). A significant difference in the development of the dislocation density was found compared to compression at temperatures above T_g, pointing at a different plastic deformation mechanism at these temperatures. Based on the individual evolutions of the dislocation density and CSD-size observed as a function of compressive strain, suggestions for the deformation mechanisms occurring below and above T_g are made.

Keywords: *thermal properties, polypropylene, dislocation, X-ray diffraction, plasticity*

1. Introduction

Semicrystalline polymers consist of a complex multiscale structure. A physical interpretation of deformation processes at the macroscopic scale can only be successful when both, micro- and mesoscopic deformation processes are considered. At the mesoscopic scale, rearrangements of lamellar crystalline blocks such as bending, rotation, fragmentation or shear band formation occur [1]. At the microscopic scale, basic micromechanisms of deformation within the crystalline and amorphous phase are active.

There is already an overwhelming amount of data demonstrating that the plasticity of semicrystalline polymers is controlled by the deformation of the crystalline phase even up to large strains [2]. In this connection, two deformation mechanisms have been discussed, those are a) an approach based on adiabatic melting and recrystallization [3], and b) the deformation by crystallographic slip [4]. The major part of publications, favor the occurrence of the latter mechanism even for a wide range of strain [5–7]. Recently it could be shown that this mechanism is governed by nucleation and propagation of dislocations [8–10], although it was also reported [9] that in some polymer systems other deformation modes have to be considered in the crystalline phase. Nevertheless, the amorphous phase still contributes to the deformation process as the stresses are being transmitted between the two phases.

In the present work, the deformation behaviour of the crystalline phase – with special respect to a dislocation mediated mechanism – has been investigated at

different deformation temperatures, in order to find out the role of the amorphous phase having varying rigidity. Therefore, in-situ compression experiments during X-ray diffraction below the glass transition temperature (T_g) were performed on polypropylene with a high volume fraction of α-phase and compared with previous observations done above T_g.

2. Experimental
2.1. Material and measurement
Isotactic polypropylene (type *BE50* from *Borealis*) was used during this investigation (melt flow rate (230°C/2,16 kg): 0,30 g/10 min, density: 905 kg/m³). Cylindrical samples were produced with 6 mm in diameter and a height of 10 mm.

In-situ Wide Angle X-ray Scattering (WAXS) measurements during compression below the glass transition temperature were performed at the Synchrotron Light Source ELETTRA in Trieste, Italy (SAXS-Beamline 5.2L). Measurements were performed with a photon energy of 8 keV which corresponds to a wavelength of λ = 1.54 Å, close to CuKα radiation. The spot size on the sample was 500 μm×150 μm while measurements were performed in a transmission setup which ensured a large sample volume to be investigated. Diffraction patterns were recorded using a curved position sensitive detector of the type *INEL CPS-590*. In order to reach high degrees of deformation without cavitation, the sample was deformed by compression using a miniature compression machine mounted to the sample stage. After a WAXS pattern was recorded of the undeformed sample at a temperature of 24.8°C, the sample was cooled below its glass transition temperature of 0, to –5°C using an Oxford Cryostream Cooler. The sample was then deformed stepwise, still being at a temperature of –5°C, using a true strain rate of $\dot{e} = 10^{-3}$ s⁻¹ to different levels of strain up to a true plastic strain of $e = 0.8$. The deformation was stopped every time a X-ray diffraction pattern was recorded.

2.2. Multi-reflection X-ray profile analysis (MXPA)
The diffraction patterns were evaluated using the Multi-reflection X-ray profile analysis (MXPA) method which allows for a detailed analysis of diffraction profiles revealing parameters such as the

coherently scattering domain size (CSD-size, also called 'crystal size' in literature) and the density of dislocations [11–15]. A physical line profile of a Bragg reflection can be expressed by the convolution of the intensity profiles originating from the limited crystal size and by lattice strains, such as from dislocations. In Fourier space the contributions of size and strain can be well separated resulting in the Warren-Averbach equation (Equation (1)) [16]:

$$\ln A_L = \ln A_L^S + \ln A_L^D = \ln A_L^S + \exp(-2\pi^2 L^2 g^2 \langle \varepsilon_{g,L}^2 \rangle)$$

(1)

where A_L^S and A_L^D are the size and the distortion coefficients respectively, with the Fourier Length L. The distortion coefficient depends on the absolute value of the diffraction vector $K = 2\sin\theta/\lambda$, where $K = g$ at the exact Bragg-position and the mean square strain $\langle \varepsilon_{g,L}^2 \rangle$. The distortion coefficient is modeled under the assumption that the mean square strain originates from the strain field of dislocations [17], as shown by Equation (2):

$$\langle \varepsilon_{g,L}^2 \rangle = \frac{\rho \bar{C} b^2}{4\pi} \ln\left(\frac{R_e}{L}\right)$$

(2)

with the absolute value of the Burgers vector b, the dislocation density ρ and the effective outer cut-off radius of dislocations R_e. The peak broadening due to dislocations is taken into account by the average dislocation contrast factor $\bar{C}$ [17, 18], while the size coefficient is calculated assuming a lognormal size distribution of the crystals [12].

2.3. Evaluation of MXPA
Before the evaluation procedure, the background scattering and the α and γ-phase have been modeled by analytical functions using the program *fityk* [19] (Figure 1). Only the α-phase was used for the final evaluation using the programs *CMWP-fit* [12] and its extension *Multi-Eval* [20], since it could be shown that dislocations play only a minor role during the plastic deformation in the γ-phase [21]. Details of the evaluation procedure have already been described in a previous work [21], however it is noticed that the error bars in Figure 2 and 3 do not represent a physical error, but a numerical one indicating the reproducibility of the evaluation process.
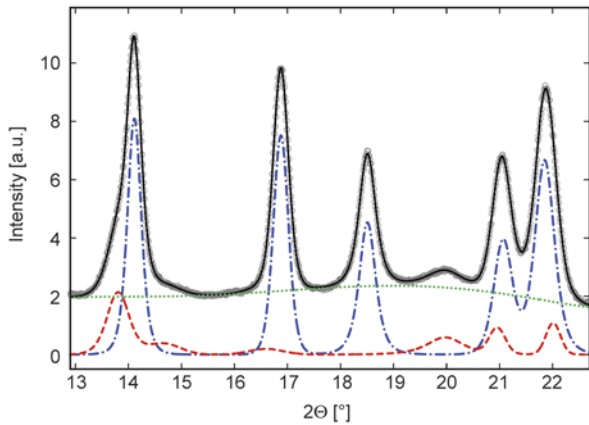
Figure 1. WAXS pattern of undeformed iPP below T_g. Measured data (o), fit (full line), α-phase (dash-dotted line), γ-phase (dashed line) and amorphous phase (dotted line).

Figure 3. The coherently scattering domain size (CSD-size) as a function of true strain. The black triangle indicates the CSD-size obtained for the unloaded sample at a temperature of 24.8°C before cooling below T_g. Some refinement of the undefected areas is found.

3. Results

At the beginning of in-situ compression below the glass transition temperature T_g, a yield stress of 120 MPa was observed in the true stress – true strain plot. This value is higher than the flow stress occurring during compression at room temperature mostly because of the increased stiffness of the amorphous phase.

The development of the dislocation density as a function of true strain is shown in Figure 2. In case of the room temperature experiment, the dislocation density increases markedly at a plastic strain of approximately 0.2 from initially $\rho = 0.5 \cdot 10^{15}$ to $\rho = 1.6 \cdot 10^{16}$ m^{-2}. In contrast to that, the change in dislocation density of the sample deformed below T_g is
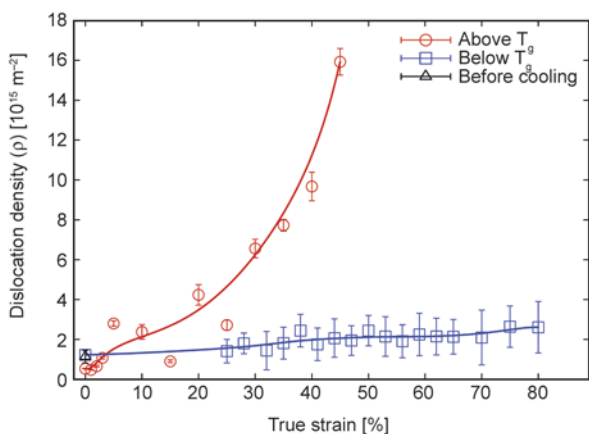

Figure 2. Development of the dislocation density of α-iPP at room temperature and below its glass transition. The black triangle indicates the dislocation density obtained for the unloaded sample at a temperature of 24.8°C before cooling below T_g.
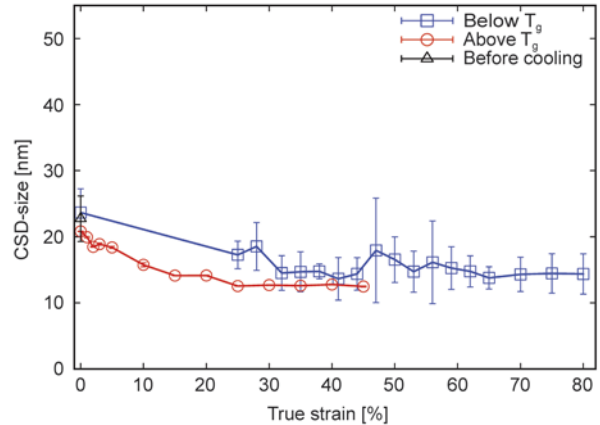
moderate: The dislocation density of initially $\rho = 1 \cdot 10^{15}$ m^{-2} increases slightly up to $\rho = 2.6 \cdot 10^{15}$ m^{-2}. In Figure 3, the development of the coherently scattering domain size (CSD-size) is depicted as a function of deformation. The CSD-size represents the smallest domain which scatters coherently. Assuming a cuboid like structure of the crystalline domains in the lamellae [10, 21, 22], the CSD-size can be related to the thickness of the lamellae. A decrease in the CSD-size can be seen at both deformation temperatures, from 20 to 12 nm for the sample deformed beyond T_g and from 23 to 14 nm for the deformation below T_g.

Crystallinity was found to decrease linearly from initially 66% to a value of 52% at a plastic deformation of $e = 0.8$ for the sample deformed below T_g and from 56 to 43% for the room temperature experiment as evaluated from X-ray diffractograms.

4. Discussion

Much experimental data are available in literature which confirm that deformation of polymer crystals operates via crystallographic slip [5, 6, 8, 23, 24]. In the case of α-iPP deformed at room temperature i.e. above the glass transition temperature T_g, crystal slip is facilitated by dislocation motion since an increasing number of dislocations are nucleated as deformation proceeds (Figure 2). The situation is markedly different when α-iPP is compressed at temperatures below its glass transition T_g where only a weak increase in dislocation density is observed pointing at another deformation mechanism being active.

Not at least due to the presence of tie molecules which connect the crystalline lamellar phase with the amorphous one, deformation occurs in each of the phases. Especially at deformations above T_g, the soft viscoelastic behavior of the amorphous phase provides additional degrees of freedom to the lamellar crystals. Here, for the deformation of the amorphous phase, three deformation modes can occur which are (i) interlamellar shear (ii) interlamellar separation and (iii) lamellae stack rotation [25–28]. During mechanism (i) the amorphous region between two crystals is exposed to shear with the shear direction being parallel to the lamellae. Interlamellar separation (ii) is characterized by a change in the spacing between two lamellae, and lamellae stack rotation (iii) causes a whole set of parallel lamellae to rotate as a unit.

In contrast, the plastic deformation of the crystalline phase in polypropylene can be the result of crystallographic slip processes [26], or twinning [29–31]. However, the slip process can accommodate also large amounts of deformation, and is thus quoted in most works to carry most of the plastic strain [26]. Crystallographic slip occurs first on the closest packed planes in the unit cell. During slip, two parts of a polymer crystal, separated by the slip plane undergo a relative translation against each other, which is achieved (at least in the actual case of α-iPP) by dislocation motion along the slip plane. However, dislocations only move if the force on the dislocation and as a consequence, the resolved shear stress τ reaches a critical value τ_0 (critical resolved shear stress) that is characteristic for the corresponding slip system.

The resolved shear stress for uniaxial tension or compression by a stress σ is given by $\tau = \sigma \cdot \cos\kappa \cdot \cos\varphi = m\sigma$ where κ and φ are the angles of the slip plane normal and the slip direction with respect to the uniaxial stress σ, respectively, and m is the Schmid-factor which can vary within 0 and 0.5. It is assumed that the preferred slip type especially at smaller deformations is chain slip, operating along the chain direction [32]. Slip transverse to the chain direction is known to be energetically less favored due to its higher τ_0 [33, 34].

At early stages of deformations above T_g, deformation primarily occurs in the amorphous phase by one or more of the possible deformation mechanisms discussed above, while the hard crystalline lamellae with ongoing deformation start to rotate

within the soft amorphous matrix [28]. When the slip planes are tilted with respect to the direction of the applied stress σ, the Schmid-factor changes accordingly leading to a change in the resolved shear stress. If τ_0 is reached due to chain orientation, more polymer crystals will experience crystallographic slip, accompanied by dislocation motion along the slip plane. With proceeding deformation, additional dislocations are generated to maintain the plastic flow, leading to an increase in the density of dislocations, especially exceeding a true strain of about 25% (Figure 2).

Below the glass transition temperature, however, the deformation of the amorphous phase, and thus, the rotation of polymer crystals are hindered. As a result, the lamellae are prohibited in rotating to a position where the Schmid-factor reaches a maximum, therefore less crystals undergo plastic slip which – in the actual material – means that markedly less dislocations are generated compared to the same material deformed at room temperature, above T_g. In such a purely crystallographic picture we can conclude that the amorphous phase is acting similarly to an additional slip system as for instance suggested by Nikolov and Raabe [35]. On a molecular scale, however, the nucleation of new dislocations is also related to molecular relaxations in the crystalline phase. Some authors have suggested thermally activated chain twist defects to be responsible for the nucleation of dislocations [36]. It is possible that the reduction of conformational degrees of freedom below T_g of polypropylene is also inhibiting the nucleation of such precursor defects for dislocations [36]. In this context a manuscript is in preparation studying the annihilation of dislocations in polypropylene as a function of molecular relaxation processes [Polt G, unpublished].

As a consequence of the starvation of dislocations for deformations below T_g, one can – independently of the underlying mechanism – expect that the deformation is accompanied by micro-cracking and or shear banding, and that the lamellae are deformed by fragmentation before crystallographic slip occurs. Such behavior was already observed in poly(3-hydroxybutyrate) (P3HB) where no increase in the dislocation density at larger strains could be found due to considerable crack formation and shear banding [9].

However, a reduction in CSD-size is seen in both experiments, below and above T_g (Figure 3). This

reduction is the result of any deformation that breaks the coherence in the crystal. If the misorientation exceeds an angle of 1.5° within the crystal, these two parts of the crystal will be registered as two separate domains by the MXPA method. Below T_g the primary deformation mechanism operating in the crystalline phase is bending of the lamellae involving the formation of geometrically necessary misfit dislocations [21], accompanied by only small amounts of crystallographic slip due to the hindered rotation of the lamellae, consequently leading to a continuous decrease in the domain size involving an only moderate increase in the dislocation density; the situation seems to be very similar to the plastic deformation of γ-modification of Polypropylene [21].

In case of the room temperature experiment (above T_g), it can be assumed that both mechanisms, i.e. bending of the lamellae including misfit dislocations, and crystallographic slip are operating simultaneously over the whole strain range. However, the distinct reduction in the CSD-size up to a true strain of 25% can primarily be attributed to misfit dislocations, operating simultaneously with crystallographic slip processes on slip planes with a low τ_0; namely chain slip planes with moving screw dislocations [26, 34].

Exceeding a true strain of about 25%, deformation by bending of the lamellae and therefore the decrease in the CSD-size becomes less dominant, while additional slip systems are being activated due to the higher resolved shear stress. The activation of additional transverse slip dislocations with edge character stimulates a pronounced increase of the dislocation density, in addition to the increasing number of screw dislocations in the chain slip system [34].

The decrease in crystallinity by 14% is most probably caused by the amorphization of the crystalline domains due to shear band formation and/or by lamellar fragmentation through micro-cracking.

5. Conclusions

α-phase polypropylene was plastically deformed below and above its glass transition temperature and has been observed in-situ by X-ray line profile analysis using synchrotron radiation.

The resulting microstructural parameters such as the size of the coherently scattering domains and the density of dislocations were evaluated as a function of deformation up to true strains of $e =0.8$. Significant differences in the development of the dislocation density were observed which can be explained as follows:

1) The distinct increase in the dislocation density *above* the glass transition temperature originates from crystallographic slip processes which are accompanied by dislocation generation and motion.

2) The less pronounced increase in dislocation density *below* the glass transition temperature results from the reduced ability of the polymer crystals to move and rotate in the amorphous matrix due to its increased stiffness in this temperature range. Therefore less slip systems reach the critical resolved shear stress, being necessary to initiate slip and/or the lamellae even undergo fragmentation without showing any crystallographic slip. However small amounts of dislocations are being created by geometrically necessary misfit dislocations accompanied by only small fractions of crystallographic slip. Crystalline deformation may operate via shear band formation also being accompanied by micro-cracking.

3) The decrease in the CSD-size observed in the present experiments at deformations below and above T_g most probably arises from bending of the lamellae leading to a misorientation within the crystal under the formation of geometrically necessary dislocations. However, exceeding a true strain of about 25% above T_g, the main deformation mechanism being active within the crystals changes to crystallographic slip. As a consequence, the CSD-size remains constant while a significant increase of the dislocation density is observed.

References

[1] Bartczak Z., Galeski A.: Plasticity of semicrystalline polymers. Macromolecular Symposia, **294**, 67–90 (2010).
DOI: 10.1002/masy.201050807

[2] Oleinik E. F.: Plasticity of semicrystalline flexible-chain polymers at the microscopic and mesoscopic levels. Polymer Science Series C, **45**, 17–117 (2003).

[3] Flory P. J., Yoon D. Y.: Molecular morphology in semicrystalline polymers. Nature, **272**, 226–229 (1978).
DOI: 10.1038/272226a0

[4] Young R.: A dislocation model for yield in polyethylene. A dislocation model for yield in polyethylene. Philosophical Magazine, **30**, 85–94 (1974).
DOI: 10.1080/14786439808206535

[5] Bartczak Z., Argon A. S., Cohen R. E.: Deformation mechanisms and plastic resistance in single-crystal-textured high-density polyethylene. Macromolecules, **25**, 5036–5053 (1992).
DOI: 10.1021/ma00045a034

[6] Gleiter H., Argon A. S.: Plastic deformation of polyethylene crystals. Philosophical Magazine, **24**, 71–80 (1971).
DOI: 10.1080/14786437108216425

[7] Séguéla R.: Plasticity of semi-crystalline polymers: Crystal slip versus melting-recrystallization. E-polymers, **7**, 382–401 (2007).
DOI: 10.1515/epoly.2007.7.1.382

[8] Wilhelm H., Paris A., Schafler E., Bernstorff S., Bonarski J., Ungar T., Zehetbauer M. J.: Evidence of dislocations in melt-crystallised and plastically deformed polypropylene. Materials Science and Engineering: A, **387–389**, 1018–1022 (2004).
DOI: 10.1016/j.msea.2004.03.099

[9] Spieckermann F., Polt G., Wilhelm H., Kerber M., Schafler E., Zehetbauer M. J.: The role of dislocations for the plastic deformation of semicrystalline polymers as investigated by multireflection X-ray line profile analysis. Journal of Applied Polymer Science, **125**, 4150–4154 (2012).
DOI: 10.1002/app.36570

[10] Spieckermann F., Wilhelm H., Kerber M., Schafler E., Polt G., Bernstorff S., Addiego F., Zehetbauer M.: Determination of lamella thickness distributions in isotactic polypropylene by X-ray line profile analysis. Polymer, **51**, 4195–4199 (2010).
DOI: 10.1016/j.polymer.2010.07.009

[11] Ribárik G.: Modelling of diffraction patterns based on microstructural properties. PhD Thesis, Eötvös Loránd University (2008).

[12] Ribárik G., Ungár T., Gubicza J.: *MWP*-fit: A program for multiple whole-profile fitting of diffraction peak profiles by *ab initio* theoretical functions. Journal of Applied Crystallography, **34**, 669–676 (2001).
DOI: 10.1107/S0021889801011451

[13] Ungár T., Borbély A.: The effect of dislocation contrast on X-ray line broadening: A new approach to line profile analysis. Applied Physics Letters, **69**, 3173–3175 (1996).
DOI: 10.1063/1.117951

[14] Kerber M. B., Zehetbauer M. J., Schafler E., Spieckermann F., Bernstorff S., Ungar T.: X-ray Line profile analysis – An ideal tool to quantify structural parameters of nanomaterials. Journal of the Minerals, Metals and Materials Society, **63**, 61–70 (2011).
DOI: 10.1007/s11837-011-0115-1

[15] Schafler E., Zehetbauer M.: Characterization of nanostructured materials by X-ray line profile analysis. Reviews on Advanced Materials Science, **10**, 28–33 (2005).

[16] Warren B. E., Averbach B. L.: The effect of cold-work distortion on X-ray patterns. Journal of Applied Physics, **21**, 595–599 (1950).
DOI: 10.1063/1.1699713

[17] Wilkens M.: The determination of density and distribution of dislocations in deformed single crystals from broadened X-ray diffraction profiles. Physica Status Solidi (a), **2**, 359–370 (1970).
DOI: 10.1002/pssa.19700020224

[18] Krivoglaz M.: Theory of X-ray and thermal neutron scattering by real crystals. Plenum Press, New York (1969).

[19] Wojdyr M.: Fityk: A general-purpose peak fitting program. Journal of Applied Crystallography, **43**, 1126–1128 (2010).
DOI: 10.1107/S0021889810030499

[20] Kerber M.: X-ray line profile analysis in theory and experiment. PhD Thesis, University of Vienna (2012).

[21] Polt G., Spieckermann F., Wilhelm H., Kerber M., Schafler E., Bernstorff S., Zehetbauer M.: The role of dislocations in γ-iPP under plastic deformation investigated by X-ray line profile analysis. Mechanics of Materials, **67**, 126–132 (2013).
DOI: 10.1016/j.mechmat.2013.05.010

[22] Baltá-Calleja F., Cruz C., Bayer R., Kilian H.: Microhardness and surface free energy in linear polyethylene: The role of entanglements. Colloid and Polymer Science, **268**, 440–446 (1990).
DOI: 10.1007/BF01411002

[23] Seguela R., Staniek E., Escaig B., Fillon B.: Plastic deformation of polypropylene in relation to crystalline structure. Journal of Applied Polymer Science, **71**, 1873–1885 (1999).
DOI: 10.1002/(SICI)1097-4628(19990314)71:11<1873 ::AID-APP18>3.0.CO;2-I

[24] Bartczak Z., Galeski A.: Yield and plastic resistance of α-crystals of isotactic polypropylene. Polymer, **40**, 3677–3684 (1999).
DOI: 10.1016/S0032-3861(98)00614-4

[25] Phillips A., Zhu P-W., Edward G.: Simple shear deformation of polypropylene *via* the equal channel angular extrusion process. Macromolecules, **39**, 5796–5803 (2006).
DOI: 10.1021/ma0607618

[26] Galeski A.: Strength and toughness of crystalline polymer systems. Progress in Polymer Science, **28**, 1643–1699 (2003).
DOI: 10.1016/j.progpolymsci.2003.09.003

[27] Lin L., Argon A. S.: Structure and plastic deformation of polyethylene. Journal of Materials Science, **29**, 294–323 (1994).
DOI: 10.1007/BF01162485

[28] Hirsch J. R., Wang P. T.: Texture and strength evolution in deformed polypropylene. Textures and Microstructures, **13**, 101–122 (1994).
DOI: 10.1155/TSM.13.101

[29] Kojima M.: Morphology of polypropylene crystals. II. Twinning of lamellar crystals. Journal of Polymer Science Part A 2: Polymer Physics, **5**, 615–622 (1967).
DOI: 10.1002/pol.1967.160050317

[30] Hibi S., Niwa T., Mizukami J., Wang C., Kyu T.: Crystal orientation and twinning in cold-rolled ultrahigh molecular weight polypropylene. Polymer Engineering and Science, **35**, 911–920 (1995).
DOI: 10.1002/pen.760351105

[31] Bassett D. C., Olley R. H.: On the lamellar morphology of isotactic polypropylene spherulites. Polymer, **25**, 935–943 (1984).
DOI: 10.1016/0032-3861(84)90076-4

[32] Jia J., Raabe D.: Evolution of crystallinity and of crystallographic orientation in isotactic polypropylene during rolling and heat treatment. European Polymer Journal, **42**, 1755–1766 (2006).
DOI: 10.1016/j.eurpolymj.2006.02.013

[33] Bartczak Z., Martuscelli E.: Orientation and properties of sequentially drawn films of an isotactic polypropylene/ hydrogenated oligocyclopentadiene blend. Polymer, **38**, 4139–4149 (1997).
DOI: 10.1016/S0032-3861(96)00996-2

[34] Spieckermann F.: Investigation of deformation induced changes of the microstructure of semicrystalline polymers and their impact on mechanical properties. PhD Thesis, University of Vienna (2010).

[35] Nikolov S., Raabe D.: Yielding of polyethylene through propagation of chain twist defects: Temperature, stem length and strain-rate dependence. Polymer, **47**, 1696–1703 (2006).
DOI: 10.1016/j.polymer.2005.12.050

[36] Boyd R. H.: Relaxation processes in crystalline polymers: Molecular interpretation – A review. Polymer, **26**, 1123–1133 (1985).
DOI: 10.1016/0032-3861(85)90240-X

Influence of the presence of medium-soft paraffin wax on the morphology and properties of iPP/silver nanocomposites

M. P. Molaba[1], D. Dudić[1,2], A. S. Luyt[1,3]*

[1]Department of Chemistry, University of the Free State, Private Bag X13, 9866 Phuthaditjhaba, South Africa
[2]Vinča Institute of Nuclear Sciences, University of Belgrade, P.O. Box 522, 11001 Belgrade, Serbia
[3]Current address: Center for Advanced Materials, Qatar University, PO Box 2713, Doha, Qatar

Abstract. The aim of this study was to investigate the presence of wax, different Ag nanoparticle contents, and different cooling rates from the melt, on the morphology, thermal and electrical conductivity, and dynamic mechanical properties of iPP. The Ag particles were well dispersed in the polymer, and formed nucleation centres for the crystallization of iPP. They were also well dispersed in iPP/wax, but they were located in the wax phase which was dispersed between the iPP spherulites. Generally the extent of filler agglomeration increased with increasing filler content. The Ag particles, whether in the iPP or wax phase, had little influence on the crystallinities and melting temperatures of iPP. The presence of Ag particles in iPP had little influence on its modulus, but the presence of both wax and Ag particles significantly improved the modulus of these nanocomposites. The thermal and electrical conductivities of the samples more significantly improved when both wax and Ag were present. With increasing Ag particle contents in both iPP/Ag and iPP/wax/Ag, the thermal conductivities increased, but leveled off at higher filler contents, while the electrical conductivities continuously increased with increasing filler contents. The slowly cooled samples had higher crystallinities than the quenched samples and therefore they were more thermally conductive than the quenched samples.

Keywords: nanocomposites, isotactic polypropylene, paraffin wax, morphology, conductivity

1. Introduction

Paraffin waxes can be used as organic phase-change materials (PCM) for thermal energy storage. This is because they are more chemically stable than inorganic substances, have a high latent heat of fusion, are commercially available at a reasonable cost, and exhibit little or no supercooling [1–3]. However, when used as PCMs, paraffin waxes need a supporting material to prevent their leakage during the phase-change process. Blending of PCMs with polyolefins has been commonly used as a method of preventing the leakage of phase-change materials. In blending, the polymer fixes the PCM in a compact shape during the phase-change process, and hence prevents leakage [4].

However, if polyolefins are used as the fixing polymers, both the polymer and the paraffin wax have low thermal conductivity which results in a slow heat transfer [5, 6]. The introduction of conductive nano-fillers has been used as a method for improving the thermal conductivity of PCMs. This is because they offer improved properties at relatively low filler content due to their larger surface areas [7]. These nano-fillers include aluminum, silver, copper, graphite and carbon black [8]. For this work we chose silver because it has very good electrical and thermal conductivies [9].

The morphology, as well as thermal and thermomechanical properties, of polyethylene (PE)/wax/wood flour composites were investigated in a few studies

---

[10–12]. Generally the authors observed two phase morphologies with the filler covered by wax. These studies reported two endothermic peaks for the composites related to the melting of the wax and the polymer. It was found that the presence, type and amount of the filler particles did not change the melting behaviour of PE or wax in the composites. A limited amount of research has been done on the dynamic mechanical properties of polymer/wax blend composites [11, 13]. When expanded graphite was used as filler, an increase in storage modulus was observed with an increase in filler content, which was an indication that the filler reinforced the matrix and countered the softening effect of the wax [13]. No specific trends related to the amount of filler particles were observed. However, the presence of wood filler particles in the polymer/wax blends reduced the storage modulus [11].

The thermal conductivity of form-stable PCM composites was investigated in a number of studies [5, 12–15]. An increase in the thermal conductivity of the composites with increasing filler content was observed, as well as the formation of thermally conductive paths. However, one of the papers [12] reported an initial decrease in thermal conductivity at low filler contents, which increased at higher filler loadings. This was attributed to the voids that formed at the interface between the polymer and the wax.

In this paper we report on the dispersion of Ag particles in iPP and an iPP/wax blend and the influence of quenching and slow cooling treatments on the morphology, thermal and dynamic mechanical properties, as well as thermal and electrical conductivities, in order to obtain more information on how the presence of wax, as well as different thermal treatments, will influence the morphology and related thermal, mechanical and conductivity properties of isotactic polypropylene.

2. Materials and methods
2.1. Materials
Isotactic polypropylene with a melt flow index of 12 g/10 min (230°C/2.16 kg), density of 0.9 g·cm^{-3} and melting point of ~160°C was supplied by Sasol Polymers in South Africa. Medium-soft paraffin wax (M3 wax) was supplied in powder form by Sasol Wax in South Africa. It consists of approximately 99% of straight chain hydrocarbons with a few branched chains. It has an average molar mass of 440 g·mol^{-1} and a carbon distribution between C15 and C78. Its density is 0.90 g·cm^{-3} and it has a melting point range around 40–60°C. The 99.99% pure silver (Ag) nanoparticles with particle size 30–50 nm was supplied by Dong Yang (HK) Int'l Group Ltd in China.

2.2. Composite preparation
All the samples were prepared by melt mixing using a Brabender Plastograph with a 55 mL internal mixer. The samples were mixed for 15 min at 190°C and 50 rpm. The dry Ag powder was ultra-sonicated for 6 hours prior to the sample preparation. For the blends, the components were premixed and then fed into the heated mixer, whereas for the composites the Ag nanoparticles were added into the Brabender mixer 5 minutes after premixing the iPP/wax blends. The samples were then melt pressed at 190°C for 5 minutes under 50 kPa using a hydraulic melt press. The prepared samples were then exposed to two thermal treatments, either quenching in ice water or slow cooling from the melt at 190°C to a temperature of 100°C.

2.3. Characterization techniques
For transmission electron microscopy (TEM) analysis the samples were sectioned at 150 nm using a Leica UC7 (Viennna, Austria) ultramicrotome, and examined with a Philips (FEI) (Eindhoven, The Netherlands) CM 100 transmission electron microscope at 60 keV.

The DSC analyses were done using a Perkin-Elmer DSC 7 differential scanning calorimeter under a nitrogen flow of 20 mL·min^{-1}. Samples with masses of 5–10 mg in aluminium pans were heated from 20 to 180°C at 20°C·min^{-1}, and cooled at the same rate. The peak temperatures of melting and crystallization, as well as the melting and crystallization enthalpies, were determined from the first heating and the cooling scans. Three samples of each composition were analysed, and the melting and crystallization values are reported as averages with standard deviations.

The dynamic mechanical properties of the samples were investigated using a Perkin Elmer Diamond DMA. The analyses were performed from –40 to 140°C in bending (dual cantilever) mode at a heating rate of 3°C·min^{-1} and a frequency of 1 Hz.

The thermal conductivities were measured using a Therm Test Inc. Hot Disk TPS 500 thermal constant analyzer. The hot disk sensor used in this study was

a Kapton sensor with a radius of 3.2 mm and samples with 10 mm thickness and a diameter of 13 mm were used for the analyses. The sensor was placed between two samples of the same composition. The measurements were done for 20 s in order to prevent the heat flow from reaching the boundary of the samples. All the measurements were repeated ten times for each sample. The thermal conductivities are reported as average values with standard deviations.

For the dielectric measurements the samples were cut from the centre of the melt-pressed sheets in the form of discs ($D = 13$ mm, $d = 1$ mm). The surfaces of the samples were made conductive using soft graphite. Dielectric measurements were done using Agilent 4263B and Agilent 4285A dielectric spectroscopy instruments in the frequency range between 1 kHz and 17 MHz at room temperature, and with an applied voltage of 1 V. Conductance (G) and susceptance (B) were measured using the Cp mode of the instrument, and the admittance (Y) was calculated as $Y = \sqrt{B^2 + G^2}$. The following relations were derived: $\tan\delta = G/B$ and $B = 2\pi f C$, where f is the frequency and C is the capacitance, and $C = \varepsilon' \varepsilon_0 S/d$, where ε' is the real part of the dielectric permittivity, ε_0 the vacuum permittivity and S/d describing the geometry of the samples ($S = \pi D^2/4$). DC measurements were done using a Keithley 2401 amperometer during 10 s of electric field application at 200 V·mm^{-1}. All the electrical conductivities (σ_{DC}, Y, G and B) are presented as their specific values calculated as $\sigma = \sigma_{measured} \cdot d/S$, where d/S is the geometry factor of the samples (S = surface area and d = thickness).

3. Results and discussion
3.1. Transmission electron microscopy (TEM)
Figure 1 shows the TEM images of some of the investigated nanocomposites that were slowly cooled from the melt. The TEM image of the iPP/Ag nanocomposite containing 2 wt% nanoparticles shows iPP spherulites containing Ag nanoparticles at their growth centres (Figure 1a, arrow A). It looks as if primary nucleation could have started at the nanoparticles that formed nucleation centres from which the spherulitic growth evolved [16]. Ag nanoparticles and their agglomerates (with diameters ranging from 0.09 to 1.15 μm) can also be seen on the edges of the iPP spherulites, and they are fairly well dispersed. However, at a higher Ag content (Figure 1b)

there are fewer individual Ag particles and more of the filler aggregates (with diameters ranging from 0.12 to 3.11 μm). The nanoparticles have a tendency of forming aggregates because they have a higher affinity for each other than for the matrix. The melt-blending used to prepare the samples was also not very effective in breaking up these aggregates.

Although the wax could not be distinguished in the TEM photos of the iPP/wax nanocomposites (Figure 1c), we assumed that most of the wax crystallized separately in the areas between the iPP spherulites, because it has been established previously that the wax co-crystallizes with iPP only at very low wax contents [17]. This separate crystallization of the wax can be expected because iPP crystallizes before the wax. The presence of molten wax during the crystallization must have influenced the crystal growth of the iPP, because the spherulites in Figure 1c are smaller and somewhat differently structured from the spherulites in Figure 1a. Individual Ag nanoparticles and some aggregates (with diameters ranging from 0.11 to 1.53 μm) are observed in Figure 1c. These nanoparticles are only dispersed in between the spherulites (arrow B), with none visible at the growth centres of the spherulites. It looks as if the nanoparticles had a higher affinity for the wax, and therefore remained in the molten wax phase during the crystallization of iPP. They were then trapped in the wax phase after wax crystallization. At higher Ag content the filler particles (with diameters ranging from 0.11 to 1.72 μm) were not well dispersed, and the extent of agglomeration increased (Figure 1d), although it was still lower than in the case of 95/5 w/w iPP/Ag (compare Figures 1b and 1d). Nanoparticles are also visible at the growth centres of the iPP spherulites (arrow C).

3.2. Differential scanning calorimetry (DSC)
The DSC curves of the iPP/wax blends are not presented, but the samples with 5 wt% wax showed a single melting peak which is associated with the melting of the iPP crystals. This indicates that the wax and iPP are probably miscible in the molten state, and could have co-crystallized at such a low wax content, although it is quite possible that individual wax chains and very small wax crystals (too small and dispersed to show visible heat flow changes during melting) were trapped in the amorphous part of iPP. However, when the wax content was 10 wt% and more, two separate melting peaks were visible.
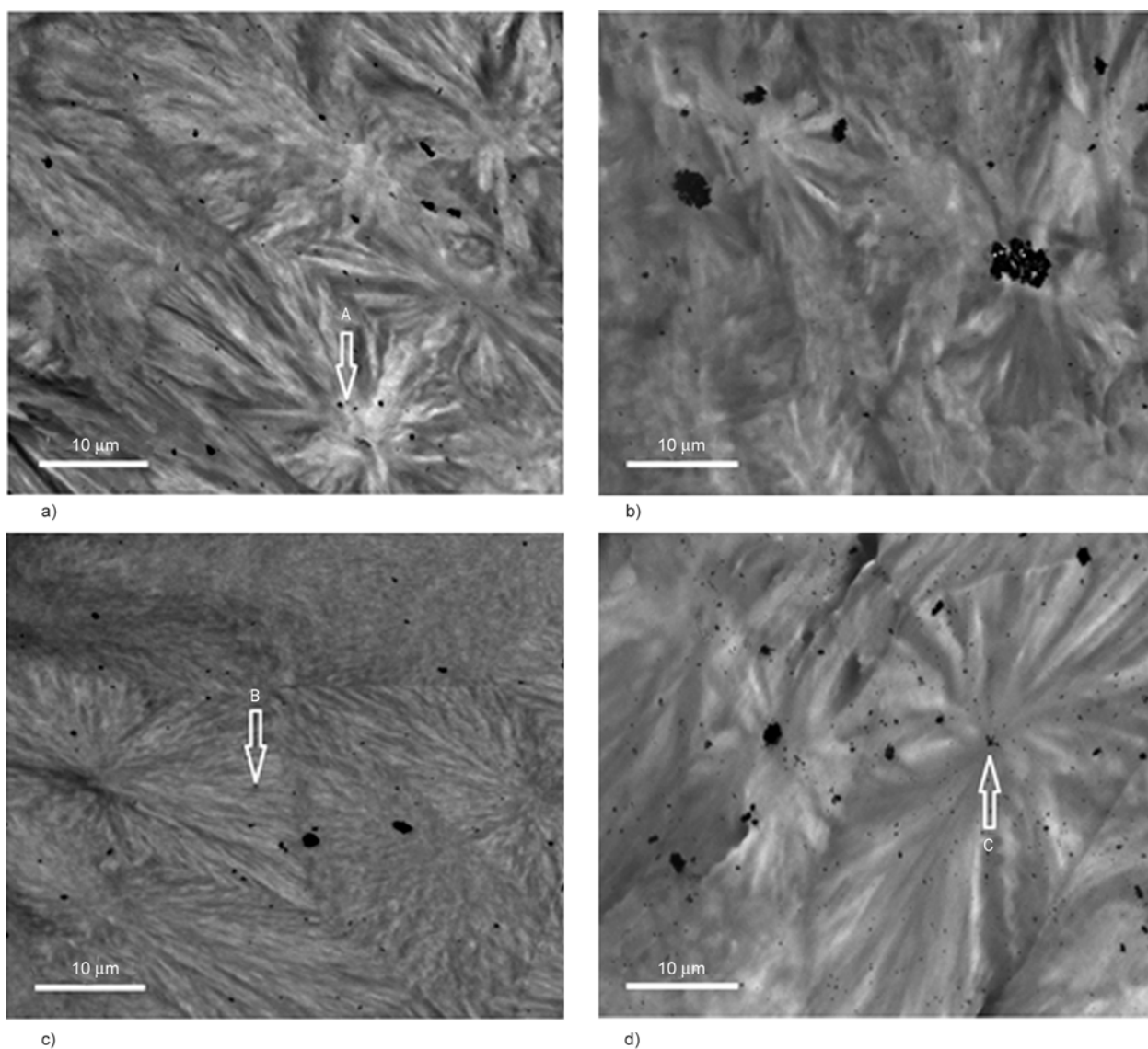
Figure 1. TEM images of (a) 98/2 w/w iPP/Ag, (b) 95/5 w/w iPP/Ag, (c) 88/10/2 w/w iPP/Wax/Ag, and (d) 85/10/5 w/w iPP/Wax/Ag slowly cooled from the melt

These were associated with the melting of wax and iPP crystals, respectively. This was observed in both the slowly cooled and quenched samples. The observed behaviour indicates the (partial) immiscibility of the blend components, and most of the wax crystallized separately from the iPP. Moreover, the melting peaks corresponding to the melting of iPP crystals shifted to lower temperatures with an increase in wax content. Other authors attributed this to the plasticization effect of the paraffin wax [17, 18].

At lower wax contents, the normalised melting enthalpies of the wax component are lower than that of pure wax (Table 1). However, at 20% wax content, they are comparable to that of pure wax. This is probably because the individual wax chains or very small crystals were trapped in the amorphous phase of iPP, or co-crystallized with iPP chains, at low wax content and as a result only a small portion of the wax crystallized separately into sizable crystals. However, at a higher content, more wax crystallized separately from iPP. The normalized melting enthalpies of the iPP component increased with an increase in wax content (Table 1). This confirms the co-crystallization of some of the wax with iPP giving rise to the higher melting enthalpy of iPP. The normalised melting enthalpies of the iPP component in the slowly cooled blends are higher than that in the comparable blends quenched from the melt. This is attributed to the higher crystallinity of the blends slowly cooled from the melt. In the slow cooling process there is enough time for the crystals to form, whereas faster cooling such as quenching reduces the time for crystal nucleation and growth [19].

Table 1. DSC melting and crystallization parameters of the investigated samples

Sample [w/w]	T_m [°C]		ΔH_m [J·g⁻¹]		ΔH_m^n [J·g⁻¹]		T_c [°C]	
	Quenched	Slowly cooled	Quenched	Slowly cooled	Quenched	Slowly cooled	Quenched	Slowly cooled
iPP	163.7±0.6	163.9±1.1	79.3±6.7	100.0±5.1	–	–	104.6±0.8	102.1±1.2
Wax	60.7±0.4	60.7±0.4	137.5±7.6	137.5±7.6	–	–	43.2±0.8	43.2±0.8
iPP/wax								
95/5 iPP/wax	161.0[b]±0.6	160.8[b]±0.2	81.3[b]±3.5	96.9[b]±2.2	85.6[b]	102.0[b]	107.2[b]±0.3	99.7[b]±0.6
90/10 iPP/wax	59.3[a]±0.8 / 161.1[b]±0.4	55.0[a]±0.3 / 161.0[b]±1.0	5.9[a]±3.6 / 83.5[b]±3.7	6.9[a]±0.7 / 86.0[b]±3.0	59.0[a] / 92.8[b]	69.0 / 95.6	43.7[a]±0.3 / 103.2[b]±0.3	42.2[a]±0.3 / 102.2[b]±4.9
80/20 iPP/wax	56.6[a]±3.2 / 158.2[b]±0.8	59.7[a]±3.2 / 157.3[b]±1.9	12.0[a]±1.8 / 82.2[b]±3.2	17.6[a]±6.1 / 100.2[b]±5.3	120.0[a] / 102.8[b]	176.0[a] / 125.3[b]	41.6[a]±0.3 / 99.4[b]±3.5	40.9[a]±0.5 / 97.2[b]±0.8
iPP/wax/Ag								
88/10/2 iPP/wax/Ag	51.0[a]±0.4 / 160.2[b]±0.2	55.3[a]±0.3 / 166.2[b]±1.4	1.7[a]±0.2 / 74.1[b]±3.1	6.0[a]±0.2 / 92.8[b]±1.7	17.0[a] / 84.2[b]	60.0[a] / 105.5[b]	45.2[a]±0.6 / 105.6[b]±0.3	42.6[a]±0.3 / 100.1[b]±0.3
87/10/3 iPP/wax/Ag	51.6[a]±0.2 / 161.9[b]±0.2	53.7[a]±0.9 / 162.1[b]±0.7	4.3[a]±0.3 / 71.7[b]±1.0	4.4[a]±0.9 / 83.8[b]±4.3	43.0[a] / 82.4[b]	44.0[a] / 96.3[b]	43.1[a]±0.3 / 98.9[b]±0.5	43.4[a]±0.5 / 100.4[b]±1.1
86/10/4 iPP/wax/Ag	54.9[a]±2.8 / 162.5[b]±0.9	54.0[a]±1.2 / 162.1[b]±0.7	3.4[a]±1.3 / 72.5[b]±8.0	5.4[a]±2.0 / 82.5[b]±3.4	34.0[a] / 84.3[b]	54.0[a] / 95.9[b]	43.1[a]±0.3 / 100.9[b]±0.9	42.2[a]±0.3 / 100.1[b]±0.3
85/10/5 iPP/wax/Ag	54.8[a]±1.6 / 162.0[b]±0.1	53.1[a]±0.7 / 160.5[b]±0.7	3.8[a]±0.5 / 69.4[b]±1.3	4.4[a]±1.0 / 83.4[b]±3.9	38.0[a] / 81.6[b]	44.0[a] / 98.1[b]	44.1[a]±0.3 / 101.9[b]±0.5	44.2[a]±0.3 / 101.9[b]±0.5
iPP/Ag								
98/2 iPP/Ag	165.0±0.5	165.3±0.7	79.6±1.6	97.2±2.9	81.2	99.2	106.7±0.8	104.2±0.3
97/3 iPP/Ag	165.3±0.4	165.3±0.7	73.7±5.8	95.0±3.0	76.0	97.9	107.7±0.3	106.7±0.6
96/4 iPP/Ag	167.3±1.9	165.8±1.2	75.1±2.0	95.0±3.2	78.2	99.0	107.9±0.9	108.1±0.3
95/5 iPP/Ag	165.6±0.7	167.1±1.4	73.3±2.6	89.9±2.7	77.2	94.6	107.4±0.5	106.6±0.3

T_m – melting peak temperature, T_c – crystallization peak temperature, ΔH_m – melting enthalpy normalised with respect to the wax and PP contents in the respective samples
[a]Melting/crystallization of wax
[b]Melting/crystallization of PP

Both the slowly cooled and quenched iPP/wax/Ag nanocomposites containing 10 wt% wax showed two separate melting peaks associated with the melting of wax and iPP crystals. There are no significant changes in the melting temperatures and normalised enthalpies of the iPP component with an increase in Ag content for both the quenched and slowly cooled samples (Table 1). This indicates that the presence of Ag nanoparticles had little influence on the crystallite sizes and mobility of the polymer chains. However, if the normalized enthalpies of the quenched and slowly cooled samples are compared, it is clear that the melting enthalpies of the slowly cooled samples are higher than those of the quenched samples. This is the result of the higher crystallinity of the slowly cooled samples. The crystallization and melting temperatures of the quenched and slowly cooled iPP/wax blends and iPP/wax/Ag blend composites are very similar within experimental error, although the values are slightly lower at higher wax content for the iPP/wax blends (Table 1). Wax normally acts as a plasticizer by enhancing the mobility of the polymer chains, leading to lower crystallization and melting temperatures. However, when Ag nanoparticles are present, they can act as nucleating sites for the crystallization of iPP, and this will give rise to higher crystallization and melting temperatures. It therefore seems as if the opposing effects of wax and Ag on iPP crystallization balance each other in the iPP/wax/Ag blend composites, which causes the crystallization and melting temperatures of iPP to remain unchanged.

Both the quenched and slowly cooled iPP/Ag nanocomposites showed a single melting peak associated with the melting of the PP crystals. There are no significant differences between the enthalpies of iPP in the iPP/Ag nanocomposites and that of pure iPP for both the quenched and slowly cooled samples (Table 1). However, the melting and crystallization temperatures are slightly higher than that of pure iPP. It is clear from this observation that the presence of Ag nanoparticles reduces the iPP chain mobility, as already mentioned before. The melting enthalpies of the slowly cooled composites are higher than those of the comparable composites quenched from the melt. The reason for this has already been discussed.

3.3. Dynamic mechanical analysis (DMA)

The storage modulus curve of iPP in Figure 2a shows a minimum at about 70°C, which is not visible in Figure 2b. This is the result of the re-crystallization of the quenched sample during the relatively slow heating in the DMA instrument. The minima observed for the other samples are related to re-crystallization effects or to the melting of the wax in the blends and composites. The storage modulus of the quenched iPP shown in Figure 2a increases with the addition of 10 wt% wax. This is attributed to the increase in crystallinity because of the much higher crystallinity of the wax. However, the storage modulus of the iPP/Ag nanocomposite changed very little compared to that of pure iPP, which indicates that the nanoparticle content was too small and the interaction with the polymer was too weak to significantly influence the polymer stiffness. When both wax and Ag are present, the storage modulus of the nanocomposites is very similar to that of the iPP/wax sample. This confirms that the highly crystalline wax provided more stiffness to the sample, while the small amount of Ag had very little influence.

In the slowly cooled samples, the storage modulus of the iPP/wax samples is significantly lower than that of iPP (Figure 2b). This can be attributed to a decrease in iPP crystallinity, or to a softening effect of the much softer wax. If one looks at the values in Table 1, it is clear that the normalised melting enthalpy of iPP in the 90/10 w/w iPP/wax sample is slightly lower than that of pure iPP, although very similar within experimental error. It is therefore doubtful that the decrease in storage modulus is the result of lower iPP crystallinity.

When comparing the storage modulus of the iPP/Ag sample with that of iPP and iPP/wax, it can be seen that it is lower than that of iPP, but higher than that of iPP/wax. According to Table 1 the melting enthalpies of iPP and iPP in iPP/wax and iPP/Ag are very similar, so the differences in their storage moduli cannot be the result of differences in iPP crystallinity. It has been reported previously that the nanoparticles can have a plasticizing effect on a polymer [20], and therefore the lower storage modulus in the case of iPP/Ag is probably the result of such a plasticizing effect. The storage modulus is the lowest when both wax and Ag are present. Again the melting enthalpy of iPP in iPP/wax/Ag is not much different from that of pure iPP (Table 1), and therefore the reduction in storage modulus cannot be the result of a change in crystallinity. It is expected that there will be a very weak interaction between iPP and wax, while it seems as if there is a strong interaction between wax and Ag (section 3.1). The wax-covered Ag particles will then increase the free volume in the sample, which will give rise to higher iPP chain mobility in the amorphous phase and reduced stiffness.

The $\tan\delta$ curves in Figure 3a show that the quenched iPP has two relaxation peaks associated with the β- and α-relaxations, respectively at about 10 and 70°C. The β-relaxation is usually associated with motions within the amorphous regions during the glass transition, and the α-relaxation is related to the crystalline phase of the polymer [19]. When wax was present, an additional peak appeared at about 60°C, which is associated with the wax melting. The β-peak of the iPP/wax sample looks very similar to that of pure iPP, and appears at about the same tem-
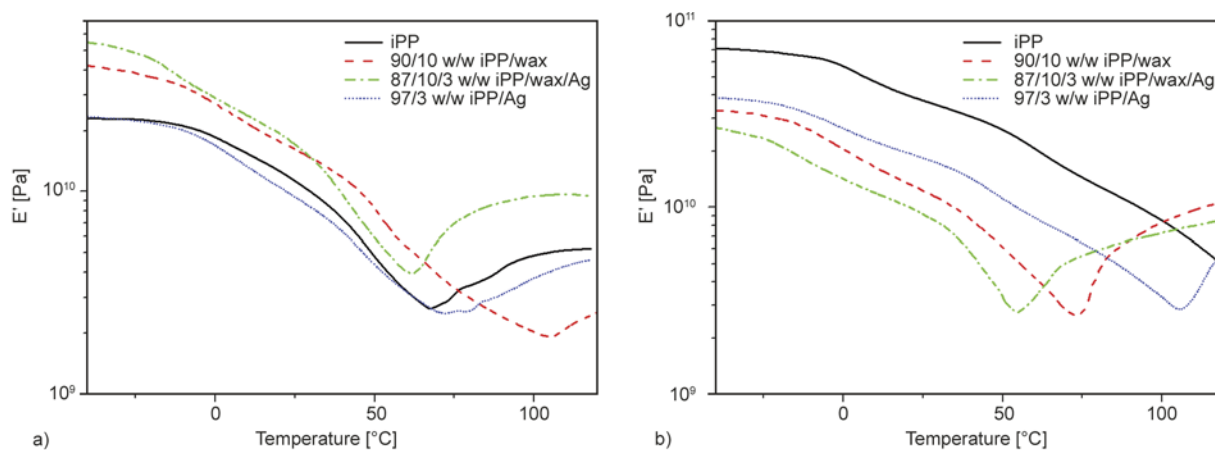

Figure 2. Storage modulus as a function of temperature of iPP, iPP/wax, iPP/Ag and iPP/wax/Ag samples (a) quenched and (b) slowly cooled from the melt
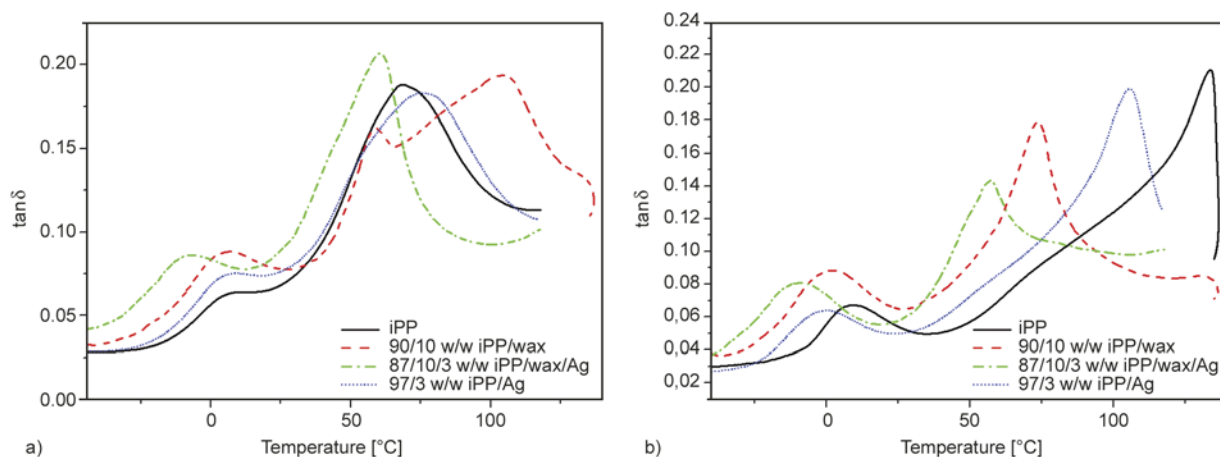
Figure 3. Loss factor as a function of temperature of iPP, iPP/wax, iPP/Ag and iPP/wax/Ag nanocomposites (a) quenched and (b) slowly cooled from the melt

perature, while the α-peak moved to higher temperatures. This indicates that the highly crystalline wax did not influence the iPP chain mobility in the amorphous phase, but in some way influenced the crystalline phase of iPP. According to Table 1 the normalised melting enthalpy of iPP in the blend is higher than that of the pure iPP, which could explain the increase in the α-transition temperature if one assumes some co-crystallization of the wax with iPP. The iPP/Ag sample also shows two relaxation peaks associated with the β- and α-relaxations. The temperature of the β-peak is very similar to that of iPP, but the α-peak appeared at a slightly higher temperature. This can be attributed to the dispersion of the Ag particles in the inter-crystalline amorphous areas of the iPP, and therefore they will have an immobilizing effect on these chain segments. However, in the presence of both Ag and wax, only the β-relaxation and the wax melting peaks are visible. The α-peak is not visible in the investigated temperature range. The β-peak appeared at an observably lower temperature and the wax melting is much more prominent than that of the iPP/wax blend. It is expected that there will be a weak interaction between iPP and wax, while there is a stronger interaction between wax and Ag. The wax-covered Ag particles will then increase the free volume in the sample, which will give rise to higher iPP chain mobility in the amorphous phase, leading to lower T_g values. It is not clear why the α-peak has disappeared, unless it has moved to an even higher temperature outside our analysis range.

The slowly cooled iPP has two relaxation peaks associated with the β- and α-relaxations at about 10 and 130°C (Figure 3b). When wax is present there

are also two relaxation peaks, respectively associated with the glass transition and wax melting. The α-peak is not visible in the investigated temperature range, probably because wax has crystallized in the inter-crystalline amorphous regions of iPP, and as a result reduced the mobility of these chain segments. The β-peak of the iPP/wax sample is at a lower temperature than that of the pure iPP, which can be attributed to the increase in free volume because of the relatively weak interaction between iPP and wax, which gives rise to higher iPP chain mobility in the amorphous phase. The iPP/Ag nanocomposites also have two relaxation peaks associated with the β- and α-transitions. In this case both the β- and α-peaks appear at lower temperatures than those of pure iPP. This is an indication that Ag particles to some extent have plasticized iPP, giving rise to an increase in iPP chain mobility in the amorphous phase [20]. The decrease in the α-transition temperature must be related to the presence of the Ag particles in the inter-crystalline amorphous areas of iPP. It is, however, not clear exactly how these particles influenced the relaxation of the chains in these areas, since for the quenched samples the temperature of this transition increased. When both wax and Ag were present, the observation is similar to that of the quenched sample, and the explanation will be the same.

Figure 4 compares the storage modulus curves of the quenched and slowly cooled samples. The storage modulus of the slowly cooled iPP and iPP/Ag nanocomposites is much higher than that of the quenched samples (Figures 4a and 4b). This is attributed to the higher crystallinity of the slowly cooled samples, as can be seen from the higher normalised
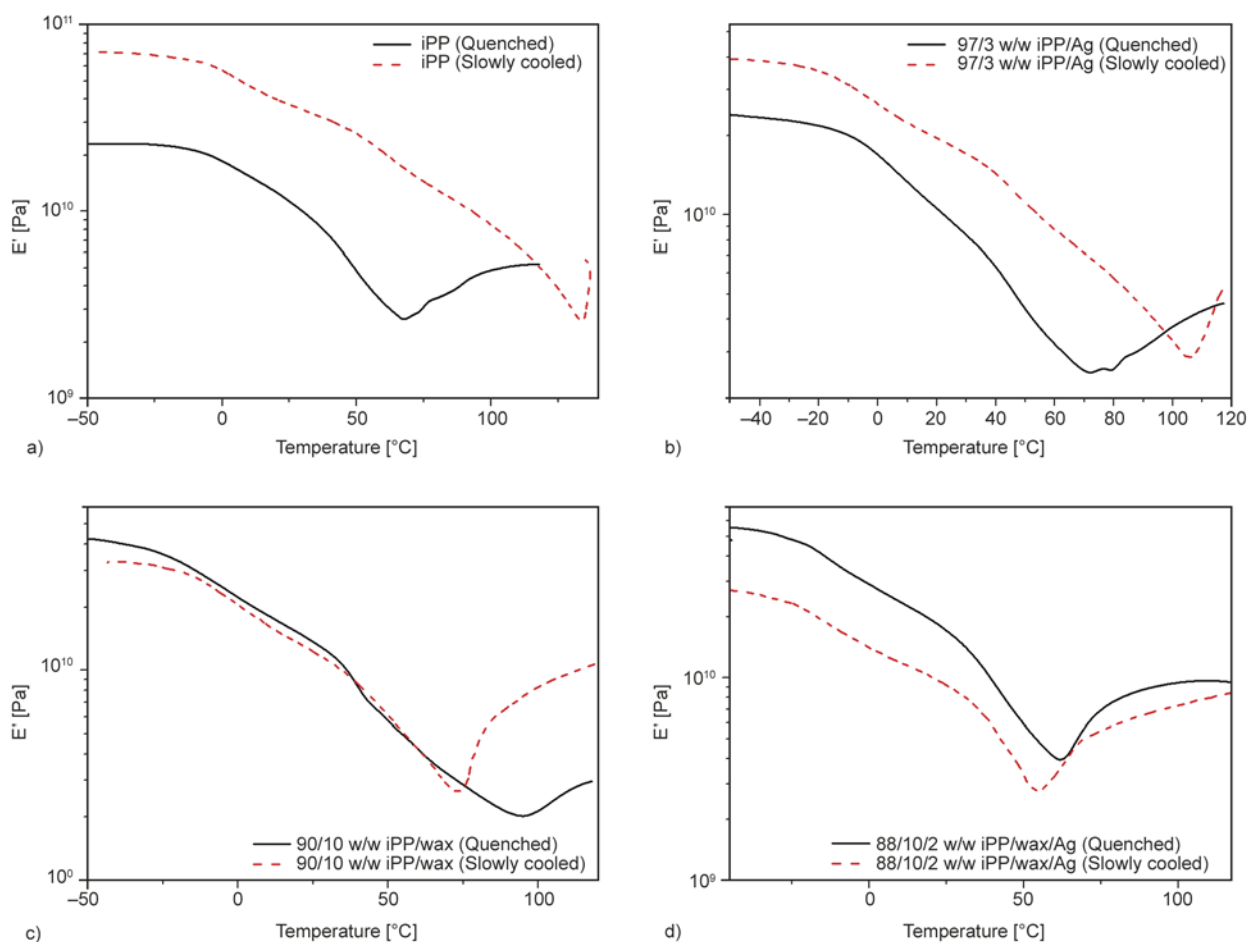
Figure 4. Storage modulus as a function of temperature of the quenched and slowly cooled (a) iPP, (b) iPP/wax, (c) iPP/Ag and (d) iPP/wax/Ag nanocomposites

melting enthalpies of the slowly cooled samples (Table 1). However, the quenched and slowly cooled iPP/wax samples show almost the same modulus (Figure 4c), indicating that the presence of the soft wax counter-acted the influence of the higher crystallinity of the slowly cooled blend. When both wax and Ag are present, the storage modulus of the slowly cooled sample is significantly lower than that of the quenched sample (Figure 4d). According to Table 1 the normalised melting enthalpy of iPP in the slowly cooled iPP/wax/Ag is higher than that in the quenched sample, and the differences in storage modulus is therefore not related to the differences in crystallinity. The only possible reason for this observation is that more wax crystallized around the nanoparticles in the quenched samples, giving rise to more rigidity from the wax-covered Ag filler.

There is no difference between the temperatures of the β-peaks in the quenched and slowly cooled iPP (Figure 5a), which is to be expected because differences in cooling rate will only influence the crystallinity of iPP. The α-peak of the slowly cooled iPP appears at a significantly higher temperature than that of the quenched iPP. This is attributed to the higher crystallinity of the slowly cooled samples (compare melting enthalpy values in Table 1). If one compares the relaxation peaks of the iPP/Ag samples, it can be seen that the β-peak of the slowly cooled iPP/Ag sample appears at a lower temperature, but the α-peak is still at a higher temperature, than those of the quenched samples (Figure 5b). The difference between the α-peaks of the samples is attributed to the difference in crystallinity between the quenched and slowly cooled samples (Table 1), although Ag had an influence in both cases, as discussed before. Therefore, the presence of Ag particles in the inter-crystalline amorphous regions (section 3.1) influences the crystalline phase more than the amorphous phase in the slowly cooled sample, because of its higher crystallinity, but the amorphous phase more than the crystalline in the quenched sample, which has a lower crystallinity.

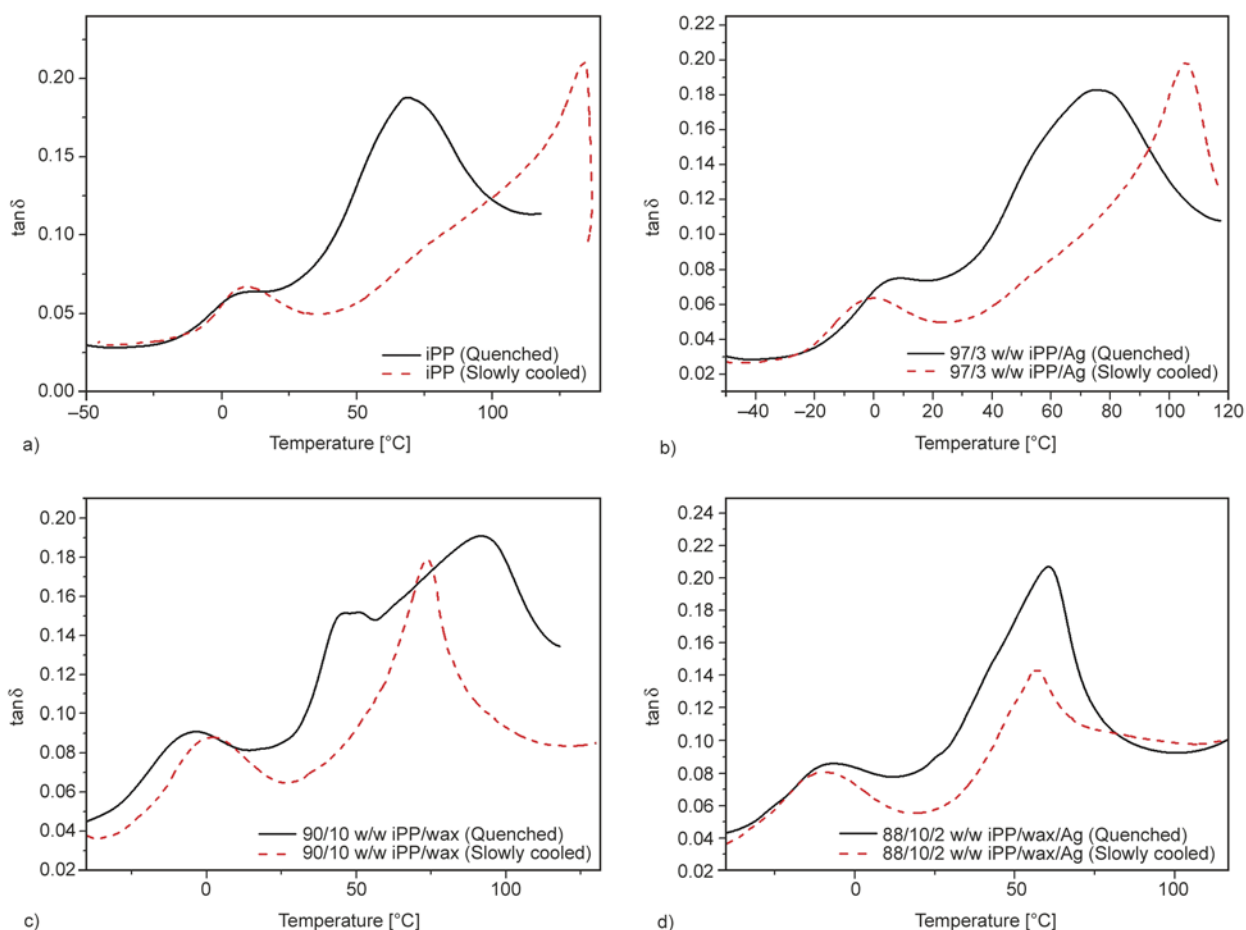In the iPP/wax samples, the β-relaxation and wax melting peaks of the slowly cooled sample appear at

Figure 5. Loss factor as a function of temperature of the quenched and slowly cooled (a) iPP, (b) iPP/Ag, (c) iPP/wax and (d) iPP/wax/Ag nanocomposites

a higher temperature than those of the quenched sample (Figure 5c). This is because larger wax crystals formed during slow cooling, which had a stronger immobilizing effect on the amorphous iPP chains and which had melted at higher temperatures. There is little difference between the β-transition and wax melting temperatures of the quenched and slowly cooled samples when both wax and Ag were present (Figure 5d), because the wax crystallized mostly around the Ag nanoparticles, and since the rate at which the sample was cooled would not seriously affect the wax crystallization, and since there is very little interaction between iPP and wax, it could be expected that these transitions would not be seriously affected by the rate at which the samples were cooled.

3.4. Thermal conductivity

The thermal conductivities of the quenched and slowly cooled iPP samples increased with increasing Ag content at lower Ag contents, but leveled off at higher contents (Figure 6). This can be attributed to

a better dispersion of the Ag particles at lower contents. At higher Ag contents the particles were not so well dispersed and formed agglomerates (Figure 1b). It has been reported previously that the agglomeration of filler particles increased with an increase in filler content [21], and that these agglomerations gave rise to lower thermal conductivities [22]. In the iPP/Ag nanocomposites, phonons are transported from one Ag particle to another *via* the polymer. Since the polymer is not a good thermal conductor, it is important that the filler particles must be well dispersed and fairly close to each other, and that there should be fairly strong interactive forces between iPP and Ag. In such a case heat will be transported by high frequency phonon vibrations leading to higher thermal conductivity values. However, if the particles are poorly dispersed and/or the interaction between iPP and Ag is weak, a small amount of heat will be transported by low frequency phonons as a result of higher thermal contact resistance. When the thermal conductivities of the quenched and slowly cooled samples are compared (Figure 6), it can be
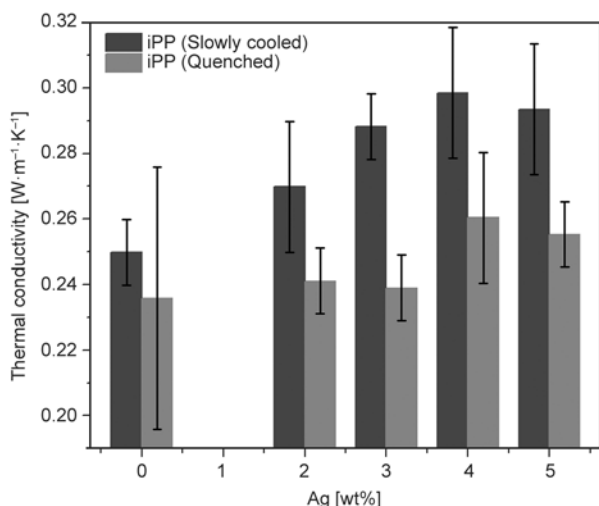
Figure 6. Thermal conductivities of iPP and iPP/Ag

seen that the thermal conductivities of the quenched samples are significantly lower than those of the slowly cooled samples. It is known that higher crystallinities give rise to better thermal energy transport [23], which is also the reason for the better thermal conductivity of the slowly cooled samples, that have previously been shown to have much higher crystallinities.

The thermal conductivity of the quenched iPP shown in Figure 7 slightly increases after the addition of 10 wt% wax. This can be attributed to the wax crystals in the sample, which increased the total crystallinity and therefore the thermal energy transport. The thermal conductivity of iPP/Ag is slightly lower than that of iPP/wax, but is very similar to that of pure iPP. Again, if one looks at the values in Table 1, it is clear that the normalised melting enthalpy of the iPP/Ag sample is very similar within experi-

mental error to that of pure iPP, but lower than that of iPP/wax. As already seen, the crystallinities of the quenched samples are significantly lower, and therefore the Ag particles are probably dispersed in the amorphous phase of iPP with little contact with the crystallites, which could inhibit the thermal transport through the iPP/Ag samples. Although Ag is thermally more conductive than wax and iPP, it is clear that the thermal conductivity of the quenched iPP sample depends more on the crystallinity than on the presence of conductive metal particles. When both wax and Ag are present, the thermal conductivity of the sample is higher than that of iPP/Ag. This can again be attributed to the higher crystallinity of the sample, but also to the dispersion of Ag within the highly crystalline wax phase. The wax-covered Ag particles therefore significantly increased the thermal conductivity of the quenched iPP sample.
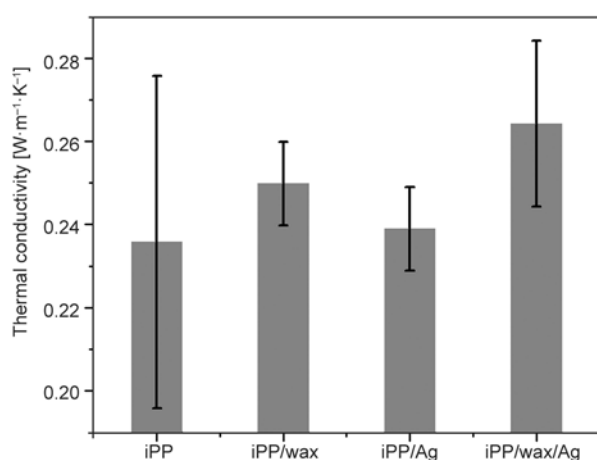
In the slowly cooled samples (Figure 8), the thermal conductivity of iPP/wax is observably higher than that of iPP, which is also the result of the presence of the more crystalline wax. The thermal conductivity of the iPP/Ag sample is significantly higher than those of the pure iPP and the iPP/wax samples. According to Table 1, the slowly cooled iPP/Ag sample has a much higher crystallinity than the quenched sample, and therefore the Ag particles should have better contact with the iPP crystallites, which probably is the reason for the improved thermal energy transport in the slowly cooled iPP/Ag sample. The thermal conductivity of the iPP/wax/Ag sample is about the same as that of the iPP/Ag sample. In the slowly cooled iPP/Ag sample, Ag particles act as nucleation centers and are therefore in intimate con-
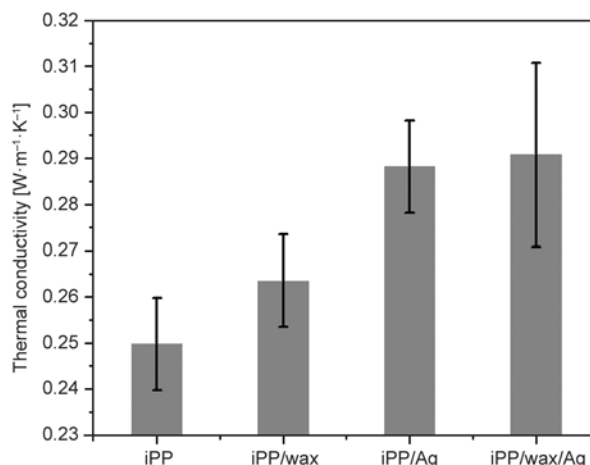

Figure 7. Thermal conductivities of quenched iPP, 90/10 w/w iPP/wax, 97/3 w/w iPP/Ag and 87/10/3 w/w iPP/wax/Ag

Figure 8. Thermal conductivities of slowly cooled iPP, 90/10 w/w iPP/wax, 97/3 w/w iPP/Ag and 87/10/3 w/w iPP/wax/Ag

tact with the iPP crystallites. However, when wax is present, the Ag particles are no longer in contact with the iPP crystallites, but are probably covered by the crystalline wax, which will also improve the thermal energy transport. Crystallites in contact with the Ag nanoparticles, whether they are iPP or wax crystallites, seem to have a very strong influence on the thermal conductivities of the nanocomposites.

There is no specific trend in the thermal conductivities of the quenched and slowly cooled iPP/wax/Ag samples shown in Figure 9. In this case there is a complex combination of effects that will influence the thermal conductivities of the samples: (1) Ag dispersion; (2) extent of agglomeration; (3) covering of Ag particles by crystalline wax; (4) extent of formation and dispersion of wax crystals in between the iPP spherulites. If the filler particles are not well dispersed, and if there are fewer (iPP or wax) crystal-

lites, high frequency phonon movement will be inhibited and the thermal conductivity will be lower. The separate crystallization of the wax in the areas between the iPP spherulites and the covering of the Ag particles by the crystalline wax should improve the thermal conductivity, but the weak interaction between iPP and wax may negatively influence the thermal conductivity. All these factors will contribute in one way or the other to the thermal conductivity, but it is difficult to isolate any one of these factors as possible reason(s) for the differences in the conductivity. However, when the thermal conductivities of the slowly cooled and quenched samples are compared, it is clear that the slowly cooled samples have higher thermal conductivities than the quenched samples because of their higher crystallinities.

3.5. Dielectric properties

Figure 10 presents the DC conductivity, conductance and susceptance of the 10 wt% wax containing iPP/Ag nanocomposites. The DC conductivity of the iPP/wax/Ag samples showed little change up to 3 wt% Ag, but increased significantly at higher Ag contents. For the lower filler content, the mean distance between the individual metal particles and aggregates must have been too large and the conductivity was therefore controlled by the insulating polymer matrix. When the distances between individual filler particles are large, electrons do not easily hop from one particle to the other. However, at higher Ag contents the individual particles and aggregates were closer to each other and the mean dis-
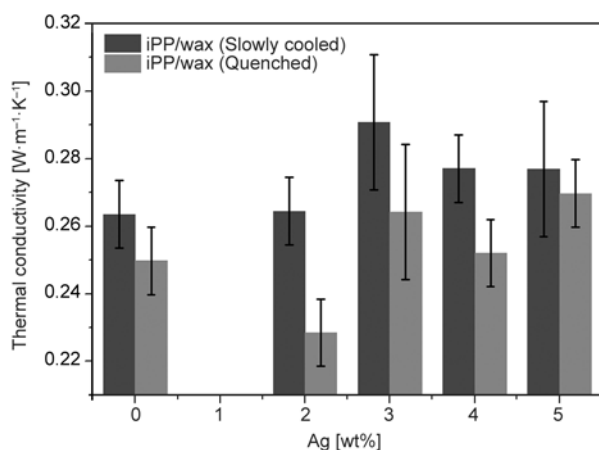

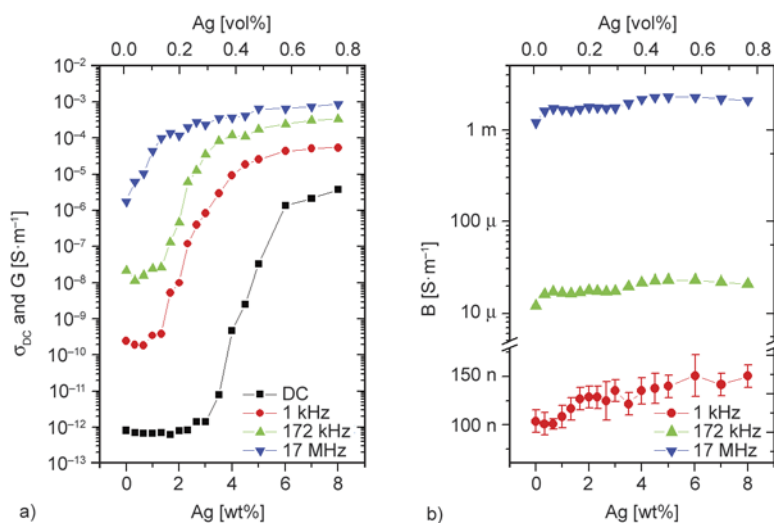**Figure 9.** Thermal conductivity of iPP/wax and iPP/Ag with 10 wt% wax

Figure 10. (a) *DC* conductivity and conductance, and (b) susceptance of 10 wt% wax containing iPP/Ag composites as function of Ag content

tance between the metal particles was small enough for the electrons to fairly easily hop from one particle to another. The conductance at different frequencies showed similar behaviour (Figure 10a), but the susceptance only showed small changes with increasing Ag content (Figure 10b). This is probably because the Ag particles do not improve the polarity of the blend. Both the conductance and susceptance increased with increasing frequency for all the investigated Ag concentrations, which indicates that the Ag particles did not form a well-developed conductive network. However, if one looks at the *DC* conductivity of the 10 wt% wax containing iPP/Ag samples, a significant increase in the *DC* conductivity is observed in the samples with 4 wt% Ag. This increase in the *DC* conductivity was not observed in
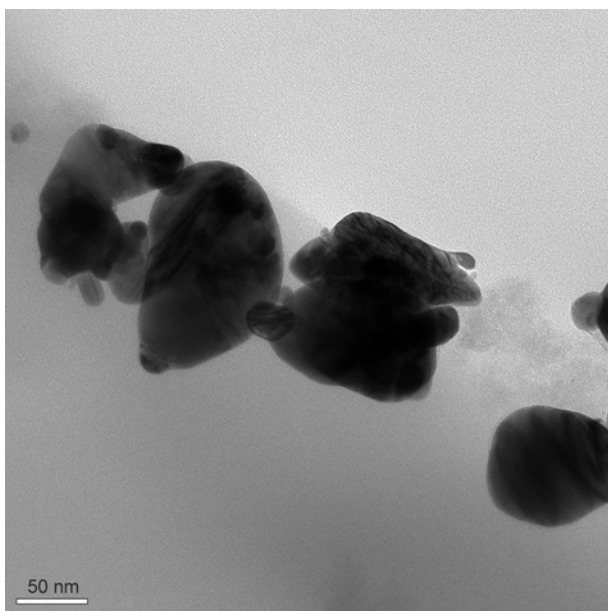
the iPP/Ag composites at 4 wt% Ag, and this confirms our previous observation that the silver particles were more concentrated in the wax phase than in the iPP phase. This is clear from the TEM photo of an iPP/wax/Ag composite (Figure 11), which clearly indicates the existence of chain-like structures of Ag particles in the samples, and which should have contributed to an increase in electrical conductivity at low concentrations of silver nanoparticles. Figure 12 presents the temperature dependence of the dielectric properties of iPP and iPP/wax composites with 2 wt% Ag nanoparticles at a frequency of 172 kHz. The conductance of the samples decreased after the addition of 10 wt% wax, which can be attributed to the presence of the interface between the immiscible wax and iPP. When Ag particles are present the conductance of the iPP/Ag sample is higher than those of pure iPP and the iPP/wax sample. In the iPP/Ag sample, the Ag particles acted as nucleation centers, as discussed in section 3.1, and are therefore in intimate contact with the iPP crystallites. The iPP crystallites in contact with the Ag particles seem to have a strong influence on the conductivity of the nanocomposites. In the presence of both wax and Ag, the conductance is even higher. When wax is present in the iPP/Ag sample, the Ag particles are no longer in contact with iPP crystals, but covered by the more crystalline wax which further improves the electrical conductivity. The conductance of iPP and iPP/Ag remained nearly constant at lower temperatures, but slowly increased at higher temperatures. When wax was present, the conductance of iPP/wax and iPP/wax/Ag also remained nearly constant at lower temperatures, but decreased at about 325 K, followed by a significant increase
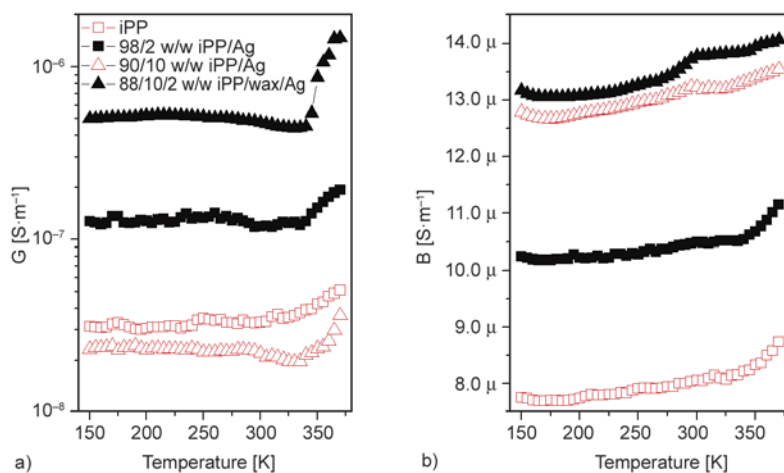

Figure 11. High-magnification TEM photo of Ag nanoparticles 89/10/1 w/w iPP/wax/Ag

Figure 12. Temperature dependence of the dielectric properties of the composites with 2 wt% Ag nanoparticles at 172 kHz

in conductivity. This indicates that the presence of the more crystalline wax had a strong influence on the conductivity.

The susceptance showed different behaviour from that of the conductance in the presence of wax (Figure 12b). The susceptance of iPP/wax is higher than those of both pure iPP and iPP/Ag. Both iPP and wax are non-polar materials, but excellent electric insulators that can be polarized by the applied electric field. When an electric field is applied to iPP/wax, the electrons do not move through the blend as they would have done in a conductor, but move only slightly, causing a small dielectric polarization because wax more easily responds to polarization than iPP. When both wax and Ag were present, the susceptance of iPP in iPP/wax/Ag sample was higher than those of iPP/Ag and iPP/wax. This shows that in the presence of both the conductor and wax, when an external electric field was applied, the electrons moved in such a way that they were free to polarize the conductor. The wax-covered Ag particles easily responded to the polarization, and the susceptance was therefore very large. When the susceptance of iPP/wax and iPP/wax/Ag are compared, the wax slightly improved the polarity of iPP, but the wax-covered Ag particles significantly improved its polarity. The susceptance is the ratio of polarization to the applied electric field, and the changes observed in the susceptance of the composites are the result of the changes in polarization.

In order to study the effect of Ag particles on the conductivity of iPP and the iPP/wax blend, the relative increase in admittance ($\Delta Y(f,T) = 100 \cdot (Y_{\text{pol+Ag}} - Y_{\text{pol}})/Y_{\text{pol}}$) of iPP and iPP/wax due to the presence of 2 wt% Ag was determined. The results are presented in Figures 13 and 14. A transition which is associated with the γ-relaxation appeared at about 173 K in both composites. It has been previously reported that the γ-relaxation of iPP appears between 150 and 230 K, and this relaxation is usually associated with the local motions in the amorphous phase [24]. The difference in conductivity between iPP and iPP/Ag slightly increases with increasing temperature up to this temperature, followed by a decrease at higher temperatures. The non-polar iPP usually shows a γ-relaxation, but the introduction of polar groups had previously made the γ-relaxation peak disappear [25]. The observed γ-relaxation in iPP/Ag therefore confirms that the Ag particles did not improve the polarity of iPP. The
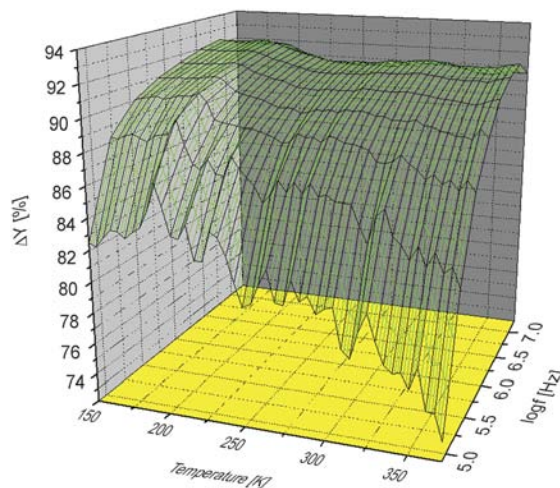

Figure 13. Relative increase of admittance due to the presence of 2 wt% Ag nanoparticles in iPP as function of temperature and frequency
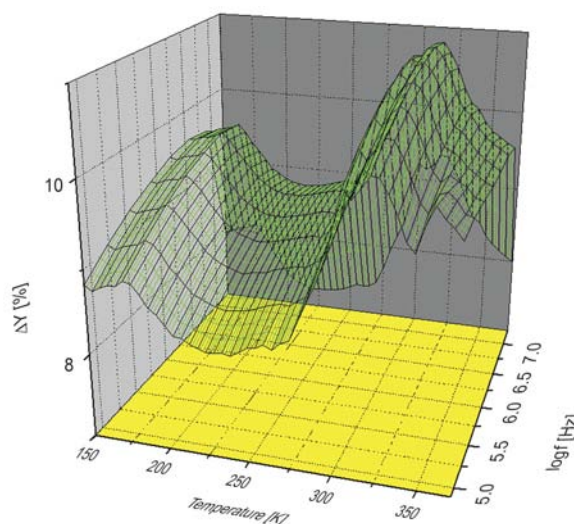

Figure 14. Relative increase in admittance due to the presence of 2 wt% Ag nanoparticles in 90/10 w/w iPP/wax as function of temperature and frequency

iPP/wax/Ag sample has two transitions associated with the γ-transition and the softening of wax, respectively at about 173 and 300 K (Figure 14). Although the conductivity of iPP/wax and iPP/wax/Ag increased with increasing temperature (Figure 12), the difference in their admittance increased up to the γ-transition of iPP, followed by a decrease in admittance at temperatures above the γ-transition. Again, the difference in admittance (ΔY) slightly increased with increasing temperature up to the onset of wax softening, followed by a significant increase up to wax melting. At temperatures above the melting of wax the admittance of iPP/wax/Ag more slowly increased than that of iPP/Ag, probably because of

the destruction of the semi-conductive paths during the softening of the wax. The difference in admittance only slightly changed during the softening of iPP, but significantly changed during the softening of the wax, which confirms that the Ag particles were mostly dispersed in the wax phase.

4. Conclusions

The purpose of the study was to correlate the morphologies of quenched and slowly cooled iPP/Ag and iPP/wax/Ag samples with the thermal and dynamic mechanical properties, as well as the thermal and electrical conductivities. At low contents the Ag nanoparticles were concentrated at the growth centres of the iPP spherulites in the iPP/Ag nanocomposites and formed nucleation centres for the crystallization of iPP, while wax crystallized separately from iPP and influenced the growth of the iPP spherulites by acting as a diluent. The Ag nanoparticles had a larger affinity for wax and were no longer observed at the growth centres of the iPP spherulites, and they had little influence on the mobility of the iPP chains and on its crystallinity. The wax-covered Ag particles significantly improved the thermal and electrical conductivities of the samples, but reduced the modulus.

With increasing Ag content in iPP/Ag, the nanoparticles remained at the growth centres of the iPP spherulites, but the filler was not so well dispersed and the extent of the agglomeration increased. In iPP/wax/Ag with higher filler contents, Ag agglomerates were also observed at the growth centres of the iPP spherulites, but they had little influence on the crystallinites of iPP in all the samples. The thermal conductivities of both the iPP and iPP/wax based samples increased with increasing Ag content, but leveled off at higher filler contents, while the electrical conductivities continued increasing with increasing filler contents. In the iPP/wax blend the melting enthalpies of iPP increased with an increase in wax content, and the highly crystalline wax increased the stiffness of the quenched samples, but it had a softening effect on the slowly cooled samples. The presence of wax increased the thermal conductivities, but decreased the electrical conductivities of the blends.

Both the quenching and slow cooling treatments had an influence on the crystallinities, and the associated properties, of the samples. In summary, the highly crystalline wax improved the thermal heat transport of both the quenched and slowly cooled samples, but decreased the electrical conductivity because of the immiscibility of iPP and wax. The presence of Ag in iPP/wax significantly improved the thermal and electrical conductivities of both the quenched and slowly cooled samples, because of the coverage of the Ag particles by the highly crystalline wax.

Acknowledgements

References

[1] Zhang K., Han B., Yu X.: Electrically conductive carbon nanofiber/paraffin wax composites for electric thermal storage. Energy Conversion and Management, **64**, 62–67 (2012).
DOI: 10.1016/j.enconman.2012.06.021

[2] Kim S., Drzal L. T.: High latent heat storage and high thermal conductive phase change materials using exfoliated graphite nanoplatelets. Solar Energy Materials and Solar Cells, **93**, 136–142 (2009).
DOI: 10.1016/j.solmat.2008.09.010

[3] Xiang J., Drzal L. T.: Investigation of exfoliated graphite nanoplatelets (*x*GnP) in improving thermal conductivity of paraffin wax-based phase change material. Solar Energy Materials and Solar Cells, **95**, 1811–1818 (2011).
DOI: 10.1016/j.solmat.2011.01.048

[4] Koning C., Van Duin M., Pagnoulle C., Jerome R.: Strategies for compatibilization of polymer blends. Progress in Polymer Science, **23**, 707–757 (1998).
DOI: 10.1016/S0079-6700(97)00054-3

[5] Xiao M., Feng B., Gong K.: Preparation and performance of shape stabilized phase change thermal storage materials with high thermal conductivity. Energy Conversion and Management, **43**, 103–108 (2002).
DOI: 10.1016/S0196-8904(01)00010-3

[6] Mills A., Farid M., Selman J. R., Al-Hallaj S.: Thermal conductivity enhancement of phase change materials using a graphite matrix. Applied Thermal Engineering, **26**, 1652–1661 (2006).
DOI: 10.1016/j.applthermaleng.2005.11.022

[7] Sari A., Karaipekli A.: Thermal conductivity and latent heat thermal energy storage characteristics of paraffin/expanded graphite composite as phase change material. Applied Thermal Engineering, **27**, 1271–1277 (2007).
DOI: 10.1016/j.applthermaleng.2006.11.004

[8] Fernandes D., Pitié F., Cáceres G., Baeyens J.: Thermal energy storage: 'How previous findings determine current research priorities'. Energy, **39**, 246–257 (2012).
DOI: 10.1016/j.energy.2012.01.024

[9] Tadjarodi A., Zabihi F.: Thermal conductivity studies of novel nanofluids based on metallic silver decorated mesoporous silica nanoparticles. Materials Research Bulletin, **48**, 4150–4156 (2013).
DOI: 10.1016/j.materresbull.2013.06.043

[10] Mngomezulu M. E., Luyt A. S., Krupa I.: Structure and properties of phase-change materials based on high-density polyethylene, hard Fischer–Tropsch paraffin wax, and wood flour. Polymer Composites, **32**, 1155–1163 (2011).
DOI: 10.1002/pc.21134

[11] Mngomezulu M. E., Luyt A. S., Krupa I.: Structure and properties of phase change materials based on HDPE, soft Fischer-Tropsch paraffin wax, and wood flour. Journal of Applied Polymer Science, **118**, 1541–1551 (2010).
DOI: 10.1002/app.32521

[12] Molefi J. A., Luyt A. S., Krupa I.: Investigation of thermally conducting phase-change materials based on polyethylene/wax blends filled with copper particles. Journal of Applied Polymer Science, **116**, 1766–1774 (2010).
DOI: 10.1002/app.31653

[13] Mhike W., Focke W. W., Mofokeng J. P., Luyt A. S.: Thermally conductive phase-change materials for energy storage based on low-density polyethylene, soft Fischer–Tropsch wax and graphite. Thermochimica Acta, **527**, 75–82 (2012).
DOI: 10.1016/j.tca.2011.10.008

[14] Sari A.: Form-stable paraffin/high density polyethylene composites as solid–liquid phase change material for thermal energy storage: Preparation and thermal properties. Energy Conversion and Management, **45**, 2033–2042 (2004).
DOI: 10.1016/j.enconman.2003.10.022

[15] Zhang L., Zhu J., Zhou W., Wang J., Wang Y.: Thermal and electrical conductivity enhancement of graphite nanoplatelets on form-stable polyethylene glycol/polymethyl methacrylate composite phase change materials. Energy, **39**, 294–302 (2012).
DOI: 10.1016/j.energy.2012.01.011

[16] Di Lorenzo M. L.: Spherulite growth rates in binary polymer blends. Progress in Polymer Science, **28**, 663–689 (2003).
DOI: 10.1016/S0079-6700(02)00035-7

[17] Krupa I., Luyt A. S.: Thermal properties of polypropylene/wax blends. Thermochimica Acta, **372**, 137–141 (2001).
DOI: 10.1016/s0040-6031(01)00450-6

[18] Krupa I., Miková G., Luyt A. S.: Polypropylene as a potential matrix for the creation of shape stabilized phase change materials. European Polymer Journal, **43**, 895–907 (2007).
DOI: 10.1016/j.eurpolymj.2006.12.019

[19] Menczel J. D., Prime R. B.: Thermal analysis of polymers. Fundamentals and applications. Wiley, New Jersey (2009).

[20] Pandis C., Logakis E., Kyritsis A., Pissis P., Vodnik V. V., Džunuzović E., Nedeljković J. M., Djoković V., Hernández J. C. R., Ribelles J. L. G.: Glass transition and polymer dynamics in silver/poly(methyl methacrylate) nanocomposites. European Polymer Journal, **47**, 1514–1525 (2011).
DOI: 10.1016/j.eurpolymj.2011.06.001

[21] Vladimirov V., Betchev C., Vassiliou A., Papageorgiou G., Bikiaris D.: Dynamic mechanical and morphological studies of isotactic polypropylene/fumed silica nanocomposites with enhanced gas barrier properties. Composites Science and Technology, **66**, 2935–2944 (2006).
DOI: 10.1016/j.compscitech.2006.02.010

[22] Song Y. S., Youn J. R.: Influence of dispersion states of carbon nanotubes on physical properties of epoxy nanocomposites. Carbon, **43**, 1378–1385 (2005).
DOI: 10.1016/j.carbon.2005.01.007

[23] Krupa I., Novák I., Chodák I.: Electrically and thermally conductive polyethylene/graphite composites and their mechanical properties. Synthetic Metals, **145**, 245–252 (2004).
DOI: 10.1016/j.synthmet.2004.05.007

[24] Suljovrujic E., Trifunovic S., Milicevic D.: The influence of gamma radiation on the dielectric relaxation behaviour of isotactic polypropylene: The α relaxation. Polymer Degradation and Stability, **95**, 164–171 (2010).
DOI: 10.1016/j.polymdegradstab.2009.11.034

[25] Suljovrujic E.: Complete relaxation map of polypropylene: radiation-induced modification as dielectric probe. Polymer Bulletin, **68**, 2033–2047 (2012).
DOI: 10.1007/s00289-012-0714-1

Effect of surface modified TiO₂ nanoparticles on thermal, barrier and mechanical properties of long oil alkyd resin-based coatings

T. S. Radoman[1], J. V. Džunuzović[2], K. T. Trifković[1], T. Palija[3], A. D. Marinković[4], B. Bugarski[4], E. S. Džunuzović[4]*

[1]Innovation center, Faculty of Technology and Metallurgy, University of Belgrade, Karnegijeva 4, 11120 Belgrade, Serbia
[2]Institute of Chemistry, Technology and Metallurgy (ICTM), Center of Chemistry, University of Belgrade, Studentski trg 12–16, 11000 Belgrade, Serbia
[3]Faculty of Forestry, University of Belgrade, Kneza Višeslava 1, 11000 Belgrade, Serbia
[4]Faculty of Technology and Metallurgy, University of Belgrade, Karnegijeva 4, 11120 Belgrade, Serbia

Abstract. Novel soy alkyd-based nanocomposites (NCs) were prepared using TiO₂ nanoparticles (NPs) surface modified with different gallates, and for the first time with imine obtained from 3,4-dihydroxybenzaldehyde and oleylamine (DHBAOA). Unmodified and surface modified anatase TiO₂ NPs were characterized by transmission electron microscopy (TEM), X-ray diffraction (XRD), Fourier transform infrared spectroscopy (FTIR) and ultraviolet-visible (UV-Vis) spectroscopy, while the amount of adsorbed ligands was calculated from thermogravimetric analysis (TGA) results. Surface modification of TiO₂ NPs was confirmed by FTIR and UV-Vis spectra. The influence of the TiO₂ surface modification on the dispersion of TiO₂ NPs in alkyd resin, thermal, barrier and mechanical properties and chemical resistance of alkyd resin/TiO₂ NC coatings was investigated. The obtained results revealed that glass transition temperature of all investigated NCs is lower than for pure resin, that the presence of TiO₂ NPs surface modified with gallates had no significant influence on the thermooxidative stability of alkyd resin, while TiO₂-DHBAOA NPs slightly improved alkyd resin thermooxidative stability. Also, the presence of surface modified TiO₂ NPs improved barrier properties, increased stress and strain at break and hardness and chemical resistance and decreased modulus of elasticity and abrasion resistance of alkyd resin.

Keywords: *thermal properties, alkyd-based coatings, TiO₂ nanoparticles, surface modification, mechanical properties*

1. Introduction

Alkyds are the most widely used synthetic resins due to their relatively low cost, compatibility with other polymers and various interesting properties which are highly desirable for the application in paint industry. The versatility of alkyd resins originates from the fact that their properties such as drying time, gloss retention, anticorrosion, mechanical, thermal and barrier properties, durability, flame retardancy, water and chemical resistance and adhesion can be easily tailored and improved by simple changing the ratio and type of the applied reactants, the oil length or by modification of alkyd resins with different reactive compounds [1]. Alkyd resins are obtained by polycondensation of polyol (glycerol, trimethylolpropane, pentaerythritol, etc.) with dicarbonic acid or its anhydride derivative in the presence of fatty acids or oil of synthetic or natural origin (soya bean oil, linseeds oil, sunflower oil, castor oil, etc.). The content of oil, which corresponds to the oil length, has significant influence on the properties of alkyd resins [1, 2]. Depending on the composition of the

fatty acids used for the synthesis, alkyd resins can be cross-linked (dried) using either oxidative drying (unsaturated fatty acids) or non-oxidative drying (saturated fatty acids) mechanism [2–4].

Alkyd resins based on non-toxic, biodegradable, multifunctional, low cost, physically and chemically stable and eco-friendly renewable resources such as vegetable oils show properties comparable with properties of products based on petroleum, and therefore have found their industrial application in paints and surface coatings [5–19]. Especially interesting low cost vegetable oil is soy bean oil, which has balanced composition of unsaturated and saturated fatty acids and it can reduce yellowing and oxidative degradation of resin [2, 16–19]. Araujo *et al.* [16] have shown that anticorrosive properties of alkyd paints prepared with soy bean oil are similar to the anticorrosive properties of alkyd resins synthesized using linseed oil, but water vapor and ions permeability in freestanding film, as well as adhesion loss, depend on the type of pigment and vegetable oil used in the formulation of alkyd resins. By comparing properties of short oil-modified alkyd resins prepared using soy bean, corn, rice bran, sunflower and dehydrated castor oil, it was revealed that soy bean based alkyd resin show the best sea water resistance [17]. Nalawade *et al.* [19] have used modified soy bean oils as reactive diluents for the preparation of long oil alkyd resin, which had significantly reduced viscosity.

Different commercial, micro-sized, inorganic pigments are usually included in alkyd resin formulations, and their presence can improve mechanical, optical and anticorrosive properties of the coatings [20, 21]. However, due to their micro-sizes, densities different from the density of alkyd resins, and other various effects, sedimentation of pigments occurs, leading to different problems considering final alkyd-based coatings (viscosity changes, covering power deterioration, poor adhesion, loss of optical transparency, low scratch and impact resistance, delamination, reduction of the storage time, etc.) [22]. Sedimentation issue can be avoided if small quantities of nano-sized pigments are used in the alkyd resin formulations instead of micro-sized ones. The main advantages of the application of nanoparticles (NPs) for the preparation of polymer nanocomposites (NCs) are high surface to volume ratios and high interfacial reactivity of NPs and properties which are significantly different from the properties of their bulk counterparts and micro- and macro-additives [23].

By adequate surface modification of NPs it is possible to enable uniform distribution of NPs through the polymer matrix and better interaction with polymer in order to achieve significant improvement of properties of polymer materials with simultaneous decrease of the final product price [24, 25]. The influence of different nano-sized pigments on the properties of alkyd-based NCs was extensively investigated in the literature [26–37]. It has been shown that application of zinc oxide (ZnO) as nano-sized pigment improves mechanical and thermal properties [26] and corrosion resistance [27] of alkyd-based coatings. Furthermore, the presence of titanium dioxide (TiO_2) NPs affects the rheological properties of alkyd resin [28], improves corrosion resistance [29, 30] and hardness of alkyd coatings [29], and can be applied for the preparation of coatings with antibacterial properties [31]. Also, hematite (Fe_2O_3) NPs are proven to be useful nano-pigment which enhances mechanical and UV blocking properties [32] and corrosion resistance [32, 33] of alkyd-based waterborne coatings. The presence of nano-ferrite (Fe_3O_4) in soy alkyd coating improved thermal stability, physico-mechanical properties and corrosion resistance [34]. The addition of aluminum oxide (Al_2O_3) nano-sized pigment into the alkyd coatings improved its corrosion [35, 36] and UV resistance and mechanical properties, without altering the optical clarity of the prepared coating [36]. Alkyd paint prepared using molybdenum oxide (MoO_3) NPs showed good antibacterial properties against pathogenic bacteria [37].

In our previous studies, we have synthesized and examined properties of NCs based on epoxy resin and TiO_2 NPs surface modified with propyl, hexyl and lauryl gallate [38], as well as the influence of the size of TiO_2 nanoparticles, their concentration and type of the surface modification on the rheological properties of alkyd resin [28].

Since there is constantly increasing demand for developing environmentally friendly materials and taking into account that alkyd resins are one of the most applied resins and TiO_2 is one of the most applied pigment in coating industry, in the present study we have made an effort to prepare novel alkyd-based NCs with improved properties, by utilizing differently surface modified TiO_2 NPs and alkyd resin based on vegetable oil. Different types of ligands, grafted on the surface of TiO_2 NPs, were applied in order to improve interactions between

NPs and polymer matrix and consequently to enhance the properties of the alkyd-based coatings.

In the present study we have used TiO_2 NPs surface modified with hexyl (C6), lauryl (C12) and cetyl (C16) gallate, and imine obtained from 3,4-dihydroxybenzaldehyde and oleylamine to prepare novel soy alkyd-based NCs. The TiO_2 NPs were synthesized using acid catalyzed hydrolysis of titanium isopropoxide. The average size and size distribution of the synthesized TiO_2 NPs were determined by transmission electron microscopy (TEM), their crystal structure was investigated by X-ray diffraction (XRD) measurements, while surface modified TiO_2 NPs were characterized using TEM, XRD, FTIR and UV/VIS spectroscopy. The amount of adsorbed molecules on the surface of TiO_2 NPs was determined by thermogravimetric analysis (TGA). The influence of the type of TiO_2 nanoparticles surface modification, as well as the length of hydrophobic part of gallates used for surface modification of TiO_2 nanoparticles, on the dispersion of TiO_2 NPs in alkyd resin and on the rheological properties of the prepared dispersions, as well as on the thermal, barrier and mechanical properties and chemical resistance of alkyd resin/TiO_2 NCs was investigated.

2. Experimental section
2.1. Materials
Titanium isopropoxide was purchased from TCI Europe N.V. (Zwijndrecht, Belgium). Gallic acid, 2-propanol, 1-hexanol, lauryl gallate (LG) and oleylamine (OA) were obtained from Sigma–Aldrich (Germany). Cetyl alcohol was obtained from Fluka (Switzerland), while 3,4-dihydroxybenzaldehyde (DHBA) from Acros Organics (Geel, Belgium). Alkyd resin (AR65), CHS-ALKYD S 653, based on soy bean oil (65% of oil) was obtained from Spolchemie (Ústí nad Labem, Czech Republic). Ca-octoate (10%), Co-octoate (4%) and Zr-octoate (15%) were purchased from Tikkurila Zorka (Šabac, Serbia) and used as driers. All chemicals were used as received without further purification.

2.2. Synthesis of TiO_2 colloid
The synthesis of TiO_2 colloid was performed by hydrolysis of titanium isopropoxide using the procedure described in the literature [39]. Briefly, 12.5 mL of titanium isopropoxide and 2.0 mL of 2-propanol were added into the dropping funnel and then the mixture was added to 75 mL of deionized water and

vigorously stirred. White precipitate was formed during the hydrolysis. Within 10 min of the alkoxide addition, 0.57 mL of 65% nitric acid was added to the hydrolysis mixture. The mixture was stirred for 8 h at 80°C, allowing 2-propanol to evaporate. Using this procedure, approximately 70 mL of stable TiO_2 colloidal solution was obtained.

2.3. Synthesis of gallic acid esters
The synthesis of hexyl (HG) and cetyl gallate (CG) was performed by esterification of gallic acid using 1-hexanol and cetyl alcohol. The esterification of gallic acid by 1-hexanol was performed using the procedure described in the literature [40]. In the reaction flask (250 mL), connected to a Soxhlet apparatus containing 10 g of sodiumsulfate as a drying agent, 50 g of gallic acid, 136 g of 1-hexanol and 1 mL of sulfuric acid were added. 80 mL of extra 1-hexanol was used to fill Soxhlet apparatus. The reaction mixture was stirred with magnetic stirrer at 165°C for 8 h. During the reaction, formed water made azeotrope with 1-hexanol and it was captured by drying agent in Soxhlet apparatus. Then, the reaction mixture was placed in Rotavapor (BÜCHI 461, Switzerland) and 1-hexanol was distilled until the mixture of 75 wt% of hexyl gallate in 1-hexanol was obtained. In order to crystallize, the reaction mixture was poured with stirring into methylene chloride. After that, the prepared suspension was washed with water, and hexyl gallate was placed between two layers. The crude product was separated by filtration, washed with water and methylene chloride and dried at 60°C in vacuum oven.

The esterification of gallic acid by cetyl alcohol was performed using the similar procedure as procedure described in the literature for the synthesis of octyl gallate [40]. In the reaction flask (250 mL), connected to a mechanical stirrer, a nitrogen inlet, a contact thermometer and a condenser for vacuum distillation, 70.24 g of cetyl alcohol was placed. The flask was heated to 60°C, and then 10.24 g of gallic acid and 0.5 mL of H_2SO_4 were added into the flask. The reaction mixture was heated up to 160°C with stirring under a stream of nitrogen. The course of the reaction was controlled by the amount of the formed water. After 5 h, a reduced pressure (0.4 bar) was applied to the flask for 1 h. The reaction mixture was then slowly cooled down to 55°C. In another flask (500 mL), equipped with a mechanical stirrer and reflux condenser, 250 mL of petrol ether heated to

55°C was added. The reaction mixture was then slowly with stirring, added into petrol ether, heated to 60°C and left to cool down to the room temperature. The precipitate was separated by filtration, washed with petrol ether and then with water. The obtained precipitate was then placed into the flask and the alcohol residue was separated by distillation with water vapor. After that, cetyl gallate was recrystallized two times from the mixture petrol ether/benzene (50:50 vol.) and dried at 60°C in vacuum oven.

2.4. Modification of TiO₂ nanoparticles with gallates

For the surface modification of TiO₂ NPs, three gallates with different hydrophobic part length (hexyl, lauryl and cetyl gallate) were applied. Modification of TiO₂ NPs with gallates was done according to the procedure described in the literature [38]. The procedure for the surface modification of TiO₂ NPs with lauryl gallate will be briefly described here. 0.1136 g of LG was dissolved in the mixture of chloroform and methanol and then mixed with 10 mL of TiO₂ colloid solution in a separation funnel. After short vigorous shaking, a dark-red chloroform phase with TiO₂ NPs surface modified with LG (TiO₂-LG) separated from the upper aqueous phase. The obtained dark-red phase was drop-wise added to 100 times larger amount of methanol. Nanoparticles of TiO₂-LG separated as precipitate, which was then redispersed in chloroform.

2.5. Modification of TiO₂ nanoparticles with imine based on 3,4-dihydroxybenzaldehyde and oleylamine

The surface modification of TiO₂ NPs with imine obtained from DHBA and OA was performed in the following manner. In one flask (50 mL), 0.09 g of DHBA was dissolved in 8 mL of methanol using magnetic stirrer, while in another flask (50 mL), 0.5 mL of 70% OA was added into 20 mL of chloroform. Then, 5 mL of TiO₂ colloid solution, previously diluted with 25 mL of distilled water, was vigorously mixed with prepared solutions. After leaving the obtained solution overnight, a dark-orange phase containing TiO₂ NPs surface modified with imine (TiO₂-DHBAOA) separated from the upper aqueous phase. The obtained dark-orange phase was then slowly, with simultaneous mixing with the magnetic stirrer, drop-wise added into 100 times larger amount of methanol. Nanoparticles of TiO₂-DHBAOA sep-

arated as precipitate, which was then redispersed in chloroform.

2.6. Preparation of the alkyd based nanocomposites

Alkyd based NCs, containing 2 wt% of TiO₂ NPs (calculated with respect to the total mass of solid mater in alkyd resin), were prepared by adding adequate amount of TiO₂ NPs surface modified with HG (TiO₂-HG), LG (TiO₂-LG), CG (TiO₂-CG) and DHBAOA (TiO₂-DHBAOA) dispersed in chloroform into AR65. So prepared mixtures were then mixed in ultrasonic bath (Sonorex Digitec, BANDELIN electronic GmbH & Co KG, Berlin, Germany) for 10 min. After that, chloroform was evaporated at room temperature under the reduced pressure. Then, in the reaction mixtures were added 50 wt% of white spirit (oil thinner), calculated with respect to the total mass of solid mater in alkyd resin, and adequate amount of driers (Table 1). In order to obtain completely cured NC films (AR65/TiO₂-HG, AR65/TiO₂-LG, AR65/TiO₂-CG and AR65/TiO₂-DHBAOA), the dispersions were drawn on two glass plates (10×10 cm and 15×20 cm) using wire-wound rods and then cured at room temperature for 21 days. Film based on the pure alkyd resin was obtained in the same manner.

2.7. Characterization of unmodified and surface modified TiO₂ nanoparticles

Transmission electron microscopy (JEOL-1200EX, Jeol Ltd. Tokyo, Japan) was applied to determine the average size of TiO₂ NPs, while the size distribution of TiO₂ NPs was obtained using Image J software. TEM images of surface modified TiO₂ NPs were recorded on JEM-1400 (Jeol Ltd. Tokyo, Japan). The X-ray powder diffraction measurements of unmodified and modified TiO₂ nanoparticles were performed on a Philips 1050 X-ray powder diffractometer (Philips, Netherlands) using Ni-filtered Cu Kα radiation and Bragg-Brentano focusing geometry. The patterns were taken in the 10–90° 2θ range

Table 1. The amount of driers used for the cross-linking of alkyd resin based nanocomposites

Drier	Metal content [%]*
Solution of Ca-octoate	0.10
Solution of Co-octoate	0.04
Solution of Zr-octoate	0.15

*Calculated with respect to the content of alkyd resin

with the step of 0.05° and exposure time of 6 s per step. Using X-ray Line Profile Fitting Program (XFIT) with a Fundamental Parameters convolution approach to generate line profiles [41], the coherent domain sizes of the prepared samples were calculated. FTIR spectra of gallic acid esters, dry unmodified and modified TiO_2 NPs in the form of KBr pellets were recorder using a Bomem MB-102 (Quebec, Canada) FTIR spectrophotometer. The absorption spectra of unmodified and surface modified TiO_2 NPs were recorded on a Perkin-Elmer Lambda-5 UV-Vis (MA, USA) spectrometer. Using thermogravimetric analysis, performed on Setaram Setsys Evolution-1750 (SETARAM S.A. France, Caluire – France) instrument in dynamic argon atmosphere (flow rate 20 cm^3/min) at a heating rate of 10°C/min, the amount of molecules adsorbed on the surface of TiO_2 NPs was determined. Before TGA measurements, investigated samples were dried in vacuum oven at 60°C for 12 h.

2.8. Characterization of alkyd resin, dispersions of modified TiO_2 nanoparticles in alkyd resin and prepared nanocomposite coatings

Complex dynamic viscosity of pure AR65 and dispersions of surface modified TiO_2 NPs in AR65, prepared by dispersing 2 wt% of surface modified TiO_2 NPs in AR65 using ultrasound, was determined on rheometer Rheometrics RMS 605 (Rheometric Scientific, Piscataway NJ, USA). Dynamic shear experiments were performed between cone and plate, at constant temperature of 25°C. The frequency was changed between 0.1 and 100 rad/s, at strain of 5%.

The dispersion of surface modified TiO_2 nanoparticles in alkyd matrix was investigated by Scanning Electron Microscopy (SEM) using JEOL JSM-6610LV (Jeol Ltd. Tokyo, Japan). In order to observe the cross section of the nanocomposite films, the piece of each examined sample was immersed in liquid nitrogen for 20 s, removed and immediately broken.

Differential scanning calorimetry (DSC) measurements were done on Q1000 (TA Instruments, USA) instrument in a nitrogen atmosphere, at a heating rate of 20°C/min. Thermooxidative stability of samples was determined by TGA (Setaram Setsys Evolution-1750) in air atmosphere (flow rate 25 cm^3/min), at a heating rate of 10°C/min.

Water vapour transfer rate (*WVTR*) through the prepared films was determined according to the method described in the standard ASTM:D1653 using BYK-Gardner permeability cup (BYK-Gardner GmbH, Geretsried, Germany), filled with a desiccant (dry calcium chloride). The investigated films were clamped and sealed across the open end of the cup and then the cup was placed in an atmosphere of controlled relative humidity (85%), which was provided by saturated potassium chloride solution. During measurements, vapour passes from a solution through the film to a desiccant within the permeability cup. Three *WVTR* measurements were performed for each investigated film and the average value is reported.

Tensile properties of the prepared samples were examined on Shimadzu Universal Testing Machine AG-Xplus (Shimadzu, Kyoto, Japan) with deformation rate of 5 mm/min using 100 N cell. Investigated specimens were cut from the dried films. For each sample the average value of five measurements was taken.

Using the non-destructive ultrasound thickness meter Posi Tector 200 (DeFelsko, USA), the thickness of dried films was calculated as average value of three measurements. The estimated thickness of the prepared dried films was 40±3 μm. The surface hardness of dried films was determined using König pendulum (Elcometer Pendulum Hardness Tester 3034, Elcometer Limited, Manchester, England). König pendulum hardness, expressed in seconds as average value of three measurements, was measured using films drawn on glass plates (10×10 cm).

Impact resistance of prepared films was determined according to the standard ASTM D 2794 using Erichsen Impact Tester, Model 304 (Hemer, Germany). The indentation was performed through the uncoated side of metal plate, i.e. the examined coating was exposed to convex deformation (extrusion). For each sample, five specimens were tested and their average has been reported. Adhesion of films coated on mild steel panels was determined by cross-cut (ISO 2409) test. For each film, three specimens were tested by cross-cut method and their average has been reported. Abrasion resistance of prepared films was determined by Taber Abraser Testing Apparatus (Taber Industries, USA) using No. CS-17 Resilent Calibrase Wheels in accordance with standard ASTM D 4060. Load applied to the abrasive wheels was

1000 g. For each film, three specimens were tested and their average has been reported.

The gel content of the prepared films was determined by immersion of square specimens (1.2×2.5 cm), placed in holder made from steel network, in xylene for 14 days, at room temperature. After that, test specimens were dried in vacuum oven at 100°C for 2 hours and then, their weight (w) was measured. Data of three different specimens of each investigated film were averaged. The gel content of the samples was calculated using the following Equation (1):

$$Gel\% = \frac{w}{w_0} \cdot 100 \qquad (1)$$

where w_0 is the weight of the sample before immersion in xylene.

The chemical resistance of the prepared films to distilled water, 1M HCl, 0.15% NaOH, 3% NaCl, ethanol, acetone and sunflower oil was investigated using films drawn on glass plates (10×10 cm). Solvent was dripped on the examined film using Pasteur pipette and appearance of the film was observed during 24 hours. Three specimens of each film were tested. The obtained results are presented as time needed to reach certain change in the appearance of the examined films: (0) completely unaffected, (1) unaffected, slightly color changed, (2) film swelled and (3) film cracked.

3. Results and discussion

3.1. Properties of unmodified and surface modified TiO$_2$ nanoparticles

TEM image of TiO$_2$ NPs, prepared by acid catalyzed hydrolysis of titanium isopropoxide, is given in Figure 1. It can be observed that synthesized TiO$_2$ NPs have approximately spherical shape and average diameter of 3.9±0.9 nm. The crystal structure and average crystalline size of TiO$_2$ NPs were determined by XRD measurements and obtained X-ray diffraction patterns are given in Figure 2. It can be seen that synthesized TiO$_2$ NPs have anatase crystal form and it has been estimated that their coherent domain size is around 3.6 nm, which is in good agreement with TEM result.

According to the literature, TiO$_2$ NPs have on their surface some Ti atoms which are not in octahedral, but in square-pyramidal position [42]. The coordination number of such Ti atoms is therefore five and not six, and one of these five bonds between Ti and
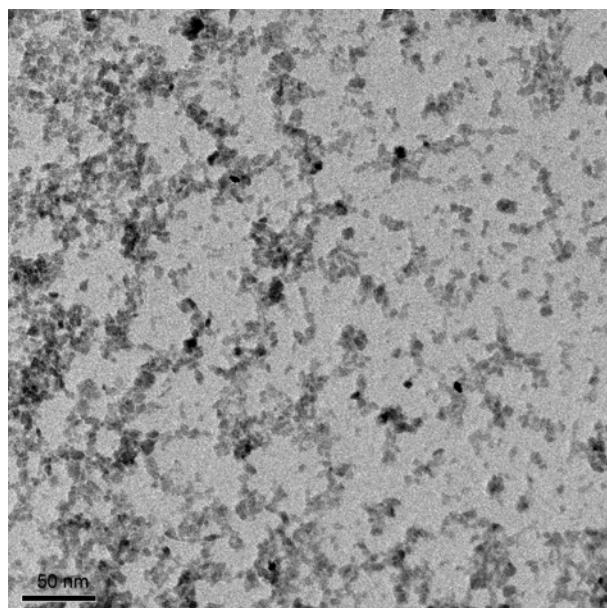
Figure 1. TEM image of TiO$_2$ nanoparticles

oxygen is shorter than others. Due to that, Ti atoms on the surface of TiO$_2$ NPs are more reactive than bulk ones and can react quite fast with hydroxyl groups of modifying agent, bonding in this manner the missing oxygen and leading to the formation of charge transfer (*CT*) complex. This process leads simultaneously to the formation of stable crystal anatase form, where coordination number of Ti atoms is six and all Ti–O bonds are of the same length.

The surface modification of nanosized TiO$_2$ colloids was performed with three alkyl gallates with different hydrophobic part length (hexyl, lauryl and cetyl gallate) and with imine obtained from 3,4-dihydrox-
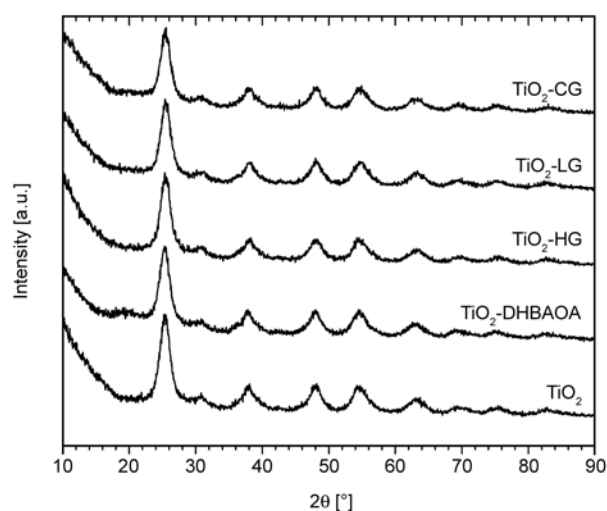

Figure 2. XRD patterns of unmodified and surface modified TiO$_2$ NPs
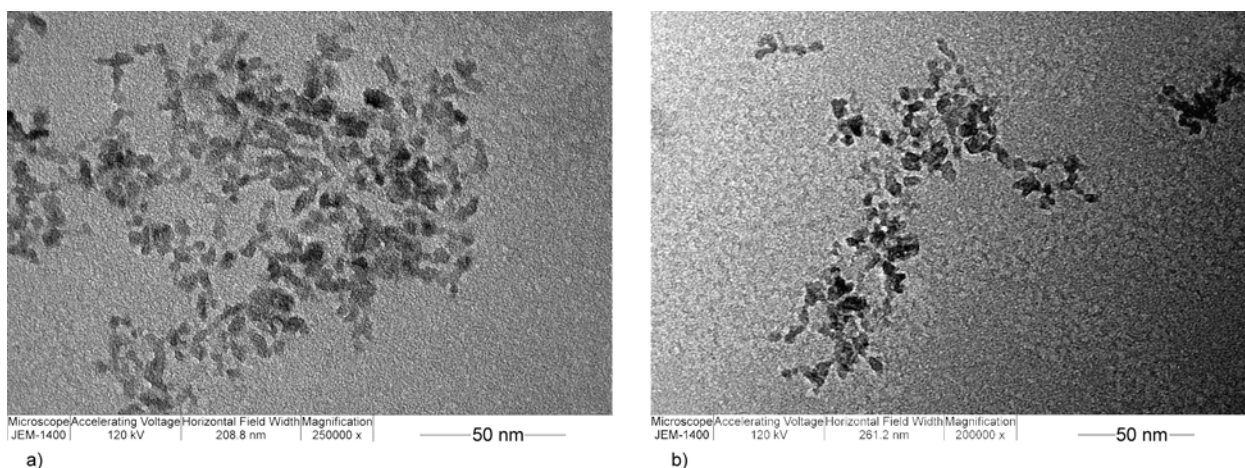
Figure 3. TEM images of TiO$_2$ nanoparticles surface modified with a) lauryl gallate and b) DHBAOA

ybenzaldehyde and oleylamine. During the modification process, a dark-red (when gallates were used for the modification) or dark-orange phase (when DHBAOA was used for the surface modification) separated, and transfer of NPs from water into organic phase occurred as a consequence of the formation of *CT* complex between TiO$_2$ NPs and gallates or DHBAOA. XRD patterns of modified TiO$_2$ NPs presented in Figure 2 show that the crystal structure and crystallite size of TiO$_2$ NPs were not changed by modification of TiO$_2$ NPs with gallates or DHBAOA, which was also confirmed by TEM analysis of modified TiO$_2$ NPs, reported in Figure 3. From the TEM analysis it can be observed that the morphology of TiO$_2$ NPs has not been changed during their surface modification.

The formation of *CT* complex between TiO$_2$ NPs and gallates or DHBAOA was confirmed by FTIR

and UV-Vis spectroscopy. As an example, FTIR spectra of CG, dry TiO$_2$ colloid, dry TiO$_2$-CG, TiO$_2$-LG and TiO$_2$-HG NPs are presented in Figure 4a. From Figure 4a it can be observed that characteristic bands of CG at 3450 and 3350 cm^{-1}, which represent the stretching vibrations of –OH groups from benzene ring, are not present in the FTIR spectrum of TiO$_2$-CG NPs. On the other hand, the bands corresponding to the stretching vibration of aliphatic C–H bonds from cetyl group at 2920 and 2850 cm^{-1} and band which is assigned to the stretching vibration of C=O group from ester at 1670 cm^{-1} are also visible in the FTIR spectrum of TiO$_2$-CG NPs. According to these results, it can be concluded that the coordinative bond between surface Ti atoms and gallate was achieved through the adjacent –OH groups from the benzene ring, by creating bridging complexes, which is in agreement with our previous results [28,
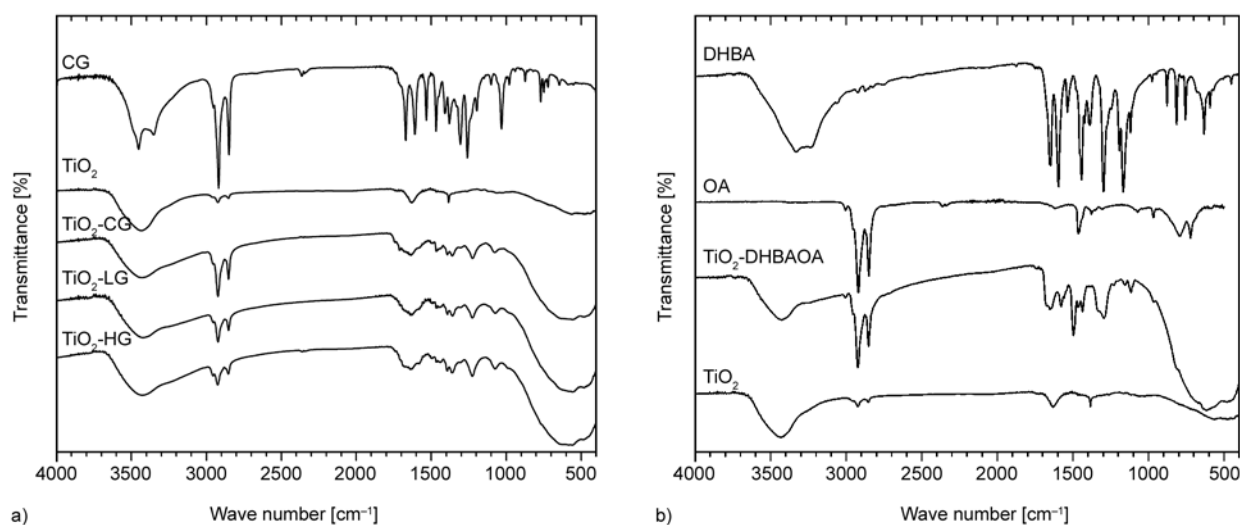

Figure 4. FTIR spectra of a) CG, dry TiO$_2$ colloid, dry TiO$_2$-CG, TiO$_2$-LG and TiO$_2$-HG NPs and b) OA, DHBAOA, dry TiO$_2$ colloid and TiO$_2$ NPs surface modified with DHBAOA

38, 43]. As can be observed from Figure 4a, similar results were obtained for the TiO$_2$-HG and TiO$_2$-LG NPs. Detailed explanation of the FTIR spectra of TiO$_2$ NPs surface modified with gallates is given elsewhere [38].

FTIR spectra of DHBA, OA, dry TiO$_2$ colloid and dry TiO$_2$-DHBAOA NPs are presented in Figure 4b. In the FTIR spectrum of TiO$_2$-DHBAOA, the bands at 3331 and 3233 cm^{-1}, assigned to the stretching vibrations of aldehyde phenolic –OH groups, and bands at 1389 and 1192 cm^{-1}, corresponding to the bending vibrations of phenolic –OH groups, are missing. Furthermore, the intensity of band at 1296 cm^{-1} (originating from the C–O stretching vibrations of phenolic group) is noticeable reduced, and the band became broader. Also, in the FTIR spectrum of TiO$_2$-DHBAOA, the band at 1576 cm^{-1}, assigned to the stretching vibrations of aromatic ring, and band at 1645 cm^{-1}, corresponding to the C=N stretching vibrations, are also visible. Furthermore, characteristic bands of the OA residue between 3000 and 2800 cm^{-1}, assigned to the asymmetric and symmetric C–H stretching vibrations of methyl and methylene groups, and at 3005 cm^{-1}, assigned to the C–H stretching vibrations in C=C–H group can also be observed. These results show that imine based on DHBA and OA was obtained and it was chemisorbed on TiO$_2$ surface through the two adjacent –OH phenolic groups of the aldehyde residue.

Absorption spectra of unmodified TiO$_2$ NPs and TiO$_2$ NPs surface modified with CG and DHBAOA

Figure 6. TGA curves of TiO$_2$-CG and TiO$_2$-DHBAOA NPs, obtained in argon atmosphere at a heating rate of 10°C/min

Figure 5. The absorption spectra of aqueous TiO$_2$ colloid solution and solutions of TiO$_2$-CG and TiO$_2$-DHBAOA in chloroform

are shown in Figure 5. It can be observed that compared to the absorption spectrum of unmodified TiO$_2$ NPs, absorption spectra of surface modified TiO$_2$ NPs are red shifted, due to the CT complex formation on the surface of TiO$_2$ NPs. The absorption onset of unmodified, gallate and imine modified TiO$_2$ NPs is around 380, 640 and 610 nm, respectively.

In order to determine the amount of gallates and DHBAOA adsorbed on the surface of TiO$_2$, TGA measurements in argon atmosphere were performed. As an example, TGA curves of TiO$_2$-CG and TiO$_2$-DHBAOA are presented in Figure 6. It can be observed that thermal stability of TiO$_2$-DHBAOA NPs is higher than thermal stability of TiO$_2$-CG NPs. The first stage of thermal degradation of surface modified TiO$_2$ NPs occurred due to the mass loss of the absorbed water, while the second stage between 210 and 800°C corresponds to the mass loss of adsorbed ligand grafted on the surface of TiO$_2$ NPs. In our previous work we have shown that theoretical amount of adsorbed ligand necessary to cover all Ti surface sites should be 1.86 mmol of ligand per gram of TiO$_2$ [38]. According to the TGA results obtained here, the amount of the adsorbed ligands, TiO$_2$-HG, TiO$_2$-LG, TiO$_2$-CG and TiO$_2$-DHBAOA, are 0.90, 0.89, 0.80 and 1.53 mmol per gram of TiO$_2$, respectively. Consequently, the calculated coverage is for the TiO$_2$ NPs surface modified with gallates similar between each other (48% for TiO$_2$-HG and TiO$_2$-LG, and 43% for TiO$_2$-CG), while the amount of DHBAOA adsorbed on the surface of TiO$_2$ NPs is 82%.

3.2. Rheological properties of prepared dispersions of alkyd resin/TiO$_2$

The influence of surface modified TiO$_2$ NPs on the rheological properties of alkyd resin was investigated by measuring the dependence of complex dynamic viscosity (η^*) on frequency. From the results presented in Figure 7 it can be observed that prepared dispersions have higher dynamic viscosity than pure AR65 and that η^* decreases with increasing frequency for all investigated samples. Dynamic viscosity of the prepared dispersions depends on the interactions between surface modified TiO$_2$ NPs, as well as on the interactions between NPs and alkyd resin. Furthermore, from the samples prepared using TiO$_2$ NPs surface modified with gallates, the AR65/TiO$_2$-CG dispersion has the highest η^* value. This was reasonable to expect since TiO$_2$-CG NPs have the highest effective diameter. On the other hand, the viscosity of alkyd resin increased more after addition of TiO$_2$-HG than after addition of TiO$_2$-LG NPs. This indicates that TiO$_2$-HG NPs have low dispersion stability, leading to the formation of agglom-

erates in AR65, which are actually the main cause for the viscosity increase. Figure 7 also reveals that AR65/TiO$_2$-DHBAOA dispersion has the lowest η^* value from the investigated samples, indicating lower hydrodynamic radius of TiO$_2$-DHBAOA in AR65 than TiO$_2$ NPs surface modified with gallic acid esters.
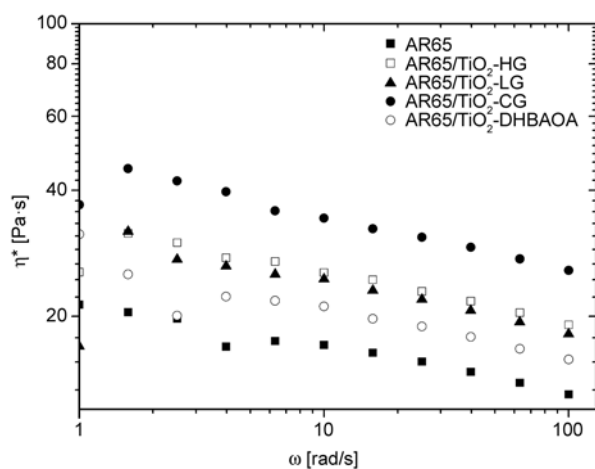
3.3. SEM image analysis of cross-sections of the nanocomposite coatings

The cross-section of the prepared nanocomposite coatings was investigated by SEM analysis in order to examine the dispersion of surface modified TiO$_2$ NPs in polymer matrix. The SEM micrographs presented in Figure 8 show that TiO$_2$ NPs formed agglomerates in alkyd resin. Furthermore, it can be observed that agglomeration is more pronounced in NCs prepared with TiO$_2$ NPs surface modified with gallates and that formed agglomerates have approximately the same size no matter which ester of the gallic acid was used for the surface modification of TiO$_2$ NPs. The presence of agglomerates can also be observed in AR65/TiO$_2$-DHBAOA nanocomposite (Figure 8d and 8f), but their size is smaller and they are better dispersed in alkyd resin.

3.4. Thermal properties of AR65/TiO$_2$ nanocomposites

Glass transition temperature (T_g) of the synthesized NCs was determined using DSC measurements and obtained results are given in Figure 9 and summarized in Table 2. Furthermore, it can be observed that T_g of all investigated NCs is lower than T_g of pure AR65, which indicates that the presence of surface modified TiO$_2$ NPs increased molecular mobility of polymer chains at the polymer/nanoparticles interface, due to the absence of the attractive interactions between NPs and polymer matrix. The increase of the hydrophobic part length of the used

Figure 7. Frequency dependence of complex dynamic viscosity (η^*) for pure AR65 and AR65/TiO$_2$-HG, AR65/TiO$_2$-LG, AR65/TiO$_2$-CG and AR65/TiO$_2$-DHBAOA dispersions

Table 2. Values of the glass transition temperature (T_g), water vapour transfer rate (*WVTR*), modulus of elasticity (*E*), stress at break (σ_B) and strain at break (ε_B) of the pure alkyd resin and prepared nanocomposites (*WVTR* values were determined as average value of three measurements, while tensile properties were determined as average value of five measurements and all results are reported with a standard deviation)

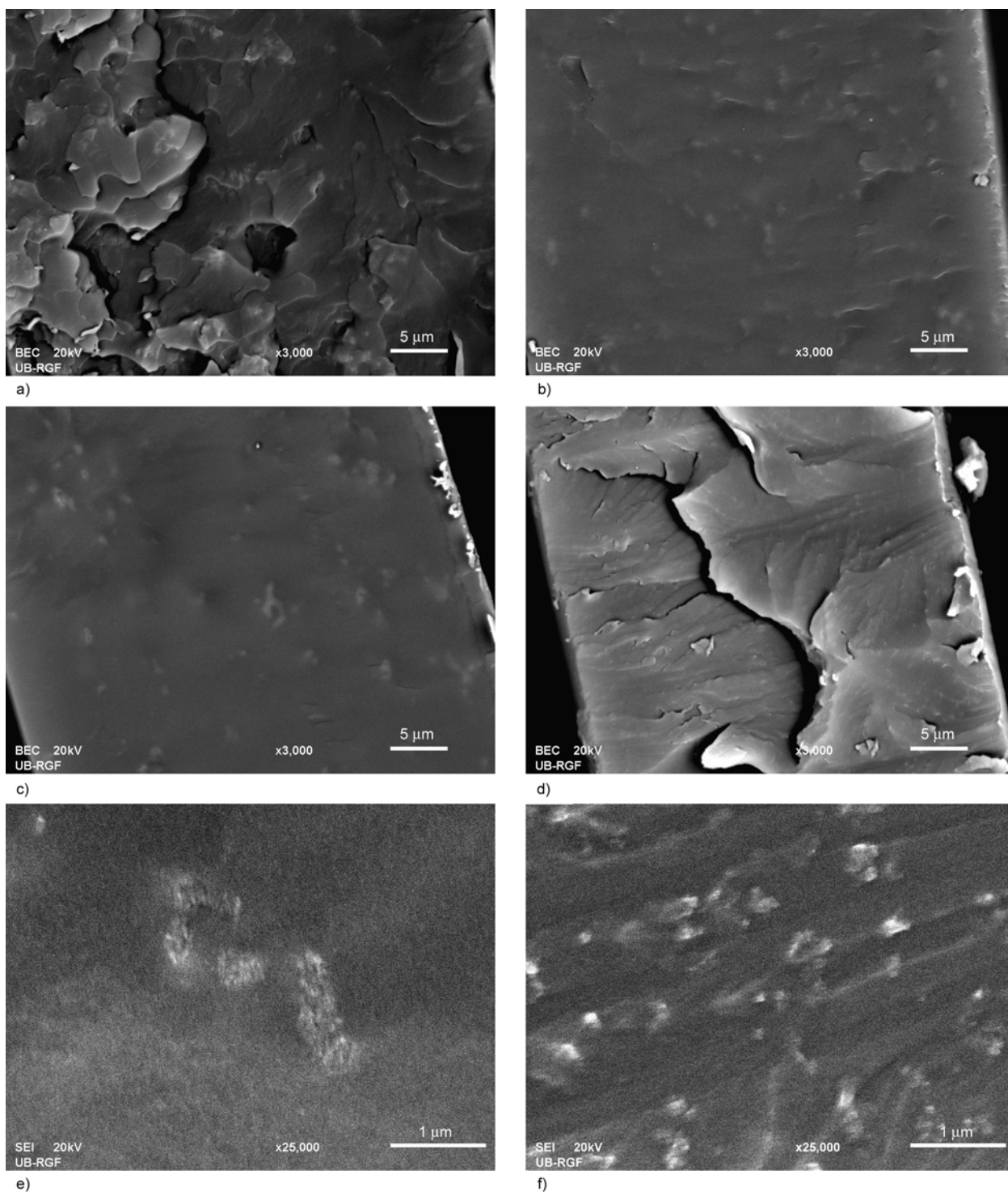| Sample	T_g [°C]	*WVTR* [g/(m²·h)]	*E* [MPa]	σ_B [MPa]	ε_B [%]
AR65	25	3.80±0.20	354±14	12.3±0.86	39.1±5.80
AR65/TiO$_2$-HG	21	2.68±0.11	279±8	13.1±1.00	47.6±5.71
AR65/TiO$_2$-LG	23	3.44±0.21	144±6	14.0±1.12	53.7±9.12
AR65/TiO$_2$-CG	23	3.40±0.18	246±12	11.9±0.71	45.8±4.72
AR65/TiO$_2$-DHBAOA	20	3.66±0.23	124±5	12.5±1.12	62.3±9.34

Figure 8. SEM micrographs of the cross-section of a) AR65/TiO$_2$-HG, b) AR65/TiO$_2$-LG, c) AR65/TiO$_2$-CG, d) AR65/TiO$_2$-DHBAOA at magnification of 3000×, and e) AR65/TiO$_2$-CG and f) AR65/TiO$_2$-DHBAOA at magnification of 25000×

gallic acid esters led to only slight increase of the T_g of prepared NCs.

The influence of differently surface modified TiO$_2$ NPs on thermooxidative stability of alkyd resin was investigated by TGA under air atmosphere, at a heating rate of 10°C/min. The results presented in Figure 10 show that thermooxidative degradation of all investigated samples took place in two stages, first at around 350°C and second at around 450°C. The first stage of thermooxidative degradation can be ascribed to the thermal degradation of polyester part of the alkyd resin chains, while the second stage occurred as a consequence of degradation of fatty acids chains [44]. The presence of surface modified
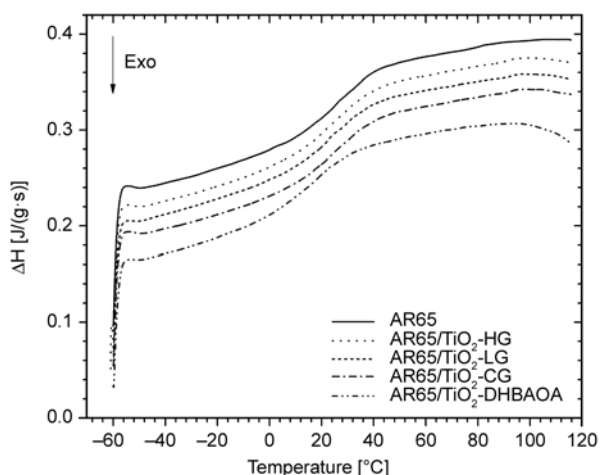
Figure 9. DSC curves of pure AR65 and AR65/TiO$_2$-HG, AR65/TiO$_2$-LG, AR65/TiO$_2$-CG and AR65/TiO$_2$-DHBAOA nanocomposites
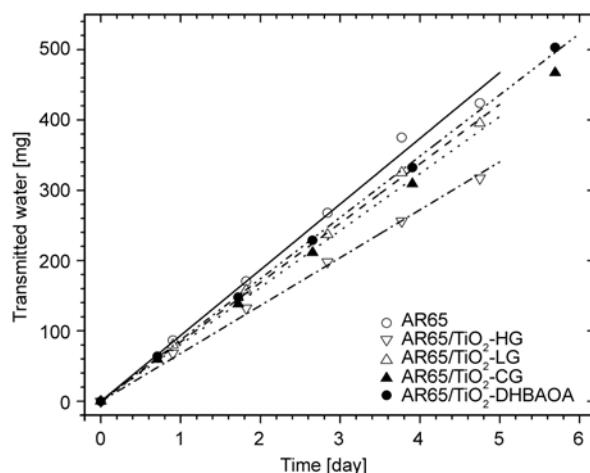
Figure 11. The dependence of the transmitted water through the pure AR65 and prepared nanocomposites on time
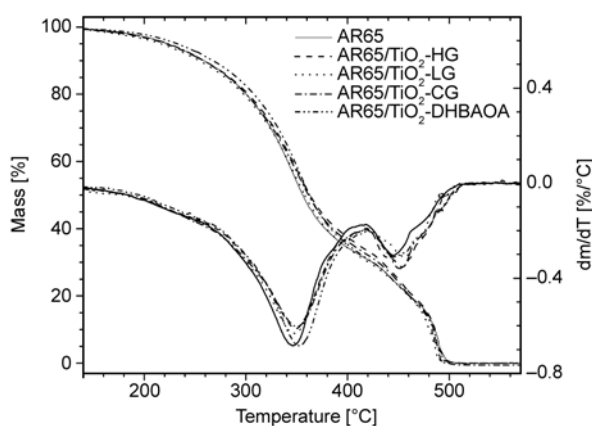
Figure 10. TGA and DTG curves of pure AR65 and AR65/TiO$_2$-HG, AR65/TiO$_2$-LG, AR65/TiO$_2$-CG and AR65/TiO$_2$-DHBAOA nanocomposites determined in air atmosphere at a heating rate of 10°C/min

TiO$_2$ NPs in AR65 shifted the position of both derivative thermogram (DTG) peaks to slightly higher temperatures compared to the DTG peaks of pure alkyd resin. This improvement of thermooxidative stability was more pronounced for AR65/TiO$_2$-DHBAOA during the first stage of degradation than for other investigated nanocomposites.

3.5. Barrier properties of AR65/TiO$_2$ nanocomposites

The cross-linking density of long oil alkyd resin is usually not enough to reduce diffusivity of permeating molecules through the prepared coating. On the other hand, the filler particles, compatible with polymer matrix and well dispersed in it, can be applied as good strategy to improve barrier properties of organic coatings [45–47]. The presence of NPs enhances the degree of tortuosity of the permeating molecules diffusion path through the polymer, by occupying the free volume within the polymer. Therefore, the water vapour barrier properties of the alkyd resin and prepared NCs were investigated by water vapour permeability measurements. Obtained results are presented in Figure 11 and listed in Table 2. According to these results it can be concluded that the presence of TiO$_2$ NPs surface modified with gallates and DHBAOA reduces *WVTR* of alkyd resin, whereby AR65/TiO$_2$-HG NC has the lowest *WVTR* value. Therefore, prepared NCs can be applied as efficient protection coating against corrosion of metal surfaces.

3.6. Tensile properties of AR65/TiO$_2$ nanocomposites

The stress-strain curves of pure alkyd resin and prepared NCs are given in Figure 12. From these results, values of the modulus of elasticity (E), stress at break (σ_B) and strain at break (ε_B) of the pure alkyd resin and prepared nanocomposites were determined and listed in Table 2. Modulus of elasticity of AR65 is higher than the value obtained for the prepared NCs, indicating that pure alkyd resin is stiffer than other investigated samples. Simultaneously, alkyd resin has also the lowest value of strain at break. The rigidity of the commercial alkyd resin originates from the presence of polyesters chains in its structure. On the other hand, the low value of strain at break comes from the relatively fast curing of alkyd resin, despite the presence of certain flexibility from
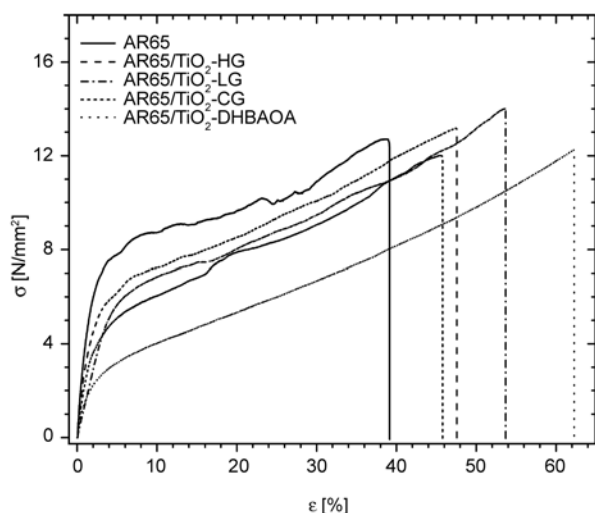
Figure 12. The dependence stress-strain of pure AR65 and AR65/TiO₂-HG, AR65/TiO₂-LG, AR65/TiO₂-CG and AR65/TiO₂-DHBAOA nanocomposites

fatty acids chains [48]. The stress-strain curves given in Figure 12 also show that tensile properties of prepared AR65/TiO$_2$ NCs are dependent on the type of NPs surface modification. After addition of surface modified TiO$_2$ NPs into AR65, the largest decrease in modulus and increase in strain at break was observed for AR65/TiO$_2$-DHBAOA nanocomposite, which is consistent with the lowest T_g value obtained for this NC. Furthermore, the increase of the gallates alkyl chain length from 6C (hexyl gallate) to 12C (lauryl gallate) induced lower E and higher σ_B and ε_B values. In contrast, further increase of the hydrophobic part length of the used gallic acid esters to 16C (cetyl gallate) led to increase of the modulus of elasticity and decrease of the stress and strain at break. The obtained results revealed that stiffness of the alkyd resin based on soy bean oil can be reduced by addition of 2 wt% of TiO$_2$ NPs surface modified with gallates, simultaneously leading to the formation of NC with relatively high values of σ_B and ε_B. The highest impact on the increase of

stress at break was observed after addition of TiO$_2$-LG NPs into the AR65.

3.7. Mechanical properties of AR65/TiO$_2$ nanocomposite coatings

The hardness of the prepared coatings was determined using König pendulum. From the obtained results, listed in Table 3, it can be observed that addition of TiO$_2$ NPs surface modified with gallic acid esters leads to the increase of surface hardness (König hardness) of the alkyd resin, while with increasing alkyl chain length of the applied gallate hardness decreased. The certain increase of the surface hardness of air dried alkyd coatings by addition of colloidal SiO$_2$ particles was also observed by Kurt *et al.* [49]. Furthermore, Bal and coworkers [50, 51] have found that NC coatings based on alkyd-melamine formaldehyde resin and modified silica, as well as films prepared from alkyd-phenol formaldehyde resin and organo clay have higher König hardness than pure resin. On the other hand, obtained results revealed that AR65/TiO$_2$-DHBAOA has slightly lower value of the König hardness than pure alkyd resin. The probable reason for such behavior could be the lowest cross-linking density of this sample. This NC sample has the lowest T_g, the lowest modulus of elasticity and the highest strain at break. Also, it has better dispersion of nanofiller in polymer matrix than other NCs. Furthermore, AR65/TiO$_2$-DHBAOA had the highest concentration of unsaturated double bonds before curing (additional double bounds originating from DHBAOA ligands), causing faster curing reaction, which can lead to the lower cross-linking density of cured sample. All this implies that this sample has the lowest cross-linking density and that was the reason why it showed the opposite behavior compared to the other NCs.

From the results listed in Table 3 it can be observed that impact strength of all investigated samples is

Table 3. Values of the König hardness, impact strength, adhesion and abrasion resistance of the pure alkyd resin and prepared nanocomposites (König hardness, adhesion and abrasion resistance were determined as average value of three measurements, while impact strength as average value of five measurements and values of König hardness and abrasion resistance are reported with a standard deviation) 80 in-lb corresponds to 9 J

Sample	König hardness [s]	Impact strength [in-lb]	Adhesion resistance (ISO 2409)	Abrasion resistance (wear index)
AR65	31±1	>80	Gt 0	103±10
AR65/TiO₂-HG	38±2	>80	Gt 0	140±11
AR65/TiO₂-LG	34±2	>80	Gt 0	109±9
AR65/TiO₂-CG	33±2	>80	Gt 0	121±10
AR65/TiO₂-DHBAOA	28±1	>80	Gt 0	115±12

larger than 80 in-lb (9 J), indicating good flexibility of the prepared coatings. Furthermore, adhesion resistance of the prepared coatings was determined according to the ISO 2409 standard and obtained results listed in Table 3 indicate that all examined coatings have very good adhesion to the metal substrate. The results of the abrasion resistance test of examined coatings are shown in Table 3. It could be seen that the wear index is higher for NC coatings, indicating the deterioration of abrasion resistance of alkyd coatings after addition of surface modified TiO_2 nanoparticles. It is well known that the quality of the interface between NPs and polymer matrics defines material capability to transfer stresses and elastic deformation from the polymer matrix to the nanofillers. According to the DSC results, NCs prepared in this work have lower T_g than pure alkyd resin, indicating the poor interaction between NPs and polymer matrix at the interface. Therefore, NPs are not able to bear the applied load and due to that the abrasion resistance of NCs cannot be better than that of the pure polymer matrix [52].

3.8. Gel content and chemical resistance of AR65/TiO₂ nanocomposite coatings

The gel content of the prepared films was determined according to the procedure described in the experimental section and obtained results are listed in Table 4. It can be observed that all examined samples have approximately the same gel content, which indicates that the presence of surface modified TiO_2 NPs has no significant influence on the content of residual soluble components.

The results of the chemical resistance investigation of the pure AR65 and prepared nanocomposite coat-

ings are given in Table 4. All examined samples show good resistance to distilled water, 1M HCl, 3% NaCl and sunflower oil and after 24 hours there was no change in the appearance of the examined coatings. Furthermore, nanocomposite coatings showed better resistance to 0.15% NaOH, acetone and ethanol than pure alkyd resin, but after certain time all NC films cracked.

4. Conclusions

Novel soy alkyd-based nanocomposite coatings were synthesized using TiO_2 NPs surface modified with hexyl, lauryl and cetyl gallate, and imine obtained from 3,4-dihydroxybenzaldehyde and oleylamine. Anatase TiO_2 NPs (average diameter of 3.9±0.9 nm) were prepared via acid catalyzed hydrolysis of titanium isopropoxide. FTIR and UV-Vis spectroscopy confirmed surface modification of TiO_2 NPs. Furthermore, TEM and XRD analysis revealed that morphology, crystal structure and crystallite size of TiO_2 NPs were not changed by surface modification of TiO_2 NPs, while the amount ligands adsorbed on the surface of TiO_2 NPs was calculated from TGA measurements. Experimental results presented in this work further demonstrated:

– Dynamic viscosity of AR65/TiO₂ dispersions is higher than for pure AR65 and it decreases with increasing frequency. AR65/TiO₂-DHBAOA dispersion exhibited the lowest η^* value, due to the lower hydrodynamic radius of TiO₂-DHBAOA NPs in AR65 than TiO_2 NPs surface modified with gallates.

– SEM analysis of the prepared NC coatings showed that surface modified TiO_2 NPs formed agglomerates in alkyd resin and that the size of TiO₂-

Table 4. The gel content and chemical resistance investigation of the pure alkyd resin and prepared nanocomposites (three specimens of each film were tested; gel content is reported with a standard deviation)

Solvent	AR65		AR65/TiO₂-HG		AR65/TiO₂-LG		AR65/TiO₂-CG		AR65/TiO₂-DHBAOA	
Gel% [%]	88.8±1.8		89.1±2.0		88.9±1.9		89.8±2.1		87.0±1.9	
Distilled water	24 h	(0)	24 h	(0)	24 h	(0)	24 h	(0)	24 h	(0)
1M HCl	24 h	(0)	24 h	(0)	24 h	(0)	24 h	(0)	24 h	(0)
0.15% NaOH	5 min	(1) d*	10 min	(1) d*	10 min	(1) d*	10 min	(1) d*	10 min	(1) l*
	70 min	(2)	70 min	(2)	70 min	(2)	70 min	(2)	70 min	(2)
	90 min	(3)	90 min	(3)	90 min	(3)	90 min	(3)	90 min	(3)
3% NaCl	24 h	(0)	24 h	(0)	24 h	(0)	24 h	(0)	24 h	(0)
Ethanol	21 min	(3)	35 min	(3)	36 min	(3)	32 min	(3)	37 min	(3)
Acetone	13 s	(3)	15 s	(3)	22 s	(3)	24 s	(3)	28 s	(3)
Sunflower oil	24 h	(0)	24 h	(0)	24 h	(0)	24 h	(0)	24 h	(0)

(0) completely unaffected, (1) unaffected, slightly color changed, (2) film swelled and (3) film cracked
*d – the change of the film color to darker, l – the change of the film color to lighter

DHBAOA agglomerates is smaller than the size of agglomerates formed by TiO_2 NPs surface modified with gallates.

– T_g of prepared NCs is lower than T_g of pure alkyd resin, indicating the absence of attractive interactions between NPs and polymer matrix. The change of the hydrophobic part length of gallates showed no significant influence on the T_g of prepared NCs.

– The presence of TiO_2 NPs surface modified with gallates had no significant influence on the thermooxidative stability of AR65, while TiO_2-DHBAOA NPs induced slightly better thermooxidative stability.

– All examined samples have approximately the same gel content, which indicates that the presence of surface modified TiO_2 NPs has no significant influence on the cross-linking density of the alkyd resin.

– The presence of TiO_2 NPs surface modified with gallates and DHBAOA reduced *WVTR*, modulus of elasticity and abrasion resistance of alkyd resin and improved strain at break and chemical resistance. Furthermore, all prepared coatings have good flexibility and very good adhesion to the metal substrate, and addition of TiO_2 NPs surface modified with gallates increased surface König hardness of the alkyd resin, while the presence of TiO_2-DHBAOA NPs had no significant influence on it.

Acknowledgements

References

[1] Hofland A.: Alkyd resins: From down and out to alive and kicking. Progress in Organic Coatings, **73**, 274–282 (2012).
DOI: 10.1016/j.porgcoat.2011.01.014

[2] Deligny P., Tuck N.: Resins for surface coatings: Alkyds and polyesters. Wiley, London (2000).

[3] Soucek M. D., Khattab T., Wu J.: Review of autoxidation and driers. Progress in Organic Coatings, **73**, 435–454 (2012).
DOI: 10.1016/j.porgcoat.2011.08.021

[4] Bal A., Güçlü G., Acar I., İyim T. B.: Effects of urea formaldehyde resin to film properties of alkyd–melamine formaldehyde resins containing organo clay. Progress in Organic Coatings, **68**, 363–365 (2010).
DOI: 10.1016/j.porgcoat.2010.03.006

[5] Alam M., Akram D., Sharmin E., Zafar F., Ahmad S.: Vegetable oil based eco-friendly coating materials: A review article. Arabian Journal of Chemistry, **7**, 469–479 (2014).
DOI: 10.1016/j.arabjc.2013.12.023

[6] Belgacem M. N., Gandini A.: Materials from vegetable oils: Major sources, properties and applications. in 'Monomers, polymers and composites from renewable resources' (eds.: Belgacem M. N., Gandini A.) Elsevier, Oxford, 39-66 (2008).

[7] Athawale V. D., Nimbalkar R. V.: Waterborne coatings based on renewable oil resources: An overview. Journal of the American Oil Chemists' Society, **88**, 159–185 (2011).
DOI: 10.1007/s11746-010-1668-9

[8] Güçlü G., Orbay M.: Alkyd resins synthesized from postconsumer PET bottles. Progress in Organic Coatings, **65**, 362–365 (2009).
DOI: 10.1016/j.porgcoat.2009.02.004

[9] Alidedeoglu A. H., Davis K., Robertson R., Smith C., Rawlins J. W., Morgan S. E.: Synthesis and evaluation of tetra(2,7-octadienyl) titanate as a reactive diluent for air-drying alkyd paints. Journal of Coatings Technology and Research, **8**, 45–52 (2011).
DOI: 10.1007/s11998-010-9276-z

[10] Atta A. M., El-Ghazawy R. A., El-Saeed A. M.: Corrosion protective coating based on alkyd resins derived from recycled poly (ethylene terephthalate) waste for carbon steel. International Journal of Electrochemical Science, **8**, 5136–5152 (2013).

[11] Ang D. T. C., Gan S. N.: Development of palm oil-based alkyds as UV curable coatings. Pigment and Resin Technology, **41**, 302–310 (2012).
DOI: 10.1108/03699421211264866

[12] Ataei S., Yahya R., Gan S. N.: Fast physical drying, high water and salt resistant coatings from non-drying vegetable oil. Progress in Organic Coatings, **72**, 703–708 (2011).
DOI: 10.1016/j.porgcoat.2011.07.013

[13] İşeri-Çağlar D., Baştürk E., Oktay B., Kahraman M. V.: Preparation and evaluation of linseed oil based alkyd paints. Progress in Organic Coatings, **77**, 81–86 (2014).
DOI: 10.1016/j.porgcoat.2013.08.005

[14] Boruah M., Gogoi P., Adhikari B., Dolui S. K.: Preparation and characterization of *Jatropha curcas* oil based alkyd resin suitable for surface coating. Progress in Organic Coatings, **74**, 596–602 (2012).
DOI: 10.1016/j.porgcoat.2012.02.007

[15] Bora M. M., Gogoi P., Deka D. C., Kakati D. K.: Synthesis and characterization of yellow oleander (*Thevetia peruviana*) seed oil-based alkyd resin. Industrial Crops and Products, **52**, 721–728 (2014).
DOI: 10.1016/j.indcrop.2013.11.012

[16] Araujo W. S., Margarit I. C. P., Mattos O. R., Fragata F. L., de Lima-Neto P.: Corrosion aspects of alkyd paints modified with linseed and soy oils. Electrochimica Acta, **55**, 6204–6211 (2010).
DOI: 10.1016/j.electacta.2010.03.088

[17] Atimuttigul V., Damrongsakkul S., Tanthapanichakoon W.: Effects of oil type on the properties of short oil alkyd coating materials. Korean Journal of Chemical Engineering, **23**, 672–677 (2006).
DOI: 10.1007/BF02706813

[18] Pathan S., Ahmad S.: s-triazine ring-modified waterborne alkyd: Synthesis, characterization, antibacterial, and electrochemical corrosion studies. ACS Sustainable Chemistry and Engineering, **1**, 1246–1257 (2013).
DOI: 10.1021/sc4001077

[19] Nalawade P. P., Mehta B., Pugh C., Soucek M. D.: Modified soybean oil as a reactive diluent: Synthesis and characterization. Journal of Polymer Science Part A: Polymer Chemistry, **52**, 3045–3059 (2014).
DOI: 10.1002/pola.27352

[20] Perera D. Y.: Effect of pigmentation on organic coating characteristics. Progress in Organic Coatings, **50**, 247–262 (2004).
DOI: 10.1016/j.porgcoat.2004.03.002

[21] Popa M. V., Drob P., Vasilescu E., Mirza-Rosca J. C., Santana Lopez A., Vasilescu C., Drob S. I.: The pigment influence on the anticorrosive performance of some alkyd films. Materials Chemistry and Physics, **100**, 296–303 (2006).
DOI: 10.1016/j.matchemphys.2006.01.002

[22] Bhavsar R., Raj R., Parmar R.: Studies of sedimentation behaviour of high pigmented alkyd primer: A rheological approach. Progress in Organic Coatings, **76**, 852–857 (2013).
DOI: 10.1016/j.porgcoat.2013.02.009

[23] Kamat P. V.: Photophysical, photochemical and photocatalytic aspects of metal nanoparticles. The Journal of Physical Chemistry B, **106**, 7729–7744 (2002).
DOI: 10.1021/jp0209289

[24] Bajpai O. P., Kamdi J. B., Selvakumar M., Ram S., Khastgir D., Chattopadhyay S.: Effect of surface modification of $BiFeO_3$ on the dielectric, ferroelectric, magneto-dielectric properties of polyvinylacetate/$BiFeO_3$ nanocomposites. Express Polymer Letters, **8**, 669–681 (2014).
DOI: 10.3144/expresspolymlett.2014.70

[25] Ju S., Chen M., Zhang H., Zhang Z.: Dielectric properties of nanosilica/low-density polyethylene composites: The surface chemistry of nanoparticles and deep traps induced by nanoparticles. Express Polymer Letters, **8**, 682–691 (2014).
DOI: 10.3144/expresspolymlett.2014.71

[26] Dhoke S. K., Bhandari R., Khanna A. S.: Effect of nano-ZnO addition on the silicone-modified alkyd-based waterborne coatings on its mechanical and heat-resistance properties. Progress in Organic Coatings, **64**, 39–46 (2009).
DOI: 10.1016/j.porgcoat.2008.07.007

[27] Dhoke S. K., Khanna A. S.: Study on electrochemical behavior of nano-ZnO modified alkyd-based waterborne coatings. Journal of Applied Polymer Science, **113**, 2232–2237 (2009).
DOI: 10.1002/app.30276

[28] Radoman T. S., Džunuzović J. V., Jeremić K. B., Marinković A. D., Spasojević P. M., Popović I. G., Džunuzović E. S.: The influence of the size and surface modification of TiO_2 nanoparticles on the rheological properties of alkyd resin (in Serbian). Hemijska Industrija, **67**, 923–932 (2013).
DOI: 10.2298/HEMIND131106081R

[29] Shi H., Liu F., Han E., Wei Y.: Effects of nano pigments on the corrosion resistance of alkyd coating. Journal of Materials Science and Technology, **23**, 551–558 (2007).

[30] Deyab M. A., Keera S. T.: Effect of nano-TiO_2 particles size on the corrosion resistance of alkyd coating. Materials Chemistry and Physics, **146**, 406–411 (2014).
DOI: 10.1016/j.matchemphys.2014.03.045

[31] Subbiah G., Premanathan M., Kim S. J., Krishnamoorthy K., Jeyasubramanian K.: Preparation of TiO_2 nanopaint using ball milling process and investigation on its antibacterial properties. Materials Express, **4**, 393–399 (2014).
DOI: 10.1166/mex.2014.1185

[32] Dhoke S. K., Khanna A. S.: Effect of nano-Fe_2O_3 particles on the corrosion behavior of alkyd based waterborne coatings. Corrosion Science, **51**, 6–20 (2009).
DOI: 10.1016/j.corsci.2008.09.028

[33] Dhoke S. K., Khanna A. S.: Electrochemical behavior of nano-iron oxide modified alkyd based waterborne coatings. Materials Chemistry and Physics, **117**, 550–556 (2009).
DOI: 10.1016/j.matchemphys.2009.07.010

[34] Rahman O. U., Ahmad S.: Physico-mechanical and electrochemical corrosion behavior of soy alkyd/Fe_3O_4 nanocomposite coatings. RSC Advances, 4, 14936-14947 (2014).
DOI: 10.1039/c3ra48068b

[35] Dhoke S. K., Khanna A. S.: Electrochemical impedance spectroscopy (EIS) study of nano-alumina modified alkyd based waterborne coatings. Progress in Organic Coatings, **74**, 92–99 (2012).
DOI: 10.1016/j.porgcoat.2011.11.020

[36] Dhoke S. K., Sinha T. J. M., Khanna A. S.: Effect of nano-Al_2O_3 particles on the corrosion behavior of alkyd based waterborne coatings. Journal of Coatings Technology and Research, **6**, 353–368 (2009).
DOI: 10.1007/s11998-008-9127-3

[37] Krishnamoorthy K., Premanathan M., Veerapandian M., Kim S. J.: Nanostructured molybdenum oxide-based antibacterial paint: Effective growth inhibition of various pathogenic bacteria. Nanotechnology, **25**, 315101/1–315101/10 (2014).
DOI: 10.1088/0957-4484/25/31/315101

[38] Radoman T. S., Džunuzović J. V., Jeremić K. B., Grgur B. N., Milićević D. S., Popović I. G., Džunuzović E. S.: Improvement of epoxy resin properties by incorporation of TiO_2 nanoparticles surface modified with gallic acid esters. Materials and Design, **62**, 158–167 (2014).
DOI: 10.1016/j.matdes.2014.05.015

[39] O'Regan B., Moser J., Anderson M., Graetzel M.: Vectorial electron injection into transparent semiconductor membranes and electric field effects on the dynamics of light-induced charge separation. The Journal of Physical Chemistry, **94**, 8720–8726 (1990).
DOI: 10.1021/j100387a017

[40] Coppens B., Sas B., van Hemel J.: Method of synthesizing alkyl gallates. WO2001030299 (2001).

[41] Cheary R. W., Coelho A.: A fundamental parameters approach to X-ray line-profile fitting. Journal of Applied Crystallography, **25**, 109–121 (1992).
DOI: 10.1107/S0021889891010804

[42] Rajh T., Nedeljković J. M., Chen L. X., Poluektov O., Thurnauer M. C.: Improving optical and charge separation properties of nanocrystalline TiO_2 by surface modification with vitamin C. The Journal of Physical Chemistry B, **103**, 3515–3519 (1999).
DOI: 10.1021/jp9901904

[43] Janković I. A., Šaponjić Z. V., Džunuzović E. S., Nedeljković J. M.: New hybrid properties of TiO_2 nanoparticles surface modified with catecholate type ligands. Nanoscale Research Letters, **5**, 81–88 (2010).
DOI: 10.1007/s11671-009-9447-y

[44] Ploeger R., Scalarone D., Chiantore O.: Thermal analytical study of the oxidative stability of artists' alkyd paints. Polymer Degradation and Stability, **94**, 2036–2041 (2009).
DOI: 10.1016/j.polymdegradstab.2009.07.018

[45] Shreepathi S., Naik S. M., Vattipalli M. R.: Water transportation through organic coatings: Correlation between electrochemical impedance measurements, gravimetry, and water vapor permeability. Journal of Coatings Technology and Research, **9**, 411–422 (2012).
DOI: 10.1007/s11998-011-9376-4

[46] Aulin C., Salazar-Alvarez G., Lindström T.: High strength, flexible and transparent nanofibrillated cellulose–nanoclay biohybrid films with tunable oxygen and water vapor permeability. Nanoscale, **4**, 6622–6628 (2012).
DOI: 10.1039/c2nr31726e

[47] Pavlacky E., Ravindran N., Webster D. C.: Novel *in situ* synthesis in the preparation of ultraviolet-curable nanocomposite barrier coatings. Journal of Applied Polymer Science, **125**, 3836–3848 (2012).
DOI: 10.1002/app.36716

[48] Wutticharoenwong K., Dziczkowski J., Soucek M. D.: Tung based reactive diluents for alkyd systems: Film properties. Progress in Organic Coatings, **73**, 283–290 (2012).
DOI: 10.1016/j.porgcoat.2011.03.017

[49] Kurt İ., Acar I., Güçlü G.: Preparation and characterization of water reducible alkyd resin/colloidal silica nanocomposite coatings. Progress in Organic Coatings, **77**, 949–956 (2014).
DOI: 10.1016/j.porgcoat.2014.01.017

[50] Bal A., Acar I., Güçlü G.: A novel type nanocomposite coating based on alkyd-melamine formaldehyde resin containing modified silica: Preparation and film properties. Journal of Applied Polymer Science, **125**, E85–E92 (2012).
DOI: 10.1002/app.35029

[51] Bal A., Acar I., Güçlü G., İyim T. B.: Effects of organo clay on film properties of alkyd-phenol formaldehyde resins. Pigment and Resin Technology, **41**, 100–103 (2012).
DOI: 10.1108/03699421211210757

[52] Kurahatti R. V., Surendranathan A. O., Srivastava S., Singh N., Ramesh Kumar A. V., Suresha B.: Role of zirconia filler on friction and dry sliding wear behaviour of bismaleimide nanocomposites. Materials and Design, **32**, 2644–2649 (2011).
DOI: 10.1016/j.matdes.2011.01.030

Assisted heterogeneous multinucleation and bubble growth in semicrystalline ethylene-vinyl acetate copolymer/expanded graphite nanocomposite foams: Control of morphology and viscoelastic properties

O. Yousefzade, F. Hemmati, H. Garmabi, M. Mahdavi*

Department of Polymer Engineering and Color Technology, Amirkabir University of Technology, No. 424, Hafez Ave., Tehran, Iran

Abstract. Nanocomposite foams of ethylene-vinyl acetate copolymer (EVA) reinforced by expanded graphite (EG) were prepared using supercritical nitrogen in batch foaming process. Effects of EG particle size, crosslinking of EVA chains and foaming temperature on the cell morphology and foam viscoelastic properties were investigated. EG sheet surface interestingly provide multiple heterogeneous nucleation sites for bubbles. This role is considerably intensified by incorporating lower loadings of EG with higher aspect ratio. The amorphous and non-crosslinked domains of EVA matrix constitute denser bubble areas. Higher void fraction and more uniform cell structure is achieved for non-crosslinked EVA/EG nanocomposites foamed at higher temperatures. With regard to the structural variation, the void fraction of foam samples decreases with increasing the EG content. Storage and loss moduli were analyzed to study the viscoelastic properties of nanocomposite foams. Surprisingly, the foaming process of EVA results in a drastic reduction in loss and storage moduli regardless of whether the thermoplastic matrix contains EG nanofiller or not. For the EVA/EG foams with the same composition, the nanocomposite having higher void fraction shows relatively lower loss modulus and more restricted molecular movements. The study findings have verified that the dynamics of polymer chains varies after foaming EVA matrix in the presence of EG.

Keywords: nanocomposites, foam, expanded graphite, morphology, viscoelastic properties

1. Introduction

The creation of polymeric cellular structures using environmentally friendly physical blowing agents in the supercritical or nonsupercritical state has been of significant interest in the past decades. Nitrogen and carbon dioxide have been applied in the polymeric foaming process as environmentally friendly blowing agents. An overview on the carbon dioxide and nitrogen assisted foaming process of glassy polymers is provided by Fleming and Kazarian [1] and Almanza *et al*. [2]. A literature review of polymeric foams shows that there are many studies on the preparation of high-performance polymeric foams by increasing the number of cells (bubbles) and decreasing cell size. To seek this aim, different continuous and discontinuous process variants have been developed to prepare microcellular foam morphologies from glassy polymers [1, 3, 4]. Similarly, there are some reports about clay reinforced nanocomposite foams based on semicrystalline polymers [5–8]. Moreover, microcellular foaming process is one of the techniques that have been studied for this purpose [9–16]. By rapid pressure quenching [17], melt blending using polymers with high glass tran-

---

sition temperature (T_g) [4] and incorporating nano-clay into polymers [7], micron or submicron size cellular structures have been successfully obtained. Most polymers investigated in the previous researches have been amorphous, though there are several papers discussing microcellular foams of semi-crystalline polymers [15, 16, 18–23].

The influences of nanofiller characteristics such as aspect ratio and surface chemistry on the properties of solid polymer nanocomposites have been extensively studied [24–27]. However, the behavior of polymer composite foams is more complex than that of solid composites. The interactions between filler surface, bubbles and matrix chains in pairs and their effects on the properties of composite foams have not been fully understood. In addition, the characteristics of one component may affect the properties of the others. Therefore, to obtain polymer nanocomposite foams with optimal properties such as high electromagnetic wave shielding effectiveness or strength, a better understanding of the interactions between nanofillers, bubbles and matrix chains in pairs is an essential prerequisite. The impact of processing methods on the nanocomposite foam morphology has been examined while the aspect ratio changes of nanofillers due to the alterations of processing variables have not been considered [12, 28]. The filler aspect ratio most likely changes the foam morphology that requires to be explored.

For polymeric foaming processes using supercritical fluids, the most controllable parameters are processing variables such as sorption pressure and temperature [15]. The influence of the sorption pressure on the foam morphology has been studied at a constant sorption temperature. Besides, diffusivity of the supercritical fluid can be highly influential [15]. Furthermore, in the case of polymer nano/microcomposites, the filler characteristics like size, aspect ratio, geometric shape and filler/polymer interaction as well as the used fluid/gas are crucially important because the bubble size, shape and formation mechanism are greatly impacted by these factors [28, 29].

In addition, dynamic mechanical thermal analysis (DMTA) has emerged as one of the most powerful tools available for viscoelastic property study of plastic materials. Since all polymers are viscoelastic in nature, this analytical method suits perfectly to evaluate the complex phenomena presented by

polymeric materials including the main chain and side-groups motions and, in particular, different relaxations of polymer chains [30]. As a result, this turns it into a powerful technique for characterizing different polymer structures such as plastic foams. Along with this advantage, there is a well-known relationship between the damping capabilities of a certain polymer and the dynamic mechanical responses that can be also investigated by DMTA [31]. Thus this method has been applied in the present work.

Because there are few published researches on semi-crystalline polymer foams containing expanded graphite (EG), microcellular nanocomposite foams of semicrystalline ethylene-vinyl acetate copolymer (EVA) and EG were chosen as the subject of this study. These foams possessing a wide range of relative density and varied cellular structures have been obtained and the influences of filler particle size, crosslinking of EVA chains and foaming temperature as a processing parameter on the nanocomposite foam morphology, void fraction and the semi-crystalline polymer viscoelastic properties have been evaluated. Different loadings of EG below and above the electrical and rheological percolation thresholds have been used to show the properties of solid and foamed nanocomposites. Efforts have been particularly made to show that the damping capability of nanocomposite is reduced by changing the microstructure to foam and molecular movements are retarded even more for the nanocomposite foams with larger void fractions. Moreover, for the first time, to the best of our knowledge, the effects of EG particle size on the foaming behavior of EVA-based nanocomposites have been researched and the heterogeneous multinucleation role of EG nanosheets has been verified. Our findings show that by incorporating large EG nanosheets at small loadings, i.e. less than 5 wt%, into non-crosslinked EVA and foaming these nanocomposites at high temperatures, very light EVA nanocomposite foams with void fractions about 70% can be obtained. In addition, for these nanocomposite foams, the optimal cell morphology with highest cell density and broadest cell size distribution is attained.

2. Experimental section
2.1. Materials
Two types of expanded graphite powder having a sheet-like structure and different aspect ratio were

prepared by intensely heating of graphite intercalation compound (GIC) at 1000°C for 30 sec. After heating, these powders were sieved. These EGs are EX100 and EX1500 grades (purchased from Ito Kokuen Co., Mie, Japan), which have an average sheet size of 149 and 2 μm, respectively. Since the thickness of graphite sheets are in the range of a few nanometers, EX100 has larger aspect ratio and the other one is the smaller aspect ratio EG used in this work. In our previous study, however, the morphology of heated and sieved expanded graphites was investigated before melt-compounding process by using microscopic observations. The SEM micrographs of pure expanded graphites showed that EX100 has much larger aspect ratio than EX1500. In addition, the morphology of EVA/EG nanocomposites was also evaluated and it was found that the graphite aspect ratio in the nanocomposite filled with EX100 is much larger than the nanocomposite containing EX1500 regardless of EG loading. However, the two-step melt process that was employed for melt-compounding of EVA and graphite filler has consisted of a vigorous elogational and shear flow. These flow fields have reduced the graphite sheet size. Despite this fact, the nanocomposites containing EX100 have larger aspect ratio sheets. The observed morphologies for the prepared nanocomposites have been delaminated and intercalated. Intercalation of graphite stacks has been completely

obvious in the micrographs of nanocomposites having different loadings of EX100 and EX1500 graphites (refer to [30] for more information).

A commercial grade of ethylene vinyl acetate copolymer with 19 wt% vinyl acetate comonomer (VAc) content (Seetec VS430) was purchased from Hyundai Co. (Sosan-gun, South Korea). One of the common crosslinking agents of EVA thermoplastic is peroxide chemicals, such as dicumyl peroxide (DCP) that was supplied by Merck KGaA, Darmstadt, Germany.

2.2. Sample preparation

Details of solid nanocomposite preparation were presented in our previous study [30]. The aforementioned EGs with different sizes were used to obtain the nanocomposites. For producing microcellular nanocomposite foams, the sheets of specimens with thickness of 1 mm were molded at 110°C and then batch foaming process was conducted in a high-pressure system. Samples were placed in the high-pressure vessel, then N_2 gas was fed to the pressure vessel. The vessel was kept at a constant pressure. Besides the whole system was kept at a constant temperature of 85°C for 4 h to allow nitrogen gas to saturate the sample and attain the equilibrium state. Next, the samples were foamed at temperatures above and below the crystallization temperature of EVA matrix, i.e. at 70 and 50°C respectively. After

Table 1. Sample codes with different formulations and processing conditions

Sample code	Crosslinking state	EG loading [wt%]	EG size [μm]	Foaming state	Foaming temperature [°C]
EVA	non-crosslinked	0	–	unfoamed	–
EV6EG149	non-crosslinked	6	149	unfoamed	–
EV6EG2	non-crosslinked	6	2	unfoamed	–
CEV6G149	crosslinked	6	149	unfoamed	–
EVFT50	non-crosslinked	0	–	foamed	50
EVxEG149FT50	non-crosslinked	variable*	149	foamed	50
EV6EG149FT50	non-crosslinked	6	149	foamed	50
EVxEG2FT50	non-crosslinked	variable*	2	foamed	50
EV6EG2FT50	non-crosslinked	6	2	foamed	50
EV15EG2FT50	non-crosslinked	15	2	foamed	50
EVxEG149FT70	non-crosslinked	variable*	149	foamed	70
EV4EG149FT70	non-crosslinked	4	149	foamed	70
EV6EG149FT70	non-crosslinked	6	149	foamed	70
EV15EG149FT70	non-crosslinked	15	149	foamed	70
EV6EG2FT70	non-crosslinked	6	2	foamed	70
CEVxEG149FT50	crosslinked	variable*	149	foamed	50
CEV6EG149FT50	crosslinked	6	149	foamed	50
CEVxEG2FT50	crosslinked	variable*	2	foamed	50
CEV6EG149FT70	crosslinked	6	149	foamed	70

*The EG loading for these samples is variable in the range of 0 to 30 wt%.

the saturation of sample at a constant pressure of 11.5 MPa, the pressure was then rapidly released and the resultant foam morphology was fixed by cooling water.

In the remaining parts, the abbreviated codes will be used for the obtained samples according to different parameters, which are summarized in Table 1.

In the abbreviated codes, C, EV, EG and FT respectively stand for crosslinked, EVA, expanded graphite and foaming temperature. If the letter 'C' is used before the code, it will show that the EVA matrix was chemically crosslinked. The numbers used before and after the letter 'EG' respectively show the EG loading and sheet size. The foaming temperature, 50°C or 70°C, is a number after 'FT'. Besides, for the solid samples, unformed ones, 'FT' will be omitted from the code like EV6G2. Similarly, for the samples that do not contain EG, 'EG' letter is not included in the codes.

2.3. Characterization methods

Scanning electron microscopy (SEM) of EVA/EG nanocomposite foams were performed on the cryofractured surfaces using a Seron Technologies Inc. Scanning Electron Microscope (Gyeonggi-do, Korea). The samples were subjected to brittle fracture in liquid nitrogen, and then the fractured surfaces were gold sputtered prior to the examination. Bubble size and Bubble size distribution were measured using Image Pro plus software (Media Cybernetics Inc., USA). Dynamic mechanical thermal characteristics of the obtained foam samples with thickness of 1–2 mm were evaluated using a DMTA analyzer (Triton Co. Lincolnshire, UK) under tension mode. The temperature sweep measurements were carried out over the temperature range of –50 to 50°C, at a frequency of 1 Hz and a heating rate of 2°C/min. For determination of the void fraction, densities of the obtained foams were measured by solvent displacement method following the standard of ASTM D792. The void fraction of the foam samples is calculated according to ASTM D2734 by using Equation (1):

$$V_f = \frac{d_u - d_f}{d_u} \qquad (1)$$

where V_f, d_u and d_f are the void fraction of foam, density of unfoamed and foamed nanocomposites, respectively.

3. Result and discussion

3.1. Morphology

The foaming process of nitrogen-swollen polymer occurs after destabilizing the thermodynamic equilibrium state, which is induced by quenching the pressure here. During the pressure quenching, the polymer mixture becomes supersaturated with nitrogen gas, which leads to cell nucleation and growth. Depending on the melting temperature or glass transition temperature of polymer, the matrix can vitrify, thereby suppressing cell growth. However, for EVA copolymer as matrix, only the melting temperature is required to be considered, since the glass transition temperature is far below the processing temperatures.

3.1.1. Effects of EG particle size

One of the parameters, which determines the cell morphology of a nanocomposite foam, is the dispersion and delamination state of nanofiller in the polymer matrix of solid nanocomposite before any foaming process. In our previous study [30], the effect of two-step melt mixing process on the dispersion of EG particles in EVA copolymer matrix was investigated. As mentioned, better dispersion state of nanofiller in polymer matrix changes the foam morphology significantly and leads to higher cell density and narrower cell size distribution. In a similar manner, the cell size and density are considerably related to the filler loading on account of the profound impact of particle content on the dispersion state, thereby affecting the accessible solid surface area for cell heterogeneous nucleation. In other words, the nanofiller aggregation is decreased at lower particle loadings, whereupon the efficiency of fillers in providing nucleation sites and foaming will improve. The effect of EG content on the foam morphology is shown in Figure 1. More bubbles in the nanocomposite foam sample filled with 15 wt% of EG are seen. Measured cell size and cell size distribution were presented in Table 2. The average cell size of EV15EG149FT70 sample is lower than the one for EV4EG149FT70 foam. At higher filler loading approximately equal to the EG percolation threshold, more aggregates of particles remain unchanged and consequently, worsen the performance of EG particle surface in cell nucleation process, thus the filler effectiveness in this process is weakened lower than that is expected. The aggregates of graphite at higher loading can be observed in Figure 1b.
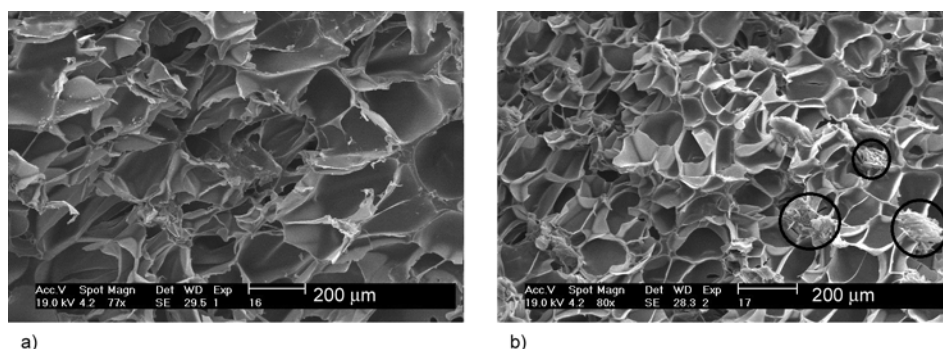
Figure 1. SEM micrographs of EVA/EG nanocomposite foams: (a) EV4EG149FT70 and (b) EV15EG149FT70; effect of EG loading on cell morphology. The black circles show some of graphite aggregates.

According to the nucleation theory, the classical theory is an approach that is currently used to describe the bubble nucleation in polymer foams, although its prediction on the nucleation rate can be easily off by several orders of magnitude. Among the polymer foaming community, the discrepancy between the classical theory and experimental results is sometimes attributed to the intervening heterogeneous nucleation provided by filler solid surface and has led to the classical theory modifications by incorporating certain aspects specific to the polymer foaming process [9, 32–34]. Nanoparticles have been validated that undoubtedly serve with heterogeneous nucleation sites and their influence on the cell density has been qualitatively represented by the classical nucleation theory [32, 34]. In heterogeneous nucleation process, the highest nucleation efficiency can be achieved only if the nucleation on the nucleant surface is energetically favored comparing with its homogeneous counterpart and the nucleant is well dispersed in the polymer matrix. In most cases, the measured cell density is much lower than the potential nucleant density, implying that either the nucleant surface is not energetically favored, or the dispersion state of nucleant is not good.

In addition, the aspect ratio of filler is another determinant of particle effectiveness in heterogeneous
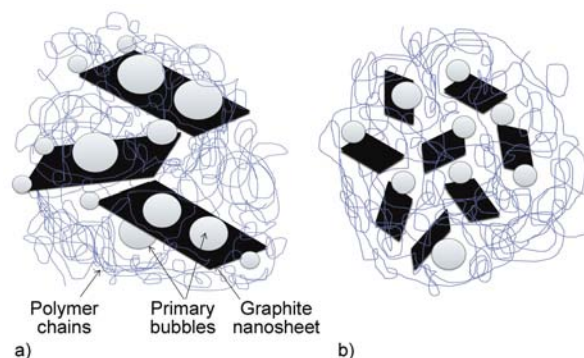
Figure 2. A schematic indicating the possible nucleation mechanism of EG particles: (a) each EG particle provides multiple nucleation sites; (b) each EG particle acts as a single nucleation site

nucleation process. As the filler aspect ratio increases, a single particle may shift from nucleating one bubble to simultaneously initiating multiple bubbles [29]. Therefore, the number of possible heterogeneous nucleation sites is most probably higher than the number of expanded graphite sheets owing to the potential for sidewall nucleation, which is schematically shown in Figure 2. The possibility of this happening is higher for larger nanosheets. This phenomenon provides a proof that for the nanocomposites filled with expanded graphite with high particle size or aspect ratio, more than one heterogeneous nucleation site is likely to be accessible along a given expanded graphite nanosheet.

As shown in Figure 3, different cell morphologies can be realized for the nanocomposite foams filled with EX100 and EX1500. Higher cell density and broader cell size distribution of sample filled with EX100 give evidence for stronger multinucleation role of EX100, which stems from larger solid surface area available for heterogeneous bubble nucleation (See the results of EV6EG2FT50 and EV6EG149FT50 samples in Table 2). Furthermore, it can be discerned in this figure that many cells are grown and

Table 2. Average cell size and the standard deviation of cell size for different EVA/EG foams

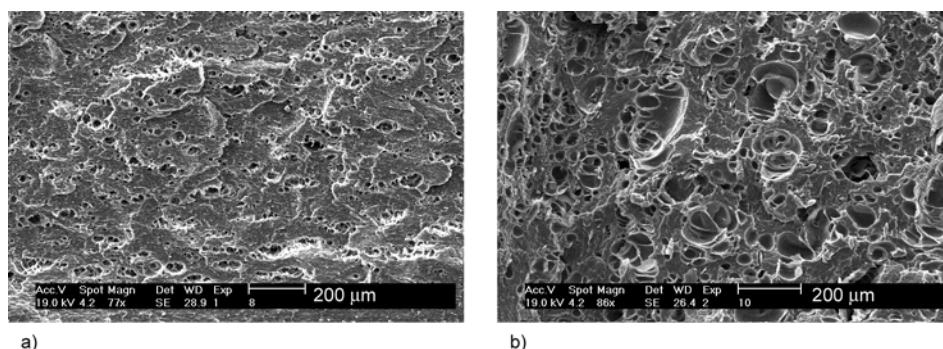| Sample	Average cell size [μm]	Standard deviation [μm]	Standard deviation [%]
EV4EG149FT70	138	52	37
EV15EG149FT70	79	30	37
EV6EG2FT50	23	11	47
EV6EG149FT50	34	21	61
CEV6EG149FT70	96	55	57
EV6EG149FT70	112	57	50

Figure 3. SEM micrographs of nanocomposite foams: (a) EV6EG2FT50 and (b) EV6EG149FT50; effect of EG particle size

impinged into each other especially in the foam sample containing EX100. According to Table 2, as it is expected, the heterogeneity of bubble size in the sample containing EX100 (EV6EG149FT50) is much more than the sample containing EX1500 (EV6EG2FT50).

3.1.2. Effects of EVA crosslinking

Another influential factor in cell evolution of polymeric foams is the polymer properties as matrix. Molecular weight and distribution, chemical and physical architecture of polymer chains, and the fluidity of polymer are substantially important to determine the cell nucleation and growth behavior [23]. Besides, the melt strength of polymer is another notable key to characterize the foams properties. For EVA copolymer as a thermoplastic matrix, the crosslinking of polymer chains is the best way to increase the melt strength. Therefore, in this study the crosslinking and foaming process of solid nanocomposites were completed in two separate steps, different from other investigations [35–37]. First, the chemical crosslinking of EVA copolymer macromolecules was carried out in the compression molding process. Second, the cured samples were foamed in the autoclave at the same conditions mentioned before. The differences in cell morphologies of cured and noncured foam samples are shown in Figure 4. Considering the fact that all foam samples were foamed under the same conditions, more nonfoamed regions of cured samples demonstrate that the presence of chemical crosslinks among polymer chains affects both cell nucleation and cell growth stages of foaming process. These stages are influenced respectively by lowering the gas diffusivity, i.e. causing insufficient nitrogen saturation state, and intensifying the local melt flow index of polymer. The results that are gathered in Table 2 show that CEV6EG149FT70

sample has much lower average cell size than EV6EG149FT70 foam.

3.1.3. Effects of foaming temperature

As mentioned earlier, along with the material parameters, the processing ones such as the foaming pressure and temperature also impact on the cell morphology and thereby, changing the foam physical and mechanical properties. In accordance with the classical nucleation theory, the cell density and the bubble shape are affected by the foaming pressure or pressure sharp drop during foaming process. In all related researches, it has been demonstrated that the number of cells per unit volume increases and the average cell size decreases by subjecting the matrix to a larger pressure decline [14, 15, 18, 25]. Contrary to the foaming pressure, the effects of foaming temperature on the cell morphology have not been understood precisely. However, it has been shown that temperature heterogeneity in polymer yields uneven foam morphologies. In addition, high temperature foaming process promotes the formation of large cells with wide size distribution (compare the results of EV6EG149FT50 and EV6EG149FT70 in Table 2), whereas lower temperatures particularly those closer to the T_g of the polymer-gas solution results in the foams with possessing a relatively uniform microcellular core [15].

As can be found in Figure 4 and Table 2, different cell morphologies are attained by varying the foaming temperature above and below the EVA crystallization temperature. Similar to different graphite structures, the crystalline regions of EVA matrix are impermeable and act as physical obstacles to dissolving the nitrogen gas in polymer and consequently, increase the nucleation activation energy. As a direct result, some nonfoamed regions can observed in the micrographs of foam samples prepared below the EVA
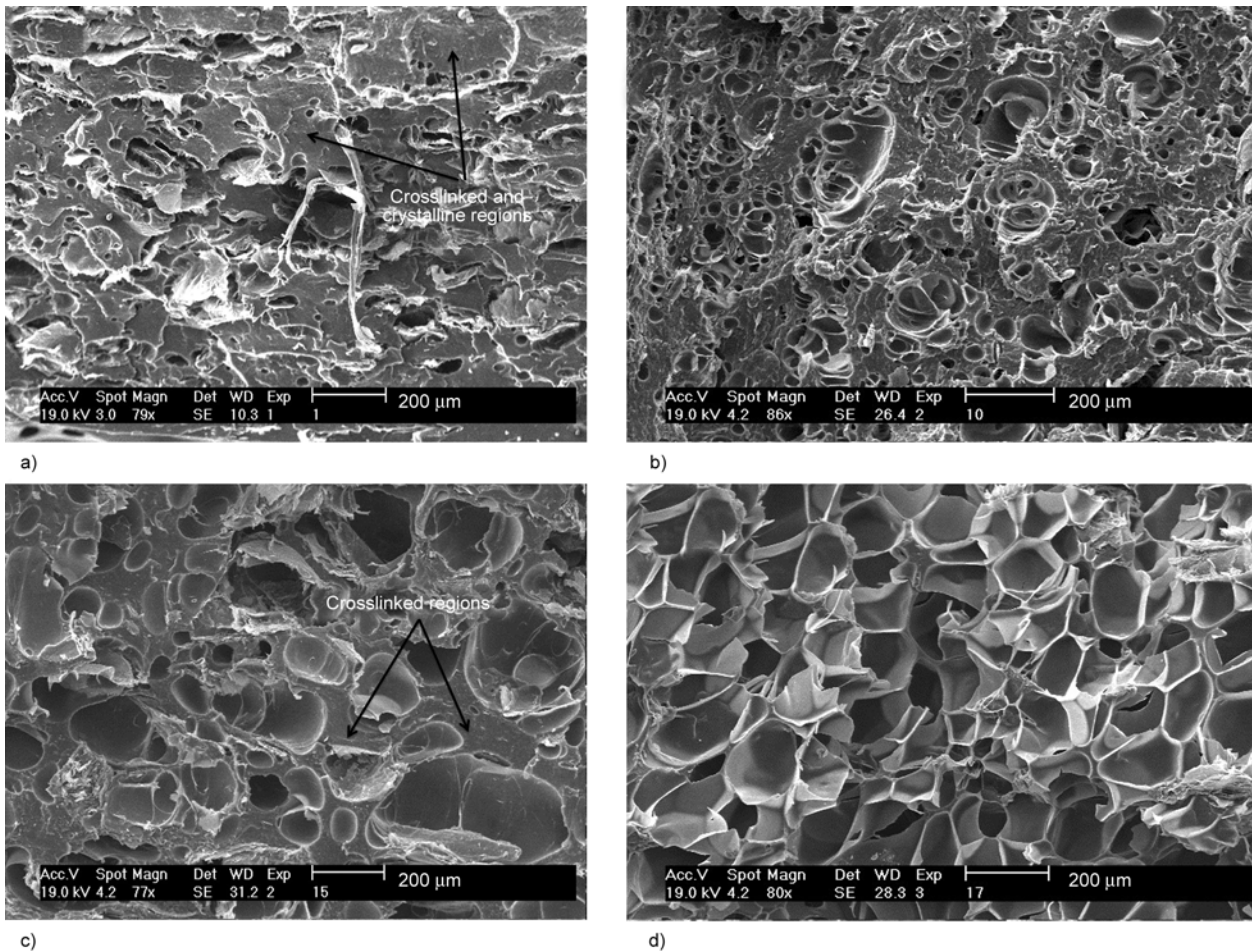
Figure 4. SEM micrographs of nanocomposite foams: (a) CEV6EG149FT50; (b) EV6EG149FT50; (c) CEV6EG149FT70 and (d) EV6EG149FT70; effect of foaming temperature and crosslinking of polymer chains

crystalline meltig point (Figure 4a and 4b). Above the crystalline meltig point, the gas molecules have enough energy to diffuse through the polymer chains and obtain the primary bubbles. Moreover, above the crystalline meltig point the polymer chains have enough mobility to allow the bubbles to grow. Therefore, larger cells are evident in the samples foamed at higher temperature (Figure 4c and 4d). Details about the melting and crystallization behavior of EVA copolymer in the presence of expanded graphite are presented in a previous study [30].

3.2. Void fraction

Physical properties of polymeric foams depend mainly on three parameters: cellular microstructure or architecture, intrinsic characteristics of polymer that constitutes the solid framework and relative density or void fraction. It seems that the void fraction or relative foam density is the most notable physical characteristic of foam sample [38].

Figure 5 illustrates the effects of aforementioned parameters on the void fraction of EVA/EG nano-
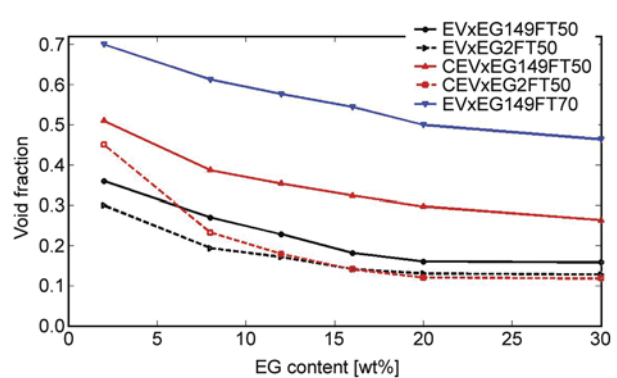
Figure 5. Void fraction versus EG content of foam samples; effect of material and processing parameters. The standard deviation for all samples is less than 3%.

composite foams. For all types of these foams, the void fraction is diminished by increasing the EG loading due to the larger accessible surface area for bubble heterogeneous nucleation and correspondingly, the formation of larger quantity of smaller cells. In addition, the existence of more EG aggregates at higher loadings of nanofiller lower the nucleation efficiency.

The nanocomposite foams containing EX100, which are prepared at the temperature above the crystallization point, show the maximum void fractions, whereas the nanocomposite foams including EX1500 that are prepared at the temperature below the crystallization temperature, have comparatively the minimum amounts of void fraction. According to the SEM micrographs, the foam sample containing EX100 with higher particle size possesses larger cell size and broader cell size distribution owing to the growth of more bubbles in the foaming process in comparison with the EX1500 incorporated foams. Another influential factor in the cell formation process particularly at lower foaming temperature is the crystallinity weight fraction of solid composites. It was found in the previous paper that the nanocomposites containing EX100 show larger degree of crystallinity than EVA/EX1500 solid samples [30]. Therefore, more crystalline regions of EVA/EX100 samples diminish the accessible domain area for bubble nucleation and growth. Furthermore, the nanocomposite foams obtained above the EVA crystallization temperature have relatively higher void fraction, which stems from large accessible matrix domains for cell nucleation and growth. One of the most striking features of Figure 5 is that for the nanocomposite foams including more than 15 wt% EG, the void fraction approximately reaches a plateau. In other words, after a certain content of EG particles, the void fraction of foam samples becomes fixed and a final plateau can be observed for highly filled nanocomposites regardless of the foam type. Seemingly, the mutual EG influences on providing heterogeneous cell nucleation sites and retarding the bubble growth in foaming process remains roughly constant at high filler loadings. Another pronounced feature of this graph is the comparatively lower void fraction of crosslinked EVA foam samples. The void fraction of these samples is significantly smaller than that of non-crosslinked EVA samples and is further supported by the morphology of these foam samples. As discussed before, the crosslinked EVA/EG foams have some crosslinked regions that are free from bubbles, thereby reducing the available matrix domains for cell formation and growth.

3.3. Dynamic mechanical analysis of foams

There are distinct relaxation processes for the EVA copolymer chains that relate to the crystalline phase (comprised of polymethylenic segments), the inter-facial regions (consisting of both ethylenic and VAc segments) and the complex amorphous phase (composed of noncrystallized methylenic segments and VAc units). These relaxation processes can be denoted by the respective transitions: α, β, and γ, which refer to the main transition, VAc segments, and the methylenic units. In the previous study, the effects of EG particle size on the DMTA results were discussed [30]. However, in the present work, the storage and loss moduli were recorded as a function of temperature for the foam samples having unequal EG particle size and different foaming temperatures. In addition, the influence of EVA crosslinking was also evaluated as a material parameter.

3.3.1. Effects of EG particle size

Figure 6 shows the storage and loss moduli of the prepared foams with different particle size. From this figure and the previous research, it can be ascertained that EVA/EG foams show different dynamic mechanical behaviors in a similar way to EVA/EG solid nanocomposites having different particle size and EG contents. However, the more effective reinforcing role of EG nanofiller in EVA matrix has been achieved for the solid nanocomposites filled with higher loadings of large aspect ratio graphite. Nonetheless, the EG particle size has reverse effect on the storage modulus of the nanocomposite foams.

According to the Figure 6a, it is clear that the addition of EG to EVA matrix improves the storage modulus of virgin foam due to the reinforcing effect of EG and the formation of more uniform cells. As mentioned earlier, the void fraction of foam is a critical parameter to determine the foam properties. This is why the foam storage modulus considerably depends on the void fraction. As can be found in Figure 6a, the nanocomposite foam containing EX100 with higher void fraction has relatively lower storage modulus in the full range of studied temperature compared to the sample containing EX1500. Polymer-filler interaction and interfacial area in the solid regions of foams, cell size, cell size distribution and void fraction of foams affect the storage and loss moduli of nanocomposite foams. The concomitant influences of these factors determine the foam void fraction and correspondingly, foam moduli. From the SEM micrographs and void fraction curves, it is apparent that the nanocomposite foam filled with 6 wt% of EG with lower aspect ratio (EX1500) has smaller cell size and lower void fraction in comparison with the EVA
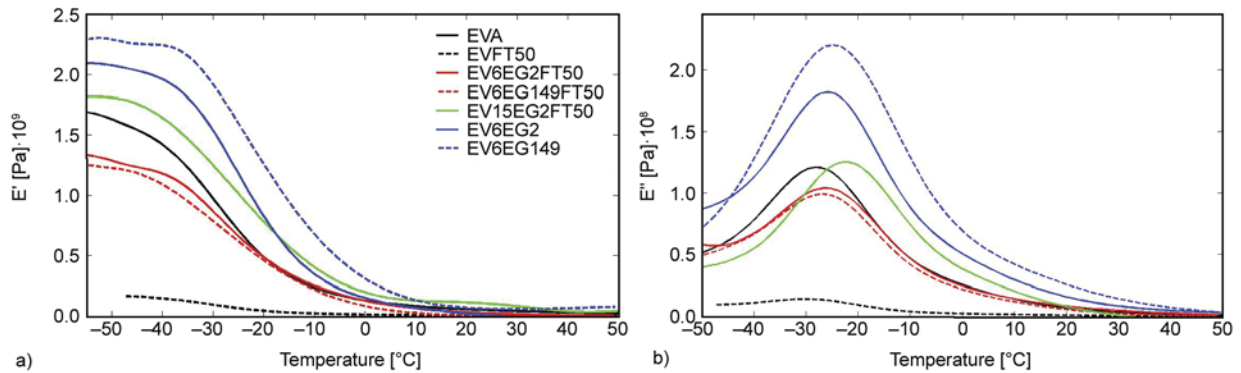
Figure 6. (a) Storage modulus and (b) loss modulus of virgin EVA, EVA foam and the solid and foamed nanocomposites with different EG particle sizes and loadings. All samples were prepared at the same conditions. The DMTA of solid nanocomposites were presented in the previous study [30].

matrix reinforced by EG with higher particle size (EX100). Seemingly, the void fraction does make a stronger impact on the foam properties than the EG aspect ratio and the dominant role of bubbles in weakening the EVA matrix is the plausible reason for the higher storage modulus of sample containing EX1500. As shown in Figure 6a, it is also obvious that the E' of foamed samples are relatively lower than the E' of solid nanocomposites due to the presence of gas phase in the foamed samples and the formation of non-uniform cell structure.

Furthermore, Figure 6b demonstrates that the foaming process of polymer in the presence of EG particle changes the loss modulus curves substantially and the incorporation of EG nanofiller into EVA matrix enhances the peak position of loss modulus or the EVA glass transition temperature. The latter is caused by the slower dynamics and restricted mobility of polymer chain segments that interact with graphite sheet surfaces.

An interesting phenomenon, which is worth noting, is that the foaming process of polymer significantly decreases the value of loss modulus. Particularly for the pure EVA foam, the obtained heterogeneous structure of polymer after foaming process is most likely to diminish the storage and loss modulus.

According to the loss modulus curves of samples containing 6 wt% of EGs, i.e. EX100 and EX1500, the foaming process of EVA nanocomposites similarly reduces the E'' peak heights, indicating that the polymer chain mobility and the resultant chain damping ability is noticeably decreased by foaming the EVA even in the presence of EG particles. During the foaming process, the formation of bubbles in polymer matrix imposes major constraints on polymer chains by passing through the macromolecules and
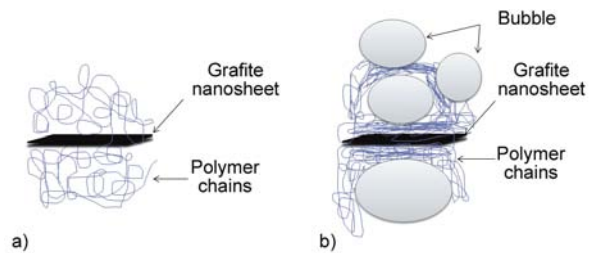
Figure 7. Schematic diagrams indicating the orientation and intermolecular distance of polymer chains in: (a) solid EVA/EG nanocomposite and (b) EVA/EG foam nanocomposite; the chains are tightly packed after foaming process

diminishing the chain-to-chain intermolecular distances. Therefore, squeezing the chains into smaller spaces, orienting the polymer chain segments towards each other and increasing the total chain segments that interact with EG nanosheets are the plausible explanations of impeded EVA molecular movements after foaming and corresponding lower foam loss modulus. Figure 7a and 7b are schematically show these phenomena. In a similar manner, this trend is also observed for the nanocomposite foams containing higher loadings of EG particles that are not shown here.

3.3.2. Effects of EVA crosslinking

As mentioned earlier, along with additive addition, polymer properties such as melt strength and crystallization behavior affect the foam structure, i.e. the bubble nucleation and growth stages of foaming process. As one of the key features that influences the EVA matrix characteristics, the implications of chain crosslinking for foam properties have been evaluated here. From the aforementioned discussion on the morphology and void fraction of the crosslinked foams, it was concluded that crosslink-
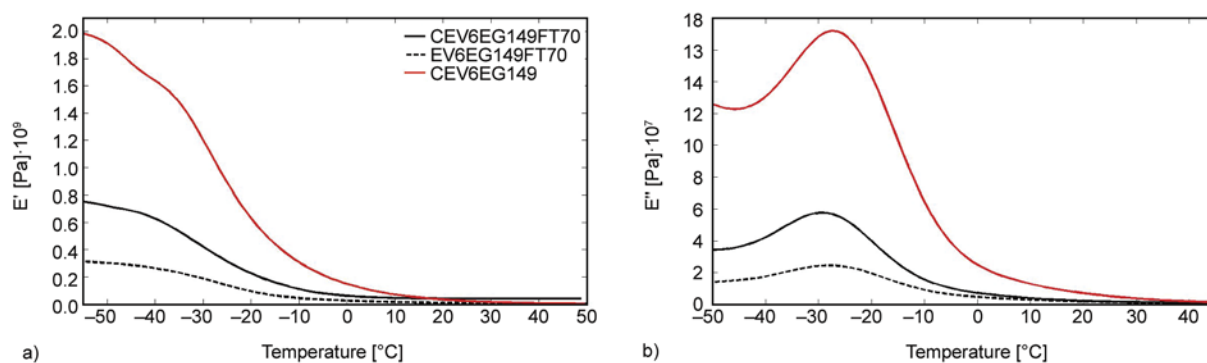
Figure 8. (a) Storage modulus and (b) loss modulus of crosslinked EVA nanocomposite and nanocomposite foams. All samples were prepared at the same conditions.

ing of polymer chains relatively reduces the foam cell density and void fraction. As it can be seen in Figure 8, crosslinked EVA foam containing 6 wt% of EX100 (CEV6EG149FT70) shows higher stiffness, storage and loss moduli at temperatures below the glass transition temperature compared to the non-crosslinked foam with the same composition (EV6EG149FT70). Chemical crosslinking of polymer chains changes both the matrix molecular structure and foam cell morphology. While foaming process weakens the solid crosslinked EVA/EG nanocomposite, namely CEV6EG149, crosslinking of polymer chains in the nanocomposite foam, EV6EG149FT70, enhances the EVA viscoelastic properties owing to the smaller cell density and void fraction. In the case of crosslinked samples, gas permittivity and bubble nucleation is influenced by the 3-dimensional network of polymer chains during the foaming process, thereby shifting the viscoelastic curves of foam samples.

Figure 8b illustrates the loss modulus variation versus temperature for crosslinked and non-crosslinked foam samples. The height of loss modulus peak and area under this curve indicate that the total constraints imposed on EVA chains in crosslinked foam sample is lower than that of noncrosslinked one. The higher damping ability of crosslinked foam sample, CEV6G149FT70, is most probably caused by the smaller void fraction and more nonfoamed regions (refer to the schematic drawings of Figure 7).

3.3.3.Effects of foaming temperature

Another crucial factor that is directly involved the foam characteristics is the foaming process temperature. Besides, in semicrystalline polymers, the crystalline regions act as major obstacles for gas mole-

cules to diffusing and for bubbles to growing in the solid polymer just similar to the impermeable graphite nanostructures. In this study, the nitrogen saturation temperature in the foaming process was near the melting point of EVA copolymer. Nevertheless, the foaming temperature was selected to be above and below the EVA crystallization temperature in order to make a temperature impact assessment. The melting and crystallization behavior of EVA/EG nanocomposites was investigated earlier [30]. Figure 9a and 9b demonstrate the variation of storage and loss modulus alongside temperature for the foam samples, which were prepared at different foaming temperatures. It is clearly evident that the foam sample obtained at the temperature below the EVA crystallization point shows higher storage modulus in glassy region due to lower void fraction and the formation of special morphology that was shown in Figure 4. Similar to the cell morphologies illustrated in Figure 4, it can be deduced that the crystalline regions of the nanocomposite foamed below the EVA crystallization temperature have markedly larger area than the one for sample prepared at higher temperature. As a result of higher crystallinity degree, the EV6EG2FT50 sample shows stronger viscoelastic properties than EV6EG2FT70 foam. Moreover, the height of loss modulus peak and area under the curve of EV6EG2FT70 sample are considerably lower than that of EV6EG2FT50. As explained earlier, the foaming of EVA in the presence of EG particles decreases the loss modulus peak height because of the EVA chain squeeze, segmental orientation increase and EVA chain/EG nanolayer interface area rise. This phenomenon intensifies the interactions of EVA chains with each other and EG solid surfaces, therefore the EVA molecular movements and the peak height of loss modulus is
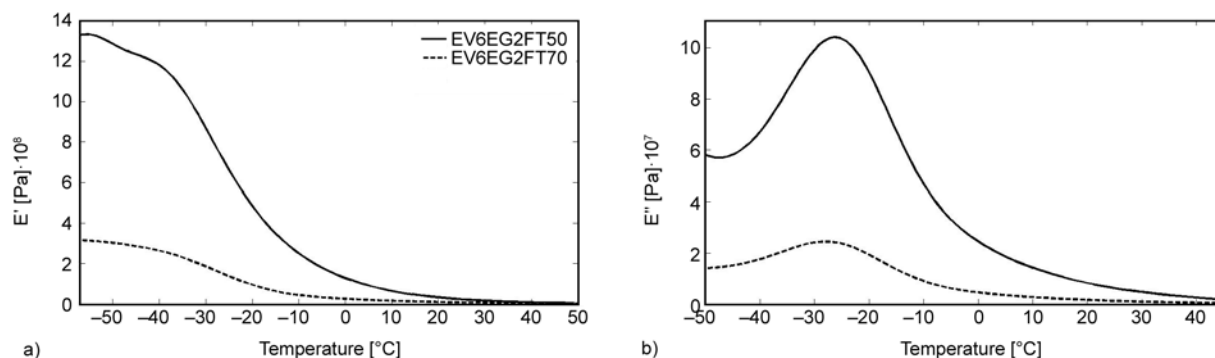
Figure 9. (a) Storage and (b) Loss modulus of EVA/EG nanocomposites foamed at different temperatures; Both samples were prepared via the same process apart from the foaming temperature.

comparatively much lower for the samples having higher void fractions.

In Figure 10, E'' is plotted as a function of E' in the studied temperature range, which is typically known as Cole–Cole plot. The relaxation time distribution of polymer chains was described more accurately by an advanced theory proposed in the work of Cole and Cole [39]. This model represents the chain relaxation time by a depressed semi-circle. Any deviation from a single relaxation time is shown up by a more imperfect semi-circle and an extra arc at lower temperatures [40]. This extra arc refers to the dynamic heterogeneity in the system and appears at different chain relaxation time. The amplitude of the additional arc at lower temperatures is more considerable for EV6EG2FT50 and EV6EG149FT50 samples, which proves the existence of greater heterogeneity in polymer chain dynamics. This finding can give a further evidence for the restricted molecular movements of foam samples having larger void fraction. However, the mechanisms of how the addition of EG affects the relaxations of all polymer

chains after foaming process needs to be studied further considering the profound impact of foam molecular motions on the product final properties.

4. Conclusions

The nanocomposite foams based on EVA/EG were made using a supercritical fluid. Different cell morphologies were obtained for the nanocomposite foams containing different EGs with unequal particle size. The solid surfaces of EG sheets act as heterogeneous nucleation sites in the foaming process and multiple cell nucleations simultaneously occur on a single nanolayer. Higher cell density and broader cell size distribution of sample filled with EX100 are the proofs of stronger multinucleations of EX100 due to the higher surface area. Furthermore, in the foam sample based on EX100, there are so many cells, which grow into one and impinge into each other. Above the EVA crystallization temperature, the gas molecules have enough energy to pass through the polymer chains, thereby producing the primary bubbles and the polymer chains themselves have quickly enough molecular movements to allow the bubbles to grow. The concomitant phenomena result in larger cell size and void fraction for nanocomposites foamed at higher temperature. The only obstacle to diffusing gas molecules and growing bubbles at this temperature is the impermeable graphite particles. Therefore, the foaming temperature plays a key role in determining the final foam properties. Besides, the void fraction decreases with increasing the EG content owing to the larger accessible heterogeneous nucleation sites and more aggregations of nanosheets at higher loadings. The nanocomposite foams containing EX100 with higher particle size prepared at the temperature above the EVA crystallization point show maximum void fraction,
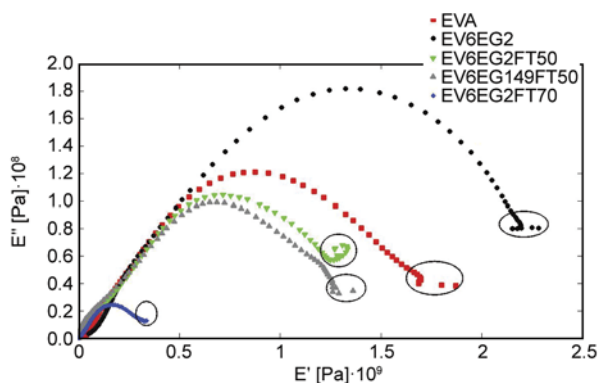

Figure 10. Cole-Cole plot for neat EVA, EVA/EG nanocomposite and EVA/EG nanocomposite foams. The ellipse indicates the aforementioned arc in the text.

whereas the nanocomposite foams incorporating EX1500 obtained at the temperature below the crystallization point possess minimum void fraction. According to the DMTA data, the addition of EG to EVA matrix improves the foam storage and loss moduli because of the reinforcing effect of EG nanofiller and the formation of more uniform cells. In agreement with the morphology analysis and void fraction results, the nanocomposite foams with higher void fraction and larger bubble size demonstrate smaller values of both storage and loss modulus. Lower polymer chain mobility after foaming of EVA in the presence of EG particles lead to these changes. EVA/EG Foam properties are also influenced by polymer chain chemical crosslinking. More non-foamed regions were observed in these samples due to the crosslinked regions in the EVA polymeric matrix.

References

[1] Fleming O. S., Kazarian S. G.: Polymer processing with supercritical fluids. in 'Supercritical carbon dioxide' (eds.: Kemmere M. F., Meyer T.) Wiley-VCH, Weinheim, 205-238 (2006).
DOI: 10.1002/3527606726.ch10

[2] Almanza O., Rodríguez-Pérez M. A., de Saja J. A.: The microstructure of polyethylene foams produced by a nitrogen solution process. Polymer, **42**, 7117–7126 (2001).
DOI: 10.1016/S0032-3861(01)00107-0

[3] Kumar V., Weller J. E.: A process to produce microcellular PVC. International Polymer Processing, **8**, 73–80 (1993).
DOI: 10.3139/217.930073

[4] Krause B., Mettinkhof R., van der Vegt N. F. A., Wessling M.: Microcellular foaming of amorphous high-T_g polymers using carbon dioxide. Macromolecules, **34**, 874–884 (2001).
DOI: 10.1021/ma001291z

[5] Okamoto M., Nam P. H., Maiti P., Kotaka T., Nakayama T., Takada M., Ohshima M., Usuki A., Hasegawa N., Okamoto H.: Biaxial flow-induced alignment of silicate layers in polypropylene/clay nanocomposite foam. Nano Letters, **1**, 503–505 (2001).
DOI: 10.1021/nl010051

[6] Fujimoto Y., Ray S. S., Okamoto M., Ogami A., Yamada K., Ueda K.: Well-controlled biodegradable nanocomposite foams: From microcellular to nanocellular. Macromolecular Rapid Communications, **24**, 457–461 (2003).
DOI: 10.1002/marc.200390068

[7] Zeng C., Han X., Lee L. J., Koelling K. W., Tomasko D. L.: Polymer–clay nanocomposite foams prepared using carbon dioxide. Advanced Materials, **15**, 1743–1747 (2003).
DOI: 10.1002/adma.200305065

[8] Lee Y. H., Wang K. H., Park C. B., Sain M.: Effects of clay dispersion on the foam morphology of LDPE/clay nanocomposites. Journal of Applied Polymer Science, **103**, 2129–2134 (2007).
DOI: 10.1002/app.24908

[9] Colton J. S., Suh N. P.: The nucleation of microcellular thermoplastic foam with additives: Part I: Theoretical considerations. Polymer Engineering and Science, **27**, 485–492 (1987).
DOI: 10.1002/pen.760270702

[10] Leung S. N., Park C. B., Li H.: Effects of nucleating agents' shapes and interfacial properties on cell nucleation. Journal of Cellular Plastics, **46**, 441–460 (2010).
DOI: 10.1177/0021955x10369418

[11] Zhai W., Yu J., Wu L., Ma W., He J.: Heterogeneous nucleation uniformizing cell size distribution in microcellular nanocomposites foams. Polymer, **47**, 7580–7589 (2006).
DOI: 10.1016/j.polymer.2006.08.034

[12] Zeng C., Hossieny N., Zhang C., Wang B.: Synthesis and processing of PMMA carbon nanotube nanocomposite foams. Polymer, **51**, 655–664 (2010).
DOI: 10.1016/j.polymer.2009.12.032

[13] Spitael P., Macosko C. W., McClurg R. B.: Block copolymer micelles for nucleation of microcellular thermoplastic foams. Macromolecules, **37**, 6874–6882 (2004).
DOI: 10.1021/ma049712q

[14] Mizumoto T., Sugimura N., Moritani M., Sato Y., Masuoka H.: CO_2-induced stereocomplex formation of stereoregular poly(methyl methacrylate) and microcellular foams. Macromolecules, **33**, 6757–6763 (2000).
DOI: 10.1021/ma000443n

[15] Siripurapu S., Coughlan J. A., Spontak R. J., Khan S. A.: Surface-constrained foaming of polymer thin films with supercritical carbon dioxide. Macromolecules, **37**, 9872–9879 (2004).
DOI: 10.1021/ma0484983

[16] Lee P. C., Wang J., Park C. B.: Extruded open-cell foams using two semicrystalline polymers with different crystallization temperatures. Industrial and Engineering Chemistry Research, **45**, 175–181 (2005).
DOI: 10.1021/ie050498j

[17] Otsuka T., Taki K., Ohshima M.: Nanocellular foams of PS/PMMA polymer blends. Macromolecular Materials and Engineering, **293**, 78–82 (2008).
DOI: 10.1002/mame.200700257

[18] Nemoto T., Takagi J., Ohshima M.: Control of bubble size and location in nano-/microscale cellular poly(propylene)/rubber blend foams. Macromolecular Materials and Engineering, **293**, 574–580 (2008).
DOI: 10.1002/mame.200800015

[19] Wright Z. C., Frank C. W.: Increasing cell homogeneity of semicrystalline, biodegradable polymer foams with a narrow processing window via rapid quenching. Polymer Engineering and Science, **54**, 2877–2886 (2014). DOI: 10.1002/pen.23847

[20] Garancher J-P., Fernyhough A.: Expansion and dimensional stability of semi-crystalline polylactic acid foams. Polymer Degradation and Stability, **100**, 21–28 (2014). DOI: 10.1016/j.polymdegradstab.2013.12.037

[21] Liao R., Yu W., Zhou C.: Rheological control in foaming polymeric materials: II. Semi-crystalline polymers. Polymer, **51**, 6334–6345 (2010). DOI: 10.1016/j.polymer.2010.11.001

[22] Jenkins M. J., Harrison K. L., Silva M. M. C. G., Whitaker M. J., Shakesheff K. M., Howdle S. M.: Characterisation of microcellular foams produced from semi-crystalline PCL using supercritical carbon dioxide. European Polymer Journal, **42**, 3145–3151 (2006). DOI: 10.1016/j.eurpolymj.2006.07.022

[23] Ghanbar S., Yousefzade O., Hemmati F., Garmabi H.: Microstructure and thermal stability of polypropylene/ bagasse composite foams: Design of optimum void fraction using response surface methodology. Journal of Thermoplastic Composite Materials, in press (2015). DOI: 10.1177/0892705714535795

[24] Bauhofer W., Kovacs J. Z.: A review and analysis of electrical percolation in carbon nanotube polymer composites. Composites Science and Technology, **69**, 1486–1498 (2009). DOI: 10.1016/j.compscitech.2008.06.018

[25] Moniruzzaman M., Winey K. I.: Polymer nanocomposites containing carbon nanotubes. Macromolecules, **39**, 5194–5205 (2006). DOI: 10.1021/ma060733p

[26] Yasmin A., Luo J-J., Daniel I. M.: Processing of expanded graphite reinforced polymer nanocomposites. Composites Science and Technology, **66**, 1182–1189 (2006). DOI: 10.1016/j.compscitech.2005.10.014

[27] Li J., Kim J-K., Sham M. L.: Conductive graphite nanoplatelet/epoxy nanocomposites: Effects of exfoliation and UV/ozone treatment of graphite. Scripta Materialia, **53**, 235–240 (2005). DOI: 10.1016/j.scriptamat.2005.03.034

[28] Lee L. J., Zeng C., Cao X., Han X., Shen J., Xu G.: Polymer nanocomposite foams. Composites Science and Technology, **65**, 2344–2363 (2005). DOI: 10.1016/j.compscitech.2005.06.016

[29] Chen L., Ozisik R., Schadler L. S.: The influence of carbon nanotube aspect ratio on the foam morphology of MWNT/PMMA nanocomposite foams. Polymer, **51**, 2368–2375 (2010). DOI: 10.1016/j.polymer.2010.03.042

[30] Yousefzade O., Hemmati F., Garmabi H., Mahdavi M.: Thermal behavior and electrical conductivity of ethylene vinyl acetate copolymer/expanded graphite nanocomposites: Effects of nanofiller size and loading. Journal of Vinyl and Additive Technology, in press (2015). DOI: 10.1002/vnl.21428

[31] Rodríguez-Pérez M. A., Almanza O., del Valle J. L., González A., de Saja J. A.: Improvement of the measurement process used for the dynamic mechanical characterisation of polyolefin foams in compression. Polymer Testing, **20**, 253–267 (2001). DOI: 10.1016/S0142-9418(00)00030-1

[32] Colton J. S., Suh N. P.: The nucleation of microcellular thermoplastic foam with additives: Part II: Experimental results and discussion. Polymer Engineering and Science, **27**, 493–499 (1987). DOI: 10.1002/pen.760270703

[33] Chen L., Wang X., Straff R., Blizard K.: Shear stress nucleation in microcellular foaming process. Polymer Engineering and Science, **42**, 1151–1158 (2002). DOI: 10.1002/pen.11019

[34] Han J. H., Han C. D.: Bubble nucleation in polymeric liquids. II. Theoretical considerations. Journal of Polymer Science Part B: Polymer Physics, **28**, 743–761 (1990). DOI: 10.1002/polb.1990.090280510

[35] Rodríguez-Pérez M. A., Simoes R. D., Roman-Lorza S., Alvarez-Lainez M., Montoya-Mesa C., Constantino C. J. L., de Saja J. A.: Foaming of EVA/starch blends: characterization of the structure, physical properties, and biodegradability. Polymer Engineering and Science, **52**, 62–70 (2012). DOI: 10.1002/pen.22046

[36] Zhang B. S., Zhang Z. X., Lv X. F., Lu B. X., Xin Z. X.: Properties of chlorinated polyethylene rubber/ethylene vinyl acetate copolymer blend-based foam. Polymer Engineering and Science, **52**, 218–224 (2012). DOI: 10.1002/pen.22071

[37] Park K-W., Kim G-H.: Ethylene vinyl acetate copolymer (EVA)/multiwalled carbon nanotube (MWCNT) nanocomposite foams. Journal of Applied Polymer Science, **112**, 1845–1849 (2009). DOI: 10.1002/app.29736

[38] Alvarez P., Mendizabal A., Petite M. M., Rodríguez-Pérez M. A., Echeverria A.: Finite element modelling of compressive mechanical behaviour of high and low density polymeric foams. Materialwissenschaft und Werkstofftechnik, **40**, 126–132 (2009). DOI: 10.1002/mawe.200900417

[39] Cole K. S., Cole R. H.: Dispersion and absorption in dielectrics I. Alternating current characteristics. Journal of Chemical Physics, **9**, 341–351 (1941). DOI: 10.1063/1.1750906

[40] Shaw M. T., MacKnight W. J.: Introduction to polymer viscoelasticity. Wiley, Hoboken (2005).

Novel electrically conductive polyurethane/montmorillonite-polypyrrole nanocomposites

S. D. A. S. Ramoa[1], G. M. O. Barra[1], C. Merlini[1], S. Livi[2], B. G. Soares[3], A. Pegoretti[4]*

[1]Universidade Federal de Santa Catarina, Departamento de Engenharia Mecânica, Florianópolis, SC, Brazil
[2]Université de Lyon, Ingénierie des Matériaux Polymères, CNRS, UMR 5223, F-69003, Lyon, France; INSA Lyon, F-69621, Villeurbanne, France
[3]Universidade Federal do Rio de Janeiro, Departamento de Engenharia Metalúrgica e de Materiais, Rio de Janeiro, RJ, Brazil
[4]Department of Industrial Engineering, University of Trento, 38123 Trento, Italy

Abstract. This work describes the production of electrically conductive nanocomposites based on thermoplastic polyurethane (TPU) filled with montmorillonite-dodecylbenzenesulfonic acid-doped polypyrrole (Mt-PPy.DBSA) prepared by melt blending in an internal mixer. The electrical conductivity, morphology as well as the rheological properties of TPU/Mt-PPy.DBSA nanocomposites were evaluated and compared with those of TPU nanocomposites containing different conductive fillers, such as polypyrrole doped with hydrochloride acid (PPy.Cl) or dodecylbenzenesulfonic acid (PPy.DBSA) or montmorillonite-hydrochloride acid-doped polypyrrole (Mt-PPy.Cl), prepared with the same procedure. The TPU/Mt-PPy.DBSA nanocomposites display a very sharp insulator-conductor transition and the electrical percolation threshold was about 10 wt% of Mt-PPy.DBSA, which was significantly lower than those found for TPU/Mt-PPy.Cl, TPU/PPy.Cl and TPU/PPy.DBSA. Morphological analysis highlights that Mt-PPy.DBSA filler was better distributed and dispersed in the TPU matrix, forming a denser conductive network when compared to Mt-PPy.Cl, PPy.Cl and PPy.DBSA fillers. This morphology can be attributed to the higher site-specific interaction between TPU matrix and Mt-PPy.DBSA. The present study demonstrated the potential use of Mt-PPy.DBSA as new promising conductive nanofiller to produce highly conductive polymer nanocomposites with functional properties.

Keywords: nanocomposites, polymer composites, rheology

1. Introduction

Since its discovery in the late 1970s, the scientific interest in understanding physical and chemical properties of the intrinsically conducting polymers (ICPs) has been increasing due to their potential in various technological applications. Among ICPs, polypyrrole (PPy) is a particularly promising material because of its high electrical conductivity, chemical and environmental stability in the oxidized state, low ionization potential, electrorheological properties, electrochromic effect and relatively easy of synthesis [1–6]. In fact, PPy can be potentially used in new advanced technology areas, including electronic and optoelectronic nanodevices [7], sensors [8–13], supercapacitors [14, 15], energy storage devices [1, 7, 16], surface coatings for corrosion protection [17], electromagnetic shielding applications [18–20], smart textiles [21, 22] and even in medical applications [4, 23–26].

However, the poor mechanical performances and the difficult processability (insolubility and infusibility) [2, 3, 19, 20, 27, 28] have hampered the use of PPy for technological applications. Intensive investigations have been carried out to solve these problems.

One approach to possibly overcome the above limitations is blending PPy with commercial insulating polymers to produce conductive polymer blends or composites [3, 11, 27, 29–33]. Among the methods mentioned in the scientific literature, melt mixing offers the advantages of large-scale production and reduced cost which are the bases for any industrial application. However, this process has been reported to be less efficient on the dispersion of PPy or other ICPs within insulating polymer matrices. In fact, the production of conducting polymer mixtures with electrical conductivity less than 10^{-7} S·cm^{-1}, percolation threshold about 30 to 60 wt% of ICP and poor mechanical properties has been reported [34–38]. Therefore, a great challenge is how to produce a conducting polymer mixture through melt blending process with higher electrical conductivity at low percolation threshold of ICP. Some works in the literature have demonstrated that montmorillonite/polypyrrole (Mt-PPy) nanocomposites are potential fillers for improving the electrical and mechanical properties of insulating matrix [27, 36, 38]. According to Boukerma *et al.* [36], the exfoliation of Mt-PPy promotes a conductive network formation in the insulating matrix with lower PPy concentration when compared with that found for neat PPy. Mravčáková *et al.* [38] have reported interesting results concerning the preparation of polypropylene/Mt-PPy composites. On the other hand, Peighambardoust and Pourabbas reported that percolation threshold of Nylon-6/Mt-PPy composites was 15 wt% of Mt-PPy [27].

In this context, thermoplastic polyurethane (TPU) is an interesting insulating matrix for developing flexible conductive Mt-PPy composites with high electrical conductivity at low percolation threshold. TPU is among the most versatile engineering thermoplastics since it associates the properties of thermoplastic polymers with those of vulcanized rubbers without vulcanizing agents [39, 40]. Moreover, to the best of our knowledge, there are no studies concerning the preparation of TPU composites with Mt-PPy through melt blending method.

Based on the above considerations, the main objective of this study is to investigate TPU/Mt-PPy.DBSA nanocomposites produced by melt blending and containing various filler contents. In particular, the attention has been focused on obtaining good electrical conductivity at low filler concentration. For comparison purpose, three different conductive fillers, such as polypyrrole doped hydrochloride acid (PPy.Cl) or dodecylbenzenesulfonic acid (PPy.DBSA) and montmorillonite-polypyrrole doped hydrochloride acid (Mt-PPy.Cl) were separately added into TPU matrix under the same processing conditions. The morphology, electrical and rheological properties of nanocomposites were experimentally investigated.

2. Experimental
2.1. Materials
Sodium bentonite, Vulgel CN 45 (Aliança Latina Indústrias e Comércio Ltda, Uruguaiana, Rio Grande do Sul, Brazil)) was kindly supplied by Ioto International (Brazil). Pyrrole, 98%, (Aldrich, Germany) was purified by distillation under reduced pressure and stored in a refrigerator before use. Iron(III) chloride hexahydrate, $FeCl_3 \cdot 6H_2O$, analytical grade (Vetec, Duque de Caxias, Rio de Janeiro, Brazil), and the surfactant dodecylbenzenesulfonic acid, DBSA, (Aldrich, Italy) were used as received. Commercially available TPU (Elastollan® 1180 A10 extrusion grade; Shore A hardness = 80, density = 1.11 g·cm^{-1}) based on polyether was purchased from BASF (Mauá, São Paulo, Brazil).

2.1.1. Synthesis of conducting nanocomposites (Mt/PPy)
The preparation procedure of the conducting nanocomposites Mt-PPy with or without a surfactant was based on the method described in our previous report with some modifications [41]. In a typical procedure, Mt (2.5 g) was dispersed into 250 mL of water or aqueous solution containing the DBSA and stirred for 2 h at room temperature. The molar ratio of the surfactant/Py used in the polymerization was 1:5. The dispersion was sonicated with 35% power (263 W) for 20 min with a Sonics VCX 750 ultrasonic processor (Sonics & Materials, Inc., USA). $FeCl_3 \cdot 6H_2O$ (0.2542 mol) dissolved in 125 mL of distilled water was added in the aqueous MMT dispersion under stirring at room temperature. 50 mL of a 0.26 mol·L^{-1} aqueous dispersion of Py (0.1105 mol) were added dropwise in 15 min. The polymerization proceeded for 1 h under stirring at room temperature. After 24 h, the conducting fillers, (Mt-PPy.Cl and Mt-PPy.DBSA) were filtered, washed with distilled water and dried at 60°C. The PPy with or without surfactant, denoted as PPy.DBSA and PPy.Cl, respectively, were also prepared using a similar procedure.

2.1.2. Preparation of TPU/Mt-PPy nanocomposites

Before processing, both TPU pellets and conducting fillers were dried in a circulating-air oven at 100°C for 3 h and vacuum oven at 60°C for 12 h, respectively. TPU were melt blended with different amounts of conducting fillers (5, 10, 15, 20, 25 and 30 wt%) in an internal mixer (Haake Polylab QC, Thermo Scientific, USA) at 170°C with a rotor speed of 50 rpm and mixing time of 15 min. The specimens were compression-molded at 170°C for 5 min under 12 MPa pressure, and air cooled to room temperature.

2.2. Characterization

The elemental analysis was used to determine the composition of conducting mixtures. Elemental analysis was performed on a CHN 2400 analyzer (Perkin-Elmer, USA). The combustion process was carried out at 925°C using oxygen with a purity level of 99.995%.

The electrical conductivity of the conducting fillers and low-resistivity TPU composites were measured using the four probe standard method with a Keithley 6220 (USA) current source to apply the current and a Keithley Model 6517A (USA) electrometer to measure the potential difference. For neat TPU and high-resistivity composites, the measurements were performed using the two probe standard method with a Keithley 6517A (USA) electrometer connected to Keithley 8009 (USA) test fixture. All measurements were performed at room temperature and repeated at least five times for each sample.

Fracture surfaces of composites were observed by a field emission scanning electron microscope (FESEM), JEOL model JSM-6701F (JEOL, USA). The specimens were fractured in liquid nitrogen and coated with gold, and then the cross-section was observed at an accelerating voltage of 10 kV.

Transmission electron microscopy (TEM) observations were performed by a Phillips CM120 microscope (Phillips, Germany) (located at the Center of Microstructure University of Lyon) at 80 kV. Specimens consisting of 60 nm-thick ultrathin sections were obtained by a Leica Ultracut UCT ultramicrotome (Leica, Germany) equipped with a diamond knife and deposited on copper grids.

Fourier transform infrared (FTIR) spectra were obtained through the attenuated total reflectance (ATR) method using a spectrometer Bruker Tensor 27 (Bruker, USA) with a resolution of 4 cm^{-1}. The wavenumbers were in the range of 2000–600 cm^{-1} for conducting fillers and 4000–600 cm^{-1} for neat TPU and TPU composites.

The X-ray diffraction (XRD) patterns of all samples were obtained on an Philips X'PERT (Philips, Germany) X-ray diffractometer, with CuKα (λ = 0.154 nm) radiation source operating at a voltage of 40 kV and 30 mA current. The samples were evaluated in a 2θ° range from 2 to 50°, at steps of 0.05° and a time step of 1 s. Mt, PPy and Mt-PPy samples were analyzed in powder form, while neat TPU and relative composites were in the form of compression molded disks.

The rheological properties of TPU and their physical mixtures were analyzed using dynamic oscillatory rheometry in the molten state through an Anton Paar MCR302 rheometer (Anton Paar GmbH, Germany). Dynamic frequency sweep test were conducted at 170°C with angular frequency range from 0.1 to 100 Hz, in an oscillatory shear mode by using a 25 mm parallel plate with a gap around 1000 μm.

3. Results and discussion
3.1. Characterization of conductive fillers

The composition of samples, electrical conductivity and PPy content inserted in the Mt are summarized in Table 1. Mt-PPy.DBSA and Mt-PPy.Cl display higher PPy content (approximately 90 wt% of PPy) than those found by our recent study due to the higher Py amount used in the in situ polymerization

Table 1. Elemental analysis, PPy content and electrical conductivity of conductive filler (PPy.Cl, PPy.DBSA, Mt/PPy.Cl and Mt/PPy.DBSA)

Samples	Compositiont			PPy content [wt%]	Electrical conductivity [S·cm^{-1}]
	C	H	N		
Mt	0.08	1.93	0.00	0.00	$(4.26\pm0.34)\cdot10^{-6}$
PPy.Cl	55.04	3.52	16.14	100.00	0.15±0.02
PPy.DBSA	66.20	6.35	9.90	100.00	4.39±1.02
Mt /PPy.Cl	44.97	3.01	13.48	83.52	4.26±0.14
Mt/PPy.DBSA	56.75	5.81	8.92	90.10	10.03±0.89

Calculated from elemental analysis.

process [41]. As expected, the electrical conductivity of PPy.DBSA (4.4 S·cm^{-1}) is higher than that found for PPy.Cl (0.2 S·cm^{-1}) due to the doping effect of DBSA molecules [41, 42]. In fact, the PPy.Cl sample was prepared in absence of protonic acid and the HCl that participates on the doping process was provided by the FeCl$_3$ used as an oxidant.

This condition should be responsible for the lower conductivity value found for the PPy.Cl sample. The electrical conductivity values found for Mt-PPy.DBSA and Mt-PPy.Cl samples are seven and six orders of magnitude higher than that of neat Mt, respectively. Furthermore, Mt-PPy.Cl nanocomposite shows an increment in the electrical conductivity of one order of magnitude higher than that found for neat PPy-Cl, probably due to the doping effect of the Mt [41].

3.2. Characterization of TPU/Mt-PPy.DBSA nanocomposites

TPU/Mt-PPy.DBSA nanocomposites show a very sharp insulator-conductor transition and the electrical conductivity increased significantly with increasing the Mt-PPy.DBSA content, as observed in Figure 1. This behavior can be attributed to the formation of a continuous conductive Mt-PPy.DBSA network in the insulating polymer. On the other hand, the electrical conductivity of the systems containing 30 wt% of Mt-PPy.Cl, PPy.Cl and PPy.DBSA show electrical conductivities of 1.3·10^{-4}, 5.4·10^{-11} and 4.3·10^{-10} S·cm^{-1}, respectively, which were much lower than the value found for TPU/Mt-PPy.DBSA nanocomposites(1.5·10^{-2} S·cm^{-1}) at the same conductive filler content.
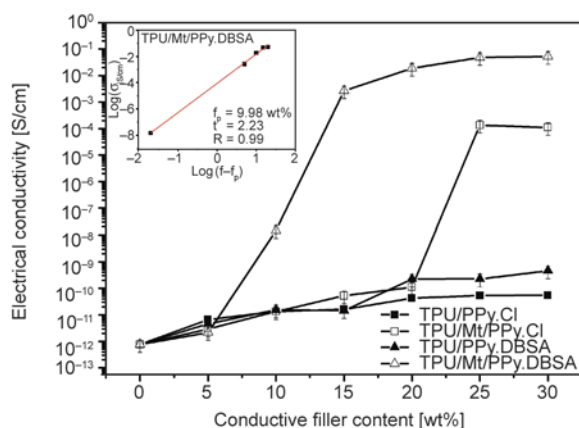
Figure 1. Effect of the conducting fillers content on electrical conductivity

For electrically percolating systems, the electrical conductivity σ of a filled material follows a power-law relationship in the form of Equation (1):

$$\sigma = \sigma_0 (f - f_p)^t \tag{1}$$

where σ_0 is a constant, f is the content of conducting filler, f_p is its percolation threshold and t is the critical exponent. The values of parameters f_p and t, as determined through the plot of $\log \sigma$ versus $\log(f - f_p)$, of TPU/Mt-PPy.DBSA nanocomposites resulted to be ~10 wt% and 2.2, respectively. A critical exponent in the range from 2 to 4 is in agreement with the classical theory for tridimensional systems. On the other hand, TPU/Mt.PPy.Cl nanocomposites show a percolation threshold of 22.5 wt%. The lower f_p value and higher electrical conductivity of TPU/Mt-PPy.DBSA nanocomposites with respect to TPU/Mt.PPy.Cl and TPU/PPy samples probably reflects the good dispersion of the conductive filler (Mt-PPy.DBSA) in the polymer matrix. These results are consistent with the morphological features of these materials, as it will be discussed later.

FESEM micrographs of cryogenically fractured samples with 20 wt% of conductive filler are shown in Figure 2. The microstructure of the TPU/PPy.Cl and TPU/PPy.DBSA blends revealed typical phase separation morphology with the presence of isolated PPy agglomerates in the TPU matrix. This morphology can explain the low electrical conductivity for these samples. On the other hand, TPU/Mt-PPy.Cl and TPU/Mt-PPy.DBSA nanocomposites present disperse agglomerates composed of conducting pathways, in which the disperse phase is better interconnected than in the case of TPU/PPy.Cl and TPU/PPy.DBSA blends. Furthermore, TEM image of TPU/Mt-PPy.DBSA nanocomposite (Figure 3) reveals a denser network formation of Mt-PPy.DBSA in the TPU matrix when compared with that found for Mt-PPy.Cl. The morphological difference of TPU/Mt-PPy.Cl and TPU/Mt-PPy.DBSA nanocomposites indicates that DBSA was able to induce the formation of conductive pathways in the TPU matrix, and consequently enhancing the electrical conductivity. This morphology can be attributed to the higher site-specific interaction between TPU matrix and Mt-PPy.DBSA.

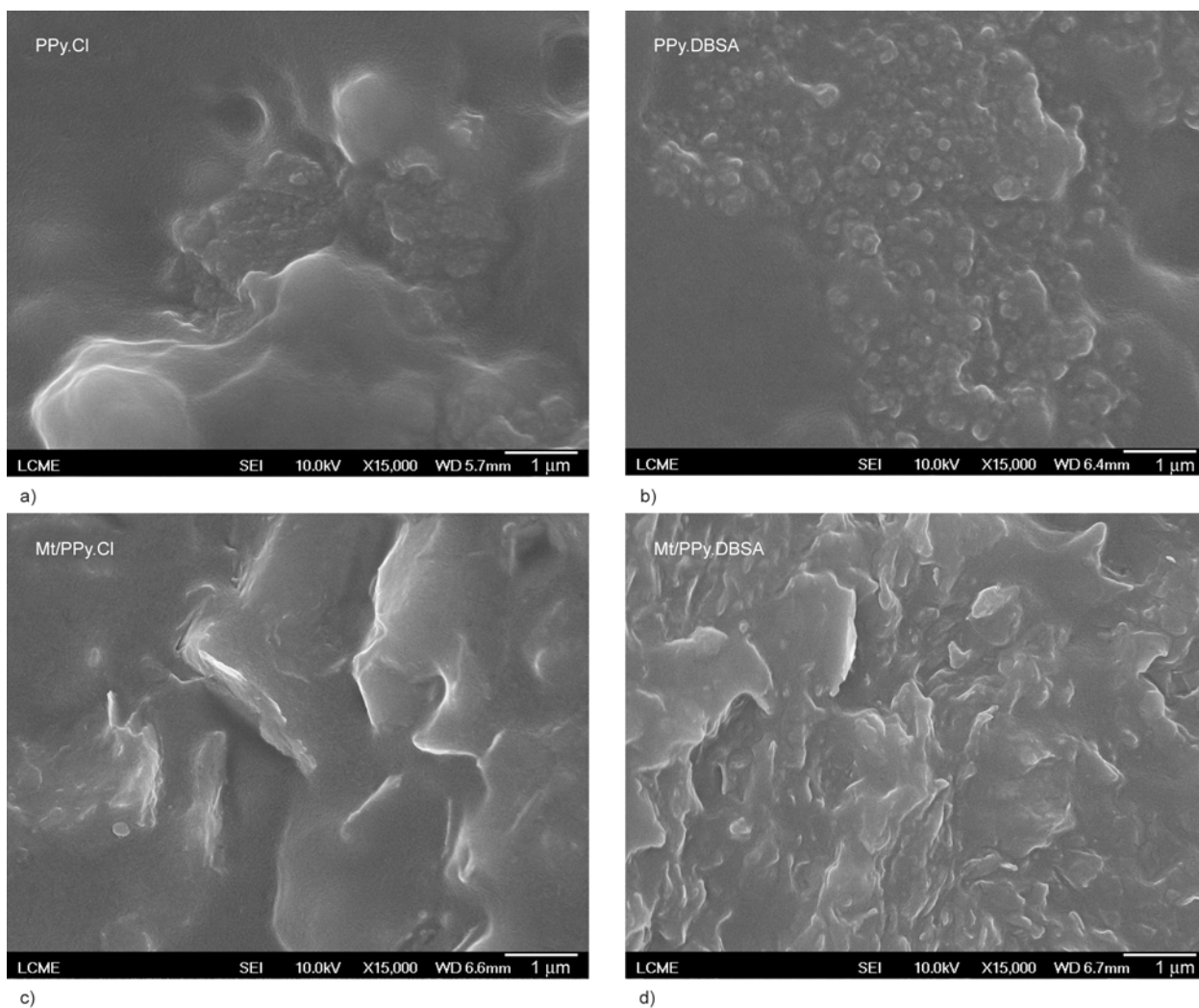The infrared spectra of neat TPU, TPU/PPy blends and TPU/Mt-PPy nanocomposites filled with 20 wt%

Figure 2. FESEM micrographs of cryogenically fractured samples with 20 wt% conductive for TPU/PPy.Cl (a), TPU/PPy.DBSA (b), TPU/Mt-PPy.Cl (c) and TPU/Mt-PPy.DBSA nanocomposites (d)
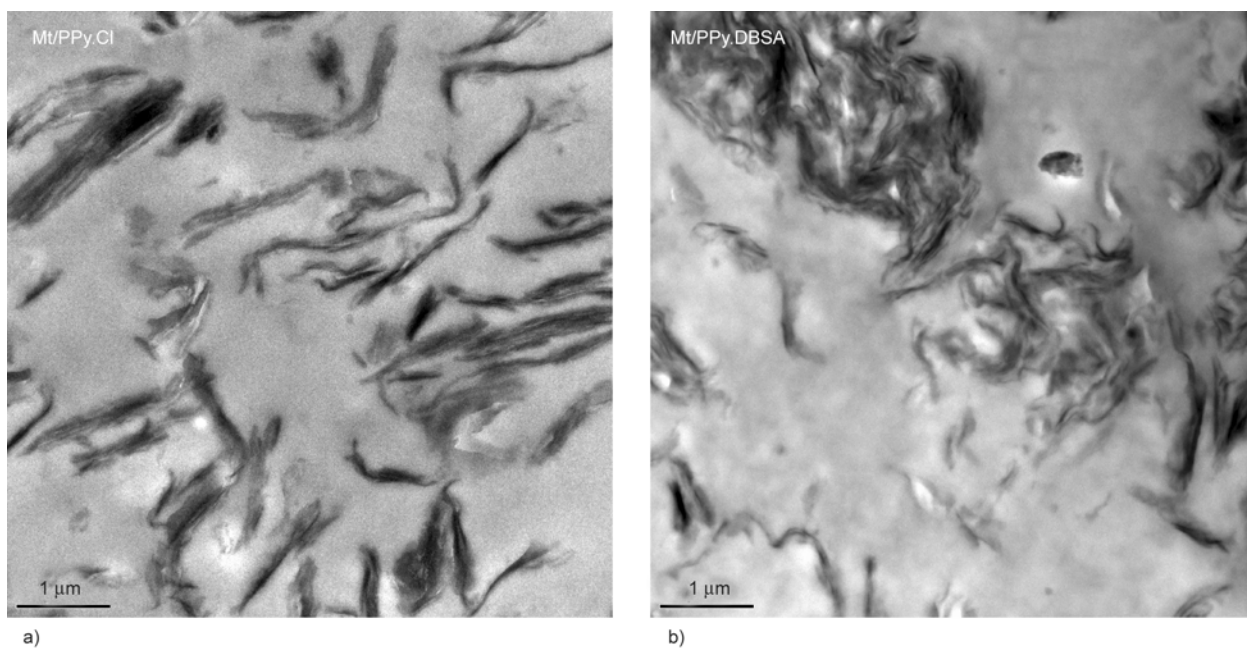

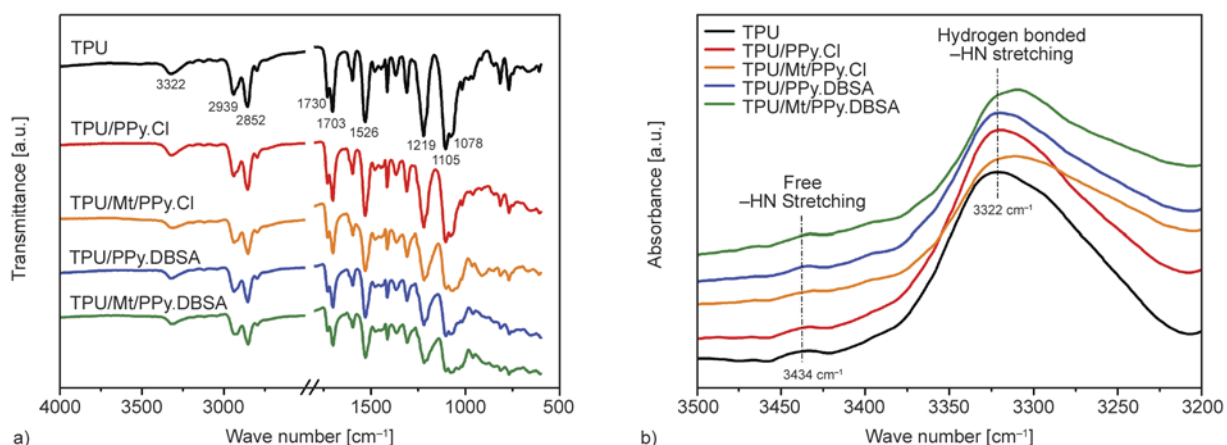**Figure 3.** TEM images of TPU/Mt-PPy.C (a) and Mt-PPy.DBSA (b)

Figure 4. FTIR spectra of (a) pure TPU and physical mixtures with 20 wt% loading of conductive filler and (b) free and hydrogen bonded N–H stretching region

of conductive filler are shown in Figure 4. The absorption bands of neat TPU in the region of 3320 cm^{-1} and at around 2900 (2939 and 2852 cm^{-1}) are assigned to the N–H and CH$_2$ absorption bands, respectively. The distinct bands that overlap intensively at 1730 and 1703 cm^{-1} are related to the free carbonyl and hydrogen-bonding absorption of the neat TPU molecules, respectively. The absorption band at 1526 cm^{-1} is attributed to –NH group of urethane while the bands at 1219 and 1105 cm^{-1} are assigned to the ether group [43–50].

The spectra of the TPU/PPy and TPU/Mt-PPy exhibited overlapped absorption bands of PPy and TPU. The band centered at 3320 cm^{-1}, related to the bonded –NH, was red-shifted to 3300 cm^{-1} for nanocomposites (Figure 4b) [51]. Furthermore, the band at 3435 cm^{-1} assigned to the free –NH group practically disappeared with the addition of the Mt-PPy.DBSA or Mt-PPy.Cl in the TPU matrix. These results suggest that the specific interaction between TPU and Mt-PPy.DBSA or Mt-PPy.Cl groups is higher than that observed for TPU and PPy.DBSA or PPy.Cl. An in-depth analysis of the infrared spectra in the range 1800 to 1650 cm^{-1} for neat TPU and its physical blends was carried out, as shown in Figure 5. The spectra with Gaussian deconvolution of absorption bands centered at 1730 and 1703 cm^{-1} are assigned to the free and site-specific interactions of the carbonyl group. As shown in Table 2, the absorption area ratio between free and bonded carbonyl groups (A1730/A1703) reduces significantly with increasing of PPy.DBSA, Mt-PPy.Cl and Mt-PPy.DBSA content, except for the PPy.Cl. The observed shifts in the –NH region (1350 to 1300 cm^{-1}) and the reduction of the free carbonyl

Table 2. Ratio of the area under the peak of C=O groups (free (A$_{1730}$) and hydrogen bonded C=O (A$_{1703}$)), with 20 wt% loading of conductive filler

Sample	A$_{(1730/1703)}$
TPU	0.46
TPU/PPy.Cl	0.48
TPU/Mt-PPy.Cl	0.35
TPU/PPy.DBSA	0.34
TPU/Mt-PPy.DBSA	0.30

absorption bands (A$_{1730}$/A$_{1703}$) provide direct support for the fact that site-specific interaction between the N–H and C=O functional groups are operative in blends and/or nanocomposites containing PPy.DBSA, Mt-PPy.Cl and Mt-PPy.DBSA. These data also reveal that there are considerable fractions of both free and bonded carbonyl amine groups even when TPU is the dominant (80 wt%) component. Moreover, the observed shifts and reduction of free carbonyl groups for TPU/Mt-PPy.DBSA are higher than those found for others blends and/or nanocomposites, suggesting higher interaction of TPU and Mt-PPy.DBSA. These results are consistent with those discussed in sections on morphology and electrical conductivity.

XRD curves of the neat TPU (Figure 6) exhibits a large and intense diffraction peak centered at 2θ = 19.98° assigned to the reflection plane (110) with d-value of 0.45 nm. This diffraction pattern can be attributed to the irregular segments of the amorphous phase and, chains arranged on short-range of the TPU rigid phase, respectively [52, 53]. According to Ramôa *et al.* [41] the neat Mt used in this study manifests a crystalline peak at 6.3° (2θ) assigned to the periodicity in the (001) direction of neat Mt and d-value is 1.4 nm. The Mt diffraction peak and basal
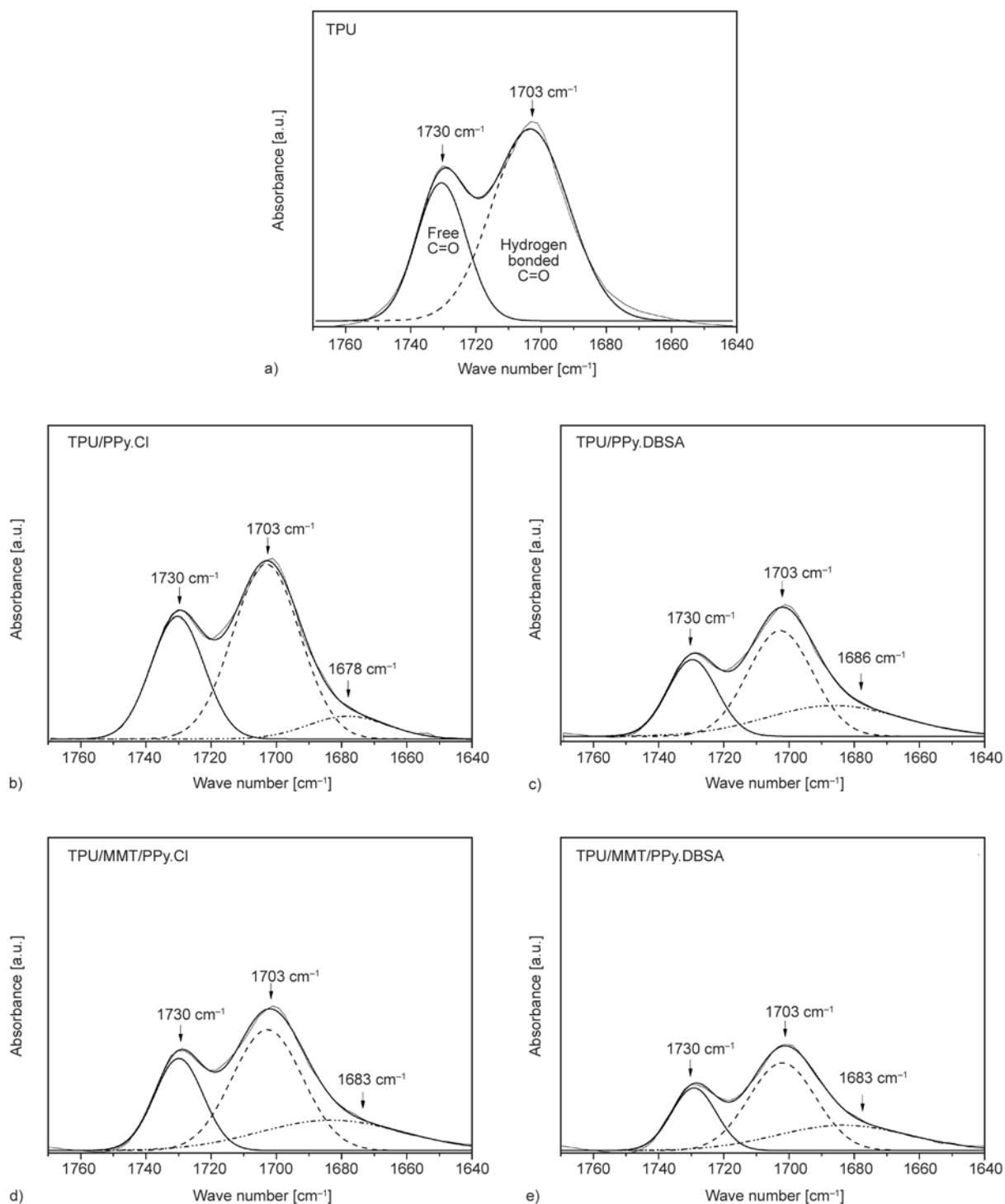
Figure 5. Deconvolution on the FTIR spectra in the free and hydrogen bonded carbonyl peaks (C=O and H–C=O) of pure TPU (a) and TPU composites with 20 wt% loading of conductive filler PPy.Cl (b), PPy.DBSA (c), Mt-PPy.Cl (d), Mt-PPy.DBSA (e)

distance $d_{(001)}$ for the TPU/Mt-PPy.Cl nanocomposites are shifted to 4.6° (1.9 nm), respectively, indicating an intercalation of Mt-PPy.Cl in the TPU matrix. However, the peak at 6.3° practically disappeared for TPU/Mt-PPy.DBSA nanocomposites. The storage (G') and loss moduli (G'') as a function frequency are shown in Figure 7 for neat TPU and its composites. At the lowest frequencies, neat TPU presents a liquid-like behavior ($G''>G'$). Furthermore, there is a transition from liquid to solid-like behavior ($G''<G'$) at a frequency of 31.8 Hz, while for TPU/PPy.Cl and TPU/PPy.DBSA composites containing 5 wt% of PPy.Cl, this transition was observed at 81.7 and 81.5 Hz, respectively. For both TPU/PPy
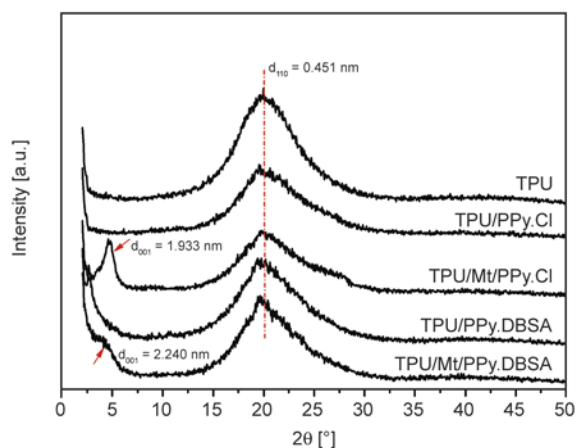
Figure 6. XRD patterns of pure TPU and TPU nanocomposites containing 20 wt% loading of conductive filler

blends, G' and G'' values decrease with increasing the amount of PPy, suggesting a certain degree of polymer matrix degradation. On the other hand, TPU/Mt-PPy.Cl and TPU/Mt -PPy.DBSA nanocomposites show a quite different behavior when compared with those found for TPU/PPy blends. For both TPU/Mt-PPy nanocomposites, G' and G'' values increase with increasing the Mt-PPy content in the TPU matrix. The significant increase in the storage modulus indicates that TPU/Mt-PPy nanocomposites exhibit a pseudo-solid-like behavior. Moreover, TPU/Mt-PPy nanocomposites with 5 wt% of Mt-PPy content show a transition from liquid to solid-like behavior at frequencies higher than 31.8 Hz, which is the same value observed for the neat TPU, while the values of G' becomes almost independent at lower frequency for nanocomposites containing 15 wt% of Mt-PPy. This behavior can be attributed to the percolative network formation, in which the conductive filler reduces the mobility of the TPU chain. The rheological percolative network increases the number of interfaces between conductive fillers, and thus an enhancement of the both elastic and viscous components is observed.

The loss tangent ($\tan\delta$) curves as a function of frequency reported in Figure 8 can provide an insight
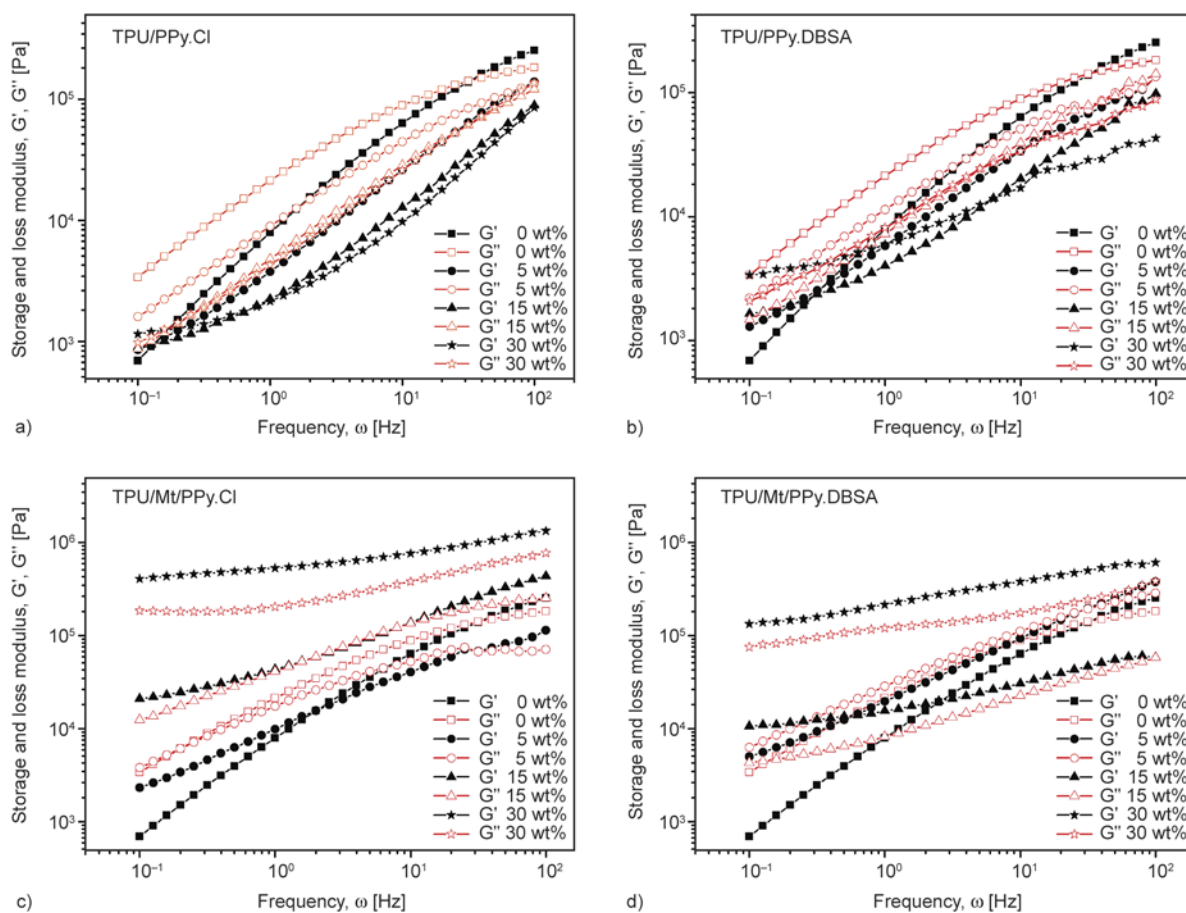
Figure 7. Storage modulus (G', full points) and loss modulus (G'', empty points) versus frequency (ω) at a temperature of 170°C for pure TPU and its composites containing 0, 5, 15 and 30 wt% of various conductive fillers: PPy.Cl (a), PPy.DBSA (b), Mt-PPy.Cl (c), Mt-PPy.DBSA (d)
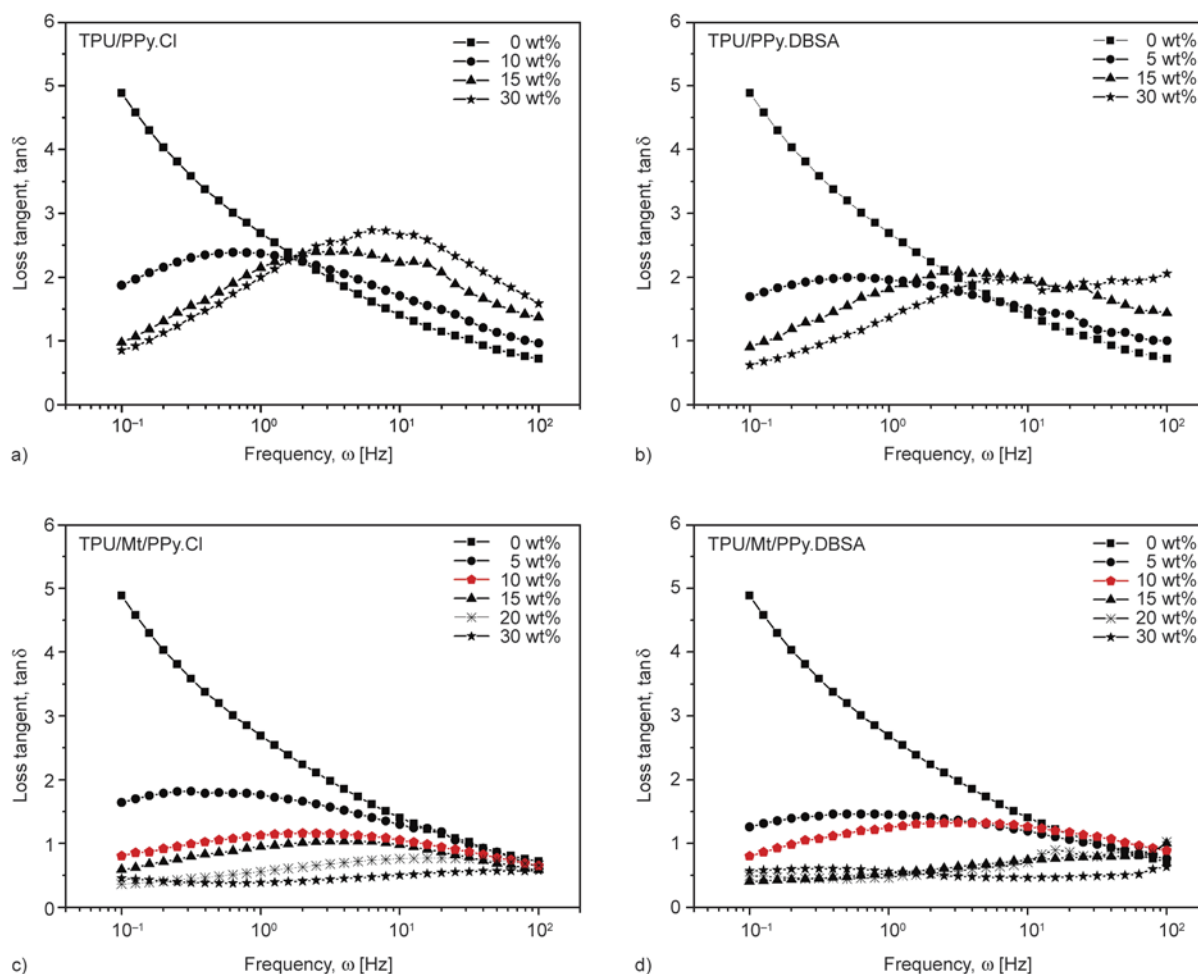
Figure 8. Loss tangent (tan δ) versus frequency (ω) at a temperature of 170°C for pure TPU and its composites containing various percentages and types of conductive fillers: PPy.Cl (a), PPy.DBSA (b), Mt-PPy.Cl (c), Mt-PPy.DBSA (d)

on the site-specific interactions between the polymer matrix and conducting fillers [54, 55]. According to Han *et al*. [56], for a composite system with high-level of conducting phase agglomeration, a larger and more intense tan δ curve with respect of neat insulating polymer can be observed. TPU/PPy.Cl and TPU/PPy.DBSA blends have shown this behavior, suggesting PPy agglomeration into TPU matrix. On the other hand, with increasing conducting filler, the TPU/Mt-PPy.Cl and TPU/Mt-PPy.DBSA nanocomposites show lower tan δ intensities when compared with the neat TPU, while for nanocomposites containing 15 and 30 wt% of Mt-Py tan δ values are practically frequency independent. In addition, TPU/Mt-PPy.DBSA composites exhibit lower tan δ values than TPU/Mt-PPy.Cl, indicating better distribution and dispersion of Mt-PPy.DBSA in the TPU matrix. According to Pötschke *et al*. [57], this behavior supports the idea that site-specific interactions at the interface of insulating polymer matrix and conductive filler could be operative.

Figure 9 shows the storage modulus *G′* as a function of loss modulus *G″* with frequency as a parameter for neat TPU and relative composites. These curves have been extensively used to investigate modifications in the structure of several polymeric systems at a fixed temperature [57–59]. According to McClory *et al*. [60] any change in the curve behavior of the composite compared with the neat PPy is an indication of network formation. It is observed that with increasing PPy.DBSA or PPy.Cl content, the variation of *G′* as a function of *G″* for TPU/PPy.DBSA and TPU/PPy.Cl blends at lower frequency region (terminal zone) is different from that found for neat TPU. This behavior is characteristic of a system with heterogeneous structure. On the other hand, in the high frequency region (rubbery plateau) these curves are overlapped to that found for the neat TPU, which highlights the occurrence of a homogeneous structure. As expected, these mixtures should present a heterogeneous system behavior for all frequency regions.
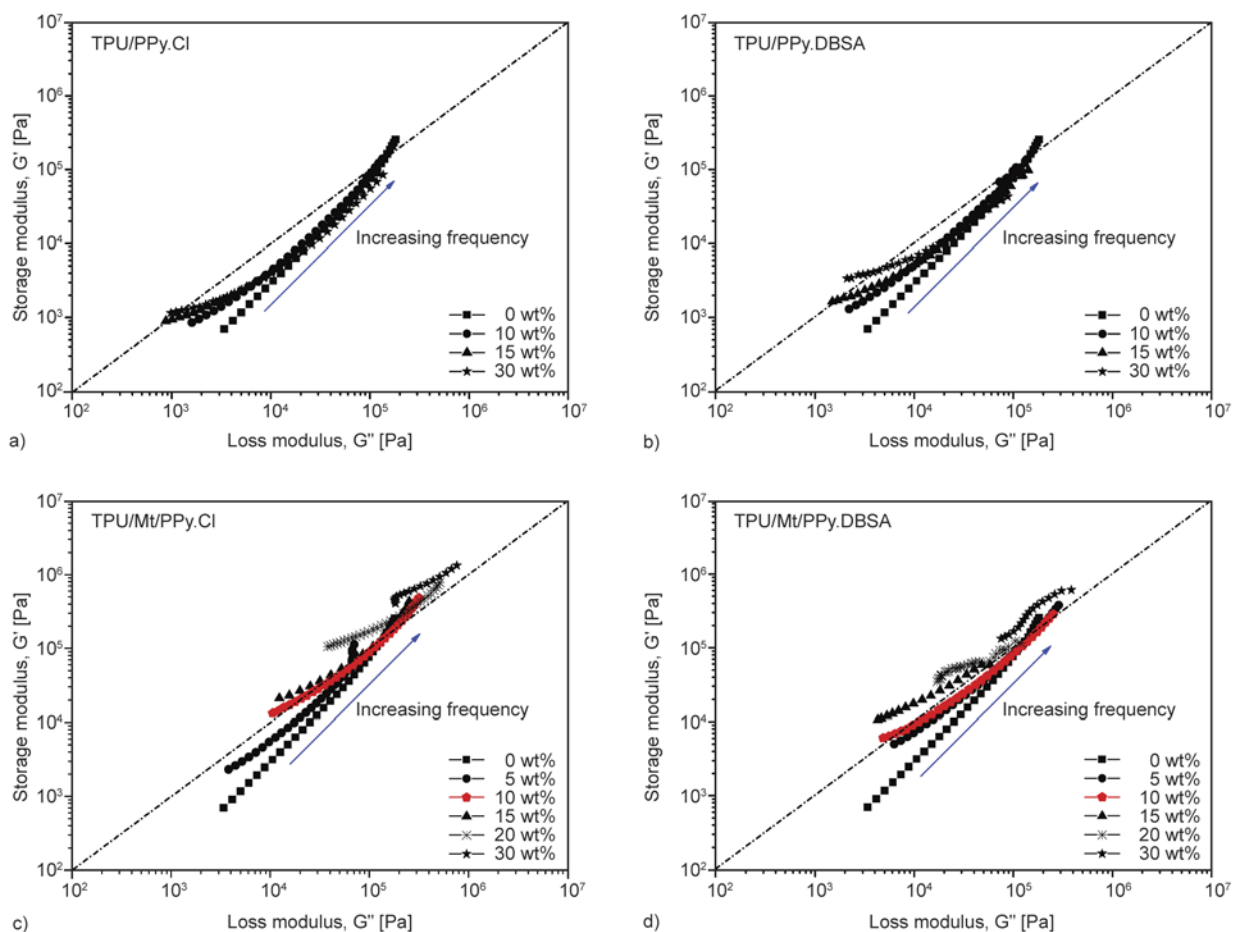
Figure 9. Han plot of storage modulus (*G′*) versus loss modulus (*G″*) at a temperature of 170°C for pure TPU and its composites containing various percentages and types of conductive fillers: PPy.Cl (a), PPy.DBSA (b), Mt-PPy.Cl (c), Mt-PPy.DBSA (d)

According to Barick and Tripathy [59] the different behavior observed for TPU/PPy.Cl and TPU/PPy.DBSA blends at higher and lower frequencies could be assigned to the difference of the dynamic relaxing processes for the neat TPU and mixtures. In addition, according to Han *et al.* [56] for a particular polymer system the applied shear stress at low frequency is not sufficient to disrupt the structure of the interconnected network due to the strong interactions between insulating polymer chains and conductive filler, resulting in a heterogeneous structure behavior below a critical shearing force. Above this critical point, with increasing the frequency, the shear stress is able to separate the conductive network structure and a homogeneous system behavior is observed. TPU/Mt-PPy.Cl and TPU/Mt-PPy.DBSA nanocomposites containing conductive filler loading up to 5 wt% show similar trend to those found for TPU/PPy.Cl and TPU/PPy.DBSA blends. However, above 10 wt% of Mt-PPy.DBSA and 15 wt% of Mt-PPy.Cl content, the curve slope of nanocom-

posites is higher than those observed for neat TPU for all the investigated frequencies. This result indicates that TPU/Mt-PPy.DBSA and TPU/Mt-PPy.Cl composites are more heterogeneous when compared to TPU/PPy.Cl and TPU/PPy.DBSA blends, due to the presence of a strong three-dimensional conductive network, which is not disrupted with the shear force. These changes in the curve slope of Mt-PPy.DBSA nanocomposites suggest that the interphase interaction of the TPU matrix and Mt-PPy.DBSA are higher in descendent order of that found for Mt-PPy.Cl, PPy.DBSA and PPy.Cl fillers [57, 61].

4. Conclusions
A new electrical conductive nanocomposite based on thermoplastic polyurethane and montmorillonite/dodecylbenzenesulfonic acid-doped polypyrrole (TPU/Mt-PPy.DBSA) with an electrical conductivity as high as 0.05 S·cm⁻¹ was successfully prepared through melt mixing process using an internal mix-

ing chamber. The structure and properties of the mixtures were strongly dependent on the site-specific interactions between the conductive filler and TPU chains. TPU/Mt-PPy.DBSA exhibits higher electrical conductivity and lower percolation threshold than TPU/Mt-PPy.Cl, TPU/PPy.Cl and TPU/PPy.DBSA mixtures. This behavior can be attributed to the strong interaction of Mt-PPy.DBSA particles and TPU matrix, which induces a better conductive network formation than those found for Mt-PPy.Cl, PPy.Cl and PPy.DBSA fillers. Furthermore, this synergistic effect can also be assigned to the presence of Mt that acts as a template for the PPy.DBSA, facilitating the formation of Mt-PPy.DBSA network in the TPU matrix. The results reported in this study prove that the morphology and electrical conductivity are significantly influenced by the composition of the conductive filler used in the melt mixing process, especially in the case of Mt-PPy.DBSA. Moreover, the present work reveals the potential use of Mt-PPy.DBSA as a new promising conductive filler for producing highly conductive polymer nanocomposites to be applied in several technological applications.

Acknowledgements

References

[1] Yang C., Liu P., Zhao Y.: Preparation and characterization of coaxial halloysite/polypyrrole tubular nanocomposites for electrochemical energy storage. Electrochimica Acta, **55**, 6857–6864 (2010).
DOI: 10.1016/j.electacta.2010.05.080

[2] Yanilmaz M., Kalaoglu F., Karakas H., Sarac A. S.: Preparation and characterization of electrospun polyurethane–polypyrrole nanofibers and films. Journal of Applied Polymer Science, **125**, 4100–4108 (2012).
DOI: 10.1002/app.36386

[3] Pojanavaraphan T., Magaraphan R.: Fabrication and characterization of new semiconducting nanomaterials composed of natural layered silicates (Na^+-MMT), natural rubber (NR), and polypyrrole (PPy). Polymer, **51**, 1111–1123 (2010).
DOI: 10.1016/j.polymer.2009.07.003

[4] Lee J-W., Serna F., Nickels J., Schmidt C. E.: Carboxylic acid-functionalized conductive polypyrrole as a bioactive platform for cell adhesion. Biomacromolecules, **7**, 1692–1695 (2006).
DOI: 10.1021/bm060220q

[5] Omastová M., Trchová M., Kovářová J., Stejskal J.: Synthesis and structural study of polypyrroles prepared in the presence of surfactants. Synthetic Metals, **138**, 447–455 (2003).
DOI: 10.1016/S0379-6779(02)00498-8

[6] Reung-u-Rai A., Prom-Jun A., Prissanaroon-Ouajai W.: Synthesis of highly conductive polypyrrole nanoparticles *via* microemulsion polymerization. Journal of Metals, Materials and Minerals, **18**, 27–31 (2008).

[7] Gurunathan K., Murugan A. V., Marimuthu R., Mulik U., Amalnerkar D.: Electrochemically synthesised conducting polymeric materials for applications towards technology in electronics, optoelectronics and energy storage devices. Materials Chemistry and Physics, **61**, 173–191 (1999).
DOI: 10.1016/S0254-0584(99)00081-4

[8] Jiang L., Jun H-K., Hoh Y-S., Lim J-O., Lee D-D., Huh J-S.: Sensing characteristics of polypyrrole–poly(vinyl alcohol) methanol sensors prepared by *in situ* vapor state polymerization. Sensors and Actuators B: Chemical, **105**, 132–137 (2005).
DOI: 10.1016/j.snb.2003.12.077

[9] Merlini C., dos Santo Almeida R., D'Ávila M. A., Schreiner W. H., de Oliviera Barra G. M.: Development of a novel pressure sensing material based on polypyrrole-coated electrospun poly(vinylidene fluoride) fibers. Materials Science and Engineering: B, **179**, 52–59 (2014).
DOI: 10.1016/j.mseb.2013.10.003

[10] Li M., Li H., Zhong W., Zhao Q., Wang D.: Stretchable conductive polypyrrole/polyurethane (PPy/PU) strain sensor with netlike microcracks for human breath detection. ACS Applied Materials and Interfaces, **6**, 1313–1319 (2014).
DOI: 10.1021/am4053305

[11] Hosseini S. H., Entezami A. A.: Conducting polymer blends of polypyrrole with polyvinyl acetate, polystyrene, and polyvinyl chloride based toxic gas sensors. Journal of Applied Polymer Science, **90**, 49–62 (2003).
DOI: 10.1002/app.12492

[12] Brady S., Diamond D., Lau K-T.: Inherently conducting polymer modified polyurethane smart foam for pressure sensing. Sensors and Actuators A: Physical, **119**, 398–404 (2005).
DOI: 10.1016/j.sna.2004.10.020

[13] Tjahyono A. P., Aw K. C., Travas-Sejdic J.: A novel polypyrrole and natural rubber based flexible large strain sensor. Sensors and Actuators B: Chemical, **166–167**, 426–437 (2012).
DOI: 10.1016/j.snb.2012.02.083

[14] Xu J., Zhu L., Bai Z., Liang G., Liu L., Fang D., Xu W.: Conductive polypyrrole–bacterial cellulose nanocomposite membranes as flexible supercapacitor electrode. Organic Electronics, **14**, 711–718 (2013).
DOI: 10.1016/j.orgel.2013.09.042

[15] Mi H., Zhang X., Ye X., Yang S.: Preparation and enhanced capacitance of core–shell polypyrrole/polyaniline composite electrode for supercapacitors. Journal of Power Sources, **176**, 403–409 (2008).
DOI: 10.1016/j.jpowsour.2007.10.070

[16] Olsson H., Nyström G., Strømme M., Sjödin M., Nyholm L.: Cycling stability and self-protective properties of a paper-based polypyrrole energy storage device. Electrochemistry Communications, **13**, 869–871 (2011).
DOI: 10.1016/j.elecom.2011.05.024

[17] Armelin E., Pla R., Liesa F., Ramis X., Iribarren J. I., Alemán C.: Corrosion protection with polyaniline and polypyrrole as anticorrosive additives for epoxy paint. Corrosion Science, **50**, 721–728 (2008).
DOI: 10.1016/j.corsci.2007.10.006

[18] Håkansson E., Amiet A., Nahavandi S., Kaynak A.: Electromagnetic interference shielding and radiation absorption in thin polypyrrole films. European Polymer Journal, **43**, 205–213 (2007).
DOI: 10.1016/j.eurpolymj.2006.10.001

[19] Yavuz Ö., Ram M. K., Aldissi M., Poddar P., Srikanth H.: Polypyrrole composites for shielding applications. Synthetic Metals, **151**, 211–217 (2005).
DOI: 10.1016/j.synthmet.2005.05.011

[20] Kim S. H., Jang S. H., Byun S. W., Lee J. Y., Joo J. S., Jeong S. H., Park M. J.: Electrical properties and EMI shielding characteristics of polypyrrole–nylon 6 composite fabrics. Journal of Applied Polymer Science, **87**, 1969–1974 (2003).
DOI: 10.1002/app.11566

[21] Wallace G. G., Campbell T. E., Innis P. C.: Putting function into fashion: Organic conducting polymer fibres and textiles. Fibers and Polymers, **8**, 135–142 (2007).
DOI: 10.1007/BF02875782

[22] Gasana E., Westbroek P., Hakuzimana J., De Clerck K., Priniotakis G., Kiekens P., Tseles D.: Electroconductive textile structures through electroless deposition of polypyrrole and copper at polyaramide surfaces. Surface and Coatings Technology, **201**, 3547–3551 (2006).
DOI: 10.1016/j.surfcoat.2006.08.128

[23] Xu H., Holzwarth J. M., Yan Y., Xu P., Zheng H., Yin Y., Li S., Ma P. X.: Conductive PPy/PDLLA conduit for peripheral nerve regeneration. Biomaterials, **35**, 225–235 (2014).
DOI: 10.1016/j.biomaterials.2013.10.002

[24] Otero T. F., Cortés M. T.: Artificial muscles with tactile sensitivity. Advanced Materials, **15**, 279–282 (2003).
DOI: 10.1002/adma.200390066

[25] Hara S., Zama T., Takashima W., Kaneto K.: Polypyrrole–metal coil composite actuators as artificial muscle fibres. Synthetic Metals, **146**, 47–55 (2004).
DOI: 10.1016/j.synthmet.2004.06.021

[26] Smela E.: Conjugated polymer actuators for biomedical applications. Advanced Materials, **15**, 481–494 (2003).
DOI: 10.1002/adma.200390113

[27] Peighambardoust S. J., Pourabbas B.: Preparation and characterization of nylon-6/PPy/MMT composite of nanocomposite. Journal of Applied Polymer Science, **106**, 697–705 (2007).
DOI: 10.1002/app.26709

[28] Peighambardoust S. J., Pourabbas B.: Synthesis and characterization of conductive polypyrrole/montmorillonite nanocomposites *via* one-pot emulsion polymerization. Macromolecular Symposia, **247**, 99–109 (2007).
DOI: 10.1002/masy.200750112

[29] Sevil B., Zuhal K.: Synthesis and characterization of polypyrrole nanoparticles and their nanocomposites with poly(propylene). Macromolecular Symposia, **295**, 59–64 (2010).
DOI: 10.1002/masy.200900164

[30] Ashraf S. M., Ahmad S., Riaz U.: Pseudothermoset blends of poly (methyl methacrylate) and polypyrrole morphological, thermal, and conductivity studies. Journal of Applied Polymer Science, **93**, 82–91 (2004).
DOI: 10.1002/app.20404

[31] Mahmud H. N. M. E., Kassim A., Zainal Z., Yunus W. M. M.: Fourier transform infrared study of polypyrrole–poly(vinyl alcohol) conducting polymer composite films: Evidence of film formation and characterization. Journal of Applied Polymer Science, **100**, 4107–4113 (2006).
DOI: 10.1002/app.23327

[32] Kotal M., Srivastava S. K., Paramanik B.: Enhancements in conductivity and thermal stabilities of polypyrrole/polyurethane nanoblends. Journal of Physical Chemistry C, **115**, 1496–1505 (2011).
DOI: 10.1021/jp1081643

[33] Muller D., Garcia M., Salmoria G. V., Pires A. T. N., Paniago R., Barra G. M. O.: SEBS/PPy.DBSA blends: Preparation and evaluation of electromechanical and dynamic mechanical properties. Journal of Applied Polymer Science, **120**, 351–359 (2011).
DOI: 10.1002/app.33141

[34] Omastová M., Košina S., Pionteck J., Janke A., Pavlinec J.: Electrical properties and stability of polypyrrole containing conducting polymer composites. Synthetic Metals, **81**, 49–57 (1996).
DOI: 10.1016/0379-6779(96)80228-1

[35] Omastová M., Pionteck J., Košina S.: Preparation and characterization of electrically conductive polypropylene/polypyrrole composites. European Polymer Journal, **32**, 681–689 (1996).
DOI: 10.1016/0014-3057(95)00206-5

[36] Boukerma K., Piquemal J-Y., Chehimi M. M., Mravčáková M., Omastová M., Beaunier P.: Synthesis and interfacial properties of montmorillonite/polypyrrole nanocomposites. Polymer, **47**, 569–576 (2006).
DOI: 10.1016/j.polymer.2005.11.065

[37] Zhu D., Bin Y., Oishi K., Fukuda Y., Nakaoki T., Matsuo M.: Conductive composite materials of polyethylene and polypyrrole with high modulus and high strength. Macromolecular Symposia, **214**, 197–216 (2004).
DOI: 10.1002/masy.200451014

[38] Mravčáková M., Omastová M., Pötschke P., Pozsgay A., Pukánszky B., Pionteck J.: Poly(propylene)/montmorillonite/polypyrrole composites: Structure and conductivity. Polymers for Advanced Technologies, **17**, 715–726 (2006).
DOI: 10.1002/pat.765

[39] Boubakri A., Haddar N., Elleuch K., Bienvenu Y.: Impact of aging conditions on mechanical properties of thermoplastic polyurethane. Materials and Design, **31**, 4194–4201 (2010).
DOI: 10.1016/j.matdes.2010.04.023

[40] Fernández-d'Arlas B., Khan U., Rueda L., Coleman J. N., Mondragon I., Corcuera M. A., Eceiza A.: Influence of hard segment content and nature on polyurethane/multiwalled carbon nanotube composites. Composites Science and Technology, **71**, 1030–1038 (2011).
DOI: 10.1016/j.compscitech.2011.02.006

[41] Ramôa S. D. A. S., Barra G. M. O., Merlini C., Schreiner W. H., Livi S., Soares B. G.: Production of montmorillonite/polypyrrole nanocomposites through *in situ* oxidative polymerization of pyrrole: Effect of anionic and cationic surfactants on structure and properties. Applied Clay Science, **104**, 160–167 (2015).
DOI: 10.1016/j.clay.2014.11.026

[42] Mravčáková M., Omastová M., Olejníková K., Pukánszky B., Chehimi M. M.: The preparation and properties of sodium and organomodified-montmorillonite/polypyrrole composites: A comparative study. Synthetic Metals, **157**, 347–357 (2007).
DOI: 10.1016/j.synthmet.2007.04.005

[43] Menes O., Cano M., Benedito A., Giménez E., Castell P., Maser W. K., Benito A. M.: The effect of ultra-thin graphite on the morphology and physical properties of thermoplastic polyurethane elastomer composites. Composites Science and Technology, **72**, 1595–1601 (2012).
DOI: 10.1016/j.compscitech.2012.06.016

[44] Bistričić L., Baranović G., Leskovac M., Bajsić E. G.: Hydrogen bonding and mechanical properties of thin films of polyether-based polyurethane–silica nanocomposites. European Polymer Journal, **46**, 1975–1987 (2010).
DOI: 10.1016/j.eurpolymj.2010.08.001

[45] Russo P., Lavorgna M., Piscitelli F., Acierno D., Di Maio L.: Thermoplastic polyurethane films reinforced with carbon nanotubes: The effect of processing on the structure and mechanical properties. European Polymer Journal, **49**, 379–388 (2013).
DOI: 10.1016/j.eurpolymj.2012.11.008

[46] Pattanayak A., Jana S. C.: Properties of bulk-polymerized thermoplastic polyurethane nanocomposites. Polymer, **46**, 3394–3406 (2005).
DOI: 10.1016/j.polymer.2005.03.021

[47] Petcharoen K., Sirivat A.: Electrostrictive properties of thermoplastic polyurethane elastomer: Effects of urethane type and soft–hard segment composition. Current Applied Physics, **13**, 1119–1127 (2013).
DOI: 10.1016/j.cap.2013.03.005

[48] Ferry A., Jacobsson P., van Heumen J. D., Stevens J. R.: Raman, infra-red and D.S.C. studies of lithium coordination in a thermoplastic polyurethane. Polymer, **37**, 737–744 (1996).
DOI: 10.1016/0032-3861(96)87248-X

[49] Yilgor I., Yilgor E., Guler I. G., Ward T. C., Wilkes G. L.: FTIR investigation of the influence of diisocyanate symmetry on the morphology development in model segmented polyurethanes. Polymer, **47**, 4105–4114 (2006).
DOI: 10.1016/j.polymer.2006.02.027

[50] Van Heumen J. D., Stevens J. R.: The role of lithium salts in the conductivity and phase morphology of a thermoplastic polyurethane. Macromolecules, **28**, 4268–4277 (1995).
DOI: 10.1021/ma00116a030

[51] Barick A. K., Tripathy D. K.: Effect of organoclay on the morphology, mechanical, thermal, and rheological properties of organophilic montmorillonite nanoclay based thermoplastic polyurethane nanocomposites prepared by melt blending. Polymer Engineering and Science, **50**, 484–498 (2010).
DOI: 10.1002/pen.21556

[52] Barick A. K., Tripathy D. K.: Preparation and characterization of carbon nanofiber reinforced thermoplastic polyurethane nanocomposites. Journal of Applied Polymer Science, **124**, 765–780 (2012).
DOI: 10.1002/app.35066

[53] Barick A. K., Tripathy D. K.: Preparation, characterization and properties of acid functionalized multi-walled carbon nanotube reinforced thermoplastic polyurethane nanocomposites. Materials Science and Engineering: B, **176**, 1435–1447 (2011).
DOI: 10.1016/j.mseb.2011.08.001

[54] Pistor V., Lizot A., Fiorio R., Zattera A. J.: Influence of physical interaction between organoclay and poly(ethylene-*co*-vinyl acetate) matrix and effect of clay content on rheological melt state. Polymer, **51**, 5165–5171 (2010).
DOI: 10.1016/j.polymer.2010.08.045

[55] Hyun Y. H., Lim S. T., Choi H. J., John M. S.: Rheology of poly(ethylene oxide)/organoclay nanocomposites. Macromolecules, **34**, 8084–8093 (2001).
DOI: 10.1021/ma002191w

[56] Han S-I., Lim J. S., Kim D. K., Kim M. N., Im S. S.: *In situ* polymerized poly(butylene succinate)/silica nanocomposites: Physical properties and biodegradation. Polymer Degradation and Stability, **93**, 889–895 (2008).
DOI: 10.1016/j.polymdegradstab.2008.02.007

[57] Pötschke P., Fornes T. D., Paul D. R.: Rheological behavior of multiwalled carbon nanotube/polycarbonate composites. Polymer, **43**, 3247–3255 (2002).
DOI: 10.1016/S0032-3861(02)00151-9

[58] Di Y., Iannace S., Di Maio E., Nicolais L.: Nanocomposites by melt intercalation based on polycaprolactone and organoclay. Journal of Polymer Science Part B: Polymer Physics, **41**, 670–678 (2003).
DOI: 10.1002/polb.10420

[59] Barick A. K., Tripathy D. K.: Nanostructure morphology and dynamic rheological properties of nanocomposites based on thermoplastic polyurethane and organically modified montmorillonite. Polymer Bulletin, **66**, 1231–1253 (2011).
DOI: 10.1007/s00289-010-0395-6

[60] McClory C., McNally T., Baxendale M., Pötschke P., Blau W., Ruether M.: Electrical and rheological percolation of PMMA/MWCNT nanocomposites as a function of CNT geometry and functionality. European Polymer Journal, **46**, 854–868 (2010).
DOI: 10.1016/j.eurpolymj.2010.02.009

[61] Lee D., Lee S-H., Kim S., Char K., Park J. H., Bae Y. H.: Micro-phase-separation behavior of amphiphilic polyurethanes involving poly(ethylene oxide) and poly (tetramethylene oxide). Journal of Polymer Science Part B: Polymer Physics, **41**, 2365–2374 (2003).
DOI: 10.1002/polb.10504